EXPERIMENTAL AND NUMERICAL STUDY OF A TWO-STROKE POPPET VALVE ENGINE FUELLED WITH GASOLINE AND ETHANOL

A thesis submitted for the degree of
Doctor of Philosophy

by

Macklini Dalla Nora

Department of Mechanical, Aerospace and Civil Engineering
College of Engineering, Design and Physical Sciences
Brunel University London

November 2015

Abstract

The restrictions imposed by CO_2 emission standards in Europe and many countries have promoted the development of more efficient spark ignition engines. The reduced swept volume and number of cylinders of four-stroke engines has significantly improved fuel economy by means of lower pumping and friction losses. This approach, known as engine downsizing, has demonstrated its potential of reducing fuel consumption on its own as well as applied to hybrid vehicles where a low weight engine is desired. However, aggressive engine downsizing is currently constrained by thermal and mechanical stresses and knocking combustion. In order to overcome these limitations, the present work evaluates the application of a conventional poppet valve direct injection engine into the two-stroke cycle.

Two-stroke engines have the ability to produce higher power with reduced swept volume and less weight than four-stroke engines thanks to the doubled firing frequency. These advantages, although, are sometimes offset by poorer emissions resulted from fuel short-circuiting; lower thermal efficiency resulted from short expansion process; and reduced engine durability due to lubrication issues. Therefore, in this research the four-stroke engine architecture was employed so these shortcomings could be addressed by the use of direct fuel injection, variable valve actuation and a wet crankcase, respectively. The burnt gases were scavenged during a long valve overlap by means of boosted air supplied by an external compressor. An electrohydraulic fully-variable valve train enabled the optimisation of the gas exchange process in a variety of engine operating conditions. The air-fuel mixture formation was evaluated through computational fluid dynamic simulations and correlated to experimental tests. In addition, the engine operation with ethanol was assessed in a wide range of engine loads and speeds. Finally, the engine performance, combustion process, air-fuel mixing and gas exchange results were presented, discussed and contextualised with current four-stroke engines.

Keywords: Two-stroke poppet valve engine; gasoline and ethanol direct injection; engine downsizing; supercharged two-stroke cycle.

List of contents

List of illustrations

List of tables

Acknowledgements

I would like to acknowledge the Brazilian government, particularly the Brazilian council for scientific and technological development (CNPq - Brasil), for funding my studies at Brunel University London.

I am deeply grateful to my supervisor, Professor Hua Zhao, for the vital guidance and by giving me the opportunity to work in one of the greatest engine research groups in the UK.

My studies at Brunel would not have been possible without the help of Dr Mario Martins from the Federal University of Santa Maria (UFSM – Brasil). His networking and encouragement were essential in this matter. Besides, Professors Luiz Wrobel (Brunel) and Paulo Romeu (UFSM) had also an important role on assisting me in the beginning of my research.

I am thankful to the assistance and friendship of the technicians Andy Selway, Chris Allan, Clive Barret and Greg Jameson. Their commitment and perfectionism were simply outstanding.

The cooperation of AVL LIST GmbH in providing the software AVL Fire used in this research, under the AST University Partnership Program, is surely worth mentioning. My sincere thanks go to Dr Reinhard Tatschl for the support.

To all my colleagues and friends, especially Vinicius, Thompson, Ian and Yan, you not only helped me in the lab but were also valuable companies and a source of motivation.

Finally, and perhaps the most important, it is the love and emotional support of my parents. For all the years that Izane and Renato dedicated to my education, this is possibly the most expressive outcome and I dedicate you such work. I am also indebted to my girlfriend Fernanda for having to stay away from me for all this time. Your affection gave me strength to carry on and I will not forget it.

Notation

A_f: engine accessories friction

A: nitrogen to oxygen ratio

ATDC: after top dead centre

B: carbon dioxide to oxygen ratio

B_f: in-cylinder peak pressure friction multiplier

BDC: bottom dead centre

BEV: battery electric vehicle

BMEP: brake mean effective pressure

BSFC: brake specific fuel consumption

c_p: specific heat at constant pressure

c_v: specific heat at constant volume

C: water vapour to oxygen ratio

C_D: particle drag coefficient

C_f: piston hydrodynamic friction multiplier

$C_{\varepsilon 1}, C_{\varepsilon 2}, C_1, C_2$: constants of the k-ζ-f model

CA: crank angle

CAI: controlled auto-ignition

CE: charging efficiency

CFD: computational fluid dynamics

CI: compression ignition

COV_{IMEP}: covariance of the IMEP

COV: coefficient of variance

CPS: cam profile switching

$C_xH_yO_z$: oxygenated general hydrocarbon fuel

D_{int}: intake pipe diameter

D_f: piston windage friction multiplier

DAQ: data acquisition

DI: direct injection

e: ethanol volume fraction in fuel

E: law of the wall's constant

EBP: exhaust backpressure

ECR: effective compression ratio

ECU: engine control unit

EER: effective expansion ratio

EGR: exhaust gas recycling

EPA: Environmental Protection Agency

EPC: exhaust port closing

EPO: exhaust port opening

EU: European Union

EVC: exhaust valve closing

EVM: eddy viscosity model

EVO: exhaust valve opening

EGR_{in}: internal exhaust gas recycling

f: elliptic function

FID: flame ionisation detector

FMEP: friction mean effective pressure

g: gravitational acceleration vector

GDI: gasoline direct injection

GHG: greenhouse gas

h: enthalpy

H_a: ambient humidity

HCCI: homogeneous charge compression ignition

HEV: hybrid electric vehicle

HHR: heat release rate

I_{turb}: turbulence intensity

ICE: internal combustion engine

IMEP: indicated mean effective pressure

IPC: intake port closing

IPO: intake port opening

ISCO: indicated specific carbon monoxide emission
ISFC: indicated specific fuel consumption
ISNOx: indicated specific nitrogen oxides emission
ISsoot: indicated specific soot emission
ISUHC: indicated specific unburnt hydrocarbons emission
IVC: intake valve closing
IVO: intake valve opening
k: turbulent kinetic energy
k_f: fuel specific factor
k_{hG}: ambient humidity correction factor
k_w: dry-to-wet correction factor
k_{FID}: correction factor for the FID response to oxygenated fuels
K: water-gas equilibrium constant
KLS: knock limited spark advance
l: turbulent length scale
L: connecting rod length
LHV_{fuel}, LHV: lower heating value of fuel
LHV_{H_2}: lower heating value of hydrogen
LHV_C: lower heating value of solid carbon
LHV_{CO}: lower heating value of carbon monoxide
LHV_{UHC}: lower heating value of unburnt hydrocarbons
LNT: lean NOx trap
LSPI: low speed pre-ignition
LTC: low temperature combustion
LVDT: linear variable displacement transducer
m/m: mass basis
m_{air}: intake air mass per cycle
$m_{trap\ air}$: in-cylinder trapped air mass per cycle
$m_{trap\ del\ air}$: in-cylinder trapped delivered air mass per cycle
m_{trap}: in-cylinder trapped mass per cycle
m_{fuel}: fuel mass injected per cycle
$\dot{m}_{air}$: air mass flow rate
$\dot{m}_{dry\ air}$: dry air mass flow rate
$\dot{m}_{fuel}$: fuel mass flow rate
$\dot{m}_{soot}$: mass flow rate of soot
$\dot{m}_{CO}$: mass flow rate of carbon monoxide
$\dot{m}_{H_2}$: mass flow rate of hydrogen
$\dot{m}_{UHC}$: mass flow rate of unburnt hydrocarbons
MBDOE: million oil-equivalent barrels per day
MBT: minimum ignition advance for best torque
MFB: mass fraction burnt
n: number of air moles
n_{cyl}: number of cylinders
n_{TOT}: total number of moles
N: engine speed
NA: naturally aspirated
NEDC: New European Driving Cycle
NOx: nitrogen oxides
NVH: noise vibration and harshness

NVO: negative valve overlap
ppm: parts per million
p: pressure
p_0: standard reference pressure
p_a: ambient pressure
p_{int}: intake pressure
p_{max}: maximum in-cylinder pressure
P_c: compressor or supercharger power consumption
P_i: indicated power
P_{is}: indicated specific power
PFI: port fuel injection
PHEV: plugin hybrid electric vehicle
PM: particle mass
PN: particle number
PPC: partially premixed combustion
PRR: pressure rise rate
PVO: positive valve overlap
$\dot{q}_{exh}$: exhaust mass flow rate
Q_{ch}: combustion energy release
Q_{ht}: heat transfer
Q_{net}: net heat release
rpm: revolutions per minute
R: specific gas constant
RANS: Reynolds averaged Navier-Stokes equations
R_c: compression ratio
R_T: reverse tumble ratio
R^2: coefficient of determination
RH: relative humidity
RON: research octane number
std: standard deviation
S: stroke
S_x, S_y, S_z, S_Φ: source terms
SACI: spark assisted compression ignition
SC_{air}: air short-circuiting
SCR: selective catalytic reduction
SI: spark ignition
SOI: start of fuel injection
SP: water saturation pressure
SR: scavenge ratio
SR_{pd}: scavenge ratio of perfect displacement
t: time
T: temperature
T_0: standard reference temperature
T_a: ambient temperature
T_{is}: indicated specific torque
TDC: top dead centre
TE_{air}: air trapping efficiency
TE_{fuel}: fuel trapping efficiency
TKE: turbulent kinetic energy
TS: time-step
TWC: three-way catalyst
u: x-component of the instantaneous flow velocity
u': velocity fluctuation component in the x-direction
u_{gas}: gas molar fraction
U: x-component of the mean flow velocity
$\mathbf{U}$: mean component of the velocity vector
$\mathbf{U}_d$: droplet velocity vector
U_{int}: intake mean flow velocity
U_s: gas sensible energy
UHC: unburnt hydrocarbons

v: y-component of the instantaneous flow velocity
v': velocity fluctuation component in the y-direction
v/v: volume basis
V: volume
V: y-component of the mean flow velocity
V_{cell}: cell volume
V_{clr}: clearance volume
V_d: displaced volume
V_{ins}: instantaneous in-cylinder volume
VCU: valve control unit
VGT: variable geometry turbine
VVA: variable valve actuation
w: z-component of the instantaneous flow velocity
w': velocity fluctuation component in the z-direction
W: compression or expansion work
W: z-component of the mean flow velocity
WLTC: worldwide light duty test procedure
$W_{c,i}$: indicated work per cycle
W_{ALF}: hydrogen mass content in the fuel
W_{EPS}: oxygen mass content in the fuel
x: normalised carbon content
y: hydrogen to carbon ratio
y^+: dimensionless wall distance
z: oxygen to carbon ratio
[CO]: volumetric exhaust carbon monoxide concentration
[NOx]: volumetric exhaust nitrogen oxides concentration
[soot]: soot concentration
[UHC]: volumetric exhaust unburnt hydrocarbons concentration

γ: specific heat ratio c_p/c_v
ε: turbulent kinetic energy dissipation
ζ: velocity scale ratio
η_c: combustion efficiency
$\eta_{i\ corr}$: corrected indicated efficiency
η_i: indicated efficiency
η_{comp}: compressor efficiency
η_t: thermal efficiency
θ: crank angle
κ: von Karman constant
λ: relative air/fuel ratio (lambda)
λ_{cyl}: in-cylinder lambda
λ_{exh}: exhaust lambda
μ: dynamic viscosity
μ_t: turbulent (or eddy) viscosity
Π: production of turbulent kinetic energy
ρ: density
ρ_{cell}: cell fluid density
ρ_{ext}: exhaust gas density
ρ_{int}: intake air density
$\sigma_k, \sigma_\varepsilon, \sigma_\zeta$: Prandtl numbers
τ: Kolmogorov time scale
Γ: diffusion coefficient
Φ: scalar
Ω: Kolmogorov length scale

Chapter One
Introduction

1.1 Preface

Mobility and power generation have played a significant role in the development of human civilisation. Particularly after the industrial revolution, started in the United Kingdom in the 18th century, it became clear the need for more efficient power sources with better power-to-weight ratio than reciprocating steam engines. The introduction of internal combustion engines, initially by means of the spark ignition (SI) combustion and lately under the compression ignition (CI) concept, marked the transition to this new type of power plant. With its development and popularisation in the early 20th century, the internal combustion engine (ICE) has become the main propulsion system for people's transportation and logistics of goods and services.

The steep increase in the ICE production in the first half of the 20th century, mostly for vehicle applications, raised concerns about pollutant emissions and their impact on the environment and human health. Besides, the every growing demand for fossil fuels required greater efficiencies from those engines, so the adoption of emissions and fuel economy standards became widely discussed. Led by the USA in the early 1960's, and followed by several European countries and Japan, emissions regulations have been proposed and constantly reviewed since then. Nowadays, these standards, or variants of them, are applied worldwide from small motorcycles to heavy duty truck engines.

Extensive research has been carried out on developing higher efficiency SI engines for passenger cars and light-duty vehicles. In the last decades several more efficient combustion principles have been proposed to replace gasoline SI combustion. Amongst them is the homogeneous charge compression ignition (HCCI) combustion, also known as controlled auto-ignition (CAI) combustion. However, whilst these concepts are not fully developed, SI combustion remains as the major heat release process in gasoline engines.

In the context of SI combustion, engine downsizing has been accepted as an effective method to reduce fuel consumption at part load operation in four-stroke engines. In this approach the engine displacement and the number of cylinders are reduced so the mid-low load operating points are shifted towards regions where pumping and friction losses are minimised. However, the higher load engine operation condition has raised concerns about thermal and structural stresses, as well as more frequent knocking combustion and even low speed pre-ignition (super-knock). Compared to larger displacement engines, the transient performance and poor torque response in the mid-low speed range have also affected highly downsized SI engines.

Compared to four-stroke engines, the SI two-stroke cycle can achieve similar values of torque with lower in-cylinder pressures and hence less structural and thermal stresses. The doubled firing frequency of two-stroke engines provides greater power density and power-to-weight ratio than four-stroke engines particularly in the mid-low speed range. However, typical ported two-stroke engines suffer from poor fuel consumption, excessive unburnt hydrocarbon (UHC) emissions and crank train lubrication/durability issues. The first two mentioned issues are primarily associated to crankcase scavenged engines, where the air-fuel mixture is prone to short-circuit to the exhaust and hence increasing fuel consumption and UHC emissions. In this regard, the use of direct fuel injection has enabled the mixture formation to take place after the exhaust ports/valves are closed, so no fuel is lost to the exhaust. The problem with the crank train lubrication and durability remains on the adoption of a dry sump, so the lubricant oil needs to be added to the intake charge. To overcome these issues the architecture employed by four-stroke engines with overhead valves and a wet sump was proposed in the two-stroke cycle in the early 1990’s, in the so called two-stroke poppet valve engine. In this concept the scavenging process is performed during a long valve overlap around bottom dead centre every crankshaft revolution. The fresh air, used to scavenge the burnt gases, is externally compressed usually by means of a supercharger and/or turbocharger.

Alongside the pursuit for more efficient SI engines, the replacement of fossil fuels by renewable sources has been subjected to extensive research. Amongst the

many fuels originated from the biomass, ethanol has proven to be the most suitable fuel for spark ignition engines. Ethanol also provides interesting physicochemical properties, such as improved knocking resistance, higher heat of vaporisation, greater oxygen content and a faster burning speed than gasoline. Therefore, its use in SI engines can result in significant improvements in thermal efficiency and emissions.

The requirement for smaller engines with higher power densities for the application in conventional and hybrid passenger cars has renewed the interest in the two-stroke cycle. Moreover, the adoption of biofuels, such as ethanol, has the potential to improve fuel efficiency whilst reducing the carbon footprint left by SI engines. For these reasons, the present research focuses on investigating a two-stroke poppet valve engine fuelled with gasoline and ethanol by means of experiments and computational fluid dynamic (CFD) simulations.

1.2 Research objectives

The primary goal of this research is to improve the two-stroke poppet valve engine operation in a diverse range of conditions using gasoline and ethanol via laboratory experiments and numerical simulation. The specific objectives of this study comprise:

- To expand the understanding about the gas exchange and mixture formation processes in the two-stroke poppet valve engine;
- To explore the effects of intake and exhaust valve parameters at different engine speeds and loads in the performance, combustion and scavenging processes of the two-stroke poppet valve engine;
- To investigate the performance, emissions and combustion characteristics of the two-stroke poppet valve engine when fuelled with gasoline and ethanol at various operating conditions.

1.3 Thesis outline

Following the introduction in chapter one, chapter two provides a review of the literature relevant to this research. Several topics as the origin of two-stroke engines and its advantages and drawbacks compared to four-stroke engines are

discussed. The reason for studying this engine cycle is contextualised with modern technologies and its possible contribution to current propulsion systems is assessed.

Chapter three details the research engine and test cell facilities used in the laboratory experiments. The equations and assumptions employed in the data acquisition and analysis of engine performance, exhaust emissions, combustion process and gas exchange phenomena are also presented and discussed.

Chapter four presents the numerical methodology employed in the transient three-dimensional (3-D) CFD simulations of cold flow and fuel spray. A brief introduction to the mathematical models used in the software is presented alongside the mesh and time-step independency studies. The cold flow two-stroke cycle and fuel spray models are also correlated to experimental results.

Chapter five provides a preliminary analysis of the performance, emissions, combustion and gas exchange processes of the two-stroke poppet valve engine. The intake and exhaust valve timings are varied with constant durations and lifts at several engine loads and speeds, whilst gasoline is used by means of the standard fuel injection system.

Chapter six evaluates the effects of distinct intake and exhaust valve timings, durations and lifts in the two-stroke poppet valve engine performance and gas exchange process. The valve configuration able to provide maximum output power at different speeds is obtained and the gas exchange process is correlated to a theoretical scavenging model.

Chapter seven presents the transient 3-D CFD simulations of the in-cylinder mixture formation with ethanol and gasoline. Different fuel injection strategies are analysed with the new side mounted multi-hole injection system. By the end of the chapter the numerical results are correlated to lab experiments.

Chapter eight presents the engine performance, emissions, combustion analysis and gas exchange process of the two-stroke poppet valve engine fuelled with

gasoline and ethanol at several engine speeds and loads. The suggested new fuel injection system is employed alongside the best valve configuration obtained from the gas exchange analysis.

Chapter nine presents the analysis of a two-cylinder configuration of the two-stroke poppet valve engine using CFD simulations and analytical considerations. The engine friction and power requirement of a real world supercharger are considered, so the full load brake performance and efficiency can be estimated from low to high engine speeds.

Chapter ten summarises the experimental and numerical findings regarding the performance, emissions, combustion and gas exchange processes of the two-stroke poppet valve engine. Recommendations for future work are proposed to improve the results obtained in this study.

Chapter Two
Literature review

2.1 Introduction

According to the Intergovernmental Panel on Climate Change (IPCC) the last three decades were the warmest period in 1400 years in the northern hemisphere [1]. This global warming is strongly related to the larger emissions of greenhouse gases (GHG) from human activity, particularly increased by the burning of fossil fuels after the pre-industrial era. The same report showed that the levels of carbon dioxide, methane and nitrous oxide, which are the main GHG alongside water vapour, were the highest in the last 800,000 years. This alteration in the earth's climate system is considered to have boosted the worldwide occurrence of natural disasters in the last decades [2], which forced governments to take measures to mitigate these emissions. Considering that the transport sector contributed to about 20% of the total GHG production in 2014 in the European Union (EU) [3], reducing such emissions from engine powered vehicles is a great concern.

At the present time, the global liquid fuel demand (diesel, gasoline, kerosene, etc.) for combustion in the transport sector is about 50 million oil-equivalent barrels per day [4]. Based on this scenario and following the expected world economic growth, the liquid fuel demand for transportation will more than double by 2040 if fuel savings (through more efficient vehicles) and fuel-switching (by replacing fossil fuels by renewable sources) are not to be implemented (Figure 2.1). Amongst the means of transportation, the light-duty and heavy-duty road vehicles have the largest impact on the global liquid fuel consumption. Consequently, these segments are expected to experience more enhancements in the upcoming years to enable the expected energy savings of 40% by 2040.

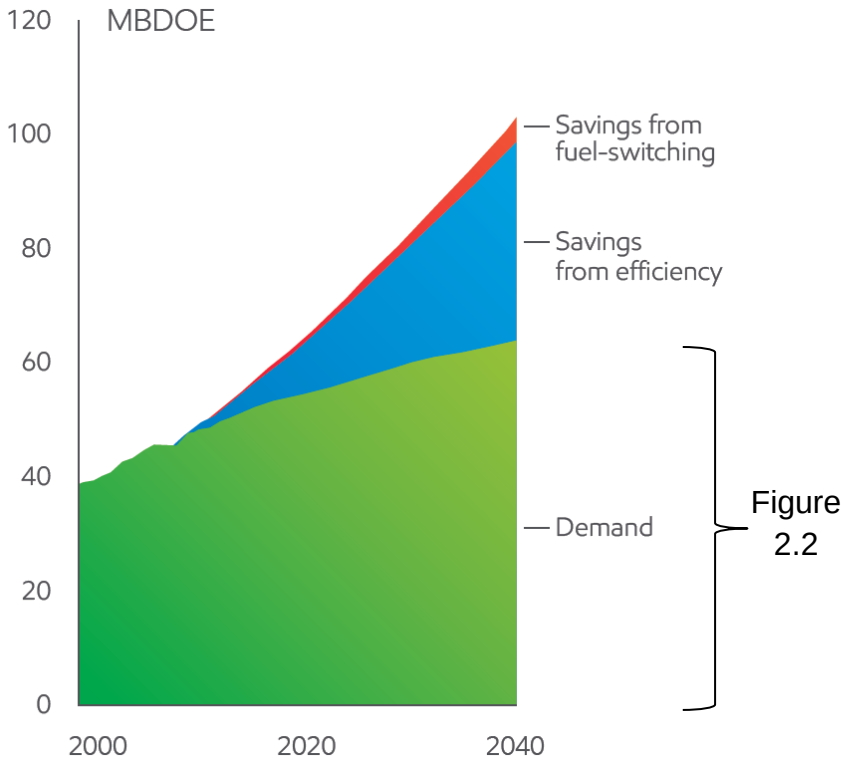

Figure 2.1 – Liquid fuel demand for the transport sector in million oil-equivalent barrels per day (MBDOE), adapted from [4].

Breaking down the transportation fuel demand seen in Figure 2.1 it is possible to assess the expected fuel savings amongst the transportation means as seen in Figure 2.2. Nowadays the fuel consumption of light-duty vehicles is roughly equal to the combined demand of heavy-duty, aviation, marine and rail together. The two major fossil fuel consumers, the light and heavy-duty vehicles, are expected to have a less steep growth after 2015. Whilst the heavy-duty segment (mostly trucks and buses) is likely to demand the highest fraction of energy in 2040, light-duty vehicles are expected to have only a slight increase of about 5% compared to 2015. The number of light-duty vehicles, which comprises passenger cars and commercial vans, is expected to reach about 1.7 billion units by 2040 (it was 852 million in 2010). This increment is projected based on the expansion of the middle class in China and the key growth countries, such as Brazil, Indonesia, Mexico, South Africa and Turkey. Nevertheless, technological improvements such as engine downsizing, higher efficiency transmissions and hybrid powertrains are expected to offset this increment and keep the fuel demand of these vehicles similar to nowadays [4].

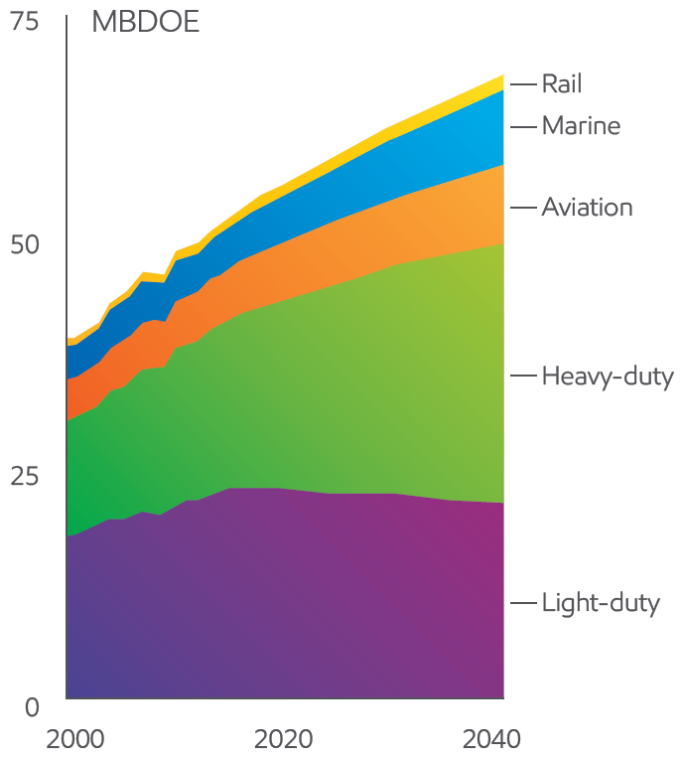

Figure 2.2 – Breakdown of the fuel demand in the transport sector in million oil-equivalent barrels per day (MBDOE), adapted from [4].

The aforementioned fuel consumption reduction in light-duty vehicles, predominantly gasoline fuelled passenger cars, requires the worldwide acceptance of CO_2 emission standards to have the expected effect. Distinct legislations have been applied around the world in the last decades, headed by the EU, Japan and the USA. In the European Union its Parliament has approved a CO_2 emission limit of 95 g/km for passenger cars and 147 g/km for commercial vehicles to be phased in by 2020 [5]. In a similar fashion the USA, by means of the Environmental Protection Agency (EPA), has approved CO_2 emissions target of 93 g/km for passenger cars by 2025. Other countries as Japan, China and Brazil have also adopted CO_2 emission targets for new passenger cars, despite different phase-in dates as presented in Figure 2.3. These emissions are calculated over a standard driving cycle meant to reproduce the driving conditions faced by the majority of drivers around the world. In the EU the current driving cycle is the new European driving cycle (NEDC), which consists of vehicle accelerations and decelerations over about 11 km with an average speed of 33.6 km/h [6]. More recently, the increasing concern with the discrepancy between the NEDC and real world driving conditions prompted the

development of the worldwide light duty test procedure (WLTP), which is expected to be adopted in the EU by 2017 [7].

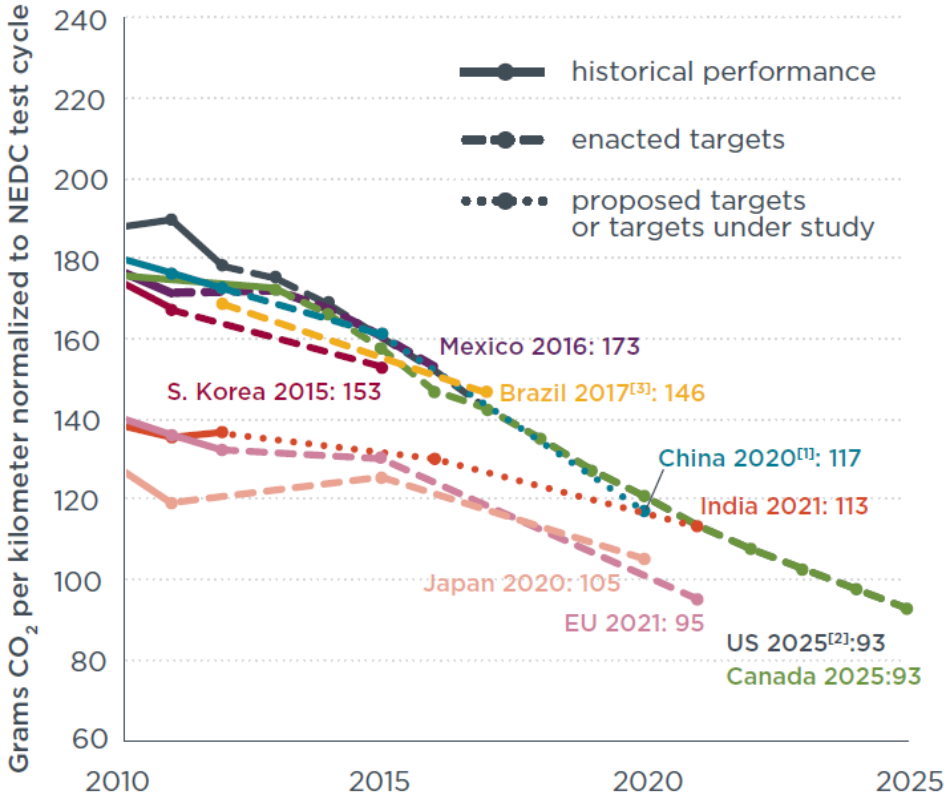

[1] The target for China was based on gasoline fuelled vehicles only. [2] USA standard set by the EPA. [3] The results were corrected from E22 (Brazilian gasoline with 22% of ethanol by volume) to pure gasoline.

Figure 2.3 – Global CO_2 regulations for passenger cars in the framework of the NEDC, adapted from [5].

Due to the different configurations of powertrain and weight that passenger cars exhibit, it is unfair to request similarly low CO_2 emissions (or fuel consumption) from different models. Instead, the targets presented in Figure 2.3 are expected to be met by the averaged emission from the whole manufacturer's car fleet considering the average vehicle weight [5]. Numerous passenger cars manufactured in the present day in the EU are already able to meet the CO_2 emission target set for 2020 without modifications. Other models, such as heavier luxury and sport vehicles, require fuel efficiency enhancements as seen in Figure 2.4. For every 100 kg extra in the average manufacturer's car fleet weight, an increment of 3.33 g/km of CO_2 is tolerated. In this case, considering

the EU average passenger car weight of about 1400 kg, the expected fuel consumption by 2020 is of 3.8 l/100km (26.3 km/l) with gasoline or diesel.

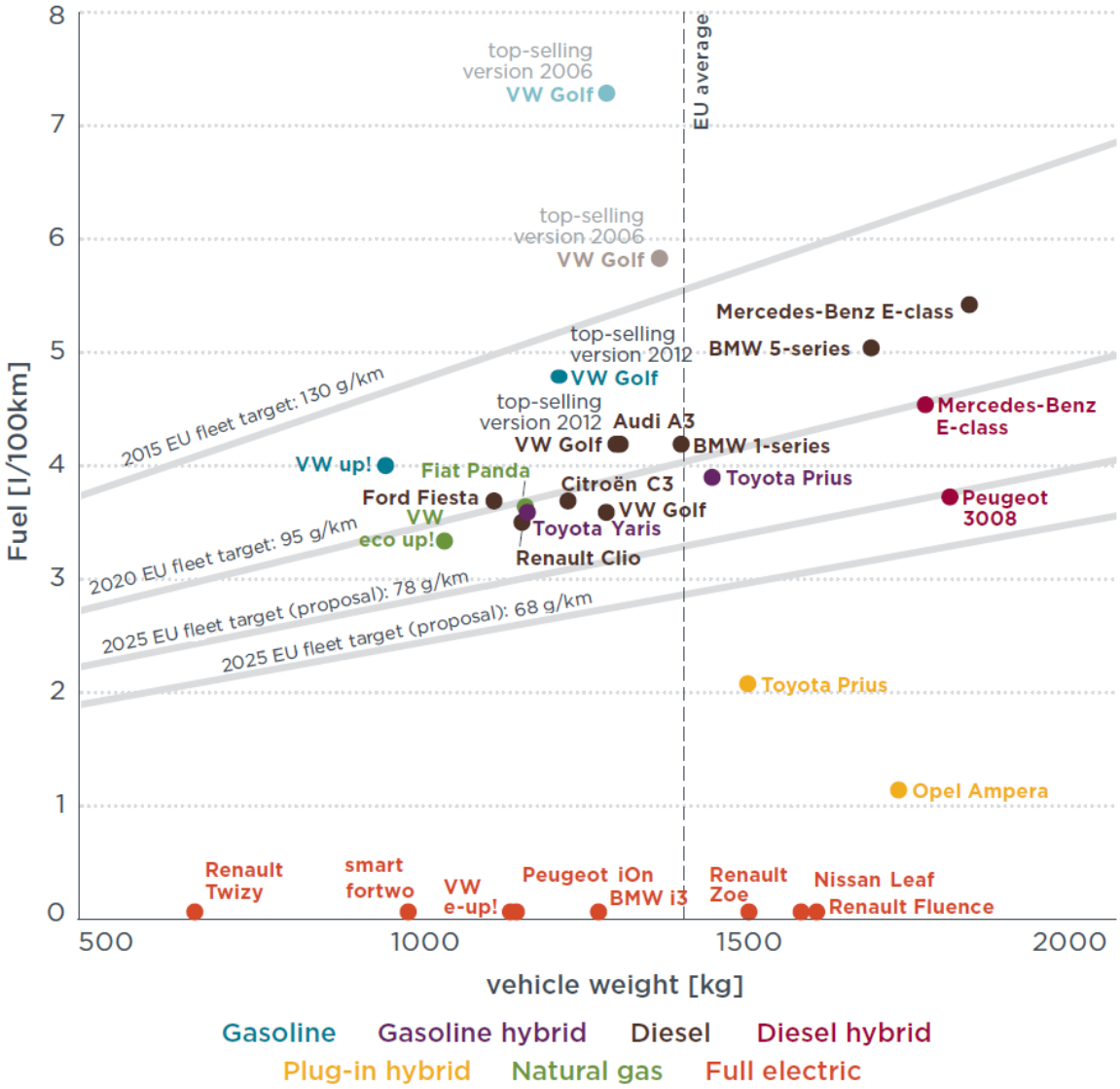

Figure 2.4 – Fuel consumption and weight from selected passenger cars in the EU in 2013. Emissions targets for 2025 not yet confirmed. Adapted from [5].

From Figure 2.4 it is clear the great challenge to be faced by gasoline fuelled passenger cars to meet the 95 g/km of CO_2 target by 2020. Even some vehicles equipped with Diesel engines can fail to meet the 2020 goal. Gasoline and diesel hybrid electric vehicles (HEV), as the Toyota Prius and the Mercedes-Benz E-class, respectively, successfully meet the 2020 CO_2 emission target. However, these models are still not able to comply with forthcoming restrictions as those proposed, but not yet approved, by the EU parliament for 2025. In this 10-year scenario, the CO_2 emission target seems to be met by plug-in hybrid electric vehicles (PHEV) and battery electric vehicles (BEV) only.

Gaseous emissions of carbon monoxide (CO), unburnt hydrocarbon (UHC) and nitrogen oxides (NOx) are also widely regulated. Their toxicity for the human health and the risk to the environment have prompted their control since the 1960's in the USA, Europe and Japan [8]. Substantial reduction in the emissions of these gases has been obtained since then, particularly with the application of three-way catalysts and electronic fuel injection to gasoline engines. In the EU the emissions standard Euro was implemented in the early 1990's and has gradually set lower pollutant emission limits since then. In its current phase for passenger cars equipped with gasoline engines, the Euro 6b, the emissions of CO, UHC and NOx are limited to 1.0 g/km, 0.1 g/km and 0.06 g/km, respectively [7]. With the introduction of gasoline direct injection (GDI) engines, particle mass (PM) and number (PN) emissions are also limited to 4.5 mg/km and $6.0*10^{11}$ #/km, respectively. For these reasons, intensive efforts are being spent in the research and development of more efficient and less polluting ICEs, particularly gasoline engines considering their dominance in the market of passenger cars.

2.2 Overview of current gasoline engines

In contemporary four-stroke gasoline engines the combustion process is mainly based on a spark ignited propagating flame that consumes a stoichiometric homogeneous air-fuel charge. Such approach has been used since the popularisation of SI engines in the early 1900's, though the mixture formation process has been greatly enhanced by improved fuel metering systems. This homogeneous charging process is relatively efficient when employed at mid-high engine loads, although at lower loads it results in poorer engine efficiency mostly attributed to pumping and heat losses [8]. Given the nature of real world driving conditions, which are dominated by mid-low load requirements, improvements in this operation region are essential to enable fuel savings.

It is widely proved that stratified charge lean-burn combustion has the potential to improve fuel consumption in SI engines [9]. In this concept, instead of filling the whole engine displacement with a homogeneous air-fuel charge, only the region around the spark plug contains the necessary amount of fuel. Meanwhile, the rest of the cylinder is filled with air and/or exhaust gas recycled (EGR). The

gains in fuel consumption resulted from lower pumping losses at unthrottled operation are claimed in the range from 20% to 25% [10][11]. However, the excess of air available during this combustion process inhibits the effective reduction of NOx emissions by currently employed three way catalysts (TWC). For the same reason, homogeneous lean-burn combustion is still not employed despite the better fuel efficiency compared to stoichiometric operation [12]. Methods to reduce NOx emissions with lean-burn combustion are available and largely used in Diesel aftertreatment, such as lean NOx trap (LNT) and selective catalytic reduction (SCR). However, these systems are still complex and relatively expensive for automotive applications.

In order to simultaneously reduce fuel consumption and NOx emissions at part load, controlled auto-ignition combustion (CAI) has been extensively studied over the last decades. Two types of CAI combustion have received distinguished attention i.e. homogeneous charge compression ignition (HCCI) combustion and partially premixed combustion (PPC) in direct injection engines. The spontaneous ignition of the air-fuel charge is mainly driven by the mixture composition, charge temperature history and fuel properties [13], so there are no direct means to control combustion phasing. HCCI combustion was able to improve fuel economy by 21% and cut NOx emissions by half compared to conventional SI operation over the NEDC with a 1.6 dm^3 engine [14]. Similarly, gasoline PPC has demonstrated diesel like efficiencies not only at low loads, but also in the mid-high load range with NOx emissions below 0.2 g/kW [15]. Nevertheless, the rapid vehicle transient response required in real world driving conditions are not entirely addressed with these combustion concepts, so their application is still under development.

Whilst the research and development of CAI and stratified lean-burn combustion is carried out, SI homogeneous combustion remains as the main heat release process in gasoline engines. In this context engine downsizing has been accepted as an effective method to reduce fuel consumption at part load operation in four-stroke engines. In this approach the engine displacement and the number of cylinders are reduced so the mid-low operating points are shifted towards regions where pumping and friction losses are minimised. Considering

the nature of driving cycles such as the NEDC, these improvements in the mid-low load range have a large impact over the vehicle's total CO_2 emissions. The gains in fuel consumption are usually reported in the range from 20% to 30% for a 50% downsized engine [16][17]. However, the longer engine operation at higher loads has raised concerns about thermal and structural stresses, particularly with engine downsizing beyond 50% (which means halving the engine displacement). The higher in-cylinder pressures and more frequent knocking combustion, as well as low speed pre-ignition (LSPI), are amongst the main issues compromising the engine operation and its durability [18].

Besides engine downsizing, the need for powertrain hybridisation amongst gasoline engines to meet future CO_2 emission legislations is evident as shown in Figure 2.4. The synergy amongst the various components of these powertrains i.e. internal combustion engine, power generator, electric motor(s) and batteries, depends on the driving cycle requirements. In this situation gasoline engines may have a secondary role in passenger cars and only operate as a range extender in case of battery depletion [19]. Therefore, not only great fuel economy is required but other characteristics such as low weight, packaging and minimum noise vibration and harshness (NVH) are equally important [20].

In this framework the two-stroke cycle operation may present several advantages concerning engine downsizing and vehicle hybridisation. Due to its doubled firing frequency the two-stroke cycle engine provides superior power density (kW/dm^3) and higher power per unit mass (kW/kg) compared to equivalent four-stroke engines. Improved low-end torque and significantly lower NVH are also obtained [21][22]. Compared to a four-stroke engine of the same swept volume and operating at the same speed, the two-stroke engine can achieve similar output torque with one half of the mean effective pressure. In other words, similar output power from contemporary four-stroke engines can be obtained with lower in-cylinder pressures and hence less structural and thermal stresses. Given these facts, the two-stroke cycle engine deserves more investigation considering the current scenario experienced by the automotive industry.

2.3 Two-stroke cycle engines

2.3.1 History and background

Prior to the introduction of the first four-stroke prototype engine by Nicolaus Otto in 1876, all internal combustion engines were operated in the two-stroke cycle as a result of the single power stroke per crankshaft revolution [23]. In 1673 Christian Huygens was the first one to build a gunpowder powered engine, represented in Figure 2.5 (a) by a sketch from 1680. In this “atmospheric engine” gunpowder was loaded by a vessel in the bottom and ignited, so the gas expansion pushed the piston upwards until the exhaust ports could be uncovered. After the expansion and exhaust of part of the burnt gases, the cooling of the remaining in-cylinder gases created a partial vacuum able to pull the piston downwards and hence provide work. The very first issue affecting the two-stroke engine operation was realised by him and by one of his assistants, which was the poor scavenging of burnt gases [24]. Numerous improvements were proposed since then, mainly resulted from the development of liquid and gaseous fuels and advances in metallurgy with the industrial revolution.

It was by the end of the 19th century that the two-stroke cycle engine had its major development, particularly in England with the work of Dugald Clerk and Joseph Day. In 1881 Clerk proposed a two-stroke gas engine in a similar fashion to the four-stroke cycle proposed five years earlier by Otto, with a sliding piston connected to a crankshaft by means of a connecting rod [25]. The inlet was performed by an intake valve in the cylinder head whilst the exhaust ports were responsible for expelling the burnt gases as the piston uncovered them around bottom dead centre (BDC), as seen in Figure 2.5 (b). To provide the boosted air necessary to scavenge the burnt gases an auxiliary piston pump was integrated beside the main cylinder. The possibility of using the crankcase as a scavenge pump, instead of employing a separate compressor as Clerk did, was proposed by Joseph Day in 1891 [26] as outlined in Figure 2.5 (c). In this two-stroke crankcase scavenged engine the intake and exhaust processes were performed by piston-controlled ports in the cylinder liner, whilst the charge was delivered to the dry sump through a one-way valve. Due to the construction simplicity with only three moving parts, this concept prevailed amongst two-stroke engines for

several decades. After the invention of the compression ignition (CI) engine by Rudolf Diesel in 1892 [27], further mechanical and gas exchange improvements were added to the two-stroke cycle engine for both gasoline and diesel applications. Nonetheless, the two concepts proposed by Clerk and Day formed the basis still embedded in current two-stroke engines.

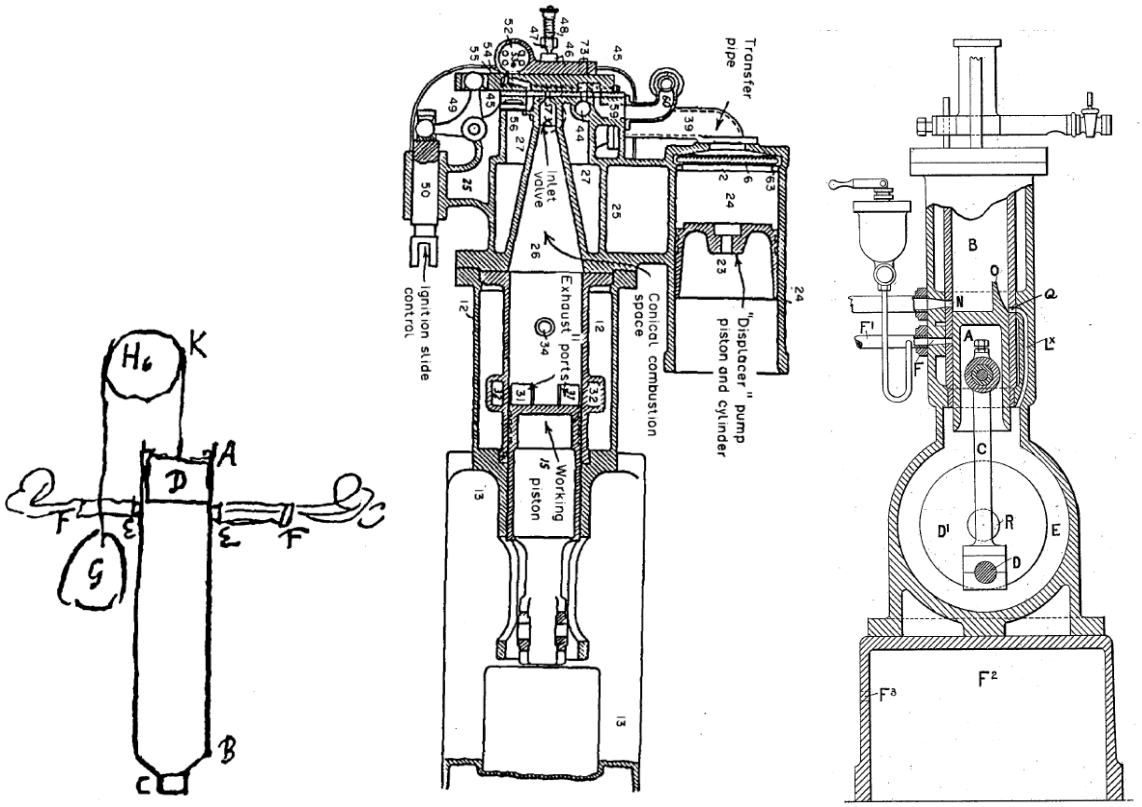

a) b) c)

Figure 2.5 – Two-stroke engine concepts: a) Christian Huygens [24], b) Dugald Clerk [25], c) Joseph Day [26].

In the 20th century the introduction of better quality fuels and materials of increased strength enabled the achievement of greater compression ratios and hence higher thermal efficiencies in the two-stroke cycle. With the development of four-stroke engines many technologies were shared between the two platforms, particularly regarding the crank train and fuel metering systems [8]. The construction simplicity and hence lower cost, besides the higher power density compared to four-stroke units, contributed to the popularisation of the two-stroke cycle amongst light-duty and heavy duty vehicles. The development of the loop scavenged gasoline engine for automotive and motorcycle applications, as well as the uniflow scavenged diesel engine for trucks and large marine vessels, were some of the achievements of the two-stroke engine [28].

However, the difficulty on meeting emission legislations in the last 30 years, mostly caused by fuel losses during the scavenging process, gradually reduced their share in the automotive and motorcycling market. Uniflow scavenged two-stroke engines, with displacements in the order of m^3 and brake efficiencies above 50%, are still employed in large marine units. Meanwhile, smaller engines with displacements between 25 cm^3 and 1000 cm^3 are used in handheld tools, recreational vehicles and racing concepts with power densities above 220 kW/dm^3 [29].

2.3.2 Engine operation fundamentals

The process by which the fuel energy is converted into mechanical work in two-stroke engines is the same as that realised in four-stroke engines. Following the compression and combustion of fuel and air, the expansion of burnt gases within the cylinder drives the piston downwards and rotates the crankshaft by means of a connecting rod. This reciprocating operation is by far the most common type of energy conversion amongst ICEs, although other concepts as rotary engines are also available [30].

The main difference between two-stroke and four-stroke cycle engines relies on the gas exchange process as presented in Figure 2.6. In the four-stroke cycle the exhaust process begins with the exhaust valve opening (EVO) around 50° crank angle (CA) before BDC after the expansion of the burnt gases. Whilst the piston is still moving downwards part of the burnt gases are expelled during the exhaust blowdown phase. Between BDC and top dead centre (TDC) the displacement of the burnt gases occurs, whilst the exhaust valve closing (EVC) occurs around 20° CA after TDC to take advantage of the exhaust gas flow inertia. The intake process starts at about 20° CA before TDC with the intake valve opening (IVO), so the intake and exhaust valves remain opened during the so called valve overlap. The charging process continues even after BDC due to the charge inertia (ram effect) until the intake valve closes around 40° CA after BDC. By this time the compression phase starts and the air-fuel charge is compressed until the ignition and subsequent combustion, restarting the cycle. The valve timings aforementioned are approximated values as suggested by [8].

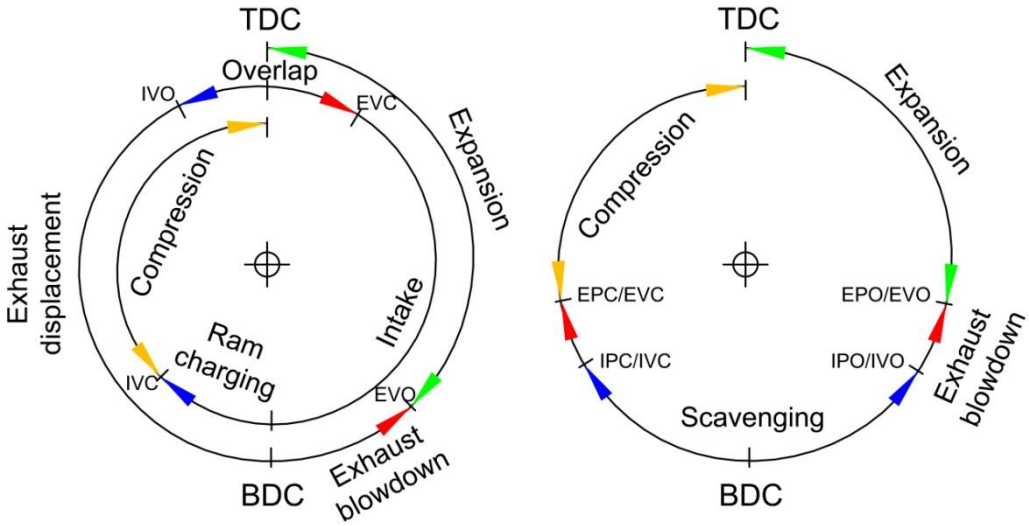

Figure 2.6 – Typical sequence of events in the four-stroke (left) and two-stroke (right) cycle engines.

On the other hand, in the two-stroke cycle engine the intake and exhaust processes occur at the same time during the so called scavenging period. In four stroke engines the gas exchange process is mostly performed through poppet valves in the cylinder head. On the other hand, in typical two-stroke engines the scavenging is achieved through piston-controlled ports in the cylinder liner. Therefore, after the combustion and expansion of the burnt gases the exhaust port(s) is uncovered and the exhaust process starts. The exhaust port opening (EPO) or EVO usually occurs around 80° CA before BDC, whilst the intake port opening (IPO) or IVO occurs at about 20° CA later and allows the exhaust blowdown phase to take place [28]. As the intake port(s) is uncovered, the boosted fresh charge enters the cylinder and displaces the combustion products towards the exhaust port(s). Due to the fixed symmetry of the ports in the cylinder liner and the necessity of EPO/EVO occurring before IPO/IVO, the port events are mirrored between the two halves of the cycle. Thus, the intake port closing (IPC) or IVC takes place around 60° CA after BDC, whilst the exhaust port closing occurs around 80° CA after BDC at the onset of compression.

It could be observed in Figure 2.6 that all phases of the four-stroke cycle (expansion, exhaust, intake, and compression) were condensed to a single revolution in the two-stroke cycle. To keep the ability of removing the burnt gases from the combustion chamber and simultaneously filling it with fresh charge, the compression and expansion phases were greatly reduced in comparison to the

four-stroke cycle. Advancing EPO/EVO deteriorates the thermal efficiency as the expansion work promoted by the burnt gases is partially lost in the blowdown phase in favour of better scavenging. Similarly, the late EPC or EVC reduces the effective compression ratio (ECR) and hence the theoretical cycle efficiency compared to an equivalent four-stroke engine.

2.3.3 The scavenging process

The simplest type of scavenging is that proposed by Joseph Day and presented in Figure 2.7 (a), where the intake and exhaust ports are placed in opposite sides of the cylinder liner (cross scavenging). To avoid the fresh charge from going straight from the intake into the exhaust i.e. short-circuiting, the piston has a protuberance to deflect the incoming flow towards the cylinder head. A limitation of this scavenging concept is the limited compression ratio attainable due to the piston deflector, as well as the formation of hot spots on its top which may induce pre-ignition [23]. An evolution of this concept is the MAN loop scavenging shown in Figure 2.7 (b), where the intake port is placed below the exhaust port. One of the drawbacks of this approach is the extensive mixing between burnt gases and fresh charge along the loop path, though the cylinder packaging is excellent for multi-cylinder applications. The third common scavenging model, and certainly the most adopted amongst motorcycle and passenger car engines, is the Schnuerle loop scavenging seen in Figure 2.7 (c). In this concept the boosted fresh charge enters the cylinder through side ports pointing in the opposite direction to the exhaust port(s), so the flow forms a 3-D loop. The flow direction avoids the necessity of using a deflector on the piston top like cross scavenging engines. Moreover, the mixing between fresh charge and burnt gases is significantly reduced compared to the MAN loop scavenging. About 20% higher output power with similar intake air flow has been obtained by the Schnuerle scavenging in comparison to the cross scavenged model [31].

In the uniflow two-stroke engine concept presented in Figure 2.7 (d) and (e) the boosted fresh charge is supplied through ports at BDC. The exhaust gases are then forced out through ports on the other extremity of the cylinder, as in the case of the opposed piston design (d), or by means of poppet valves in the cylinder head (e). The opposed piston design has the great advantage of larger

combustion chamber volume to surface ratio, so heat losses are minimised and the thermal efficiency is improved. Compared to a single piston engine, the reduction in surface-to-volume ratio was found at 36% at TDC for a 1.6 dm^3 engine [32]. However, the complexity of coupling two crankshafts at each end of the engine has limited its use for larger CI engines. In the uniflow scavenging with poppet valves in the cylinder head greater scavenging efficiencies can be achieved compared to other methods [33]. Despite some attempts to implement it in passenger cars [34], the production complexity and packaging restrictions have limited its application to heavy-duty diesel and large marine engines so far.

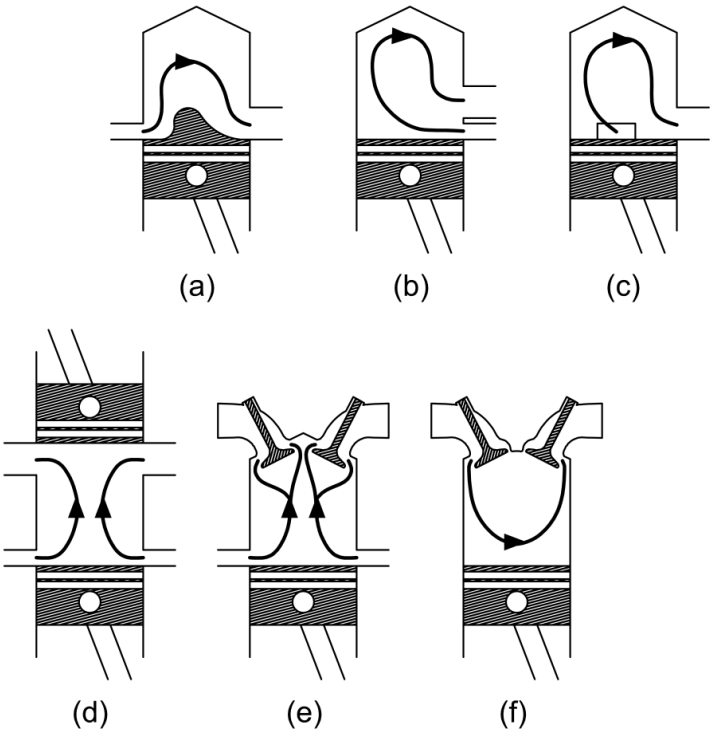

Figure 2.7 – Common types of scavenging in two-stroke engines: (a) cross scavenging, (b) loop scavenging (MAN type), (c) loop scavenging (Schnuerle type), (d) opposed piston uniflow scavenging, (e) uniflow scavenging, (d) poppet valve scavenging.

The ports in the cylinder liner, employed by all scavenging methods described to this point, have raised several questions regarding engine durability along the years. The presence of cold intake and hot exhaust ports asymmetrically distributed in the cylinder liner is regarded as the main cause of bore distortion in two-stroke engines [35]. Moreover, the piston movement wipes the oil film from the cylinder liner to inside the intake port(s), so the unavoidable combustion of part of the lubricant oil results in UHC emissions [22]. If oil control rings are

placed at the piston skirt to avoid the oil reaching the intake port(s), then the poor lubrication leads to increased friction and hence reduced durability of piston, rings and liner. Furthermore, in ported two-stroke engines the intake and exhaust timings are fixed and solely defined by the piston position during the cycle, so the gas exchange process is penalised at off-design operating conditions. The main issue regarding the constant port timing takes place between IPC and EPC at part-load and lower engine speeds, when the fresh charge spills out the cylinder until EPC occurs. Several approaches have been adopted to correct this issue, such as exhaust sliding valves [36][37]. However, its long term use, especially if the engine is largely operated at idle and light loads, may lead to faulty operation due to carbon deposits [38]. At higher engine speeds and loads, tuned exhaust pipes are often employed to trap the fresh charge by means of wave propagation. If well designed, tuned exhaust pipes can also improve the scavenging by reducing the exhaust backpressure through rarefaction, so the intake-exhaust pressure ratio increases and more charge is inducted [28].

Following the limitations encountered in ported two-stroke engines, the use of poppet valves to promote the whole gas exchange process started being investigated in the 1990's by Honda [39], Ricardo [40] and Toyota [22]. This concept, presented in Figure 2.7 (f), was originally proposed by the French Jean Melchior in 1976 [41]. This scavenging process is based on the development of a reverse tumble "U" flow between the valves. The absence of intake and exhaust ports in the cylinder liner eliminates the problems associated with oil consumption and durability of previous two-stroke engine concepts. To avoid the boosted inlet fresh charge from going straight into the exhaust i.e. short-circuiting, several approaches have been considered as seen in Figure 2.8. These include: intake port deflector [39], masked cylinder head [22], stepped cylinder head [42], intake valve shrouding [43][44], and vertical intake ports [40].

The intake port deflector, seen in Figure 2.8 (b), performs well at low engine loads, although at higher loads it largely restricts the intake air flow [39]. With a cylinder head mask, as shown in Figure 2.8 (c), the charge short-circuiting can be improved at all operating conditions despite the reduction in effective valve curtain area. This approach was recently used by Renault in a light duty two-

cylinder Diesel engine [21]. The stepped cylinder head presents similar intake flow performance to the masked approach, though the exhaust valve curtain region is restricted as seen in Figure 2.8 (d). The result is poorer performance compared to the masked approach as the intake pressure requirement increases [42]. The use of shrouded valves, seen in Figure 2.8 (e), largely improves the trapping efficiency, although methods to prevent the valve from spinning during the engine operation add even more complexity to this approach [43][44]. A wide range of valve shroud angles between 70° and 108° were found to perform well in a single cylinder four-valve 370 cm^3 engine [35]. Finally, the vertical intake port promotes the least flow restriction amongst all methods, although when solely used it cannot ensure high scavenging with low charge short-circuiting [42]. When employed in conjunction with a masked cylinder head, the vertical intake port improves the port's discharge coefficient as the majority of the flow is directed towards the valve region not blocked by the mask [45]. Such configuration, seen in Figure 2.8 (g), was employed in a switchable two/four-stroke engine [46].

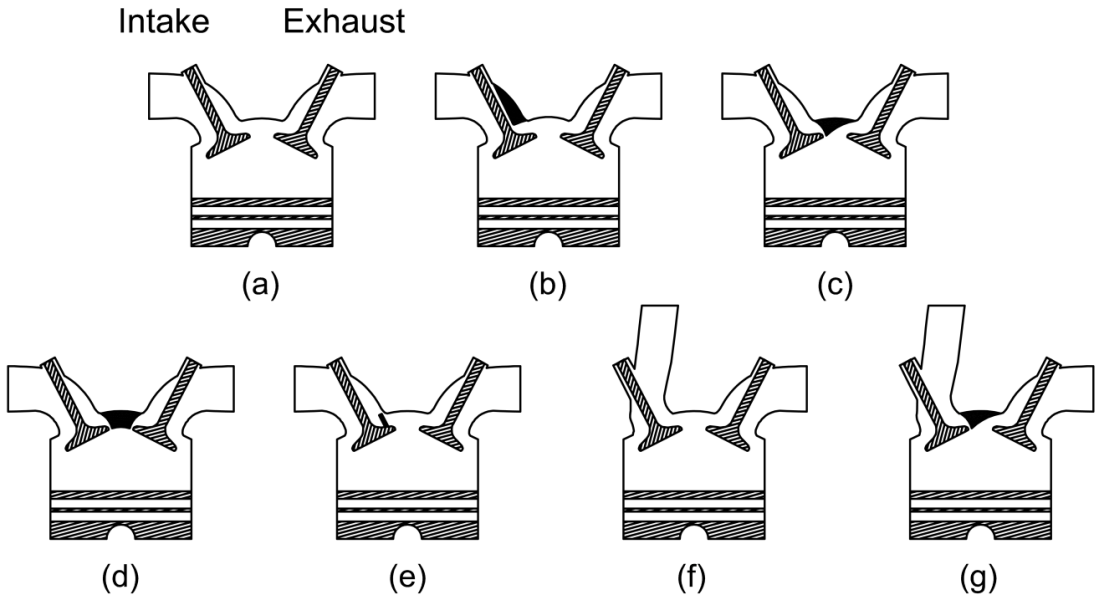

Figure 2.8 – Improvements in the scavenging of two-stroke poppet valve engines: (a) standard setup, (b) intake port deflector, (c) masked cylinder head, (d) stepped cylinder head, (e) intake valve shrouding, (f) vertical intake port, (g) masked cylinder head with vertical intake port.

The scavenging performance in two-stroke poppet valve engines is usually inferior to that obtained in ported engines due to the smaller effective flow area, which limits the engine operation speed. Nevertheless, the use of poppet valves

provides greater flexibility regarding the intake and exhaust valve events, as they are no longer symmetrically fixed by the cylinder liner but controlled by camshafts. This characteristic is particularly important regarding the occurrence of IPC/IVC before EPC/EVC as seen in Figure 2.6, when the fresh charge spills out the cylinder. In the case of two-stroke poppet valve engines IVC can be set even after EVC, so instead of losing fresh charge the engine can take advantage of ram effect and hence improve the charging process [23]. Furthermore, the development of variable valve actuation (VVA) systems over the years [47] can certainly improve the performance of this concept. By advancing and retarding the intake and exhaust valve timings, the effective expansion and compression ratios can be enhanced over a wide range of engine speeds and loads.

2.3.4 The charging process

In four-stroke engines the charging process occurs when the in-cylinder pressure drops below the intake pressure, mostly during the descending piston movement in the pumping loop. On the other hand, in two-stroke engines the piston movement has little impact on the scavenging process despite the opening and closing of ports (when present). Therefore, a positive intake-exhaust pressure ratio is always necessary to expel the burnt gases from the cylinder regardless the use of ports or valves. The boosted fresh charge is often supplied by crankcase compression, as seen in Figure 2.9 (a) for a cross scavenged two-stroke engine. Following this approach the fresh charge is drawn into the crankcase through its intake port(s) (left down in Figure 2.9 (a)) as a depression is created during the ascending movement of the piston. When the crankcase pressure equals the intake pressure around TDC, the crankcase charge supply is interrupted usually by reed or disc valves [28] installed on its inlet. As the piston moves down it compresses the charge in the crankcase until the cylinder intake port(s), also referred as transferring port(s) (right in Figure 2.9 (a)), is uncovered allowing the charge to flow into the cylinder. By the end of the in-cylinder charging phase the piston starts moving upwards and covers the intake port, whilst in the crankcase the pumping process restarts. In conventional four-stroke engines the crankcase contains lubricant oil (wet sump) required for the force-feed lubrication of the crank train and valve train. Conversely, in crankcase scavenged two-stroke engines the oil necessary to lubricate the crank train

needs to be added to the fresh charge in fuel-oil proportions usually between 60:1 and 450:1 [38]. When the lubricant oil addition is precisely controlled, its consumption may be similar to that of four-stroke engines of about 5 dm^3 every 10 000 km [38]. In this case, instead of disposing and replacing the lubricant oil as in four-stroke units, the oil is consumed in about the same travelled distance.

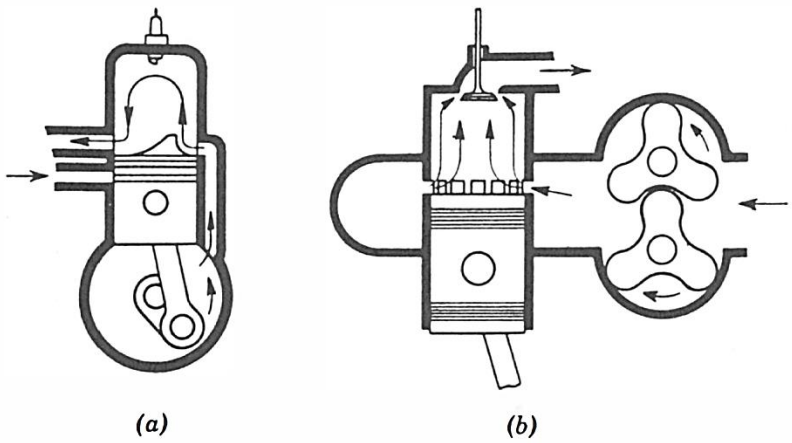

Figure 2.9 – Typical methods of charging in the two-stroke cycle: (a) crankcase charged and (b) externally charged. Adapted from [48].

Despite the simplicity and associated lower production cost of crankcase scavenged two-stroke engines, some applications require the adoption of a wet sump to overcome the lubrication and durability issues. In this case, the crankcase becomes similar to that of four-stroke engines and an externally charge boosting device is required. Roots type superchargers are usually employed as seen in Figure 2.9 (b) for a uniflow scavenged engine, although arrangements with centrifugal chargers, turbochargers and electric compressors have been also evaluated [49]. Furthermore, a wet sump enables the piston cooling by means of an underneath oil jet, which is not possible in crankcase scavenged engines. Due to the doubled combustion rate of two-stroke engines the heat rejection to the piston is greater than in four-stroke engines, so its top land temperature can be higher. Hence, this oil cooling minimises the formation of hot spots on the piston surface which could induce pre-ignition.

The use of turbochargers in two-stroke engines requires careful matching between turbine and compressor operation. As the exhaust backpressure hinders the scavenging process, greater intake pressures are required to provide the same pressure ratio. In a recent study [50] several boosting devices were

experimented in a two-stroke poppet valve diesel engine, such as: single, dual and variable drive ratio superchargers, waste-gate turbocharger, variable geometry turbine (VGT) turbocharger and centrifugal compressor. Different arrangements between supercharger and turbocharger were also evaluated. The configuration which best suited the requirements was a turbocharger (lower pressure stage) placed upstream a dual-drive supercharger (higher pressure stage), so the minimum BSFC of 238 g/kWh at 2000 rpm could be attained. The use of a waste-gate turbocharger was preferred over the VGT considering its lower cost. The single drive ratio supercharger was not able to meet the mid-speed full torque requirement, whilst the variable-drive ratio option was discarded due to increased friction losses.

With the current research on downsized four-stroke engines several improvements in boosting systems have been proposed. Most of them can be shared with externally scavenged two-stroke engines, such as the unit proposed by [51]. This concept integrates a supercharger and a turbocharger coupled by a variable drive ratio to the crankshaft, which also enables turbocompounding operation. When applied to a 2.0 dm^3 engine, the torque curve of a naturally aspirated (NA) 4.2 dm^3 engine could be matched with 36% better fuel economy over the NEDC. In a similar study, aimed at improving the transient response of a 60% downsized engine, a variable speed centrifugal compressor was coupled to an electric motor/generator [52]. At lower engine speeds and higher loads, the electric motor assisted the compressor to provide boosted intake air. At higher engine speeds and loads, when the turbocharger was able to deliver the required intake pressure, the supercharger was bypassed and the whole unit worked as a generator for the vehicle electrics. The electric motor was also able to start the engine by means of its connection to the crankshaft, which is an advantage for current stop-start systems [53]. In the end, the vehicle transient response in “time-to-torque” (the time necessary to build-up 90% of the requested torque) was improved in 68% at 1000 rpm.

2.3.5 Mixture formation and combustion

In the previous sections the scavenging process was assumed to be performed by a fresh charge containing fuel and air, which is the most common approach

amongst two-stroke SI engines. Bearing in mind the inevitable mixing between intake charge and burnt gas, besides the occurrence of short-circuiting, it is expected that some of the fuel is lost in the exhaust of mixture scavenged engines [54]. This short-circuiting of fresh charge results in poor fuel economy and excessive UHC emissions. The adoption of exhaust valve throttling greatly improved this issue in ported engines by increasing the trapping efficiency, although the engine-out emissions were still beyond four-stroke engine levels [55][56]. Interestingly, the lubricant added to the intake charge was found to have much less effect on UHC emissions as modern units use proportions as low as 1% of lubricant oil in the fuel [29].

With more stringent UHC emission regulations, as well as increased concern about fuel consumption, the use of direct fuel injection in two-stroke SI engines has become greatly accepted [33]. The scavenging process, previously performed by the air-fuel mixture, is then completed by solely air whilst the start of fuel injection (SOI) occurs after EPC/EVC. Even though UHC emissions are reduced by the absence of fuel short-circuiting, the shorter time available for mixture formation reduces the combustion completeness and enlarges the production of CO and PM [57].

The popularisation of solenoid type fuel injectors, and more recently piezoelectric injectors, amongst four-stroke engines has reduced their production cost over the years. However, for small two-stroke engines, such as motorcycle and small outboard marine engines, the cost of high pressure direct injection is still commercially prohibitive. This fact has led to the development of lower cost air-assisted fuel injection systems since the 1990's, with particular attention to those developed by the French Institute of Petroleum (IFP) [58] and Orbital [59]. The latter, for instance, incorporated a crank-driven air pump providing 0.55 MPa of air to the injector where fuel at 0.62 MPa was locally mixed. This concept was able to promote gasoline stratified charge combustion at part loads, which greatly improved combustion stability especially at high levels of residual gas trapped. When applied to a 1.2 dm^3 three-cylinder engine, this combustion system complied with the emissions legislation in Australia in 2000 using only a two-way catalyst (UHC+CO), given the exceptional engine-out NOx emissions

[38]. Whilst fuel short-circuiting is avoided by direct fuel injection, the exhaust gas dilution during the scavenging process cannot be completely removed. Thus, given the requirement of fuel rich or stoichiometric exhaust gas composition by current TWC to provide acceptable NOx conversion performance [27], the use of this aftertreatment in two-stroke SI engines may be challenging.

In homogeneously charged four-stroke engines the residual gas trapped level is usually around 20% at light loads [8]. This value is proportional to the valve overlap, intake and exhaust pressures, and the compression ratio. The engine load is then controlled by the air mass induced via throttling, so pumping losses prevail at mid-low loads. On the other hand, in two-stroke engines the load is proportional to the replacement of burnt gases by fresh charge in the cylinder, so at low loads the residual gas trapped can reach values above 65% [28]. Whilst this dilution avoids the occurrence of pumping losses, the increased charge heat capacity and reduced oxygen availability often results in unstable combustion and misfire. However, if enough hot residual gas is trapped, either by means of a VVA system in a poppet valve engine [60] or by using a sliding exhaust timing valve in a ported engine [61], CAI combustion can be obtained. Unlike SI operation where the start of combustion is set by the spark timing, CAI combustion is mainly driven by the mixture composition, charge temperature history and fuel properties [13]. Despite the absence of direct control over combustion phasing, excellent fuel efficiency and NOx emissions are obtained.

2.4 Two-stroke engines in the contemporary automotive sector

Apart from racing purposes, two-stroke gasoline engines are currently employed to power mopeds, light marine vehicles, snowmobiles, microlights and handheld tools [62]. The key factor for choosing these engines relies on the production cost, packaging and lightness compared to equivalent four-stroke engines. The use of two-stroke engines for such applications, which are largely crankcase mixture scavenged models, is only possible due to mild emission regulations in course. If engine durability and fuel consumption equivalent to contemporary four-stroke engines is requested, then the adoption of external scavenging and DI becomes necessary [29]. In the end, the complexity and additional cost of DI and external boosting systems may offset the aforementioned advantages of

two-stroke engines. This is an accepted reason why two-stroke engines lost their share in the transport sector, especially amongst motorcycles and passenger cars. However, with the development of DI and boosting technologies for downsized and hybrid vehicles, the production costs of these technologies may be favourable to the adoption of two-stroke engines once again.

The development of GDI engines in the early 1990's, following their introduction into passenger cars in 1996 by Mitsubishi [9], greatly improved four-stroke engines performance and emissions. GDI engines present improved fuel economy at high engine loads compared to port fuel injection (PFI) mainly due to lower fuel enrichment required to reduce the combustion chamber temperature. As the heat absorbed during the fuel vaporisation comes from the combustion chamber only, instead of partially from intake ports as in PFI engines, the charge cooling effect greatly reduces the in-cylinder temperature [27]. Hence, greater compression ratios and more advanced spark timings towards the minimum ignition advance for best torque (MBT) can be realised, which results in better fuel economy. During cold start the fuel film development required by PFI engines is not necessary in GDI engines, so improved fuel economy and lower UHC emissions are obtained [9]. The advantages presented by GDI four-stroke engines, besides those mentioned for the two-stroke cycle as fuel short-circuiting, renewed the interest in two-stroke engines as seen in Figure 2.10. This plot presents the occurrence of the subject "two-stroke" between 1955 and 2015 on the database of the Society of Automotive Engineers (SAE), recognised as the main powertrain showcase.

The results presented in Figure 2.10 are not exclusively related to the automotive industry, but it also considers smaller engines i.e. motorcycle and tools, as well as larger marine and truck engines. This is particularly true by analysing the nearly constant occurrence of two-stroke engines until the late 1970's. By that time a large portion of motorcycles used two-stroke gasoline engines i.e. Honda, Piaggio and Yamaha, to name a few [28]. Also, uniflow diesel engines were common amongst trucks, particularly in the UK with Foden and in the USA with Detroit Diesel [8]. Nonetheless, the steep promotion of two-stroke engines based on the development of GDI systems for the automotive industry in the late 1980's

is greatly noticeable. The large interest in two-stroke engines remained beyond the 2000's, although stricter emission legislations and the requirement for minimum engine durability of 100,000 km given by the Euro 4 in 2005 [7] biased the attention towards four-stroke engines.

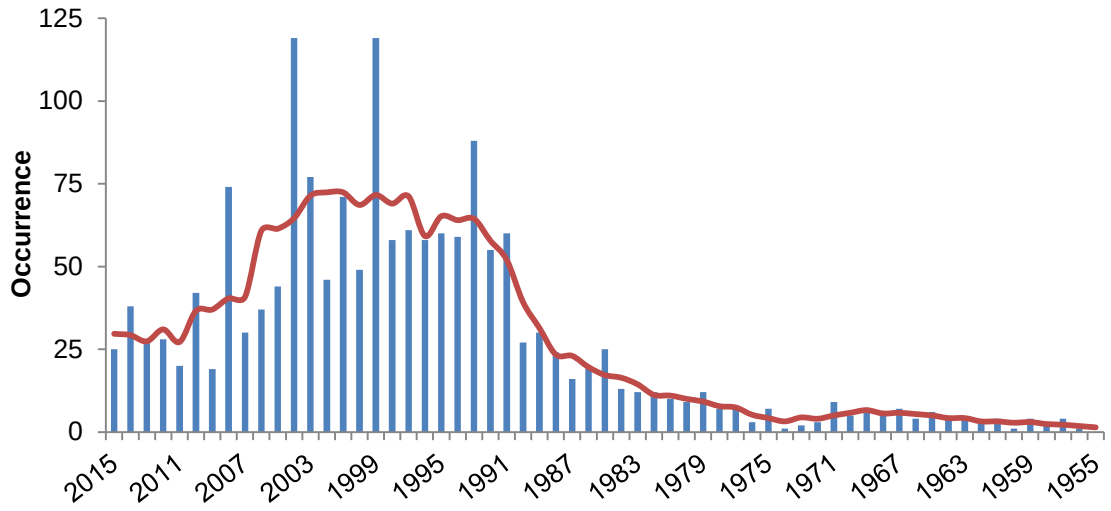

Figure 2.10 – Occurrence of the subject "two-stroke" amongst technical papers, journal articles, magazines and books in the SAE International Digital Library [63] between 1st January 1955 and 22nd November 2015.

In response to the durability and fuel consumption concerns raised to the application of gasoline two-stroke engines in passenger cars, Orbital set a real-world driving test with a 100-vehicle fleet in the early 2000's in Australia [38]. These passenger cars supplied by Ford were fit with a 1.2 dm^3 three-cylinder air-assisted DI crankcase scavenged engine and set for a three-year trial amongst normal customers. The engine was able to meet all safety, NHV and emission regulations in course at the time. The combined distance travelled by all 100 vehicles was found in excess of 5.5 million kilometres, although only a few cars exceeded 100,000 km. The customer satisfaction results demonstrated very similar vehicle performance compared to the same car fitted with a four-stroke engine. The fuel consumption of the two-stroke engine was found 20% and 15% better in the urban and highway cycles, respectively, than the counterpart four-stroke engine. Therefore, the application of two-stroke engines in passenger cars was hindered by poor engine durability compared to four-stroke engines. Moreover, the needs for modification in manufacturers' assemble lines also limited the adoption of two-stroke engines.

The development of specific manufacturing process for four-stroke engines by the automotive industry along the years has reduced the possibility of producing conventional two-stroke engines [52]. Despite some recent attempts on developing two-stroke engines with intake and exhaust ports [36][64], the research on the two-stroke cycle for passenger cars focused on concepts more alike contemporary four-stroke engines. Uniflow scavenged engines for gasoline [65][66] and diesel [32][62][67] applications, as well as poppet valve scavenged two-stroke engines [21][68], have received more attention in the last decade. Whilst two-stroke poppet valve engines share the same architecture of four-stroke engines, uniflow scavenged engines still have ports in the cylinder liner despite the similar cylinder head. Therefore, the possibility of using these concepts in passenger cars is greater due to the analogy to the four-stroke engine manufacturing process.

2.4.1 Engine downsizing

The concept of engine downsizing has been accepted as the most feasible solution for SI four-stroke engines to attend upcoming CO_2 emission legislations. Following this principle the engine displacement and the number of cylinders are reduced, so the engine operates more frequently at higher loads near the minimum fuel consumption region. The fuel economy is greatly enhanced by lower pumping losses due to more opened throttle operation. Better mechanical efficiency (ratio between BMEP and IMEP), resulted from lower friction losses, is also obtained [69]. Heat rejection is also minimised due to fewer cylinders, especially when singular displacements above 400 cm^3 are employed [70]. Further gains in engine friction and gas exchange are obtained when the engine is operated at higher loads and lower speeds by means of longer gearbox ratios. Applied to a 1.6 dm^3 engine, this downspeeding effect presented about 9% fuel efficiency improvement over the NEDC [70]. Moreover, the constant higher load operation compared to larger displacement engines reduces the engine warmup period, so fuel consumption and emissions are improved [52]. To ensure the similar full load performance of the counterpart larger engines, supercharging and/or turbocharging is used to increase the charge density [71].

In order to deal with excessive heat release rates near the border knock in downsized engines, split cooling circuits (block + cylinder head) are used. The presence of hot spots in the combustion chamber is also undesirable and therefore sodium-filled exhaust valves are often employed [16]. The use of direct fuel injection is essential to increase the charge cooling effect and reduce knocking occurrence. Centrally mounted injectors provide better charge homogeneity and less fuel impingement than side mounted injectors, although their use has a negative effect on the bore size. Larger bores imply higher temperatures in the end-gas before the flame front arrival [72], which requires retarded ignition timings to avoid abnormal combustion. The central position of the spark plug is also crucial on reducing the flame traveling distance. Actually, a slight offset in the spark plug towards the intake valve(s) reduces the knock tendency, as such cold region slows down the flame propagation and makes the end-gas more susceptible to auto-ignition [18].

Table 2.1 and Figure 2.11 present a benchmark on the most prominent downsized gasoline engines. The performance in specific torque units (Nm/dm^3) and BMEP (MPa) of all models is compared to a conventional four-stroke baseline PFI engine. The level of engine downsizing does not necessarily reflect the engine efficiency in this case, as it may have been penalised by retarded ignition timings to reduce structural stresses and combustion noise. Moreover, fuel enrichment is often used to reduce the exhaust temperature to about 900-1300 K, so that turbine and/or aftertreatment damage is avoided [16][17][73].

The baseline 2.0 dm^3 four-stroke engine model seen in Figure 2.11 has the advantage of nearly flat full load torque from 1500 rpm to 5500 rpm. Any 50% downsized engine i.e. the Ricardo HyBoost and the Ford EcoBoost, present a peak torque at least 2.5 times higher from 2000 rpm to 3500 rpm. When comparing the baseline model to a heavily boosted engine of the same displacement, as the JLR Ultraboost, it can be observed up to 3.2 times greater torque. This 2.0 dm^3 concept was meant to replace a 5.0 dm^3 NA engine (60% downsizing) and was able to reach up to 3.3 MPa BMEP and 257 Nm/dm^3 at 3500 rpm. Nevertheless, all downsized concepts still face limitations concerning low speed torque as shown in Figure 2.11 between 1000 rpm and 2000 rpm. The

transient response of such engines is also an issue considering that at least 50% of boost build-up is required to meet the transient torque response of a 30% downsized engine [71]. The adoption of VVA, two-stage turbocharging, superchargers and e-boosters showed promising results in this matter [74]. Improved quality gasolines [75] and alcohol fuels [76] are often employed to avoid knocking combustion. Abnormal combustion is also avoided by using cooled external EGR at higher loads and speeds so the rates of heat release are reduced [77]. All downsized engines presented were operated at stoichiometric conditions and have at least one turbocharger. Some kind of VVA system (cam phaser, variable duration and variable lift) was also employed.

Table 2.1 – Details of the selected downsized engines.

Model	Number of cylinders	Displacement (dm^3)	Year	Ref.
Baseline - Ford Duratec	4	2.0	2005	[46]
Bosch MPE	2	0.85	2013	[17]
Fiat Multiair	4	1.4	2015	[78]
Ford EcoBoost	3	1.0	2012	[79]
JLR Ultraboost	4	2.0	2014	[73]
Mahle	3	1.2	2008	[69]
Ricardo HyBoost	3	1.0	2012	[74]
Toyota ESTEC	4	1.2	2015	[80]

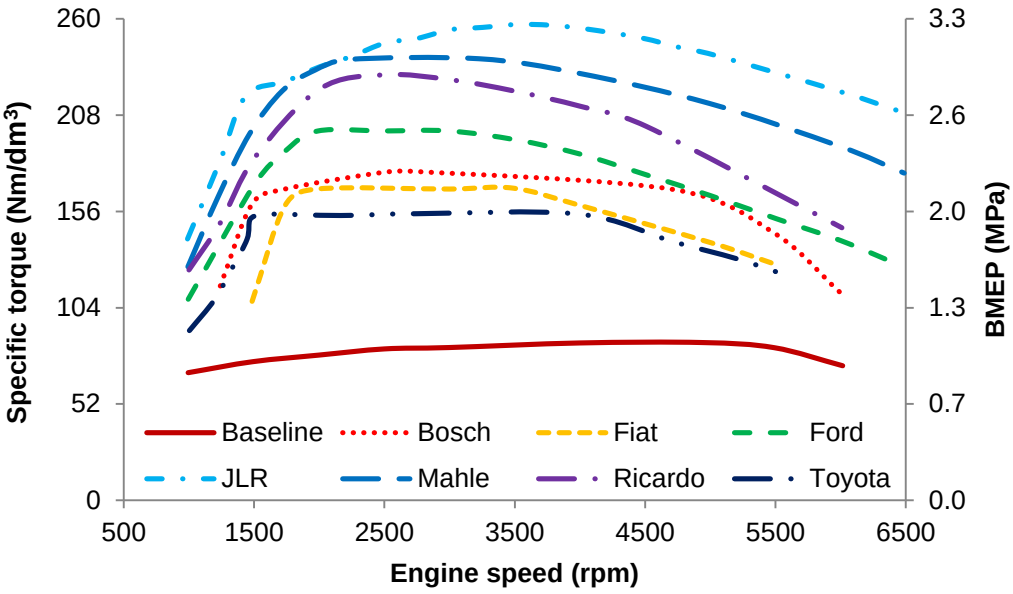

Figure 2.11 – Benchmark of contemporary downsized four-stroke engines.

One of the first downsized engines able to reach 120 kW/dm^3 was proposed by Mahle in 2008 [69] and presented up to 30% better fuel efficiency than its counterpart 2.4 dm^3 engine. Performance results from the two-cylinder Bosch MBE engine [17] described 24% improvement in fuel consumption compared to a four-cylinder 1.6 dm^3 NA engine. Similarly, the 60% downsized JLR Ultraboost demonstrated up to 38% better fuel economy in certain regions of the NEDC [73] compared to the larger counterpart engine. The higher knock resistance of ethanol, besides its larger cooling effect resulted from higher heat of vaporisation, enabled a 53% downsized engine to reach nearly 3.3 MPa BMEP [76]. Up to 44% brake efficiency was obtained in this 1.4 dm^3 two-stage turbocharged engine running on E100.

When extreme engine downsizing is desired i.e. beyond 50%, high in-cylinder temperatures and pressures are obtained at high loads. The long exposure of the unburnt charge to high temperatures during the flame propagation period may result in knocking combustion. It has been observed that the occurrence of knocking combustion, especially at low engine speeds, may be also induced by pre-ignition. Though this low speed pre-ignition (LSPI) has not been fully understood, numerous authors agree that hot spots containing lubricant oil may be its cause [81][82]. The occurrence of LSPI, also known as super-knock or mega-knock, poses serious risk for the components of downsized engines [18]. The reduction of lubricant oil consumption by means of improved piston ring sealing proved to be effective on reducing its incidence [83].

The greatest advantage of SI over CI engines relies on the reduced cost of fuel metering systems. Lower engine robustness required to deal with lighter in-cylinder pressures and inexpensive aftertreatment systems are also a plus of gasoline engines [73]. However, with highly downsized SI engines, in-cylinder pressures comparable to CI engines are obtained and hence a similar structural strength is required. The requirement for more sophisticated GDI systems, such as piezoelectric injectors, also reduces the production cost difference between SI and CI engines.

Given the limitations faced by downsized gasoline engines, mostly attributed to the higher loads attained, the two-stroke cycle may represent an alternative thanks to its doubled firing frequency. Recently, a two-cylinder uniflow GDI two-stroke engine showed the possibility of achieving a BSFC of 250 g/kWh at 2000 rpm and 0.9 MPa IMEP [66]. Two exhaust cam phasers enabled the achievement of CAI combustion at lighter loads. Despite the fact the exhaust air/fuel ratio was lean, lower cost aftertreatment systems could be employed considering the minimum NOx emissions from this low temperature combustion mode. Two-stroke poppet valve engines have been also quoted to provide high power with lower in-cylinder pressures and hence less structural stresses. With the same architecture of conventional four-stroke GDI engines, a switchable two/four-stroke three-cylinder 1.0 dm^3 engine was proposed to replace a 1.6 dm^3 unit [46]. In such project the engine operated in the four-stroke cycle at mid-low loads only, where four-stroke engines have usually better performance than two-stroke engines due to the residual gas dilution. On the other hand, a fast actuation electrohydraulic valve train enabled the two-stroke cycle operation at full load conditions. When applied to a C-class passenger car this strategy enabled 24% better fuel economy over the NEDC compared to the four-stroke counterpart engine. In another research using a four-cylinder engine, half of the cylinders were operated in the four-stroke cycle whilst the other half run in the two-stroke cycle. With the over expansion of the burnt gases from the four-stroke cycle into the two-stroke cycle, up to 10% fuel economy was realised at mid-high loads and below 2500 rpm [84].

2.4.2 Stratified charge combustion

Alongside engine downsizing, stratified charge combustion is also an option to improve fuel consumption at light loads in gasoline engines. In this approach a flammable air-fuel mixture is delivered in the vicinity of the spark plug by a late injection whilst the rest of the cylinder is predominantly filled with air and/or burnt gases. The pumping losses are minimised due to unthrottled operation and the thermodynamic efficiency of the cycle increases as a result of the greater ratio of heat capacities under lean charge conditions. This concept has been studied since the 1920’s [8], although its application to small vehicles took over only in the 1990’s with the development of higher pressure solenoid type fuel injectors.

Mitsubishi was the first company to implement a stratified charge combustion system to passenger cars in 1996 using the “first generation” wall guided concept [9], as seen in Figure 2.12 (left). In this method the mixture is prepared and transported towards the spark plug by means of a piston cavity, which is assisted by the air flow through oriented intake ports. However, the formation of a fuel film on the piston top becomes a source of UHC and soot emissions if the fuel is not entirely vaporised at the onset of combustion [27]. The operation range of wall-guided systems is also limited by the engine speed due to the essential matching between SOI timing and piston position [85].

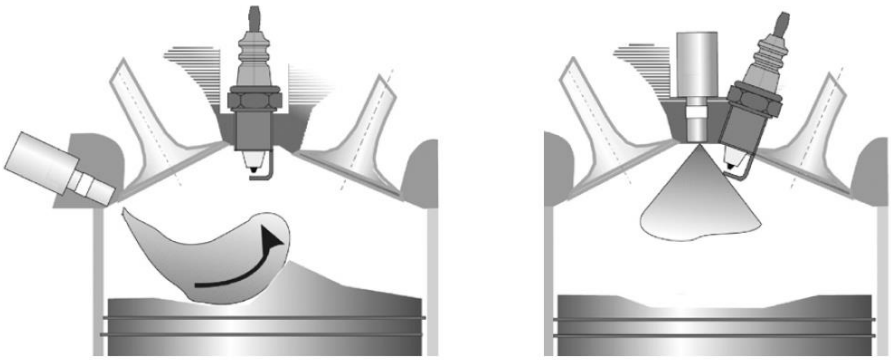

Figure 2.12 – Wall-guided (left) and spray-guided (right) direct fuel injection systems, adapted from [9].

Given the limitations of the wall-guided approach and with the development of more sophisticated fuel injectors, the spray guided concept was introduced in 2006 by BMW and Mercedes-Benz [9]. This “second generation” of stratified charge combustion system, seen in Figure 2.12 (right), employed higher injection pressures and enabled wider operation regions under stratified combustion. Improvements around 10% in fuel consumption were found over the NEDC compared to homogeneously charged PFI engines [27]. Nevertheless, the centrally mounted injector induced packaging constraints in the combustion chamber and increased the risk of fuel impingement on the spark plug.

The lower the engine load the greater is the improvement in fuel consumption offered by stratified charge combustion. The use of multiple injections at low loads was also able to improve fuel economy by 30% compared to homogeneous charge combustion [12]. As the load increases, lean homogenous charge combustion can be an option to avoid excessive combustion deterioration

resulted from late injections. Although lean homogeneous combustion does not necessarily take advantage of unthrottled operation, the gains due to greater ratio of heat capacities are still present. Moreover, the excess of oxygen ensures that nearly all of the injected fuel is oxidised, which is particularly the case with an excess of air around 10% above the stoichiometric condition [27]. If the combustion becomes excessively lean, the lower temperature hinders the oxidation process and increases CO and UHC emissions.

In the Ricardo Volcano concept the stratified charge combustion was extended up to 1.5 MPa BMEP and resulted in BSFC values below 225 g/kWh [11]. The maximum brake efficiency registered in this engine was 42% at 1.0 MPa and 2500 rpm. The implementation of stratified charge combustion in the two-stroke cycle has been also reported for loads as high as 0.8 MPa IMEP [64], which resulted in 10% improvement in fuel consumption compared to homogeneous charge combustion. This three-cylinder 1.0 dm^3 two-stroke GDI turbocharged engine, able to reach 90 kW/dm^3 at 4500 rpm, also demonstrated 25% greater torque than an equivalent four-stroke engine of the same displacement.

The use of ethanol enabled the enlargement of the maximum load attainable with stratified charge combustion. Its oxygen content improved the oxidation of over rich regions and less soot was obtained compared to gasoline operation [86]. In another study [12], 35% lower NOx emissions were obtained in a 0.5 dm^3 engine when replacing gasoline by ethanol. However, the engine efficiency was penalised by the longer spray penetration resulted from the larger amount of fuel injected for the same energy substitution than gasoline. In this case the fuel plumes reached farther in the cylinder and the combustion occurred closer to the chamber walls, which resulted in increased heat losses.

Despite the numerous advantages of stratified charge combustion in SI engines, particularly at lower loads, its application to passenger vehicles still presents challenges regarding exhaust aftertreatment [73]. During stratified operation NOx emissions are higher compared to homogeneous combustion due to the greater combustion temperature in over-rich zones. The higher in-cylinder pressure and oxygen availability, resulted from unthrottled operation, also contribute to

increase NOx production. Furthermore, by the end of the combustion the flame front quenches in lean regions and results in large amounts of UHC and CO. Due to the lower in-cylinder temperature associated with the overall-lean mixture, these emissions are hardly post-oxidised and the combustion efficiency drops [9]. CO and UHC emissions are further deteriorated if cooled EGR is employed to mitigate NOx emissions, in view of the current inefficiency of TWC to do so.

Therefore, the implementation of stratified charge combustion in SI engines relies on the development of more cost-effective lean-NOx aftertreatment systems than LNT and SCR. Although SCR systems with liquid urea injection are already common amongst Diesel trucks and buses regulated by the Euro 6 standard, its application for passenger cars is still very costly. Nevertheless, the use of such aftertreatment systems may be required in the future considering the fuel economy improvements of stratified charge combustion. Besides, currently downsized engines have larger valve overlaps to reduce the residual gas trapped at higher loads, so part of the fresh air is short-circuited to the exhaust and increases its air/fuel ratio. Fuel enrichment is then employed to reduce the exhaust lambda back to the stoichiometric condition, though the fuel efficiency obviously drops in such cases [17].

2.4.3 Controlled auto-ignition combustion

Controlled auto-ignition (CAI) combustion has been extensively studied in the last decades in four-stroke engines, although it was firstly conceived in two-stroke engines operating at light loads [13]. Such combustion concept has the potential to enhance thermal efficiency and reduce NOx emissions compared to SI flame propagated operation [14]. The shorter burning duration and inferior temperature combustion result in lower heat losses, which is the main drive of improved fuel efficiency. Numerous methods have been proposed to achieve auto-ignition combustion in four-stroke gasoline engines, such as intake air heating [87], residual gas trapping through negative valve overlap (when the exhaust valve closes before TDC and the intake valve opens after it) [88], and exhaust gas rebreathing (when the intake valve opens during the exhaust phase and/or the exhaust valve opens during the intake phase) [89]. Negative valve overlap (NVO) induces higher in-cylinder turbulence compared to exhaust gas

rebreathing [90], which is advantageous considering the slow-down effect of charge dilution on the combustion rates. Conversely, NVO increases the pumping losses due to the recompression loop resulted from earlier EVC. In the two-stroke cycle CAI combustion is readily achieved when a large amount of hot residual gas is trapped at low scavenging efficiencies [91].

CAI combustion is obtained by increasing the in-cylinder temperature until the occurrence of auto-ignition of the air-fuel mixture, which is usually around 1000-1100 K for gasoline fuelled engines [13]. The result is the appearance of multiple auto-ignition points throughout the combustion chamber instead of a propagating flame as in SI combustion. As the NOx production is largely enhanced beyond 1800 K, its emissions with CAI combustion are greatly minimised. However, this low temperature combustion presents a negative effect on CO emissions, once its full oxidation into CO_2 occurs in the range of temperatures of 1400–1500 K [13]. Due to the short burning duration resulted from the rapid heat release process, CAI combustion is usually not employed at higher engine loads as a result of excessive combustion noise. On the other hand, at lower loads the heat release process weakens in the diluted charge, so the in-cylinder temperature drops below the auto-ignition threshold and results in unstable combustion.

The greatest challenge of CAI combustion relies on the combustion phasing control to maximise thermal efficiency and attenuate combustion noise. In PFI engines, controlled auto-ignition combustion is often referred as homogeneous charge compression ignition (HCCI) combustion given the higher degree of charge homogeneity compared to DI engines. In such cases internal/external EGR management and VVA systems [92][93] provide some means to control combustion timing. In DI engines the heat release process can be controlled by charge stratification at late SOIs, which is often called partially premixed compression ignition (PPCI) combustion or partially premixed combustion (PPC) [94]. This concept is able to extend the limits of controlled auto-ignition combustion whilst keeping an acceptable trade-off between thermal efficiency and combustion noise. Compared to EGR and VVA systems, the mixture stratification provides a faster response and more effective control of the combustion event after IVC/EVC [95]. Dual-fuel injection strategies, such as

reactivity controlled compression ignition (RCCI) with gasoline and diesel, showed great control over combustion phasing by means of charge and fuel reactivity stratification [96]. Whilst this approach uses DI and PFI to deliver fuels of different reactivity, a more recent study presented indicated efficiencies as high as 47% by directly injecting both fuels into the combustion chamber [97]. The spark assistance for CAI combustion has been also investigated to extend the operation range of gasoline [98][99] and ethanol [100] fuelled engines, which is known as spark assisted compression ignition (SACI). In this hybrid combustion mode the heat release process is divided into an initial flame propagation phase with later auto-ignition combustion. As the flame front propagates, it compresses the end-gas against the combustion chamber walls and increases its pressure and temperature until auto-ignition occurs [101].

Numerous studies have demonstrated the potential of CAI combustion on improving fuel economy and NOx emissions in four-stroke gasoline engines. In a recent study, gasoline PPC was applied to a 1.8 dm^3 four-cylinder GDI engine with unthrottled operation [15][102]. Diesel-like efficiencies as the BSFC of 214 g/kWh at 2000 rpm were obtained. The exceptional fuel economy was largely resulted from lean-burn combustion and a compression ratio of 15:1. Multiple late injections of gasoline were employed to control combustion phasing and pressure rise ratio (PRR). Two oxidation catalysts were used to convert CO and HC. Emissions of NOx and PM remained below 0.2 g/kWh and 0.1 FSN, respectively, from 800 rpm to 2500 rpm and from 0.2 MPa to 1.5 MPa IMEP. The engine was able to run from idle until 2.0 MPa BMEP at 2000 rpm on pure PPC, whilst simulations showed the ability of controlling combustion phasing at speed/load transitions. In a similar study, ethanol demonstrated great potential for reducing the combustion noise at boosted operation when mixed with gasoline in volumetric proportions of 10% and 20% [103].

The application of CAI combustion in a two-stroke poppet valve GDI engine was found to reduce fuel consumption in 11% compared to a similar four-stroke engine operating at 0.36 MPa IMEP and 1500 rpm [60]. Fuel savings above 20% were obtained in comparison to two-stroke SI operation at the same engine load and speed. In another two-stroke poppet valve engine running on gasoline PPC,

indicated efficiencies compared to diesel operation were achieved with lower NOx and soot emissions [104]. At 0.55 MPa IMEP and 1500 rpm the ISFC of 223 g/kWh was assessed with NOx and smoke emissions below 0.25 g/kWh and 0.4 FSN, respectively. In a three-cylinder 0.9 dm^3 uniflow scavenged engine 10% better fuel consumption over the NEDC was obtained with CAI combustion compared to a 1.6 dm^3 four-stroke NA engine [65]. Nevertheless, similarly to what happens in four-stroke engines, the CAI combustion in two-stroke engines is limited by the abrupt heat release at high loads resulted from the greater in-cylinder thermal condition. At near idle the auto-ignition process is hindered by the large residual gas fraction that slows down the chemical reaction rates [68].

2.4.4 Vehicle hybridisation

The results presented in Figure 2.4 demonstrate the inevitable powertrain hybridisation path to attend future CO_2 emission legislations for passenger cars. Pure electric vehicles, also known as battery electric vehicles (BEV), are a possible solution to reduce these emissions. However, the energy density in current batteries for vehicular application is around 0.7 MJ/dm^3 [105], compared to 32 MJ/dm^3 of gasoline at ambient conditions. Such limitation still presents a trade-off amongst vehicle autonomy/weight and production cost. The use of fuel cells in passenger cars also results in null CO_2 emissions, though the current methods employed to obtain hydrogen and the distribution grid required for so is still cost prohibitive [106]. Therefore, a plausible solution for reducing CO_2 emissions from passenger cars in the next decades relies on hybrid units with electric motor(s), batteries and an internal combustion engine (ICE).

In electric hybrid vehicles (EHV) both ICE and electric motor(s) are able to directly power the vehicle, so the propulsion strategy is upon the driving conditions. EHVs do not have an external connection to the electrical grid, so the batteries are charged by means of regenerative braking and other energy saving arrangements. Conversely, plugin hybrid electric vehicles (PHEV) share similar features to HEVs but can be also recharged by an external power source. The larger capacity batteries in these vehicles allows greater flexibility of propulsion strategies, such as serial/parallel connection between electric motor(s) and ICE [107]. In parallel connection both electric motor(s) and ICE provide propulsion to

the vehicle as in the case of high power demand. In serial mode the ICE runs to power an electric generator, which then provides energy to the batteries or electric motor. In some cases the ICE does not even have connection to the driveline, which is entirely powered by the electric motor(s). Therefore, in these conditions the ICE is used as a range extender to the electric system and is usually activated when the battery load reaches a minimum level [20].

In 2014 the global sales of electric vehicles (BEV, HEV and PHEV) reached about 300,000, which represented an increase of 53% compared to 2013. The most successful country on adopting electric vehicles is Norway with nearly 13% of the total fleet, followed by the Netherlands with about 4% of the fleet in 2014 [105]. Worldwide, it is expected that the sum of electric vehicles outnumbers the new sales of light-duty gasoline/diesel vehicles by 2040 as seen in Figure 2.13.

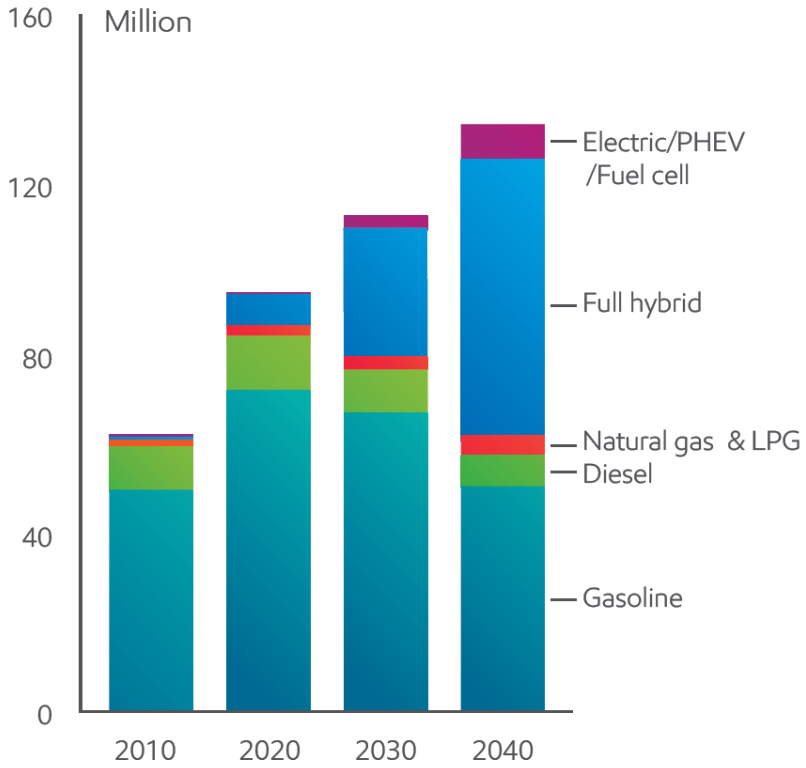

Figure 2.13 – Annual world new light-duty vehicle sales, adapted from [4].

With the increasing hybridisation of powertrains the ICE may turn out to assume a secondary role in the vehicle propulsion. In this framework the two-stroke cycle engine has been quoted as a potential power unit for serving as a range extender in PHEVs [62]. Its higher power density, reduced weight and compactness are the major advantages compared to four-stroke engines.

Moreover, if the ICE operation is intermittently required due to battery recharging strategies, the reduced NVH of two-stroke engines may represent a large advantage over the four-stroke counterparts. In a comparison between two/four-stroke GDI engines for a 30 kW range extender, both engines demonstrated similar BSFC, though the two-stroke unit was found 15% lighter and 38% more compact [108]. In another study, a loop scavenged two-stroke GDI engine was developed as a range extender to produce 122 kW/dm^3 with a minimum BSFC of 242 g/kWh at 3000 rpm [109]. The NVH of this concept was further improved by placing the scavenging pump (a conventional piston-cylinder assembly) at 90° with the single powering cylinder.

The power generation with two-stroke engines may also take advantage of the more frequent firing operation to linearly arrange the cylinder as a free-piston engine [110]. Instead of converting the reciprocating movement into rotation, the electric components are assembled in a single rigid connecting rod between two opposed pistons. In this case the friction losses in the crank train are minimised and the set ICE-generator is compacted in a single linear electric machine. Mechanical simplicity, elimination of side forces and variable compression ratio are amongst the advantages of such concept [111].

2.5 Biofuels

The depletion of oil reserves and the requirement for reducing GHG emissions has encouraged the use of biofuels in the transport sector. A large range of fuels obtained from the biomass have been proposed to replace (or blend with) fossil fuels. In CI engines the addition of biodiesel obtained from vegetable oils to conventional diesel is already adopted in small quantities (7%) in the EU, which is known as B7 [112]. In the context of SI engines alcohol fuels have been quoted as a promising add-on or even replacement to gasoline, with particular attention to methanol, ethanol, propanol and butanol. The first two “lower” alcohols present interesting characteristics as greater knock resistance and heat of vaporisation. However, their reduced lower heating value (LHV) results in higher volumetric fuel consumption than gasoline. Meanwhile, propanol and butanol present larger LHV due to the longer carbon chain, but their knocking resistance and heat of vaporisation are not so attractive for using in highly

charged SI engines [47]. Even though ethanol has inferior knocking resistance and lower heat of vaporisation than methanol, its production from widely available feedstocks such as corn, sugar cane, sugar beet and cassava has disseminated its use. Ethanol production from cellulose and algae, known as second and third generation ethanol, respectively, has been also subjected to extensive research [113]. On a global basis the ethanol production reached 93 million cubic metres in 2014, amongst which the USA accounted for nearly 60% of it, Brazil 25% and the European Union 6% [114].

The idea of using ethanol as a fuel in passenger cars is as old as the automobile itself and dates back to 1908 with the Ford Model T in the USA. Ethanol, called by Henry Ford as “the fuel of the future”, was shortly after replaced by gasoline due to government concerns regarding its consumption by the population as an alcoholic beverage [115]. With the oil shortage in the 1970’s some countries renewed their interest in ethanol for automotive applications, amongst which Brazil was the most prominent. Aiming at reduced dependency on the oil imports, the Brazilian government launched in 1975 the “Proalcool” program. In this campaign ethanol was widely implemented in the transport sector from motorcycles to passenger cars and trucks [116]. After some shortages in the supply of ethanol and with the stabilisation of the oil prices in the 1990’s, ethanol fuelled passenger cars lost their share in the market to fuel flexible vehicles [117]. These flex-fuel vehicles could run on any blend of gasoline-ethanol and have been greatly accepted by the market since the 2000’s. At the present time all gasolines sold in Brazil have between 25% and 27% of ethanol in its volumetric composition [118]. Hydrous ethanol fuel (~94% ethanol and ~6% water) is also nationally available for passenger cars. Worldwide, ethanol is currently added to gasoline in volumetric proportions of 5% to 10% (E5 - E10), which requires minor hardware modifications in SI engines [119]. In the EU E10 is available in France, Finland and Germany, whilst Austria and Sweden have also E85 (85% v/v of ethanol in gasoline) [112]. In the USA E15 is available in 16 out of the 50 states, though E85 is still restricted to a few places [114].

In a “tank-to-wheel” (TTW) analysis of a passenger car, which is basically the vehicle’s fuel conversion efficiency, the reduction in CO_2 emissions by switching

from gasoline to ethanol is not particularly high as seen in Table 2.2. Actually, any replacement of pure gasoline (E0) by its blends with ethanol (E10, E20, E85 and E100) has a small impact of about 6% in the TTW CO_2 emissions. Even though the TTW analysis is the contemporary approach chosen by the EU and other countries to impose fuel consumption restrictions, is does not reproduce the real CO_2 emissions considering the fuel production processes [106]. In this framework the "well-to-tank" analysis shown in Table 2.2 exposes the real gains in replacing gasoline by ethanol. The negative values presented for E85 and E100 indicate that, unlike gasoline and diesel, the ethanol production process does not necessarily increases the levels of CO_2 in the atmosphere. In other words, the CO_2 released during its production process is offset by that absorbed during the photosynthesis of the plants whereby ethanol is obtained. Considering the whole fuel life cycle on a "well-to-wheel" basis, ethanol fuelled passenger cars can reduce net CO_2 emissions compared to gasoline operation depending on its production process and crop employed (sugar cane, corn, cassava, etc.).

Table 2.2 – Estimation of equivalent averaged CO_2 emissions in a well-to-tank (WTT), tank-to-wheel (TTW) and well-to-wheel (WTW) basis. Adapted from [112].

Fuel	**WTT CO_2 (g/km)**	**TTW CO_2 (g/km)**	**WTW CO_2 (g/km)**
E100 (pure ethanol)	-127 to 30	146	19 to 176
E85	-82 to 29	143	61 to 171
E20	6 to 28	148	154 to 176
E10	17 to 28	150	166 to 178
E0 (pure gasoline)	29	156	185
Diesel	25	120	145
B7	14 to 19	120	137 to 140

Besides the environmental advantages of replacing gasoline by ethanol, its use in internal combustion engines yields numerous positive characteristics such:

Higher heat of vaporisation

It improves the charge cooling effect and reduces the exhaust gas temperature, so fuel enrichment is less frequently required than in gasoline fuelled engines to avoid aftertreatment and turbine damage [120]. In GDI engines this cooling effect can also reduce the volume of the induced charge and increase the charging

efficiency. The lower charge temperature during the compression phase reduces the compression work, so a greater thermodynamic efficiency is obtained [121]. In CAI combustion the lower in-cylinder temperature retards the combustion timing and enables higher loads to be achieved with lower combustion noise [87]. In a two-stroke poppet valve engine the use of E85 allowed 60% higher IMEP compared to pure gasoline, although the lower load range of CAI was shortened by misfiring due to the lower combustion temperature [68].

Higher octane number

It reduces the knock tendency and improves combustion phasing towards MBT, particularly in heavily super/turbocharged engines [122]. According to [123], ethanol enabled an increase of five units in the compression ratio compared to gasoline operation. This allowed the thermal efficiency to be enhanced in more than 12%. In a downsized engine fuelled with E85 up to 27% improvement in efficiency was achieved over the FTP75 driving cycle compared to gasoline operation [77].

Faster laminar flame speed

In the lambda range from 0.9 to 1.0 ethanol presents around 45% higher laminar flame speed than gasoline [76]. This advantage reduces the knock probability once the residence time of the end-gas prior to the flame front arrival is shortened. As the EGR or air dilution slows down the flame propagation process, ethanol presents greater dilution tolerance than gasoline [47].

Simpler oxygenated molecule

It enables the reduction of PM and PN compared to gasoline operation [124][125]. Also, the particles size emitted by ethanol combustion was found around half of that produced by gasoline [86]. The soot reduction, although, was not found proportional to the addition of ethanol in gasoline according to [119]. In this study E22 presented more soot than E0 at certain speeds and loads. The absence of aromatics and sulphur on ethanol composition ensures no deposits on GDI injectors even with ethanol blends as low as E20 [126]. This situation is further improved by the higher heat of vaporisation of ethanol, which reduces the injector tip temperature.

More moles of burnt gases

At stoichiometric condition and at a similar energy substitution of gasoline, the combustion of ethanol results in a larger volume of burnt gases and hence a greater pressure [126]. The combustion products from ethanol have 30% larger water content, which increases the burnt gas heat capacity and reduces the combustion temperature [127]. The lower combustion temperature has a positive effect on heat losses and improves the thermal efficiency of the cycle.

Lower adiabatic flame temperature

It also reduces the combustion temperature and hence heat losses, so the thermodynamic efficiency of the cycle is improved [121]. According to [120], this feature lengthens the catalyst heating time in PFI engines compared to gasoline operation. Conversely, in DI engines the difference in exhaust temperature (~50 K) was not found to pose any issue regarding the aftertreatment operation [119].

Ethanol also presents several drawbacks compared to gasoline operation in SI engines, such as:

Reduced LHV

The lower energy content per unit mass of ethanol results in a higher volumetric flow rate for the same energy substitution (engine load) of gasoline. In case of DI engines the larger fuel mass injected can lead to fuel impingement and oil dilution [123][86]. The larger volumetric fuel consumption also raises questions regarding the vehicle autonomy. However, smaller portions of ethanol blended in gasoline can improve the efficiency and offset the volumetric fuel consumption. According to [128], the use of E30 with a compression ratio of 13.1 greatly improved the engine efficiency by proper combustion phasing and stoichiometric operation at full load. Therefore, the reduced LHV of E30 caused only 2% penalty in volumetric fuel consumption in the USA EPA metro-highway driving cycle. Meanwhile, in a highway driving cycle (US06) the volumetric fuel consumption improved by 1% with E30. In case of PFI engines the larger amount of fuel injected may have a negative effect on charging efficiency, as the

vaporisation of part of the fuel in the intake port displaces the incoming air and compromises the charging process [124].

Lower vapour pressure

It leads to cold start problems and driveability issues under low ambient temperatures [121]. The engine start ability is improved by late injections in DI engines, as the fuel vaporisation enhances at higher in-cylinder temperatures [120]. Ethanol blends below 50% (E50) tend to vaporise more readily than E85 and E100 due to similar Reid pressure (absolute vapour pressure exerted by the fuel at 311 K) to gasoline [47].

Corrosion

Ethanol requires different materials to be employed in fuel handling and storage systems compared to those used with commercial gasoline [119]. Ionic impurities, such as chloride ions and acetic acid, are the main causes for corrosion in ethanol fuelled systems [129]. The azeotrope ethanol-water mixture with about 5% of water is also a source of oxidation in metallic components.

Emissions of toxic compounds

The combustion of ethanol produces large fractions of unburnt ethanol, aldehydes and formaldehydes [130]. Despite their toxicity, these compounds are still less toxic than butadiene and benzene emissions from gasoline combustion [127]. In the WLTP, to be introduced in the EU by 2017, regulations for unburnt ethanol and aldehydes are expected [7].

Gaseous emissions in ethanol fuelled SI engines have distinct trends in the literature in comparison to gasoline operation. In the case of UHC and CO some authors found lower emissions when using ethanol due to its increased oxygen content and faster laminar flame speed [68][86][131]. Conversely, the larger amount of fuel injected for the same energy replacement of gasoline leads to greater fuel impingement and longer fuel vaporisation times. Hence, it results in poorer combustion and larger UHC emissions [123][126]. The improved knock resistance of ethanol also allows better combustion phasing, so the peak in-cylinder pressure increases and more charge is pushed into the combustion

chamber crevices. During the expansion phase this trapped fuel comes back into the cylinder and results in larger UHC emissions [125].

Regarding NOx emissions ethanol also presents different trends in SI engines. With knock limited spark advance (KLS) operation in gasoline engines the in-cylinder peak temperature and pressure is limited. Therefore, ethanol can produce higher NOx due to better combustion phasing and hence higher in-cylinder temperature [125][132]. Whilst the increase in NOx emissions is more linked to the combustion temperature, the greater oxygen availability promoted by ethanol may also improve NOx levels [47]. On the other hand, charge cooling effect and lower adiabatic flame temperature of ethanol may reduce the combustion temperature and hence NOx production [12][68][123]. This is particularly the case of GDI engines where the majority of the heat absorbed by the fuel during its vaporisation comes from the in-cylinder charge. In PFI engines part of the vaporisation heat comes from the intake port and so the in-cylinder mixture is found at higher temperatures [124].

2.6 Summary

The necessity of developing more efficient internal combustion engines to reduce GHG emissions and the possible ways to achieve so were briefly presented and discussed. The role that two-stroke cycle engines may have on this transformation, if incorporated to passenger cars, was evaluated and contextualised with technologies expected to take over in the near future. Amongst these improvements, engine downsizing, stratified charge combustion, controlled auto-ignition combustion, and vehicle hybridisation are the highly quoted paths whereby light-duty vehicles may undergo. The large impact on total CO_2 emissions obtained by replacing fossil fuels by renewable sources, such as ethanol, was also described in the context of spark ignition engines. In the meanwhile, a short history about the two-stroke cycle engine was presented and its operation fundamentals detailed and compared to current four-stroke engines. The main pros and cons of two-stroke engines were accessed regarding the scavenging and charging procedures, followed by a basic description of the mixture formation and combustion processes.

Chapter Three
Experimental methodology

3.1 Introduction

The research work was carried out in a single cylinder prototype engine equipped with an electrohydraulic valve train system designed to operate in both two-stroke and four-stroke cycles [46]. The engine main control and instrumentation systems were developed during earlier researches [133]. As the present study focused on the two-stroke operation with gasoline and ethanol fuels, a number of improvements were conducted on fuel injection and metering systems, intake air management and exhaust gas analysis. Following the description of the research engine and test cell facilities in section 3.2, section 3.3 describes the data analysis and presents the equations used during real-time and post-processing analysis.

3.2 Experimental setup

All engine experiments were conducted in a camless single cylinder research engine mounted on a fully instrumented transient test bed as presented in Figure 3.1. A schematic view of the experimental facilities is shown in Figure 3.2, with the main engine parts in black; the intake air conditioning system in orange; the data acquisition and control in red; the emission analysers in navy blue; the dynamometer system in yellow; the hydraulic valve train unit in purple; the fuel supply system in blue; the lubrication system in green and the cooling system displayed in pink. The supercharger and gas analyser units were located outside the test cell. The engine control and data acquisition equipment were operated in the control room situated in the next bay.

Figure 3.1 – Overview of the engine test bed and experimental facilities.

3.2.1 Engine specifications

The research engine was equipped with an electrohydraulic fully variable valve train unit, capable of two-stroke and four-stroke cycles operation by means of independent control over the intake and exhaust valves. The engine had an 81.6 mm bore, 66.9 mm stroke and a 144.5 mm connecting rod length. The resulting swept volume was 350 cm^3 with an “oversquared” bore-to-stroke ratio of 1.22. A geometrical compression ratio of 11.8:1 was achieved with a dome-in-piston and a 126° pent roof combustion chamber. The intake valves were 28 mm in diameter whilst the exhaust valves were 30 mm, which is peculiar compared to conventional four-stroke engines where the intake valves are usually larger. However, in the two-stroke cycle the scavenging process at high engine speeds is more dependent on the exhaust flow characteristics and hence the effective exhaust flow area was greater. The engine had two conventional side mounted exhaust ports joining close to the interface to the exhaust pipe and two individual upright-straight intake ports, shown in Figure 3.3 in blue and green, respectively. These intake ports joined at the 1.63 dm^3 intake plenum. A 40 mm manual throttle was installed in place of the original drive-by-wire throttle in the course of this research to optimise the air flow control under light loads at steady state tests. Also, the operation became safer at very high boost pressures considering the possibility of electrical failure and sudden throttle closure. A 50 mm manual

butterfly valve was installed in the exhaust pipe so the exhaust backpressure could be also controlled. The engine block used was a Ricardo Hydra with under-piston oil cooling designed for two-stroke operation. The Denso Iridium IXU 24 spark plug, centrally mounted in the pent-roof chamber as seen in Figure 3.3, was powered by a single fire (up to 0.1 J) Bosch 0 221 604 006 coil-on-plug with an integrated ignition driver.

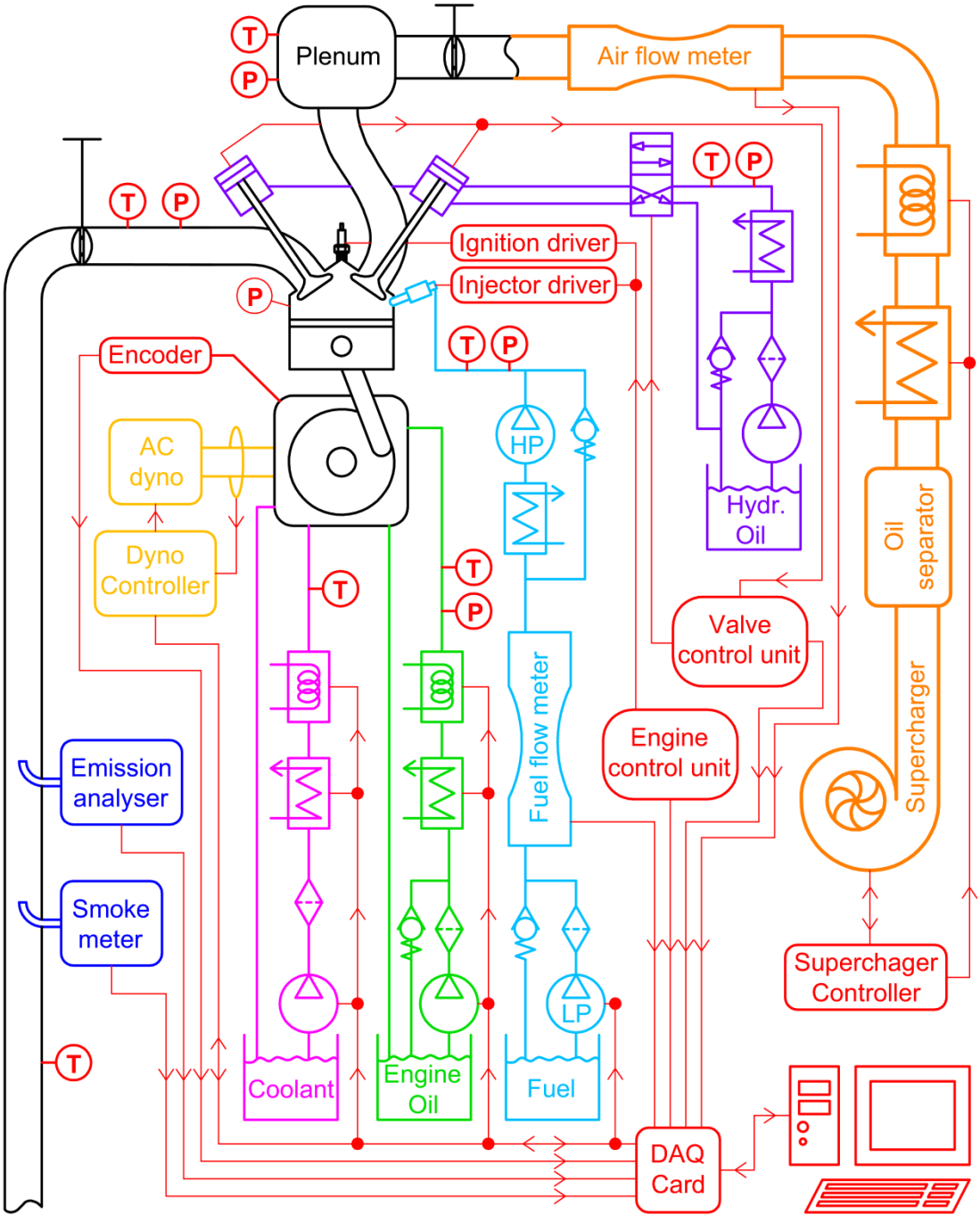

Figure 3.2 – Schematic representation of the research engine and test cell facilities.

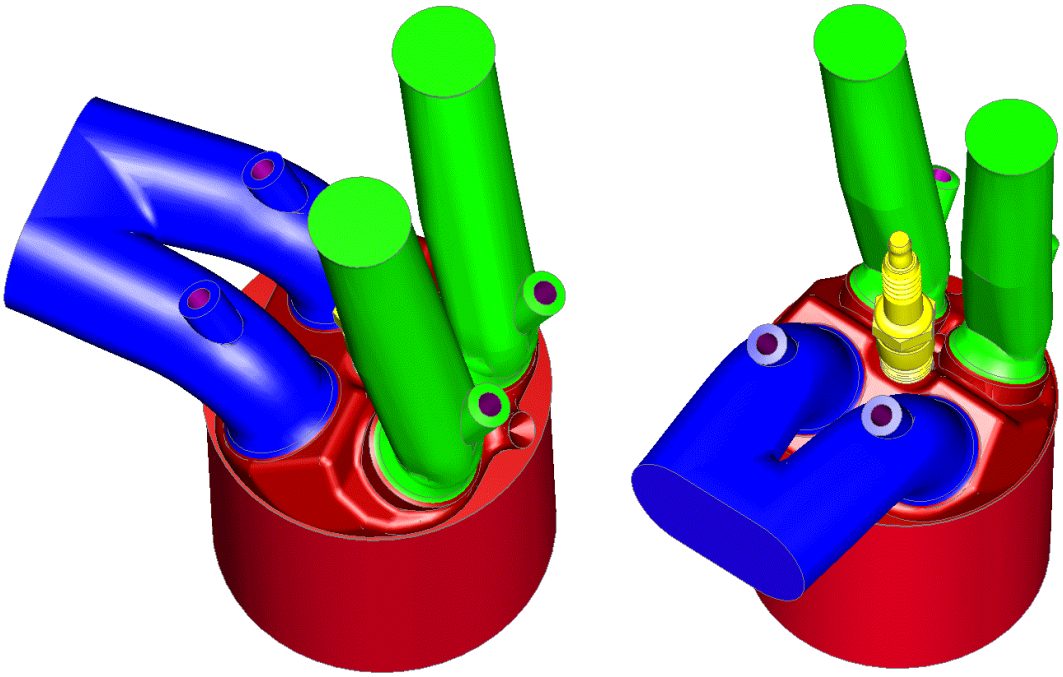

Figure 3.3 – Combustion chamber, cylinder and intake/exhaust port details.

3.2.2 Emissions measurement

The engine-out emissions were analysed regarding carbon monoxide (CO), carbon dioxide (CO_2), unburnt hydrocarbons (UHC), oxygen (O_2) and nitrogen oxides (NOx) in a Horiba MEXA 7170DEGR. Both CO and CO_2 measurements were performed on a dry basis in two non-dispersive infrared AIA-722 analysers, based on the individual radiation absorption of each gas in a given wavelength. The measurement range was set to 0-120000 ppm volume by volume (v/v) for CO and 0-200000 ppm v/v for CO_2. NOx emissions were analysed on a dry basis by a heated chemiluminescence detector model CLA-720MA. This measurement was based on the light emission of excited molecules of nitrogen dioxide (NO_2) resulted from the combination of nitrogen monoxide (NO) and ozone (O_3). The light emitted was proportional to the amount of NO sampled and injected into a reactor. On the other hand, NO_2 emissions were firstly converted to NO by means of a catalyst and then injected into the same reactor at alternated times with the original NO samples. Summing up the emissions of NO and NO_2 the final value of NOx was obtained, which in the case of this analyser ranged from zero to 50000 ppm v/v. To measure the free O_2 in the engine exhaust a MPA-720 paramagnetic sensor with an operation range from zero to 250000 ppm v/v dry was used. Its working principle was based on the paramagnetic property of oxygen (rare amongst the gases). Such characteristic made its molecules react

differently from the other gases in the sampled exhaust portion when they were immersed in a magnetic field. Finally, a heated flame ionisation detector (FID) model FIA-725A was employed to measure UHC emissions on a wet basis in the range 0-50000 ppm v/v. This detector operated by mixing the sampled exhaust gas with hydrogen-helium and injecting it into a burner with the addition of high purity air. The resulted flame carried ions which were detected in the form of electric current by two electrodes on each sides of the burner. The resulted electric current was closely and solely proportional to the number of carbon atoms found in the sample. Therefore, there was no differentiation between the types of hydrocarbons in the engine exhaust. All gaseous emissions were measured with an error below 1% of full scale or 2% of the reading (whichever smaller) and a repeatability within 0.5% of full scale.

In addition to CO, CO_2, UHC, O_2 and NOx emissions, engine-out soot was also evaluated by an AVL 415 Smoke meter. Its repeatability remained below 0.62 mg/m^3 with a resolution of 0.12 mg/m^3. The smoke meter measurement principle was based on the changes in the reflectance of paper, through which a sample of the exhaust gases had been previously drawn. The smoke value of 5437 mg/m^3 corresponded to total absorption of the light by the black soot, whilst a smoke value of zero meant that all the light was reflected by the clean paper. More details about emission analysers and their working principles can be found in [134].

An important detail considered was the exhaust emission sampling point, which was set close enough to the engine to avoid water condensation and subsequent unburnt hydrocarbon dilution. A heated line was used to connect the gas analyser to the exhaust pipe, besides a heated pre-filter in the joint so that any large particle of soot could be retained. On the other hand, the gas sampling point could not be set so close to the engine due to the air short-circuiting taking place in the two-stroke cycle. The existence of “pockets” of different gas concentrations in the exhaust pipe could affect the measurements depending on the emission analyser sampling rate. A surge tank is often employed in the exhaust pipe between the cylinder head and the sampling point, so that a better gas homogeneity can be achieved prior to the examination. However, in the two-

stroke cycle the exhaust gas temperature is found lower than that achieved in four-stroke engines due to the burnt gases dilution by intake air. Thus, there was a trade-off between exhaust gas homogeneity and enough gas temperature to avoid water vapour condensation. As presented in [23], the oxygen concentration in the exhaust pipe of a ported two-stroke engine showed a constant and uniform concentration after about 0.5 m from the cylinder head, regardless of the engine speed. It was therefore convenient to guarantee an adequate exhaust pipe length for mixing prior to the emission sampling point, but the gas temperature had to be constantly monitored to ensure at least 383 K. For these reasons two different gas sampling positions were adopted: the first one was set to about 0.2 m from the cylinder head and used exclusively for engine loads below 0.4 MPa IMEP when the exhaust temperature and air short-circuiting were lower. For loads beyond this, both gas and smoke analysers were moved downstream the exhaust pipe to about 2.7 m from the cylinder head. It should also be pointed out that the gas analyser probe was kept at least 1.5 m upstream the smoke meter sampling probe, considering its automatic purge function and the consequent risk of false readings by the gas analyser.

3.2.3 Fuel supply system

The fuel system, shown in blue in Figure 3.2, provided gasoline or ethanol at 15.0±0.5 MPa and 293±5 K for all the tests. A low pressure Bosch 0 580 464 070 pump supplied fuel through a conventional paper filter to the high pressure pump, a Bosch 0 261 520 016 three piston @ 120° reciprocating type. The fuel pressure at the low pressure side of the fuel line was controlled by a standard automotive pressure regulator at 0.35 MPa. The fuel pressure at the high pressure side was controlled by a SUN hydraulics 0BZ9K1 regulator, returning the excess of fuel to the inlet of the high pressure pump. Considering the large amount of fuel recirculating through the pressure regulator, a liquid-to-liquid heat exchanger was placed between it and the inlet of the high pressure pump. The instantaneous fuel mass flow rate was measured by an Endress+Hauser Promass 83A Coriolis flow meter type, with a maximum error of ±0.2% in the flow range studied. This type of flow measurement is based on the oscillation of the tube where the substance flows, which has different nodal points according to the velocity the fluid is transported. An exciter emitted constant oscillation pulses

towards the tube, whilst sensors at the inlet and outlet of the flow meter detected the phasing (twisting) taking place in the tube as a result of the liquid's inertia. The higher the flow velocity, the greater was the deflection in the oscillating tube. As the fluid density has also a known effect on the oscillation frequency of the tube, the mass flow rate could be determined and corrected for temperature and pressure. This meter was installed on the high pressure side of the fuel line to avoid flow cavitation as recommended by the manufacturer. However, such arrangement was found to be prone to the pressure wave due to the fuel injector opening and closing. At certain engine speeds and loads the injector operation propagated waves in the fuel line which interfered on the measuring sensors inside the flow meter. Therefore, the flow meter was relocated between the low and high pressure fuel pumps, where the pressure remained around 0.35 MPa and cavitation was still avoided. The fuel pressure was measured close to the fuel injector by a Druck PTX 500 with linearity better than 0.3% of full scale.

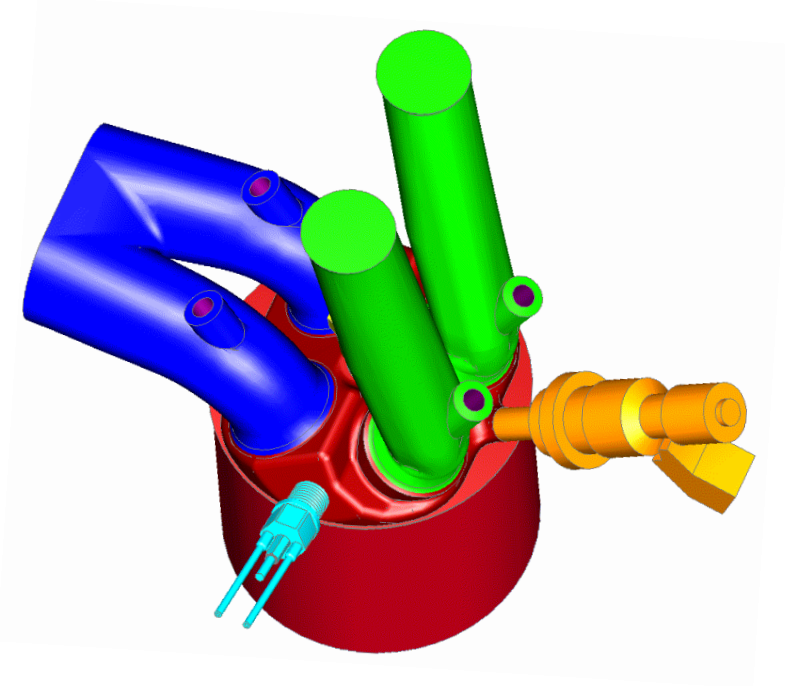

Figure 3.4 – Standard cylinder head assembly with the Denso double slit fuel injector (orange) and Kistler pressure transducer (light blue).

The gasoline or ethanol fuel was directly injected into the cylinder by two different types of injectors. The original injector was a Denso double-slit solenoid type mounted between the intake ports as presented in orange in Figure 3.4. This injector produced a double fan shaped spray from the first generation of gasoline direct injection (GDI) systems and was powered by a Denso injector

driver, popularly employed in the Lexus IS 250 [135]. This injector was used during the experiments presented in chapters five and six. On the second part of this research (chapter seven onwards) a Magneti Marelli IHP 072 asymmetrical six-hole injector, used in the VW Golf 1.4 TSI, was employed. This multi-hole GDI injector (in black in Figure 3.5) was also side mounted in the cylinder head, but in a different location from the first injector by switching positions with the in-cylinder pressure transducer. As a result, an AVL pressure transducer (in pink) was installed under the intake ports through an adaptor whilst the multi-hole injector was placed along the direction of the pent-roof through another adaptor (light blue in Figure 3.5). Due to the new injector's higher power demand, a Life Racing driver, able to power GDI injectors under fuel pressures of up to 35 MPa, replaced the standard injector driver.

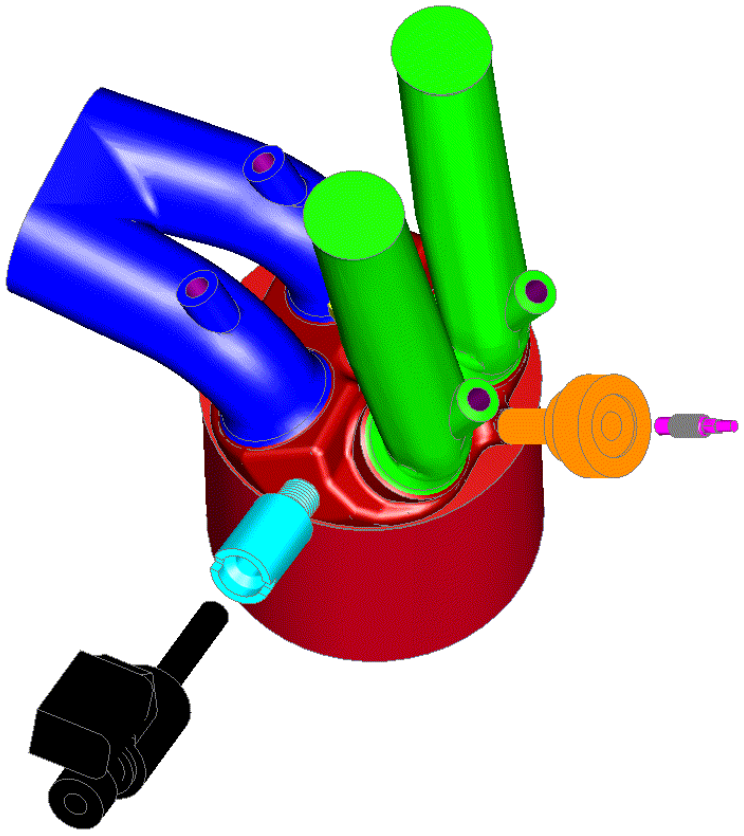

Figure 3.5 – Cylinder head assembly with the Magneti Marelli multi-hole fuel injector (black) and the AVL pressure transducer (pink), besides the demanded adaptors (light blue and orange, respectively).

Two different fuels were used in this research: commercial gasoline and pure ethanol. During the preliminary study on the mid-high load performance of the two-stroke poppet valve engine (chapter five) and its investigation regarding the

gas exchange process (chapter six), only gasoline was employed. In the following chapters both fuels were tested and their characteristics can be found in Table 3.1. According to the British standard BS EN 228 from 2012 [136], the "Unleaded petrol 95" sold in the United Kingdom has up to 2.7% by mass of alcohol content. The preferred oxygenated biofuel used in this case is ethanol, which results in a splash blended mixture of up to 5% by volume in gasoline (E5). The pure ethanol (E100) used was supplied by Hayman Limited UK.

Table 3.1 – Summary of gasoline and ethanol fuels characteristics.

Fuel properties	Gasoline (E5)	Ethanol (E100)
Normalised chemical formula	$CH_{1.93}O_{0.027}$ *	$CH_3O_{0.5}$
Density at 293 K (g/cm^3)	0.72-0.75	0.79
Research octane number (RON)	95	109
Heat of vaporisation (kJ/kg)	350	840
Oxygen content (m/m)	<0.027	0.348
Lower heating value (MJ/kg)	42.5	26.9
Vapour pressure at 293 K (kPa)	45.0-100.0	5.7

(*) Normalised gasoline formula [8] with the addition of 2.7% (m/m) of alcohol [136].

3.2.4 Data acquisition and control

The data acquisition and control systems, shown in red in Figure 3.2, were mainly composed of an engine control unit (ECU), a valve control unit (VCU), a data acquisition (DAQ) board and a PC. The ECU used, a Dual core Ricardo rCube, was responsible for controlling spark timing and injection timing/quantity through CAN protocol communication to the host computer running ETAS Inca V5.4. This calibration software also created the interface required to control the intake and exhaust valve timings and lifts by means of the VCU. A National Instruments 6353 USB X card with 32 analogic inputs and 1 Mega samples per second (MS/s) multichannel was used for data acquisition purposes. Temperature and pressure signals (labelled as "T" and "P" in Figure 3.2, respectively) were collected by the DAQ card. The crank angle position, generated by a LeineLinde encoder with a resolution of 720 pulses per revolution, was also collected and processed on real-time. The ECU feedback to the DAQ card, containing injection timing, injection pulse width and spark timing, was processed and displayed on a transient combustion analysis program

developed by Dr Yan Zhang [133] as shown in Figure 3.6. This software enabled the calculation of the indicated mean effective pressure (IMEP), covariance of the IMEP, indicated specific fuel consumption (ISFC) and combustion parameters based on the equations to be presented in section 3.3. The VCU feedback to the DAQ card, with valve opening and closing times (detected at 0.7 mm of lift) and valve lifts, was also processed on real time. Several other parameters were logged and averaged over 100 cycles, as engine speed, brake torque, fuel and air mass flow rates and the emission results sent by the gas analyser via TCP/IP protocol.

Amongst the pressure and temperature signals processed, the most important one, the in-cylinder pressure, was measured by two different pressure transducers throughout this study. During the early experiments with the original fuel injection system, as presented in chapters five and six, a Kistler 6061B piezoelectric transducer was used (shown in light blue in Figure 3.4). The linearity of this sensor was ±0.5%, with a sensitivity of 0.25 pC/kPa and a maximum working pressure of 30 MPa. On the second part of this research (chapter seven onwards), an AVL GH15D piezoelectric transducer was employed as shown in pink in Figure 3.5. This sensor had a linearity of ±0.3%, with a sensitivity of 0.19 pC/kPa and a maximum working pressure of 25 MPa. Such piezoelectric sensor contains a quartz crystal that, when stressed, produces an electrical charge proportional to the force applied onto them. This electrical charge, although, has very low amplitude (in the order of picocoulombs) and hence a charge amplifier needed to be used. This device amplified and converted the output signal to a voltage that the DAQ card could receive [134]. For both pressure transducers a Kistler 5011B10 charge amplifier with disabled low pass filter and a long time constant (high pass filter) of more than 1000 s was employed. The resulting error was found smaller than 1%.

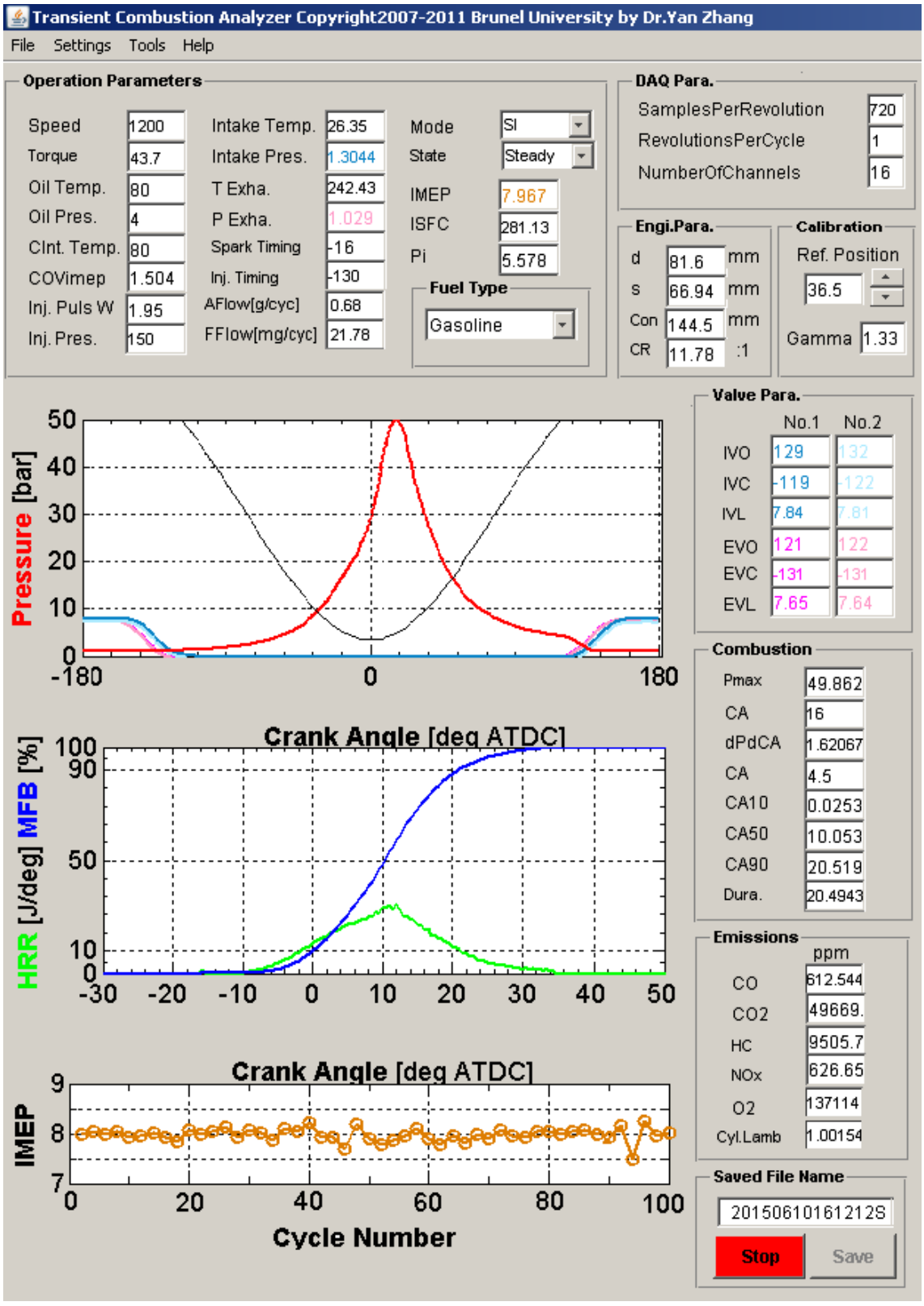

Figure 3.6 – Adapted view of the transient combustion analysis software.

Piezoelectric transducers only respond to pressure variations and hence their output must be correlated to an absolute pressure at some point of the engine cycle, which is known as “pegging”. In this case the in-cylinder pressure was

referenced at bottom dead centre (BDC) to the instantaneous intake pressure, measured by a Kistler 4007BA20F piezoresistive pressure transducer installed in the intake plenum. Another water cooled piezoresistive pressure transducer (Kistler 4007BA5F), with an error smaller than 0.1%, was also applied to the exhaust port so that the instantaneous exhaust gas pressure could be logged. Both transducers had their signals amplified by two Kistler 4618 amplifiers with output voltages in the range 0-10 V. Close to the pressure measurements points, K-type thermocouples were installed to acquire averaged gas temperatures with accuracy better than 1%. The temperature in several other points was also evaluated with the same class of thermocouples, as the engine oil gallery, coolant jacket, fuel rail, valve train hydraulic oil gallery and the emission analysers sampling points.

3.2.5 Dynamometer, intake air supply and hydraulic systems

The dynamometer used, a 48 kW alternated current four quadrant from C&P Engineering, enabled both motored and fired operations up to 6000 rpm by means of an ACS800 ABB drive. The dyno controller allowed constant speed or constant torque tests, although in this research only constant speed (±5 rpm) experiments were carried out. The software Cadet V12 provided the interface necessary for the dyno management. The brake torque was measured by an SSM S-type Interface load cell, with linearity better than 0.5% of full scale (330 Nm). The dyno controller, shown in yellow in Figure 3.2, was also in charge of controlling the coolant and oil temperatures through closed loop control over liquid-to-liquid heat exchangers and electric heaters. The engine oil pressure was kept at 0.4±0.05 MPa and its temperature at 353±3 K during all tests. The engine coolant, a 50% mixture of water and ethylene-glycol, was also held at 353±3 K during all experiments.

The scavenging process in the two-stroke cycle was driven by the pressure ratio across the intake-exhaust ports and hence boosted inlet air was required. In this case an AVL 515 sliding vanes compressor able to supply up to 5 m^3/s of air at 320 kPa was employed. A proportional-integral-derivative (PID) controller provided a closed loop control over the intake air pressure at ±3 kPa. Pressure steps of 10 kPa were allowed by the controller, besides the fine tuning provided

by the intake throttle valve. The air supplied by the supercharger unit had all possible oil removed by an oil separator unit. A liquid-to-air heat exchanger and an electric heater kept the closed loop control over the air temperature at 300±5 K at all experiments. The air mass flow rate was measured by a Hasting HFM-200 laminar flow meter with an error of ±1% in the range studied.

The valve train unit was fed by hydraulic oil at 10±0.2 MPa and 313 K (max) provided by a DGB Hydraulics unit with 225 dm^3 oil capacity, as seen on the right side of Figure 3.1 (in green). The main oil pump was able to provide up to 1150 cm^3/s of oil at a maximum pressure of 35 MPa, whilst a secondary pump was responsible for recirculating the oil through a liquid-to-liquid heat exchanger. Four Moog UK electrohydraulic valves were employed to open and close the hydraulic actuators installed on each of the intake/exhaust valves at the instants predetermined by the VCU. The valve position feedback was recorded by four Lord DVRT linear variable displacement transducers (LVDT) placed on the top of each valve. The signal from each LVDT was pre-processed by a Lord Multichannel conditioner before being sent to the VCU, with a resolution better than 6 μm and a maximum error of ±1% in the valves position. Due to the response time of all equipment comprising the camless valve train, the maximum engine speed tolerable was 3000 rpm in the two-stroke cycle.

3.3 Data analysis

Some of the signals acquired by the DAQ board were processed by the transient combustion analysis software and displayed on real-time on the host PC, i.e. IMEP, ISFC, COV_{IMEP}, indicated power, net heat release rate (HRR), mass fraction burnt (MFB), pressure rise rate (PRR), cycle-resolved air and fuel flow rates and the in-cylinder lambda. Other parameters as charging efficiency (CE), scavenge ratio (SE), supercharger power consumption, indicated specific emissions of CO, NOx, UHC and soot, combustion efficiency, indicated efficiency, corrected indicated efficiency, thermal efficiency, valve overlap, effective compression and effective expansion ratios were post-calculated. The equations and considerations used for these calculations are described as follows, with the acronyms and symbols defined in the section notation. The

international system of units was adopted throughout the equations unless otherwise stated.

3.3.1 Heat release analysis

With the in-cylinder pressure and crank position measurements, a heat release analysis was performed based on the first law of thermodynamics. In this case the combustion chamber contents (burnt and unburnt regions) were considered as a single zone, so the pressure changes were correlated to the energy released during the combustion. After the end of fuel injection and by the time that all the valves were shut, the chemical energy released by the combustion (Q_{ch}) could undergo four different ways as shown in Equation (3.1): part of the energy released resulted in expansion work over the piston (W); the sensible energy of the gas (U_s) changed as a result of the exothermic reaction; heat transfer (Q_{ht}) occurred and dissipated part of the combustion energy as the chamber walls were not adiabatic; or part of the in-cylinder charge and burnt gases flowed into and out of the chamber crevices ($h_i dm_i$).

$$dQ_{ch} = dW + dU_s + dQ_{ht} + \sum h_i dm_i \tag{3.1}$$

After determining the mean gas temperature from the ideal gas law and neglecting changes in the ideal gas constant, mathematical manipulation of Equation (3.1) resulted in the following formulation according to [8]:

$$dQ_{ch} = \left(\frac{c_v}{R}\right) V\, dP + \left(\frac{c_v}{R} + 1\right) p\, dV + dQ_{ht} + (h_{cr} - u + c_v T) dm_{cr} \tag{3.2}$$

Combining the energy released term with the heat transfer and crevices contributions, Equation (3.2) becomes easier to handle and its output results in the net heat release (Q_{net}). In this case only the work transferred to the piston and the sensible energy change in the gas are considered. Relating the combustion data to the crank angle position, as well as replacing the term $\left(\frac{c_v}{R}\right)$ by $\left(\frac{1}{\gamma - 1}\right)$, Equation (3.2) becomes:

$$\frac{dQ_{net}}{d\theta} = \frac{\gamma}{\gamma - 1} p \frac{dV}{d\theta} + \frac{1}{\gamma - 1} V \frac{dp}{d\theta} \quad (3.3)$$

The application of Equation (3.3) every 0.5° CA (set by the encoder resolution) besides the in-cylinder pressure reading resulted in the instantaneous heat release rate. The ratio of specific heats (γ) was kept constant at 1.33 throughout the whole engine cycle as suggested by [134], although it is well-known this value changes with the gas temperature and mixture composition.

With the integration of Equation (3.3) and its normalisation to 100%, the fraction of energy released as the combustion advanced on time could be obtained. The result, the mass fraction burnt (MFB) curve, was useful to estimate the initial flame development period (0-10% of the MFB) and the combustion duration (10-90% of the MFB). The initial part of the combustion event was excluded from the combustion duration calculation as a significant mass of fuel needed to burn prior to any measurable pressure variation could be detected. Likewise, the later burning stage (90-100% of the MFB) was more prone to heat transfer so the heat release rate became hard to quantify.

The instantaneous in-cylinder volume (V_{ins}) used to calculate the HRR was obtained by the crank position and engine geometric parameters (discussed in section 3.2.1), as presented in Equation (3.4).

$$V_{ins} = V_{clr} 0.5(R_c + 1) \left[\frac{2L}{S} + 1 - \cos\theta - \left(\left(\frac{2L}{S} \right)^2 - \sin^2\theta \right)^{\frac{1}{2}} \right] \quad (3.4)$$

The pressure rise rate (PRR) expressed in Pa/°CA was obtained by correlating the instantaneous in-cylinder pressure to the crank angle position. This parameter was an indicative of how abrupt the heat release process was taking place and its threshold was mainly dependent on the engine robustness and human noise perception. In gasoline engines this factor is often related to the appearance or not of knocking combustion, with limiting values ranging from 0.2 MPa/°CA to 0.8 MPa/°CA [137][138]. In this research the value of 0.5 MPa/°CA

was chosen to identify abrupt combustion, as suggested by [92][139] with similar engine configurations.

3.3.2 Overall engine parameters

The integration of the pressure signal over the cylinder volume during the compression and expansion resulted in the indicated work per cycle ($W_{c,i}$):

$$W_{c,i} = \oint p\, dV \tag{3.5}$$

When dividing the indicated work per cycle by the displaced volume (V_d), the indicated mean effective pressure (IMEP) was obtained as presented in Equation (3.6). This parameter was useful to compare the present engine to others of different sizes as it gave an insight about how effectively the swept volume was being used.

$$IMEP = \frac{W_{c,i}}{V_d} \tag{3.6}$$

An important evaluation of the engine's cyclic variability could be achieved by comparing the standard deviation of the IMEP to its averaged value obtained over at least 100 cycles. In this case the coefficient of variation (COV) of IMEP, seen in Equation (3.7), expressed the variation in the indicated work per cycle resulted from combustion instabilities. In this work a threshold of 10% for this variable was established as recommended by [8].

$$COV_{IMEP} = \frac{IMEP_{std}}{IMEP_{average}} * 100 \tag{3.7}$$

This limiting value of 10% seems high in case of four-stroke engines, where a value around 5% has been quoted for contemporary applications [9]. However, bearing in mind the doubled firing frequency of two-stroke engines, the torque variation is lower and the level of vibration and harshness can be attenuated.

The indicated power, defined as the rate of work transferred from the in-cylinder gas to the piston, was evaluated and is presented in Equation (3.8). As the engine used in this research was a single cylinder prototype, it was more convenient to express the power divided by the displacement volume so that direct comparisons to production engines could be done. In this case the indicated specific power had units of W/dm^3 as shown in Equation (3.9).

$$P_i = W_{c,i}N \tag{3.8}$$

$$P_{is} = \frac{W_{c,i}N}{V_d} \tag{3.9}$$

As four-stroke engines have one firing cycle every two revolutions, their IMEP values are twice as high as those found in two-stroke engines of the same displacement. Bearing this in mind, and to avoid misunderstandings in the loads achieved during the tests in the two-stroke cycle, the specific indicated torque (T_{is}) was also evaluated as shown in Equation (3.10).

$$T_{is} = \frac{W_{c,i}}{2\pi V_d} \tag{3.10}$$

To measure the engine's efficiency on converting the fuel energy into useful work, the indicated efficiency was calculated as seen in Equation (3.11). This expression correlates the amount of energy supplied to the engine, given by the fuel mass (or mass flow rate) times its lower heating value (LHV_{fuel}), to the actual observed work (or power in case of using the fuel flow rate).

$$\eta_i = \frac{W_{c,i}}{m_{fuel}LHV_{fuel}} = \frac{P_i}{\dot{m}_{fuel}LHV_{fuel}} \tag{3.11}$$

Differently from crankcase-scavenged two-stroke engines where the piston works as an air/mixture pump, the two-stroke poppet valve concept relies on an external compressor to enable the scavenging. Therefore, in real world conditions part of the engine's output power would be delivered to an external compressor responsible for supplying boosted air. The estimated supercharger

power consumption was based on the first and second laws of thermodynamics in a total-to-static compression process, as shown in Equation (3.12) from [8].

$$P_c = \dot{m}_{air} c_p T_a \left(\left(\frac{p_{int}}{p_a} \right)^{\frac{\gamma-1}{\gamma}} - 1 \right) \frac{1}{\eta_{comp}} \tag{3.12}$$

Based on a realistic value of compressor efficiency (η_{comp}) of 0.65 [140], the compressor power consumption was evaluated. A value of γ equal to 1.4 and c_p equal to 1.004 kJ/kg.K were considered. Consequently, by subtracting this power requirement from the indicated power seen in Equation (3.8), the corrected indicated efficiency ($\eta_{i\ corr}$) was obtained.

$$\eta_{i\ corr} = \frac{(P_i - P_c)}{\dot{m}_{fuel} LHV_{fuel}} \tag{3.13}$$

The instantaneous in-cylinder volume was also used to calculate the effective compression and expansion ratios. The effective expansion ratio (EER) was determined by the in-cylinder volume at exhaust valve opening (EVO) or intake valve opening (IVO), whichever earlier. Similarly, the effective compression ratio (ECR) was calculated at exhaust valve closing (EVC) or intake valve closing (IVC), whichever later, as presented below:

$$EER = \frac{V_{ins\ EVO} + V_{clr}}{V_{clr}} \ \ or \ \ \frac{V_{ins\ IVO} + V_{clr}}{V_{clr}} \tag{3.14}$$

$$ECR = \frac{V_{ins\ EVC} + V_{clr}}{V_{clr}} \ \ or \ \ \frac{V_{ins\ IVC} + V_{clr}}{V_{clr}} \tag{3.15}$$

3.3.3 Engine-out emission analysis

The conversion of emission results from parts per million (ppm), given by the emission analyser, to g/kWh was performed following the UN Regulation number 49 [141]. The gases measured on a dry basis (CO and NOx) were converted to a wet basis, whilst a humidity correction was applied to NOx emissions considering the dependence upon ambient conditions. Each exhaust gas concentration (in

ppm) was multiplied by its molar mass fraction (u_{gas}), which is fuel dependent as presented in Table 3.2. The exhaust mass flow rate ($\dot{q}_{exh}$) was found by the sum of instantaneous fuel and air mass flow rates.

$$ISCO = \frac{u_{CO}[CO]k_w\dot{q}_{exh}}{P_i} \tag{3.16}$$

$$ISNOx = \frac{u_{NOx}[NOx]k_w k_{hG}\dot{q}_{exh}}{P_i} \tag{3.17}$$

$$ISUHC = \frac{u_{HC}[UHC]k_{FID}\dot{q}_{exh}}{P_i} \tag{3.18}$$

Table 3.2 – Molar mass fractions of exhaust gases for gasoline and ethanol, adapted from [141].

Exhaust gas	$\boldsymbol{u_{gas}}$	
	Gasoline	Ethanol
CO	0.000966	0.000980
NOx	0.001587	0.001609
UHC	0.000499	0.000780

The dry-to-wet correction factor (k_w) applied to CO and NOx emissions was dependent on ambient conditions and mass flow rates of fuel and air as seen in Equation (3.19). Even under extreme ambient conditions this adjustment is usually in the range from 0.91 to 0.98. Besides, the hydrogen (W_{ALF}) and oxygen (W_{EPS}) contents in the fuel, in percent mass, were also taken into consideration in the fuel specific factor (k_f).

$$k_w = 1.008\left(1 - \frac{1.2442H_a + 111.19W_{ALF}\left(\frac{\dot{m}_{fuel}}{\dot{m}_{dry\ air}}\right)}{773.4 + 1.2442H_a + 1000\left(\frac{\dot{m}_{fuel}}{\dot{m}_{dry\ air}}\right)k_f}\right) \tag{3.19}$$

$$k_f = 0.055594W_{ALF} + 0.0070046W_{EPS} \tag{3.20}$$

A further correction was required in the case of NOx emissions regarding the ambient humidity (H_a), so the factor k_{hG} was introduced:

$$k_{hG} = 0.6272 + 0.04403H_a - 0.000862{H_a}^2 \tag{3.21}$$

H_a, given in grams of water per kilogram of dry air, was a function of relative humidity (RH), water saturation pressure (SP) and ambient pressure (p_a) as presented in Equation (3.22).

$$H_a = \frac{6.211 * RH * SP}{p_a - \frac{(RH * SP)}{100}} \tag{3.22}$$

To avoid using a lookup-table operation over the air-water psychrometric chart, the water saturation pressure was estimated from the ambient temperature (T_a) using a fifth order polynomial regression as suggested by [142].

$$\begin{aligned} SP = {} & 604.8346 + 45.9058(T_a - 273.15) + 1.2444(T_a - 273.15)^2 \\ & + 0.03522481(T_a - 273.15)^3 \\ & + 0.00009322061(T_a - 273.15)^4 \\ & + 0.000004181281(T_a - 273.15)^5 \end{aligned} \tag{3.23}$$

In the case of UHC emission there was an extra correction factor (k_{FID}) accounting for the analyser's FID response to oxygenated fuels. Flame ionisation detectors, as explained in section 3.2.2, work by detecting carbon atoms in the form of electrical current. However, when oxygenated compounds are introduced into the exhaust the ionisation current from the carbon atoms is inhibited and the organic gas emission is underestimated. Results from gas chromatography measurements showed that around one half of the organic exhaust emission of pure ethanol fuelled engines corresponds to oxygenated composites. From this, nearly 40% is unburnt ethanol and 10% are acetaldehydes [130]. In this case a FID correction factor for oxygenated fuels was used based on the work of [130] and [143] presented in Equation (3.24).

$$k_{FID} = \frac{1}{1 - (1 - 0.74)(0.608e^2 + 0.092e)} \tag{3.24}$$

The variable "e" stands for the volume fraction of ethanol in the fuel. Hence, in the case of E100 operation the increase in UHC emission is 22% of the reading.

The indicated specific soot emission (ISsoot) was calculated from the raw values of soot (mg/m^3), the fuel mass flow rate ($\dot{m}_{fuel}$), the air mass flow rate ($\dot{m}_{air}$) and the indicated power (P_i), as presented in Equation (3.25).

$$ISsoot = \left(\frac{soot}{1000}\right)\left(\frac{\dot{m}_{fuel} + \dot{m}_{air}}{\rho_{ext} * P_i}\right) \tag{3.25}$$

The exhaust gas density (ρ_{ext}) was calculated according to [141] by means of the fuel specific factor (k_f) and ambient humidity (H_a), as already presented in Equations (3.20) and (3.22), respectively.

$$\rho_{ext} = \frac{1000 + H_a + 1000\left(\frac{\dot{m}_{fuel}}{\dot{m}_{dry\ air}}\right)}{773.4 + 1.2434H_a + 1000k_f\left(\frac{\dot{m}_{fuel}}{\dot{m}_{dry\ air}}\right)} \tag{3.26}$$

After the conversion of all gaseous and soot emissions to mass flow rates, the combustion efficiency was evaluated by comparing the fuel energy supplied to the engine to that actually released during the combustion. To do so, the combustible species found in the exhaust (CO, UHC, H_2 and soot) and resulted from incomplete combustion were multiplied by their heating values [8]. The LHV values used for CO, H_2 and soot were 10.1 MJ/kg, 120 MJ/kg and 32.8 MJ/kg (solid carbon), respectively. The LHV of UHC was assumed the same as the fuel used in the respective test (42.5 MJ/kg for gasoline and 26.9 MJ/kg for ethanol).

$$\eta_c = 1 - \frac{\dot{m}_{CO}LHV_{CO} + \dot{m}_{UHC}LHV_{UHC} + \dot{m}_{H_2}LHV_{H_2} + \dot{m}_{soot}LHV_C}{\dot{m}_{fuel}LHV_{fuel}} \tag{3.27}$$

When defining combustion efficiency it was clear that not all the energy contained in the fuel could be released during the combustion. In this case it was useful to separate the effects of combustion completeness from the indicated

efficiency presented in Equation (3.11). Thus, the thermal efficiency defined the actual heat engine efficiency as seen in Equation (3.28). According to this definition any loss resulted from mixture preparation or supercharger ineffectiveness could not interfere in the engine's potential of delivering work.

$$\eta_t = \frac{\eta_i}{\eta_c} \tag{3.28}$$

Also based on the exhaust emissions provided by the gaseous analyser, the relative air/fuel ratio (lambda) was calculated according to the algorithm developed by Brettschneider-Spindt and described in [144]. This method simultaneously solves a set of five equations to provide the coefficients for the combustion equation of a general hydrocarbon fuel (oxygenated or not) with air, shown in Equation (3.12).

$$C_xH_yO_z + n(O_2 + A * N_2 + B * CO_2 + C * H_a * H_2O) \rightarrow \tag{3.29}$$
$$aCO_2 + bCO + cH_2 + dH_2O + eO_2 + fN_2 + gNO_X + hC_xH_yO_z$$

From the carbon, hydrogen, oxygen, nitrogen and total moles (n_{TOT}) balances in Equation (3.29), the following equations could be obtained bearing in mind the concentrations of CO, CO_2, NO_x, O_2 and UHC are known:

$$a = [CO_2] * n_{TOT} \tag{3.30}$$

$$b = [CO] * n_{TOT} \tag{3.31}$$

$$c = \frac{y(1-h)}{2} + n * C * H_a - d \tag{3.32}$$

$$d = \frac{y(1-h) + 2n * C * H_a}{2\left(\frac{b}{a * K} + 1\right)} \tag{3.33}$$

$$e = [O_2] * n_{TOT} \tag{3.34}$$

$$f = n * A - \frac{g}{2} \tag{3.35}$$

$$g = [NO_X] \ * n_{TOT} \tag{3.36}$$

$$h = \frac{[UHC] * (n_{TOT} + d)}{x} \tag{3.37}$$

$$n = \frac{2a + b + c + d + 2e + g + z(h-1)}{2 + 2B + C * H_a} \tag{3.38}$$

$$n_{TOT} = \frac{x + (B * n)}{[CO] + [CO_2] + [UHC]} \tag{3.39}$$

The coefficients A, B and C represented the nitrogen, carbon dioxide and water vapour to oxygen ratio in atmospheric air, considered 3.774, 0.0014 and 0.0016, respectively. A value of 3.5 was used for the water-gas equilibrium constant (K) as suggested by [8]. The simultaneous solution of equations (3.30) to (3.39) resulted in the number of air moles (n). The lambda value was then acquired by dividing n by the number of moles required for stoichiometric air/fuel ratio combustion, as seen in Equation (3.40).

$$\lambda_{exh} = \frac{n}{\left(x + \frac{y}{4} - \frac{z}{2}\right)} \tag{3.40}$$

3.3.4 Gas exchange calculations

The air trapping efficiency in two-stroke engines is defined as the ratio of in-cylinder trapped air mass ($m_{trap\ air}$) at IVC or EVC (whichever later) to the intake air mass (m_{air}) supplied per cycle. Several experimental methods have been proposed to measure it under engine firing conditions, such as the exhaust gas sampling valve [48], the tracer gas method [145] and the analysis of exhaust oxygen content under fuel-rich operation [28]. The last technique is not applicable to stratified combustion, as in diesel engines, when the exhaust oxygen concentration results from both scavenged air and overall lean-burn combustion. In case of homogeneously charged two-stroke SI engines running

with richer than stoichiometric in-cylinder mixtures, this method yields acceptable results. It is based on the presumption that any remaining oxygen in the exhaust derives from scavenging inefficiencies, such as mixing-scavenging and air short-circuiting. Because of its simplicity, this method was chosen to be used in this research with the knowledge that inaccuracies may have taken place due to some charge stratification resulted from direct injection. Based on the work of [146] the air trapping efficiency was more accurately calculated by considering all exhaust gases instead of oxygen only.

$$TE_{air} = \frac{m_{trap\,air}}{m_{air}}$$

$$= \frac{0.5[CO] + [CO_2] + 0.25\left(\frac{yK[CO_2]}{[CO] + K[CO_2]}([CO] + [CO_2])\right) + 0.5[NOx]}{0.5[CO] + [CO_2] + [O_2] + 0.25\left(\frac{yK[CO_2]}{[CO] + K[CO_2]}([CO] + [CO_2])\right) + 0.5[NOx]} \quad (3.41)$$

The presence of oxygenated fuels in the UK commercial gasoline, detailed in Table 3.1, represented a variation of about 1.5% in the calculation of the air trapping efficiency. Thus, the exhaust oxygen concentration was corrected based on the total number of moles of combustion products seen in Equation (3.39).

The scavenge ratio is defined as the ratio between the intake air mass supplied to the in-cylinder reference mass under intake conditions. The reference volume used (to calculate the reference mass) was the sum of the clearance volume (V_{clr}) and the instantaneous in-cylinder volume at EVC or IVC, whichever later.

$$SR = \frac{m_{air}}{(V_{ins} + V_{clr})\rho_{int}} \quad (3.42)$$

To quantify the effectiveness of the charging process, or in other words how efficiently the cylinder was filled with air, the charging efficiency was employed. This parameter expressed the ratio between the in-cylinder trapped air mass at IVC or EVC (whichever later) and the in-cylinder reference mass at intake conditions (intake air density, ρ_{int}). By definition, it resulted from the product between scavenge ratio and trapping efficiency as seen in Equation (3.43).

$$CE = \frac{m_{trap\ air}}{(V_{ins}+V_{clr})\rho_{int}} = SR * TE_{air} \quad (3.43)$$

Under idealised flow conditions the in-cylinder charge and burnt gases assume identical densities [28], so the internal EGR fraction can be deduced from the difference between the charging efficiency and the unit.

Due to scavenging inefficiencies, such as mixing between intake air and burnt gases and air short-circuiting to the exhaust, the measured exhaust lambda differed from the in-cylinder lambda. The in-cylinder lambda (λ_{cyl}) was then estimated by subtracting the excess of air from the exhaust stream, here denoted by the air trapping efficiency as suggested by [146].

$$\lambda_{cyl} = \lambda_{exh} \left(\frac{TE_{air}}{TE_{fuel}}\right) \quad (3.44)$$

Where (TE_{fuel}) is the fuel trapping efficiency calculated based on the exhaust emissions of CO, CO_2 and UHC, as presented in Equation (3.45) from [146].

$$TE_{fuel} = \frac{[CO] + [CO_2]}{[CO] + [CO_2] + [UHC]} \quad (3.45)$$

The inclusion of the TE_{fuel} in the calculation of the in-cylinder lambda aimed at considering any short-circuited fuel, whether not measured it would under-predict the real in-cylinder lambda. In mixture-scavenged two-stroke engines it is expected that some fuel exits the exhaust port during the scavenging process and hence the fuel trapping efficiency deteriorates. The adoption of direct fuel injection was able to remove the fuel short-circuiting issue from the two-stroke poppet valve engine as the SOI took place after EVC and IVC. However, due to the short time available for air-fuel mixing, some fuel remained unburnt in the cylinder at EVO and hence the denominator in Equation (3.45) increased due to UHC emission. Besides, it was sometimes interesting to advance the SOI before EVC to improve the charge homogeneity especially at high engine speeds, so the fuel trapping efficiency decreased.

From all equations presented in this section of data analysis, it is clear that accurate gaseous emission measurements are critical. Besides the evaluation of the engine-out emission itself, reliable values of gas composition in the exhaust pipe were necessary when calculating combustion and gas exchange parameters. Therefore, the accuracy of emission measurements was assessed by calculating the total dry emissions as reported by [146][147]. This technique consisted of summing all measured exhaust gases, as well as those gases which were not measured but calculated using Equations (3.30) to (3.39).

$$Total\ emissions_{dry} = [CO_2] + [CO] + [H_2] + [O_2] + [N_2] + [NOx] + [UHC] \quad (3.46)$$

Figure 3.7 presents all testing points acquired in this research, where each one characterises the average of at least 100 engine cycles. The expected result from Equation (3.46) was the unit, although satisfactory measurements lie between two standard deviations (std) [147]. Values below this threshold could be due to any water vapour remained after the analyser cooling unit, which led to lower values of [CO] and [CO_2]. Values above the unit would be linked to the UHC multiplier in NDIR analysers [146], although in this research a FID was employed for UHC and hence this was not the case. So in this circumstance the few values above 2std were attributed to poor equipment calibration.

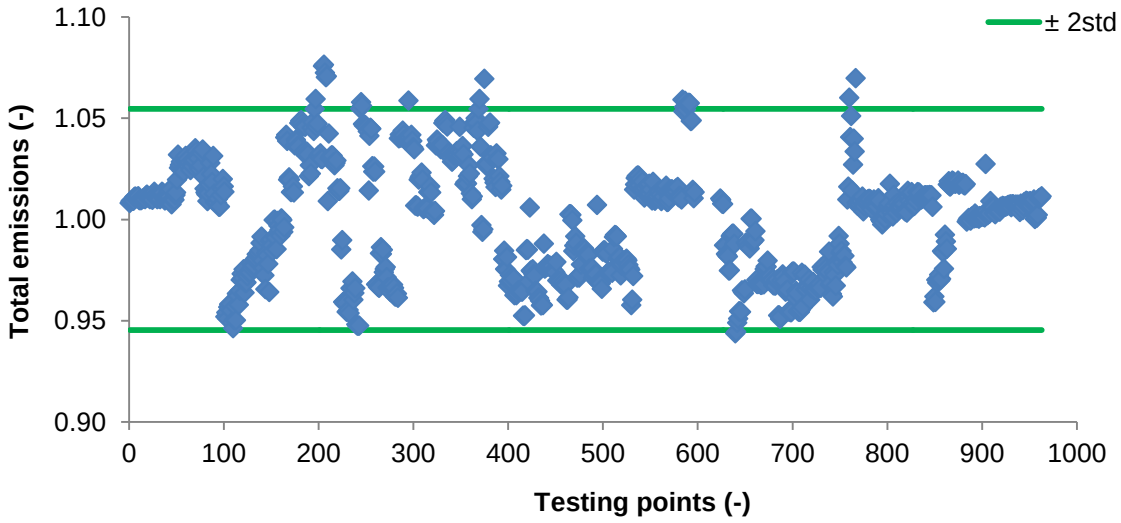

Figure 3.7 – Accuracy of emission measurements throughout all testing points collected in this research.

3.4 Summary

The research engine and test cell facilities employed were assessed alongside the equations and assumptions used in the data acquisition and analysis processes. The main sensors and actuators used were detailed and brief comments about their working principles were given, particularly concerning gaseous and soot emissions, fuel flow and pressure measurements. The commissioning of the new fuel injection system with a multi-hole GDI injector was presented, as well as the consequent alterations in the cylinder head. In the data analysis section the mathematical methods used to calculate combustion heat release, engine performance, gaseous/soot emissions and gas exchange properties were presented and the corresponding equations detailed.

Chapter Four
Numerical methodology

4.2 Introduction

Computational fluid dynamics (CFD) has become a widely used technique for analysis of fluid systems in the last decades. The advances in computing resources and the establishment of user-friendly software with graphical interfaces have aided to spread the adoption of this tool. The application of CFD to internal combustion engines for analysis of fluid flow, heat transfer and chemical reactions emerged as a reliable and low cost alternative to physical engine experiments. Another advantage of the numerical evaluation is the provision of all relevant variables throughout the calculation domain, whilst in experiments many locations are inaccessible and/or the measurement techniques would impact on the expected results [148]. Nevertheless, experimental procedures are still required in fields where numerical simulation is not yet developed or in circumstances when numerical models need to be validated. In this research a transient 3-D CFD analysis of the gas exchange process and air-fuel mixture formation was performed in the two-stroke poppet valve engine. The numerical methods used in the cold flow analysis (absence of fuel injection and combustion) are explained first, followed by the mesh size and time-step independency studies and model validation. In section 4.5 the fuel spray analysis is introduced and its comparison with experiments is evaluated.

4.3 Mathematical model

The CFD simulations were performed in the software AVL Fire, where the conservation equations of mass, momentum and energy for compressible and incompressible flows were solved by means of the finite volume method. Although the turbulent fluid motion can be described by the Navier-Stokes partial differential equations, the calculation of the mean flow and all turbulent velocity fluctuations in ICE flows is still computationally prohibitive. Instead, as in engineering problems usually the time-averaged fluid flow properties are of interest, the Navier-Stokes equations were statistically averaged using the Reynolds decomposition [149]. This mathematical procedure consists of

substituting the instantaneous flow velocities (u, v, w) by a steady mean velocity component $(\mathrm{U}, \mathrm{V}, \mathrm{W})$ plus a time-dependent statistical fluctuation component (u', v', w'). Equations (4.1) to (4.4) present the Reynolds averaged Navier-Stokes (RANS) equations for the conservation of mass (continuity equation), x-momentum, y-momentum and z-momentum, respectively.

$$\frac{\partial \rho}{\partial t} + \nabla \cdot (\rho \mathbf{U}) = 0 \tag{4.1}$$

$$\frac{\partial (\rho \mathrm{U})}{\partial t} + \nabla \cdot (\rho \mathrm{U} \mathbf{U}) = \nabla \cdot (\mu \nabla \mathrm{U}) - \frac{\partial p}{\partial x} + \left[-\frac{\partial (\rho \overline{u'u'})}{\partial x} - \frac{\partial (\rho \overline{u'v'})}{\partial y} - \frac{\partial (\rho \overline{u'w'})}{\partial z} \right] + S_x \tag{4.2}$$

$$\frac{\partial (\rho \mathrm{V})}{\partial t} + \nabla \cdot (\rho \mathrm{V} \mathbf{U}) = \nabla \cdot (\mu \nabla \mathrm{V}) - \frac{\partial p}{\partial y} + \left[-\frac{\partial (\rho \overline{u'v'})}{\partial x} - \frac{\partial (\rho \overline{v'v'})}{\partial y} - \frac{\partial (\rho \overline{v'w'})}{\partial z} \right] + S_y \tag{4.3}$$

$$\frac{\partial (\rho \mathrm{W})}{\partial t} + \nabla \cdot (\rho \mathrm{W} \mathbf{U}) = \nabla \cdot (\mu \nabla \mathrm{W}) - \frac{\partial p}{\partial z} + \left[-\frac{\partial (\rho \overline{u'w'})}{\partial x} - \frac{\partial (\rho \overline{v'w'})}{\partial y} - \frac{\partial (\rho \overline{w'w'})}{\partial z} \right] + S_z \tag{4.4}$$

The same decomposition could be applied to the energy equation, but in this case a more general transport equation was preferably used. The scalar Φ in Equation (4.5) was not assumed to be the temperature only. Instead, any other transported specie subject to the diffusion coefficient (Γ) could be calculated in the same way. This was particularly important when estimating the flow parameters in the two-stroke cycle as a passive scalar was attributed to the intake flow. Hence, the residual gas could be distinguished from the fresh air charge in the absence of combustion.

$$\frac{\partial (\rho \Phi)}{\partial t} + \nabla \cdot (\rho \Phi \mathbf{U}) = \nabla \cdot (\Gamma \nabla \Phi) + \left[-\frac{\partial (\rho \overline{u'\varphi'})}{\partial x} - \frac{\partial (\rho \overline{v'\varphi'})}{\partial y} - \frac{\partial (\rho \overline{w'\varphi'})}{\partial z} \right] + S_\Phi \tag{4.5}$$

The variables with an overbar in the above equations indicate an ensemble averaged value. The last term S represents a source of momentum (in the case of Equations (4.2), (4.3) and (4.4)) or a source of any scalar being considered (Equation (4.5)). The terms marked with an apostrophe are the fluctuation components of the Reynolds decomposition and μ is the dynamic viscosity of the fluid. The term $\mathbf{U}$, which appears in all conservation equations, is the mean component of the velocity vector.

By averaging the Navier-Stokes equations several unknown variables ($-\rho\overline{u'u'}, -\rho\overline{u'v'}, -\rho\overline{u'w'}, -\rho\overline{v'v'}, -\rho\overline{v'w'}, -\rho\overline{w'w'}$) appeared as a result of the interaction between the turbulent fluctuations. These terms, the Reynolds stresses, were not computed but modelled by means of turbulence models so the well-known "turbulence closure problem" could be addressed. Numerous turbulence models have been proposed in this matter and the majority of them follow the Boussinesq hypothesis presented in Equation (4.6). This approach correlates the Reynolds stresses to the mean rates of fluid deformation.

$$-\rho\overline{u'_i u'_j} = \mu_t\left(\frac{\partial \mathrm{U}_i}{\partial x_j} + \frac{\partial \mathrm{U}_j}{\partial x_i}\right) - \frac{2}{3}\rho k \delta_{ij} \tag{4.6}$$

$$k = \frac{1}{2}(\overline{u'u'} + \overline{v'v'} + \overline{w'w'}) \tag{4.7}$$

The variable μ_t represents the turbulent/eddy-viscosity, whilst k is the turbulent kinetic energy defined by Equation (4.7). To avoid the repetition of all Reynolds stresses in Equation (4.6) the suffix notation was employed. In this case when the values 1, 2, 3 were attributed to i or j, the coordinates x, y, z were called, respectively. By the end of the equation the Kronecker delta equals to one if $i = j$, otherwise it assumes zero.

A widely used and validated turbulence model based on the Boussinesq approach is the two-equation k-ε model. This simple eddy viscosity model (EVM) performs well for solving general engineering problems, but fails when resolving complex geometries with rotating flow structures, flow detachment and stagnations points [150]. This is particularly the case found in ICEs and hence

more accurate models were sought. The four-equation k-ζ-f turbulence model proposed by [151] is considerably robust and more precise than others simpler two-equation EVM's. Its computational cost is about 15% higher than the conventional k-ε model [152] due to the solution of four equations instead of two. The results yielded by this refined turbulence model are still inferior to those achieved by second-order/moment closure models as the seven equation Reynolds Stress Model (RSM). Nevertheless, the computation speed is severely degraded by using the RSM and hence the k-ζ-f model was the logical option for this research. The eddy-viscosity was then obtained by means of Equation (4.8).

$$\mu_t = \rho C_\mu \zeta \frac{k^2}{\varepsilon} \tag{4.8}$$

Following this, the transport equations for turbulent kinetic energy (k), dissipation of turbulent kinetic energy into heat by the action of viscosity (ε), velocity scale ratio (ζ) and the elliptic function (f) are presented as follows:

$$\rho \frac{Dk}{Dt} = \rho(\Pi - \varepsilon) + \frac{\partial}{\partial x_j}\left[\left(\mu + \frac{\mu_t}{\sigma_k}\right)\frac{\partial k}{\partial x_j}\right] \tag{4.9}$$

$$\rho \frac{D\varepsilon}{Dt} = \rho \frac{C_{\varepsilon 1}\Pi - C_{\varepsilon 2}\varepsilon}{\tau} + \frac{\partial}{\partial x_j}\left[\left(\mu + \frac{\mu_t}{\sigma_\varepsilon}\right)\frac{\partial \varepsilon}{\partial x_j}\right] \tag{4.10}$$

$$\rho \frac{D\zeta}{Dt} = \rho f - \rho \frac{\zeta}{k}\Pi + \frac{\partial}{\partial x_k}\left[\left(\mu + \frac{\mu_t}{\sigma_\zeta}\right)\frac{\partial \zeta}{\partial x_k}\right] \tag{4.11}$$

$$\Omega^2 \nabla^2 f - f = \frac{1}{\tau}\left(C_1 + C_2 \frac{\Pi}{\varepsilon}\right)\left(\zeta - \frac{2}{3}\right) \tag{4.12}$$

Where Ω and τ are the Kolmogorov length and time scales, respectively, which define the lower bounds of turbulence. The variable Π is the production of k by the mean flow deformation whilst the constants $C_{\varepsilon 1}, C_{\varepsilon 2}, C_1, C_2$ assumed values of 1.4(1+0.012/ζ), 1.9, 0.4 and 0.65, respectively. Finally, the Prandtl numbers ($\sigma_k, \sigma_\varepsilon, \sigma_\zeta$) were considered equal to 1.0, 1.3 and 1.2, respectively.

In the solution of the numerical problem using the finite volume method, the governing equations were integrated over defined non-overlapping control volumes. The result of filling the whole geometry of interest with these control volumes, or cells, was the numerical grid (mesh). The k-ζ-f turbulence model was originally developed under the low Reynolds approach, which required a greater mesh refinement near the walls of the geometry to capture the boundary layer effects. In this case, the cell growth ratio from the walls towards the core of the flow could not be abrupt so a maximum ratio of 1.3 had to be used. In regions of large volumes, as the engine cylinder, this method resulted in a great number of elements in the grid and turned out to be computationally prohibitive. To overcome this drawback a hybrid wall treatment was adopted based on the dimensionless wall distance (y+) condition: in case of small values of y+ the conservation equations were integrated down to the wall or; wall functions were applied when the values of y+ were found higher than 11.63. The accuracy of the near wall solution was slightly reduced by the use of this method, although the computational effort was greatly improved. These semi-empirical wall functions avoided the fluid zone adjacent to the walls and bridged the solution at the first cell centroid to the wall properties (no-slip condition). The flow mean velocity was then given by Equation (4.13), where κ (kappa) is the von Karman constant (equal to 0.41) and E is the additive constant of the law of the wall (equal to 9.0). Besides the flow velocity, similar consideration was given to the temperature in the thermal boundary layer [152].

$$\mathrm{U}^{+} = \frac{1}{\kappa}\ln(Ey^{+}) \qquad y^{+} > 11.63 \tag{4.13}$$

During the numerical solution all flow variables were stored in the geometrical centre of the volumes, which assumed hexahedral, pyramidal, tetrahedral or wedged shapes. To calculate the convective and diffusive terms at the cell faces it was necessary to interpolate the properties between the centre volumes. Spatial discretisation schemes are used in this case, which may be first order, blended first-higher order and pure higher order schemes, with accuracy increasing in this sequence. In this research only second order accurate differencing schemes were used, such as the central differencing and the MINMOD methods. The former one was used for the continuity equation, whilst

the latter was applied to momentum, energy and turbulence equations. The MINMOD differencing scheme combined features from both linear upwind and central differencing schemes, operating as a limiter. More details about these schemes and the equations used can be found in [152]. In order to advance the solution in time (time-steps), also referred as time-marching, an unconditionally stable two level Euler implicit scheme was selected.

In compressible flows each variable (u, v, w, ρ, T, p) is advanced in time by one equation. The three components of the velocity field are updated by the three momentum equations, the density is updated by the continuity equation, the temperature is updated by the energy equation and the pressure is advanced in time using equations of state (in this case the perfect gas law). However, if the fluid density does not change, as in incompressible or nearly incompressible flows, the continuity equation cannot be used to update the density. The density is then calculated by the equation of state, but the pressure cannot be updated since there is no remaining equation to do so. In this case the pressure could be determined by an algorithm as the Semi-Implicit Method for Pressure-Linked Equations (SIMPLE) [153]. This algorithm basically guessed-and-checked the pressure field so that the corrected pressure could be used in the momentum equations to calculate the velocity components.

4.4 Cold flow simulation

The engine geometry was discretised in a hexahedra-dominated unstructured moving mesh generated through the octree approach in the software AVL Fame Engine Plus. Due to the complexity of the cylinder head geometry, mainly attributed to the masked region around the intake valves, the unstructured method produced improved quality cells over the structured approach. To reduce the mesh dependency during the simulations, and at the same time minimising the computational effort, a mesh size sensitivity study was carried out. This procedure aimed at finding the approximate number of volumes necessary in the computational domain to describe the proposed flow with sufficient accuracy, but maintaining the computational cost at its minimum. A similar sensitivity study was carried out for the time-step (time-marching) size considering its large effect on the simulation duration.

4.4.1 Mesh independency study

Five different meshes ranging from 1.1 to 2.1 million elements (volumes) were studied under the same cold flow boundary and initial conditions as presented in Table 4.1. Some of these conditions were acquired from previous experiments [133] operating on CAI combustion. Other boundary conditions, as the intake pressure and engine speed, were set to higher values so that the “worst case scenario” could be achieved during the mesh and time-step independency studies. The high values of engine speed and intake pressure aimed at creating a greater velocity gradient in the engine geometry, particularly close to the valve curtain region. In this case, if the mesh resolution could capture all the flow phenomena at such extreme conditions, then any other case at lower engine speed/intake pressure would be equally well described by the numerical model. Unlike naturally aspirated four-stroke engines where the mesh independency study usually focus at the maximum piston speed [154], in the two-stroke cycle the piston movement has little impact on the gas exchange process. The in-cylinder velocity field in this case was predominantly determined by the intake pressure, which was the main drive of the scavenging process.

Table 4.1 – Boundary and initial conditions used in the mesh independency study.

Effective compression ratio	11:1
Engine speed (rpm)	6000
EVC (°CA ATDC)	196
EVO (°CA ATDC)	153
Exhaust pressure (kPa)	103.2
Exhaust temperature (K)	503
Initial in-cylinder pressure (kPa)	103.2
Initial in-cylinder temperature (K)	503
Initial velocity components (m/s)	1.0
Intake pressure (kPa)	200
Intake temperature (K)	289
IVC (°CA ATDC)	216
IVO (°CA ATDC)	164
Simulation duration (°CA)	180 to 720
Valve lift (mm)	2.9

At both intake and exhaust surfaces the boundary conditions were set to averaged total pressures with constant values throughout the simulations. The wall temperatures on the intake side (intake ports, back of intake valves and

runners) were set to 320 K, whilst on the exhaust side they were set to 400 K. The piston, cylinder head and liner wall temperatures were set to 450 K, 420 K and 400 K, respectively, based on the fire deck temperature correlation of [155]. The intake and exhaust valve lift profiles were set according to those measured by the LVDTs installed on the top of the valves. The in-cylinder initial conditions were estimated from the in-cylinder pressure recorded during the experiments considering air as an ideal gas. The cycle simulation started at 180° CA (BDC) and finished at 720° CA, so that a complete cycle could be simulated after a half first part. The time-step size was set to 0.2° CA throughout the engine cycle, though reduced to 0.1° CA at IVO and EVO during approximately 4° CA. This reduction avoided numerical instabilities due to the high velocity flow in the valve curtain region.

The turbulence models, as described in section 4.2, required values of turbulent kinetic energy (k) and turbulent length scale (l) at intake and exhaust boundaries. Equations (4.14) and (4.15) from [149] were then used to estimate these variables based on the intake mean flow velocity (U_{int}), turbulence intensity (I_{turb}) and intake runner diameter (D_{int}).

$$k = \frac{2}{3}(\mathrm{U}_{int}\mathrm{I}_{turb})^2 \tag{4.14}$$

$$l = 0.07 D_{int} \tag{4.15}$$

The mean flow velocity was simply assumed to be the air flow rate divided by the runner cross-section area, whilst the turbulence intensity was considered 5% as suggested by [154].

In the meshing software AVL Fame Engine Plus the grid element size could not be directly determined by the user, but only the maximum cell size. In this case refinement levels were applied to specific regions with large velocity gradients (i.e. valve curtain), so the flow phenomena could be better captured and the numerical convergence improved. These refinement levels (i.e. 0, 1, 2, 3…) acted in the octree approach by dividing a single cell into four cells, so the mesh density increased in the regions with refinement levels greater than zero. During

the mesh independency study the same refinement levels were applied to key points as valve seats, valve guides, spark plug location, injector location and valve pockets. The only parameter changed in this case was the maximum element size (given by the cell's longest edge), which was varied from 1.05 mm to 1.50 mm as presented in Table 4.2.

Table 4.2 – Details of the meshes used in the size sensitivity study.

Mesh parameters at BDC										
Mesh	Max. cell size	Average cell size	Cells distribution			Types of cells				Total cells
			Cylinder	Exhaust	Intake	Tetra	Hexa	Pyramid	Prism	
1	1.50 mm	0.81 mm	778323	149869	147373	11412	845413	80235	138505	1.1E+06
			72%	14%	14%	1%	79%	7%	13%	
2	1.35 mm	0.76 mm	921144	186068	184716	13484	1021565	94383	162496	1.3E+06
			71%	14%	14%	1%	79%	7%	13%	
3	1.25 mm	0.73 mm	1059010	218241	216150	14570	1190536	105489	182806	1.5E+06
			71%	15%	14%	1%	80%	7%	12%	
4	1.17 mm	0.70 mm	1185623	248944	266636	15662	1347661	115960	202120	1.7E+06
			71%	15%	16%	1%	80%	7%	12%	
5	1.05 mm	0.66 mm	1393449	328143	330714	17342	1662307	134434	238223	2.1E+06
			68%	16%	16%	1%	81%	7%	12%	

From the table above it is possible to see the element type distribution through the meshes studied, as well as the maximum and average cell sizes. The most common element type was the hexahedron and its occurrence increases as the number of volumes rose due to a better accommodation of squared cells. The hexahedron is the preferable element type in 3-D CFD simulation as the occurrence of numerical diffusion is significantly reduced [156]. The elements distribution across the engine geometry at BDC is also presented, with about 70% of the elements settled in the cylinder (displacement and clearance volumes) and the remained 30% equally divided between intake and exhaust ports. To minimise the computational effort, the intake and exhaust ports were detached from the engine geometry whilst the valves were closed. The intake and exhaust ports were then reconnected at IVO and EVO, respectively.

Four parameters were evaluated in the mesh independency study i.e. air mass flow rate, in-cylinder pressure, reverse tumble ratio and turbulent kinetic energy (TKE). The reverse tumble (charge motion around the z-axis in Figure 4.1) was chosen for its significance during both the scavenging and mixture preparation

processes in the two-stroke poppet valve engine. The magnitudes of swirl (charge motion around the y-axis) and cross tumble (charge motion around the x-axis) were found very small and therefore were not considered. The in-cylinder reverse tumble flow was generated by the cylinder head mask around the intake valves and the upright-straight intake port seen in Figure 4.1.

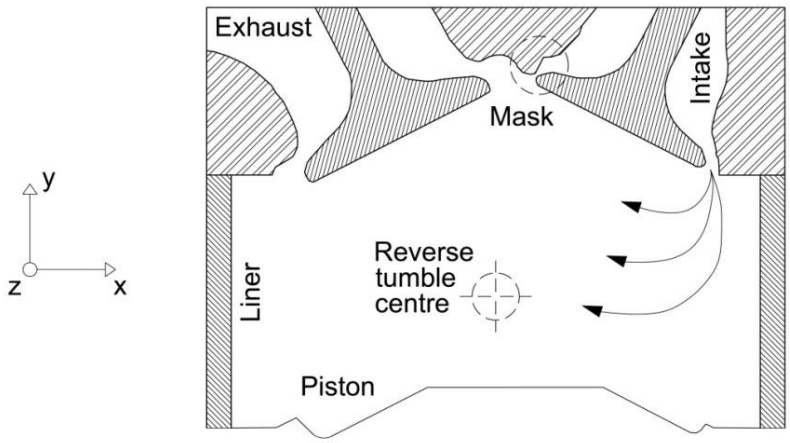

Figure 4.1 – Masked cylinder head and port arrangement.

The reverse tumble flow was computed based on the relative angular speed of the in-cylinder charge motion around a moving axis located halfway between the piston and the cylinder head. The resulted angular speed in each cell was then summed and divided by the engine speed, so the dimensionless reverse tumble ratio (R_T) could be obtained as presented in Equation (4.16) from [152]. The subscript "$cell$" indicates the contribution of each cell to the in-cylinder grid, whilst the subscript "cm" refers to the instantaneous bulk centre of mass. Only the flow velocities in the x and y-coordinates were of interest, being represented by U and W, respectively. The coordinates of each cell and the instantaneous centre of rotation of the bulk volume are given by x, y, z.

$$R_T = \frac{\sum \rho_{cell} V_{cell} [(z_{cell} - z_{cm}) U_i - (x_{cell} - x_{cm}) W_i]}{\sum \rho_{cell} V_{cell} [(x_{cell} - x_{cm})^2 + (z_{cell} - z_{cm})^2]} * \frac{1}{2\pi N} \tag{4.16}$$

The comparison between each simulated mesh to the finest mesh regarding the four parameters aforementioned is presented in Figure 4.2. As the mesh density increased, the variables analysed converged to a constant value where the simulation was said mesh independent. If only the air mass flow rate, in-cylinder pressure and reverse tumble ratio were considered of interest, even the coarsest

mesh tested with 1.1 million volumes would have fit the cold flow analysis. The mesh resolution in this case would be enough to capture all the flow phenomena and the case would be said mesh independent. However, considering the TKE as the major factor on the propagation and vaporisation of fuel spray droplets [152], its evaluation was necessary to ensure a reliable representation of the air-fuel mixing process. In this case, around 1.7 mi elements were needed to keep the TKE mean difference to the finest mesh around 8%.

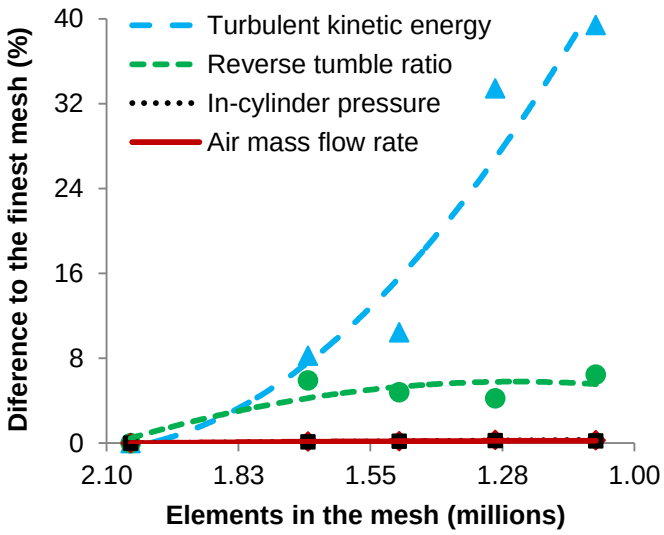

Figure 4.2 – Mean difference in the selected parameters from the coarsest to the finest mesh.

The “ideal” number of volumes in the engine grid necessary to accurately calculate the TKE was beyond 2.1 million, though the major reduction in its variation took place between 1.3 mi and 1.7 mi elements. Further refinement beyond this point did not have the same effect on reducing the error, but radically increased the computational cost. In Figure 4.3 it is clear the peak in TKE right after IVO (524° CA), followed by the steep difference in TKE due to the poor mesh resolution up to 1.3 million volumes.

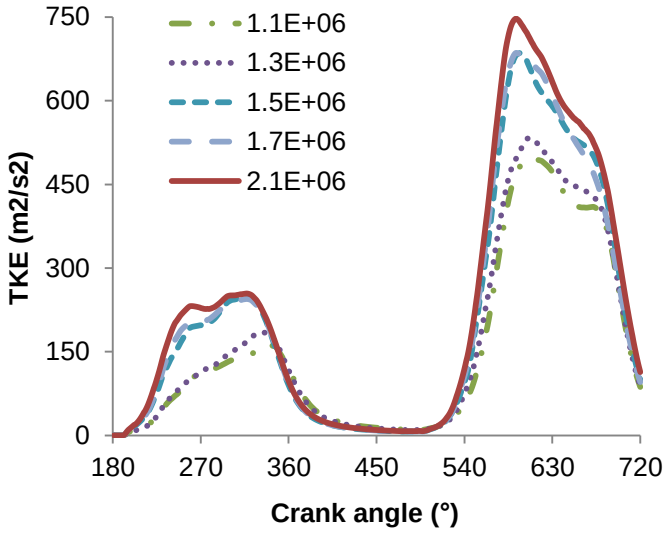

Figure 4.3 – Crank-angle-resolved TKE from the coarsest to the finest mesh.

Figure 4.4 shows the chosen 3-D engine mesh with about 1.7 million volumes with the piston at BDC. Its cross-section at the valve plane illustrates the refinements necessary in the valve curtain region, valve guides and piston top.

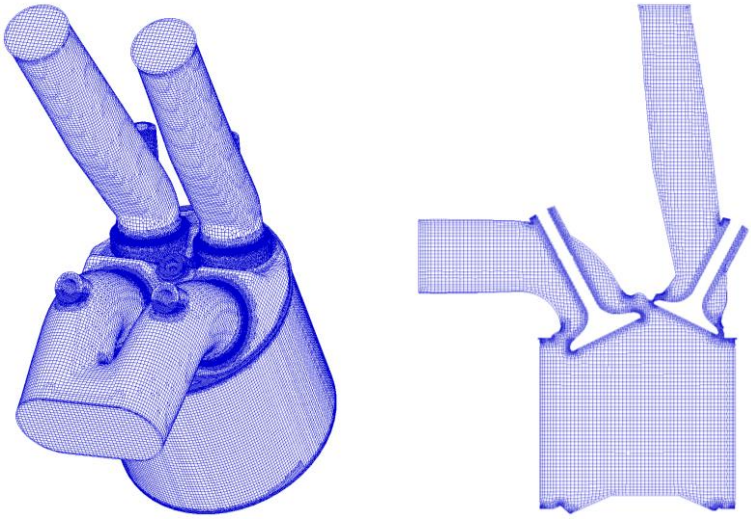

Figure 4.4 – Engine mesh and its cross-section at the valve plane.

4.4.2 Time-step independency study

With the 1.7 million elements mesh, the computational time-step (TS) was also evaluated based on the same parameters used in the mesh independency study. Four different time-steps ranging from 0.1° CA to 0.4° CA were tested and plotted from the largest to the smallest TS as seen in Figure 4.5. Clearly the effect of TS on the simulation results was not as severe as those found in the mesh size independency study. The time-step chosen of 0.2° CA could keep the

difference to the shortest TS in all variables below 6%, whilst resulting in a reasonable computational effort. The TS was further reduced during IVO/EVO to 0.1° CA for approximately 4° CA to minimise computational instabilities due to the large velocity gradients formed in the valve curtain region.

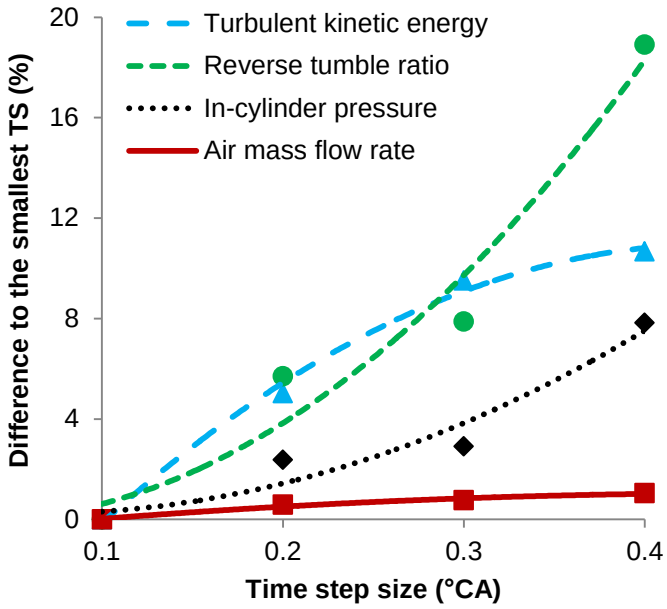

Figure 4.5 – Mean difference in the selected parameters from the largest to the smallest time-step.

4.4.3 Cold flow model validation

After determining the mesh and time-step sizes, the transient two-stroke cycle simulation was compared to motored experiments by means of the in-cylinder pressure. The boundary and initial conditions used were those already presented in Table 4.1, although the intake pressure and engine speed were lowered back from the “worst case scenario values” to 126.9 kPa and 1500 rpm, respectively. The comparison between experimental and simulation results is presented in Figure 4.6, where two complete cycles were simulated to ensure completely independency on the imposed initial conditions. The mean difference in in-cylinder pressure in the first cycle was found at 2.5% with a standard deviation of 2.7%. In the second cycle the difference remained nearly constant at 2.6% and the standard deviation was kept at 2.7%.

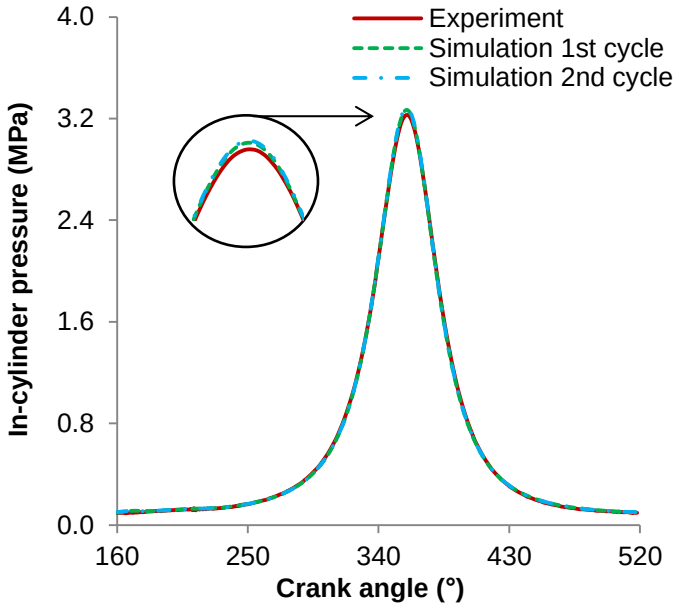

Figure 4.6 – In-cylinder pressure comparison between experiment and simulation in the two-stroke cycle.

From the in-cylinder pressures it could be assumed that the correct amount of air was trapped at IVC and the heat transfer modelling was accurate enough considering the imposed wall temperatures. The main challenge during the validation process was the intake and exhaust valve opening/closing timings, as it had a severe impact on the in-cylinder trapped mass and consequently the pressure. In conventional four-stroke engines the beginning of the valve movement is often considered equal to the valve lash. However, in the present research engine the absence of camshafts and the slight (but present) cycle by cycle variation of the hydraulic actuated valves imposed some difficulties on determining the exact valve moments. The best compromise for the valve opening/closing times was found at 0.1 mm, when the intake and exhaust ports were effectively connected to the calculation domain.

4.5 Fuel spray simulation

Besides the cold flow analysis performed in the two-stroke poppet valve engine geometry, the air-fuel mixture formation was also evaluated. The methods used in the spray simulations are firstly presented and followed by the model validation against experimental data.

4.5.1 Spray calculation

The spray calculations were based on the discrete droplet method (DDM) where momentum, trajectory, heat and mass transfer equations were solved for a group of identical droplets called a “parcel” [157]. The droplets were tracked under the Lagrangian space frame in a two-way interaction between gas and liquid phases. The particle resultant acceleration was calculated considering drag forces, gravity, buoyancy, environment pressure and medium acceleration/deceleration as shown in Equation (4.17). The droplet velocity vector is represented by $\mathbf{U}_d$, whilst the subscripts “g” and “d” refer to the gas and droplet properties, respectively. The particle drag coefficient is given by C_D, whilst $\mathbf{g}$ is the gravitational acceleration vector. Integration of Equation (4.17) results in the instantaneous droplet velocity vector, whilst the second integrative gives the particle position vector.

$$\frac{d\mathbf{U}_d}{dt} = \frac{3}{4} C_D \frac{\rho_g}{\rho_d} \frac{1}{D_d} \left|u_g - u_d\right| \left(\mathbf{U}_g - \mathbf{U}_d\right) + \left(1 - \frac{\rho_g}{\rho_d}\right) \mathbf{g} \tag{4.17}$$

Besides the particle momentum and trajectory, several sub-models were made necessary to account for heat and mass transfer, particles interaction, fuel impingement and spray breakup. The fuel vaporisation was modelled by the Dukowicz two-component theorem accounting for convection effects. This model assumed spherical shaped droplets with uniform temperature distribution and treated the surrounding fluid with uniform physical properties [158]. Additionally, when fuel is injected into the cylinder of a real engine, the droplets interact with the flow eddies and are deflected by them. As the instantaneous fluctuation components of the turbulence were not calculated, but modelled in the RANS approach, a turbulent dispersion sub-model was employed to estimate these effects. The O’Rourke model was used in this matter considering its flexibility for greater time-steps and hence reduced computational cost. This model suggests that the particle position was subjected to random forces proportional to the mean gas velocity and turbulent kinetic energy of the surrounding fluid [159].

When two particles were found in the same computational grid cell there was a possibility of interaction between them, so the Nordin sub-model was used to

estimate collision or coalescence of the droplets. The occurrence of collision or coalescence was accounted by means of a critical collision-coalescence impact parameter. This critical threshold took into account the droplets diameter, the relative velocity between them and their surface tension, so only one of the two events could occur. The Nordin model is considered an improvement of the original O'Rourke model due to its reduced mesh size dependency [157], which is important in case of poor mesh resolution. The use of an adaptive mesh refinement is recommended in spray simulations, although this feature was not available (for moving meshes) in the version 2013.2 of the software AVL Fire.

The occurrence of fuel impingement onto the chamber walls was considered by means of the spray-wall interaction model of Bai and Gosman [160]. The use conventional wall film modules, originally developed for port fuel injection (PFI) simulation, is not recommended for DI applications as the in-cylinder conditions differ from the intake port environment [161]. The increased environment pressure/temperature and the higher droplets mean velocity imply that spray reflections are more important. The Bai and Gosman sub-model approximated the wall film through particles reflection at narrow incidence angles, so the droplets propagated next to the wall after fuel impingement (adhesion). Based on a critical Weber number, this sub-model also predicted the occurrence of rebounding or splashing of particles in case of dry surfaces.

Finally, the spray breakup was resolved by the Kelvin Helmholtz Rayleigh Taylor (KH-RT) analogy based on the velocity difference between the droplets and the surrounding gas [162]. In this sub-model there is a constant competition between the KH breakup, favoured by higher gas phase densities, and the RT breakup, favoured by the particles deceleration and growth of waves on their surfaces. Several constants (eight in total) were available in this model so that the breakup time and length could be biased towards the KH or RT principles.

4.5.2 Spray model validation

A common method used to compare simulation and experiments with sprays is regarding the spray penetration acquired by optical measurements in constant volume chambers [163]. The spray penetration length is then determined as the

distance between the nozzle and 99% (or 95%) of the accumulated total liquid mass. In this research a multi-hole GDI injector was employed and hence the penetration value was averaged for all the asymmetric six beams (Figure 4.7). The angles presented in this figure were used to input the nozzle direction by means of Cartesian coordinates emerging from a single point in the mesh.

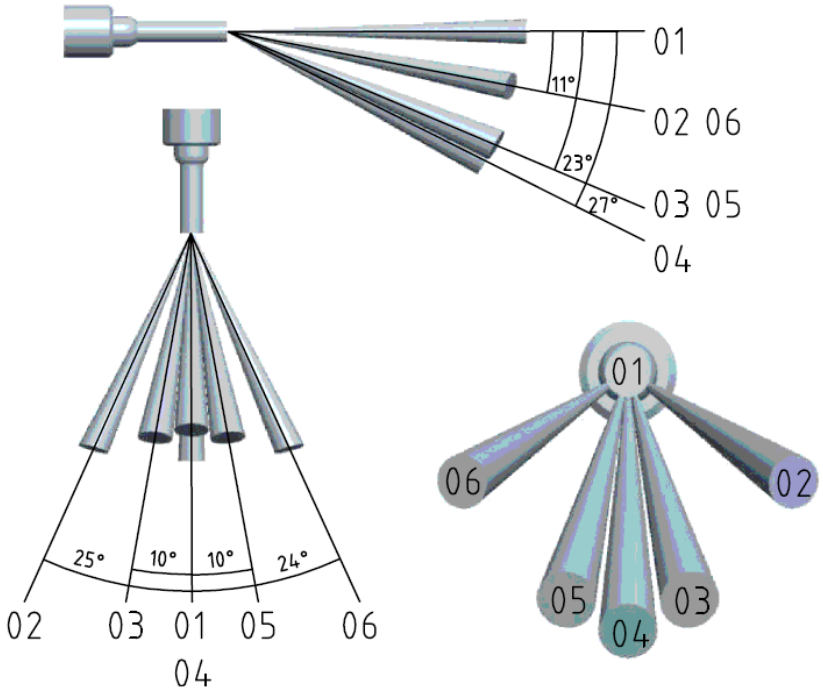

Figure 4.7 – Multi-hole injector spray pattern, adapted from [164].

The spray model validation was firstly carried out in a constant volume box-shaped grid with a maximum element size of 1.17 mm. This maximum element size was set according to the mesh independent study applied to the engine geometry seen in section 4.4.1. The spray simulation results were compared to experimental data published in [164][165] with the same injector model and under the same injection pressure of 15 MPa. The former reference presented the fuel spray penetration curve whilst the latter contributed with pictures of the spray plume obtained through Schlieren imaging.

The spray validation was carried out for gasoline only (mixture of n-octane and n-heptane) considering its similarities with ethanol regarding spray penetration and plume formation [166]. The differences in droplet mean diameter (which do exist) were beyond the scope of the present research. In Figure 4.8 the experimental spray penetration is shown with several untuned breakup sub-models tested.

Amongst all the sub-models presented in the previous section, the breakup one represented the largest difference in spray penetration and for such reason different sub-models were evaluated. The Reitz-Diwakar, Huh-Gosman and Wave sub-models were tested alongside the KH-RT, which presented the best results as seen in the detailed view in Figure 4.8.

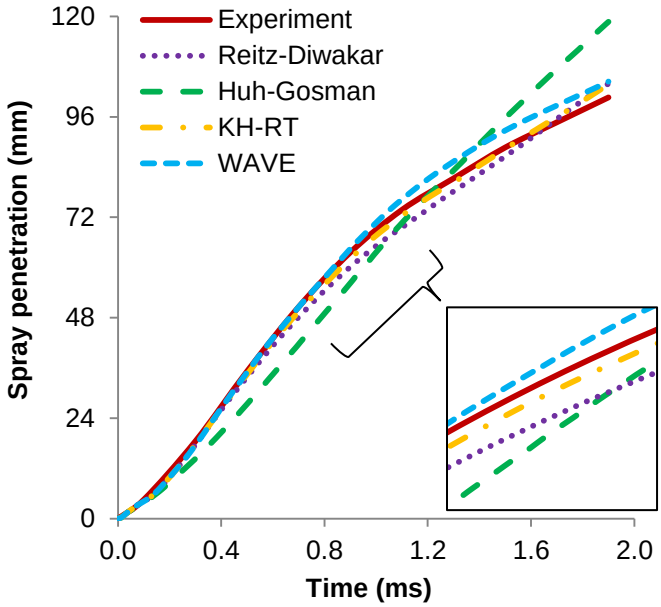

Figure 4.8 – Comparison between the simulation results with untuned breakup sub-models and the experimental spray penetration adapted from [165].

Four different time-steps were also tested during the fuel spray validation, ranging from 0.001 ms to 0.100 ms (Figure 4.9). It is clear that further reduction on the TS beyond 0.010 ms could not improve the spray penetration curve and thus it was the optimum choice. At 1500 rpm this TS corresponded roughly to 0.1° CA, which was the same time-step used during IVO/EVO. Longer time-steps detached the penetration curve from the experimental results, although the final value was quite similar amongst the time-steps evaluated.

The final tuned spray model penetration is presented in Figure 4.10 alongside the experimental curve adapted from [165]. The mean difference between the spray penetrations was found below 2.5% with a standard deviation of 1.5%.

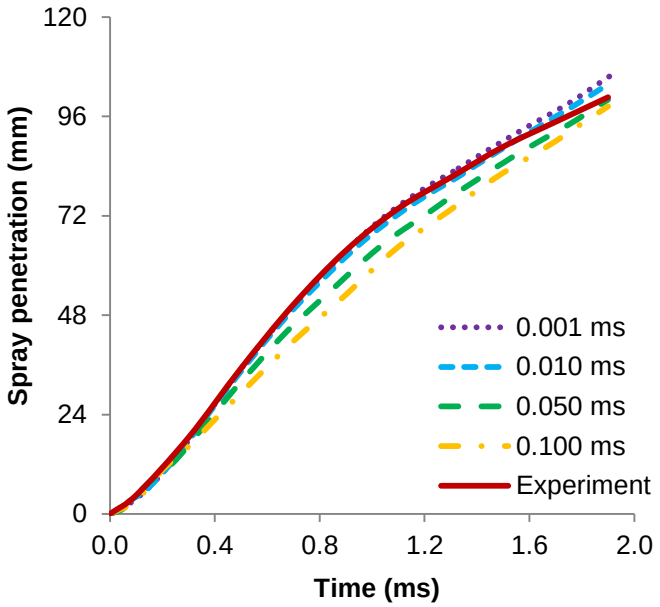

Figure 4.9 – Comparison between the simulation results with different time-steps and the experimental spray penetration adapted from [165].

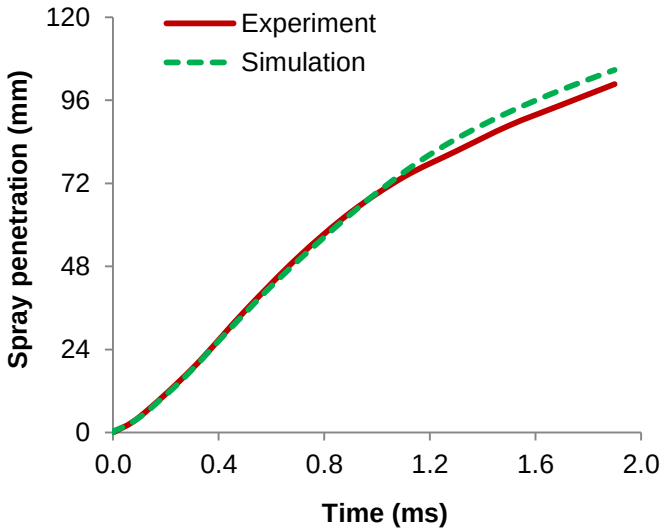

Figure 4.10 – Comparison between the final simulated model and the experimental spray penetration adapted from [165].

Simulation images of the spray plume were also compared to optical results [164] at three different instants after the SOI as seen in Figure 4.11. At 0.7 ms and 1.9 ms after the SOI the fuel vaporisation in the vicinity of the nozzle could not be properly modelled and resulted in a skew jet until the secondary breakup took place. Near the spray tip the secondary breakup enhanced the particle deceleration and improved the correlation to the experiments.

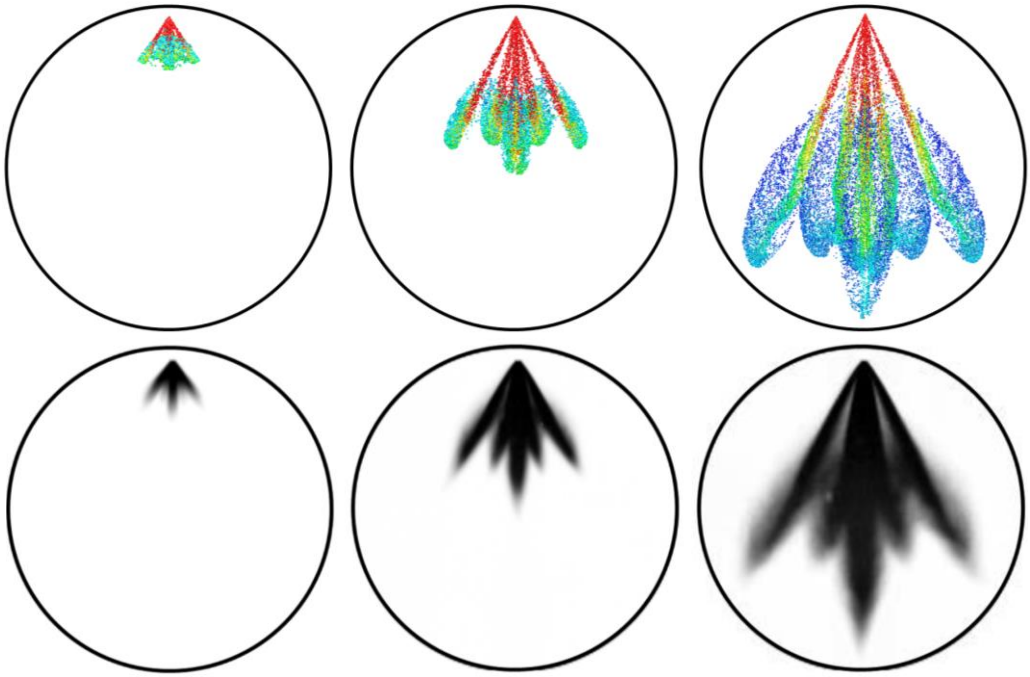

Figure 4.11 – Comparison between the simulation results and optical measurements adapted from [164] at 0.3, 0.7 and 1.9 ms after the SOI.

4.6 Summary

The numerical methodology employed in the transient 3-D CFD simulations was introduced and the main equations embedded in the AVL Fire solver were presented and briefly discussed. A mesh size independency study was carried out with five distinct meshes, so the compromise between computational expense and accuracy could be assessed. Four criteria were employed in this case: in-cylinder pressure, air mass flow rate, reverse tumble ratio and TKE. Using the same principle a time-step independency study was also performed during the cold flow and spray simulations to improve the computational cost. It was found that a 1.7 million elements mesh simulated with a 0.2° CA time-step resulted in the best compromise between accuracy and computational time. In the end, both cold flow and spray simulations were correlated with experimental results. The former comparison was based on the in-cylinder pressure, whilst in the latter the spray penetration and optical results were used in the evaluation. In both cases appreciable results were obtained and the models were believed to properly represent the physical engine operation.

Chapter Five

Experimental assessment of the two-stroke poppet valve GDI engine

5.1 Introduction

A preliminary experimental evaluation of the two-stroke poppet valve engine was conducted so that key issues could be initially identified. Considering the linkage between engine output and boost pressure, a sweep of intake pressures was proposed to investigate the engine performance in the mid-high load range. At the same time, the intake and exhaust valve timings were advanced and retarded independently at constant valve durations and lifts. The engine speed was also evaluated in the range of conditions supported by the test cell facilities, so its effect on the gas exchange and combustion processes could be understood. Gaseous and smoke emissions were investigated and the combustion process was evaluated using the heat release analysis discussed in section 3.3.1. Before the presentation of all results section 5.2 explains the test conditions and assumptions used in this initial study.

5.2 Test procedures

The two-stroke cycle operation was achieved by opening both intake and exhaust valves around BDC every cycle as seen in Figure 5.1. The positive valve overlap period allowed the boosted inlet air to scavenge the combustion products and fill the cylinder with fresh charge. The start of fuel injection (SOI) occurred after all the valves were closed to avoid fuel short-circuiting to the exhaust or its backflow to the intake. This latter occurred when the instantaneous in-cylinder pressure became higher than the instantaneous intake pressure before IVC. Therefore, the fuel remaining in the intake port could be carried back into the cylinder and pass directly to the exhaust port in the following cycle. This would not only reduce the overall efficiency but also increase UHC emissions.

Several engine speeds were tested i.e. 800, 1500, 2200 and 3000 rpm. At each engine speed five intake pressures were applied (where possible) as a way to

control the engine load. Increasing the boost pressures from 120±2 kPa to 280±3 kPa caused the charging efficiency to increase, which resulted in a larger air mass in the cylinder and hence higher engine output power. At some operation points stable combustion was not achieved as the covariance of the indicated mean effective pressure (COV_{IMEP}) reached the limit of 10%.

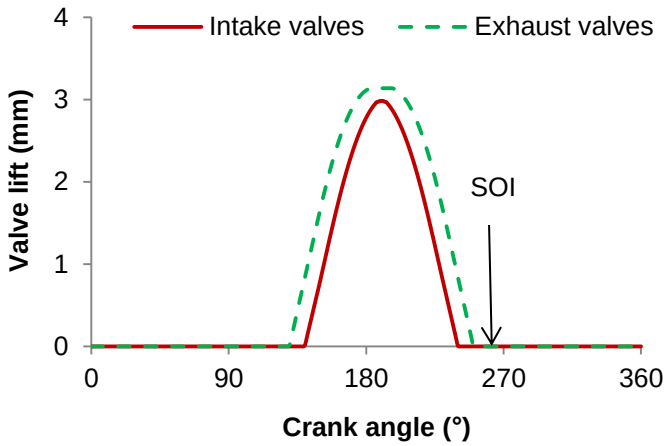

Figure 5.1 – Two-stroke cycle operation principle.

Different combinations of intake and exhaust valve opening/closing timings were also tested as shown in Figure 5.2 and Figure 5.3. The intake and exhaust valve opening durations were kept constant at 100° CA and 120° CA, respectively, based on values from the literature for low speed ported two-stroke engines [27]. At each engine speed and a given boost pressure, the exhaust valve timing was kept fixed first and then the intake valve opening (IVO) was varied from 130° CA to 150° CA after top dead centre (ATDC). Then, the intake valve timing was fixed and the exhaust valve opening (EVO) was varied from 120° CA to 140° CA ATDC. In both cases the valve timings were varied in steps of 5° CA. The valve lift was maintained at 3 mm to take advantage of the masked cylinder head, which protrudes 3 mm from the valve seat plane as seen in Figure 4.1.

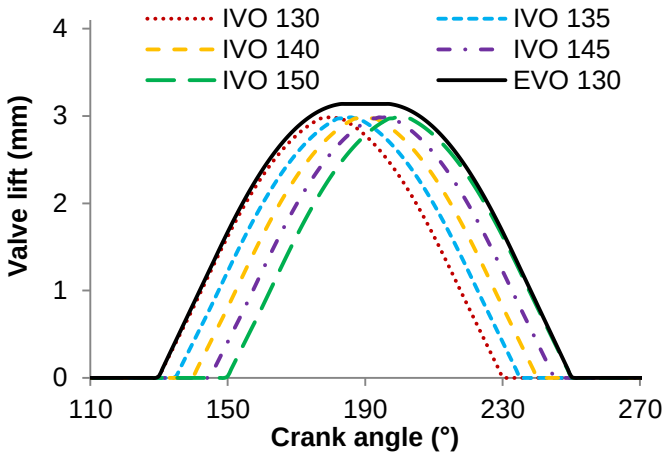

Figure 5.2 – Intake valve timing optimisation.

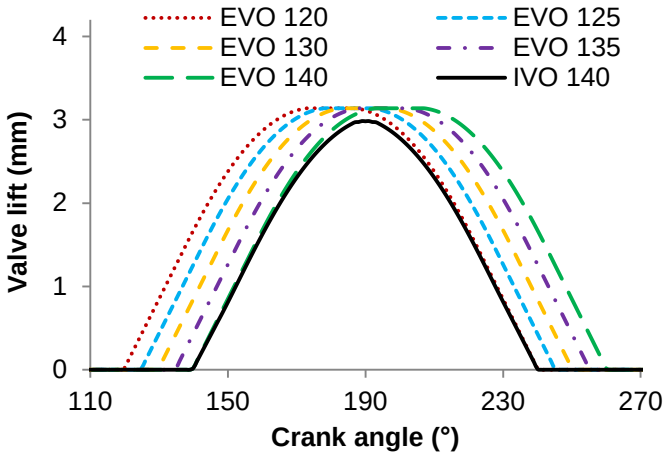

Figure 5.3 – Exhaust valve timing optimisation.

The standard double-slit fuel injection system was employed in this part of the study and gasoline was solely used. To ensure the same air-fuel mixing conditions for all the valve timings studied, the SOI was set to 260° CA ATDC, which was the latest EVC timing tested. At each intake pressure and engine speed tested, the fuelling rate was increased until a fuel rich or stoichiometric in-cylinder charge was obtained. This fuelling rate was then kept constant as the intake and exhaust valve timings were varied, so that the sole effect of the gas exchange process could be evaluated. Furthermore, as the engine speed changed, the fuel flow rate was also varied accordingly to ensure a fuel rich in-cylinder charge. The reason why lean mixtures could not be employed relies on the method used to calculate the gas exchange parameters, particularly the air trapping efficiency. The evaluation of the exhaust gas composition, detailed in section 3.3.4, considered that all free oxygen in the exhaust resulted from inefficiencies during the scavenging process. In this case a sufficiently rich

mixture was required during the combustion process to ensure the minimum possible oxygen remaining within the cylinder at EVO.

5.3 Results and discussion

The results presented here were averaged over 100 consecutive cycles and plotted as a function of valve timings at given engine speeds and intake pressures. The nomenclature of the different valve timings studied consisted of IVO and EVO timings in °CA ATDC. The Y-axis was further divided into four parts according to the engine speed.

5.3.1 Performance and gas exchange analysis

The indicated mean effective pressure (IMEP) results in the range of speeds and boost pressures tested are presented in Figure 5.4. Highly boosted operation was not possible at higher speeds (2200 rpm and 3000 rpm) due to violent and unstable combustion. When the fuelling rate was reduced to avoid excessive heat release rate at higher boost pressures, unstable combustion occurred as measured by higher COV_{IMEP} values. On the other hand, when the fuelling rate was increased to avoid combustion instabilities, the dP/dθ rose above the limit set. The occurrence of violent or unstable combustion was related to the large amount of hot residual gas trapped caused by insufficient time available for scavenging at higher engine speeds [91]. The presence of hot residual gas raised the charge temperature and accelerated the occurrence of auto-ignition combustion in the unburnt mixture, resulting in rapid and violent heat release. Additionally, as the SOI took place at 260° CA ATDC (similar to values used in four-stroke GDI stratified charge operation), significant fuel stratification was present and larger cycle-to-cycle variations were expected.

At 800 rpm all the boosting levels could be tested throughout the valve timings studied except for the latest IVO (150° CA) and the earliest EVO (120° CA), when combustion became unstable due to lean operation at higher intake pressures. In these cases the engine output could have been increased if more fuel was injected, although it would not have been possible to compare solely the valve timings effect under different fuelling rates. From the left to the middle point along the x-axis in the plots, IVO was retarded from 130 to 150° CA ATDC at a

constant EVO of 130° CA ATDC. At the lowest boost pressure of 120 kPa the IMEP values varied little with IVO and the combustion process became nearly independent of the air management system. When the boost pressure was higher than 160 kPa, the IMEP increased with the retarded IVO and reached its peak at IVO 150° CA ATDC. It is noted that the higher the boost pressure the more pronounced was the change in IMEP with IVO. This could be explained by an increase in the charging efficiency as presented in Figure 5.5, which resulted from the higher pressure ratio between the intake and exhaust ports. When IVO was retarded a more effective blowdown event took place without intake air contamination. Moreover, a shorter time was available between IVC and EVC so that less fresh charge was lost to the exhaust at lower speeds. At 1500 rpm the IVO and EVO sweeps had similar effects on the IMEP, but no stable combustion could be achieved at the maximum boost pressure tested.

From the right to the middle alongside the x-axis in Figure 5.4 and Figure 5.5, EVO was advanced from 140° to 120° CA ATDC whilst IVO was kept at 140° CA ATDC. This change had little impact on the charging efficiency (and thus the IMEP) at lower boost pressures, although at higher intake pressures it rose steadily to reach its peak at the earliest EVO. This behaviour mirrored the left part of the curve and could be explained by the increased blowdown period and higher pressure ratio across the exhaust valves at an earlier EVO. In addition, the pressure ratio between the intake charge and the in-cylinder gases was greater at the same IVO as the in-cylinder pressure had dropped to a lower value due to the extended exhaust blowdown.

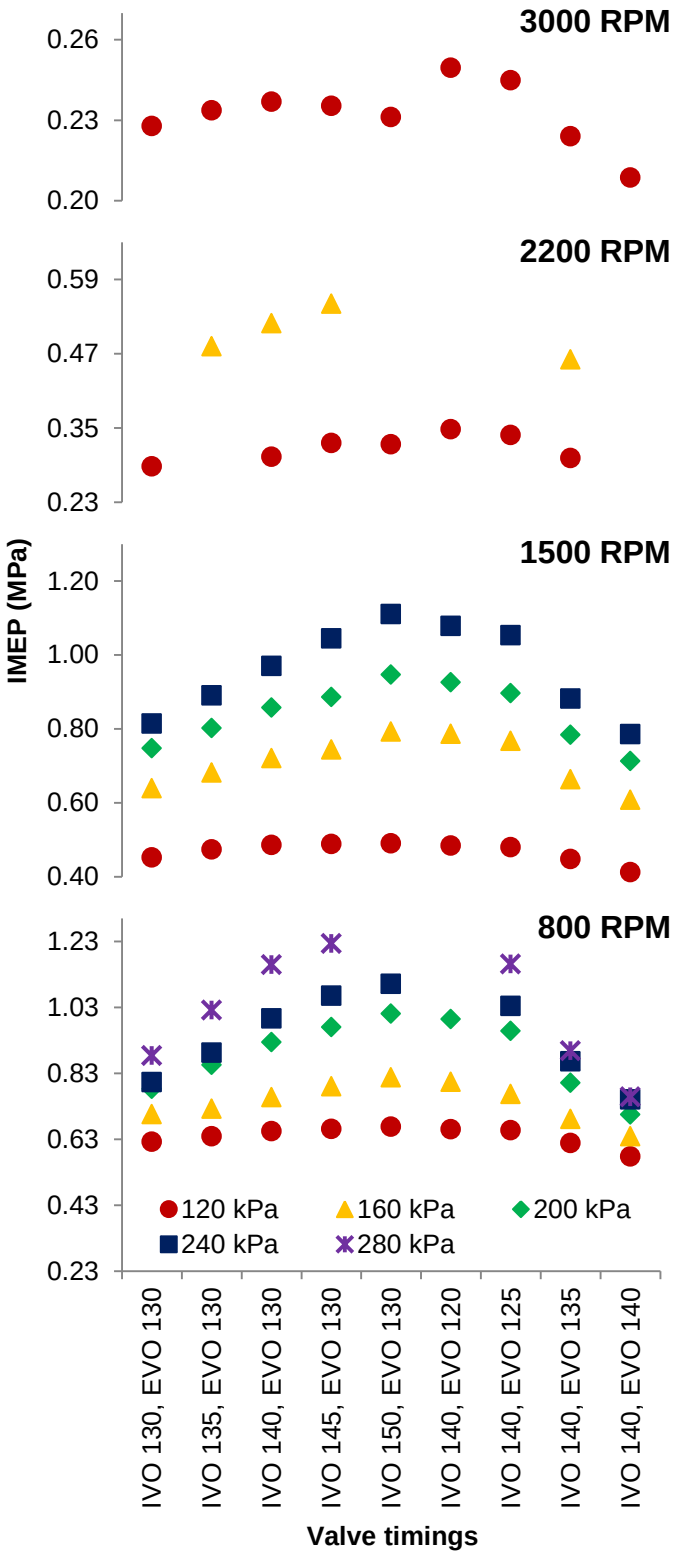

Figure 5.4 – IMEP at different engine speeds, intake pressures and valve timings.

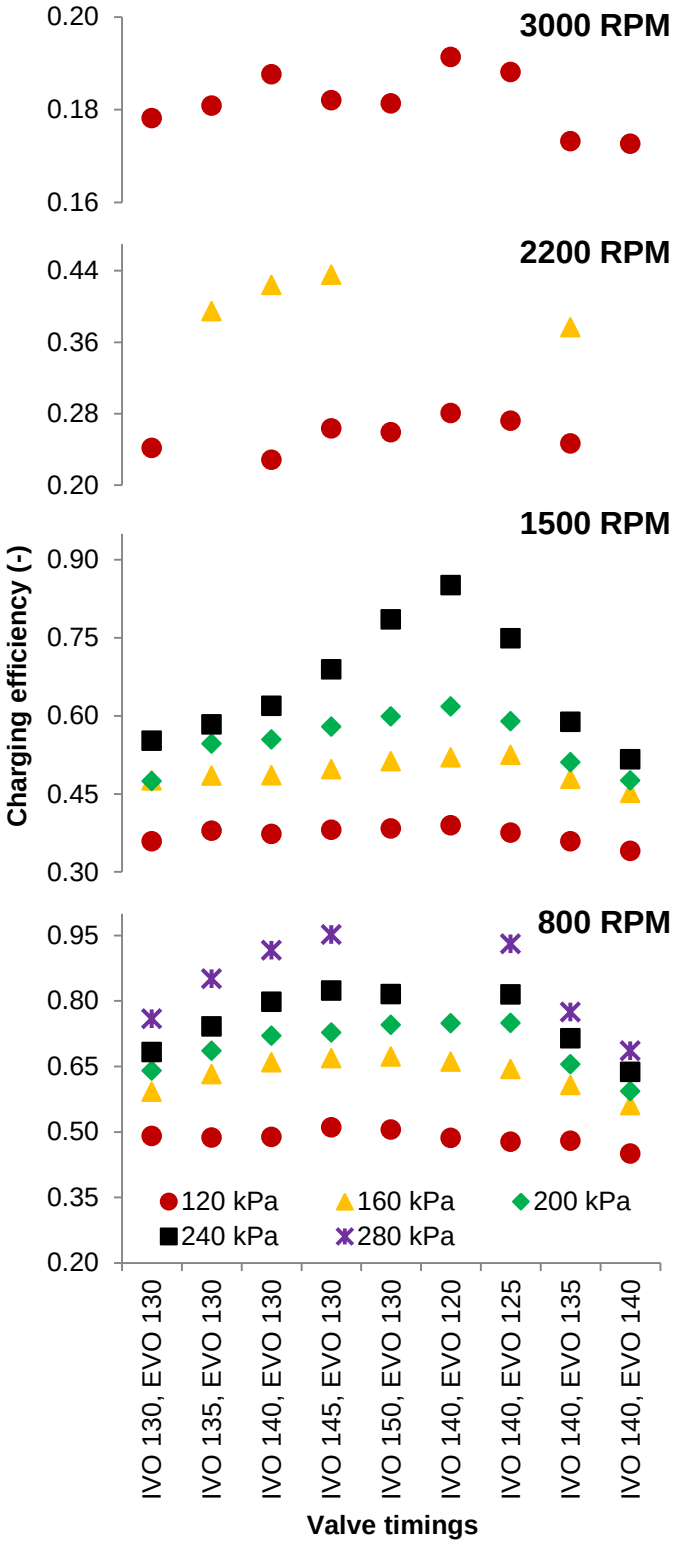

Figure 5.5 – Charging efficiency at different engine speeds, intake pressures and valve timings.

At higher engine speeds the poor charging efficiency prevented higher load operation to be achieved. For instance, at 800 rpm and 120 kPa intake pressure, the levels of internal EGR were found at 35% (considering an idealised flow regime as shown in section 3.3.4). Meanwhile, at 3000 rpm and at the same

intake pressure, the internal EGR fraction increased to about 0.82. These high levels of residual gas trapped not only reduced the oxygen availability (and hence the IMEP) but also increased the thermal load of the charge inducing violent combustion. The overall results in Figure 5.5 illustrate that the maximum IMEP values were a direct consequence of the most completed scavenging process, as those achieved at the latest IVO and earliest EVO.

At 800 rpm the peak IMEP of 1.2 MPa was achieved at an intake pressure of 280 kPa, producing a specific torque of nearly 200 Nm/dm^3 with the in-cylinder peak pressure as low as 6.8 MPa as seen in Figure 5.6. For the sake of comparison, to produce the same torque at the same speed in a four-stroke engine of the same displacement, the engine would need to be operated at 2.4 MPa IMEP. This would only be achieved with a higher in-cylinder pressure in a highly downsized engine, assuming the operation would not be limited by knocking combustion and/or LSPI (super-knock) [167]. Such high value of torque at low speeds is comparable to extremely boosted modern diesel engines under the concept of downspeeding, where the engine operation region is shifted towards lower speeds with minimised friction and gas exchange losses [70]. Figure 5.6 also shows the linear trend of specific torque and in-cylinder pressure with the engine speed. As the engine speed increased, the charging efficiency dropped and hence lower loads could be realised. Nevertheless, the low values of in-cylinder pressure compared to equivalent four-stroke engines running at similar conditions were still attractive regarding structural and thermal stresses.

At any given IVO and EVO timings the charging efficiency dropped with the increased engine speed because of the reduced time available for gas exchange. Furthermore, at each engine speed the charging efficiency decreased from the middle to the both sides of the x-axis, reaching a minimum when the valves opened at the same time i.e. “IVO 130, EVO 130” and “IVO 140, EVO 140”. In order to better understand the scavenging results, the pressure-volume (P-V) diagrams of four selected valve timings at 800 rpm and 200 kPa are presented in Figure 5.7.

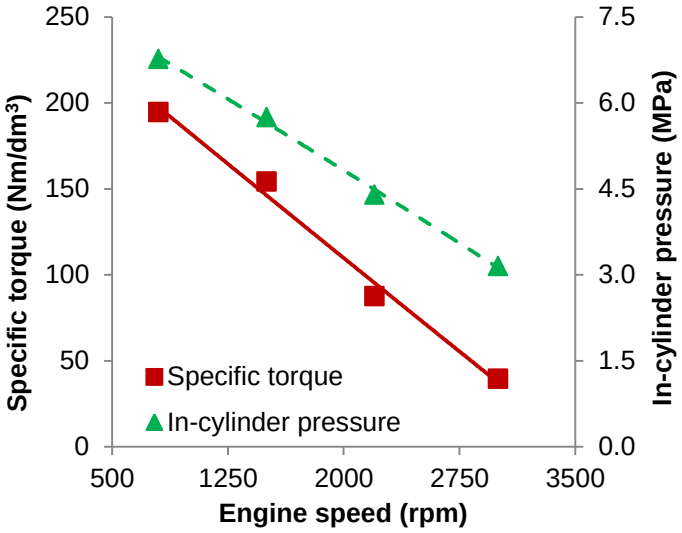

Figure 5.6 – Maximum specific torque and corresponding in-cylinder pressure achieved at the engine speeds tested.

It can be seen from the P-V diagram that the largest amount of useful work was achieved with the earliest EVO (120° CA ATDC) and the latest IVO (150° CA ATDC), when the scavenging process was improved and less residual gas was trapped. As the valve timings moved towards “IVO 130, EVO 130”, the greater charge dilution promoted by the internal EGR reduced the heat release rate and hence the peak pressure. It can be seen that in this case, as the intake and exhaust valves opened at the same time, part of the burnt gases mixed with the intake charge and compromised the in-cylinder charge purity in the next cycle [88]. The valve timing “IVO 140, EVO 140” was characterised with even lower in-cylinder peak pressure as a result of greater amounts of residual gas trapped, as shown by the lower charging efficiency (Figure 5.5).

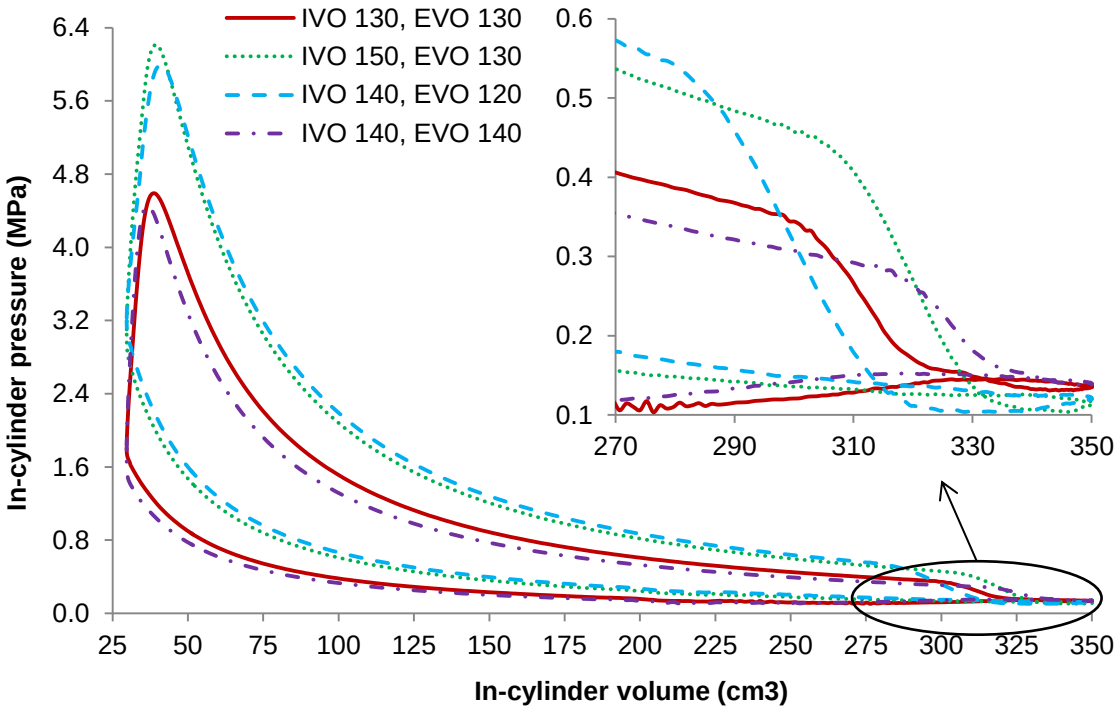

Figure 5.7 – Pressure-volume diagrams for selected valve timings at 800 rpm and 200 kPa of intake pressure.

As presented by the zoomed part of the P-V diagram in Figure 5.7, the most retarded EVO had the longest expansion loop amongst those evaluated. The two extreme valve timings ("IVO 130, EVO 130" and "IVO 140, EVO 130") also showed the highest in-cylinder pressures around BDC, which caused poor scavenging as the pressure drop across the intake valves decreased. Moreover, the in-cylinder pressure at the end of the compression phase for these two cases was about 50% lower than that for "IVO 150, EVO 130" and "IVO 140, EVO 120". This was a result of less trapped fresh air mass and higher levels of residual gas with larger heat capacity. The two intermediate valve timings in Figure 5.7 presented similar peak pressures (less than 4% difference), although the earlier EVO case had reduced useful work and hence a slightly lower IMEP. At this speed (800 rpm) it was possible to confirm that the exhaust blowdown phase could be partially replaced by a later EVO (130°) with improved expansion work without compromising the purity of the charge. For these two valve timings the difference in charging efficiency was less than 0.5% (Figure 5.5), whilst the IMEP increased by 2% with later EVO (Figure 5.4).

The gas exchange process in the two-stroke poppet valve engine was significantly affected by the actuation speed of the electrohydraulic valve train.

As shown in Figure 5.8, the valve opening and closing slopes became less steep as the engine speed increased and resulted in smaller effective flow area. Such limitation of the camless system could be overcome by using a conventional camshaft of higher lift driven by and at the same speed the crankshaft.

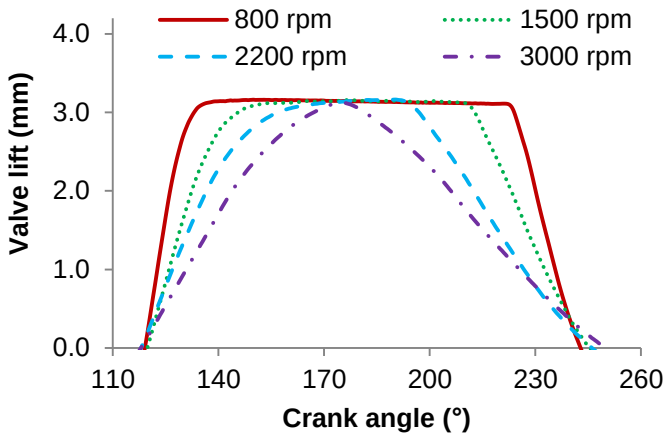

Figure 5.8 – Effect of engine speed on valve opening and closing durations.

The air trapping efficiency was calculated to determine how effectively the supplied fresh air was being used. As shown in Figure 5.9, the air trapping efficiency rose steadily with the engine speed as a result of shorter time available for the gas exchange. Higher trapping efficiencies were found with earlier EVO and EVC particularly at 2200 rpm and 3000 rpm with “IVO 140, EVO 120”. In this case the valve overlap period was reduced but the charging efficiency was still maximised (Figure 5.5).

When the intake air pressure was set to 120 kPa the air trapping efficiency at 800 rpm and 1500 rpm exhibited different trends from the other pressures. This different pattern might be attributed to a transition from a displacement dominated scavenging phase to a mixing dominated scavenging phase, as idealised by the Benson-Brandham two-part scavenging model for two-stroke engines [168]. According to this theory the scavenging was firstly dominated by a displacement process until it reached a certain value of scavenge ratio. After this point the fresh air and the burnt gases were more prone to mix until the end of the scavenging process, so lower values of air trapping efficiencies were registered.

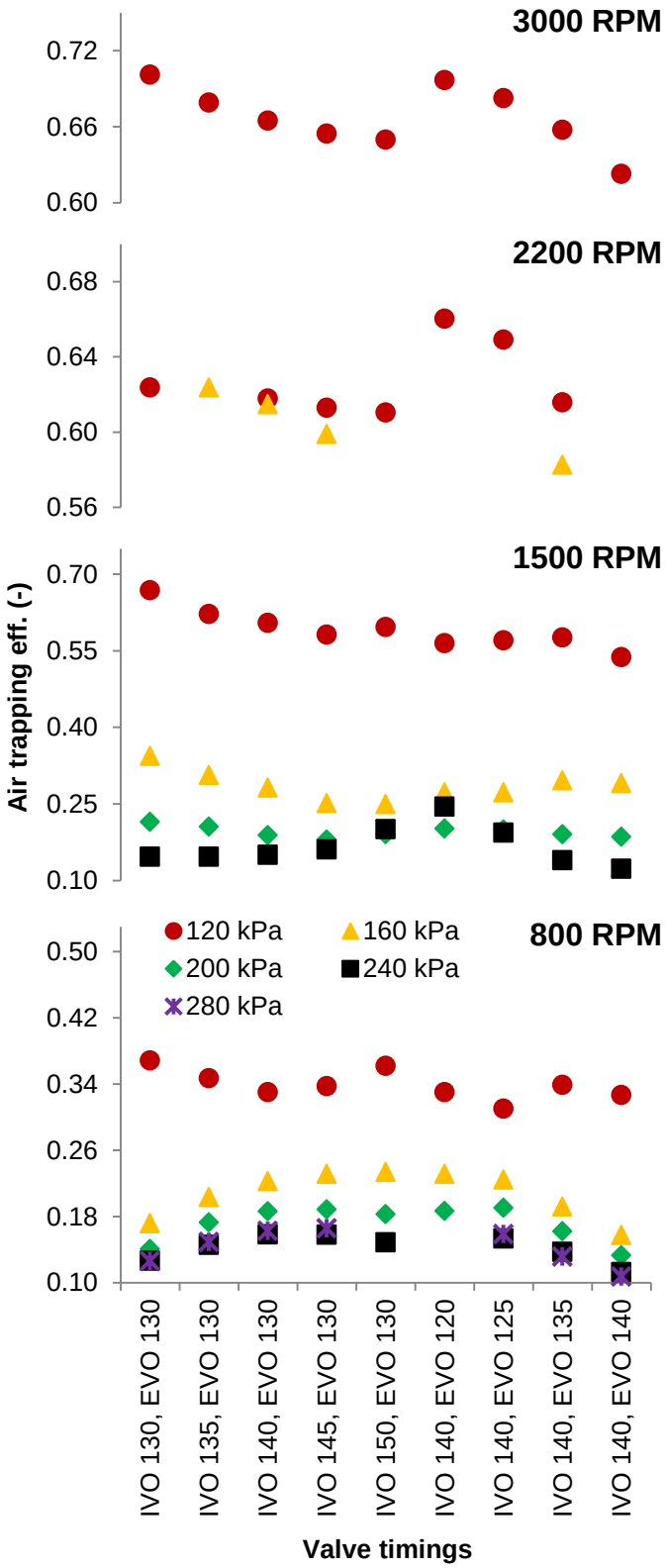

Figure 5.9 – Air trapping efficiency at different engine speeds, intake pressures and valve timings.

5.3.2 Combustion and heat release analysis

The combustion duration calculated from 10% to 90% of the mass fraction burnt (MFB) is presented in two parts according to the intake pressures: the first part for 200/240/280 kPa (Figure 5.10) and the second part for 120/160 kPa (Figure 5.11). At 800 rpm it is noted that the combustion durations decreased slightly as the intake pressure increased due to the higher charge temperature and pressure. In addition, it can be seen from Figure 5.11 and Figure 5.10 that the combustion duration lied between 13° CA and 19° CA at 800 rpm, which is shorter than typical values of SI combustion in four-stroke engines. The same trend was visible at 2200 rpm where both controlled auto-ignition (CAI) and spark ignition (SI) combustion modes were found amongst the valve timings tested. This suggests that the heat release process might have taken place in the form of a spark ignited flame around the spark plug and auto-ignition combustion of some premixed charge in the end-gas.

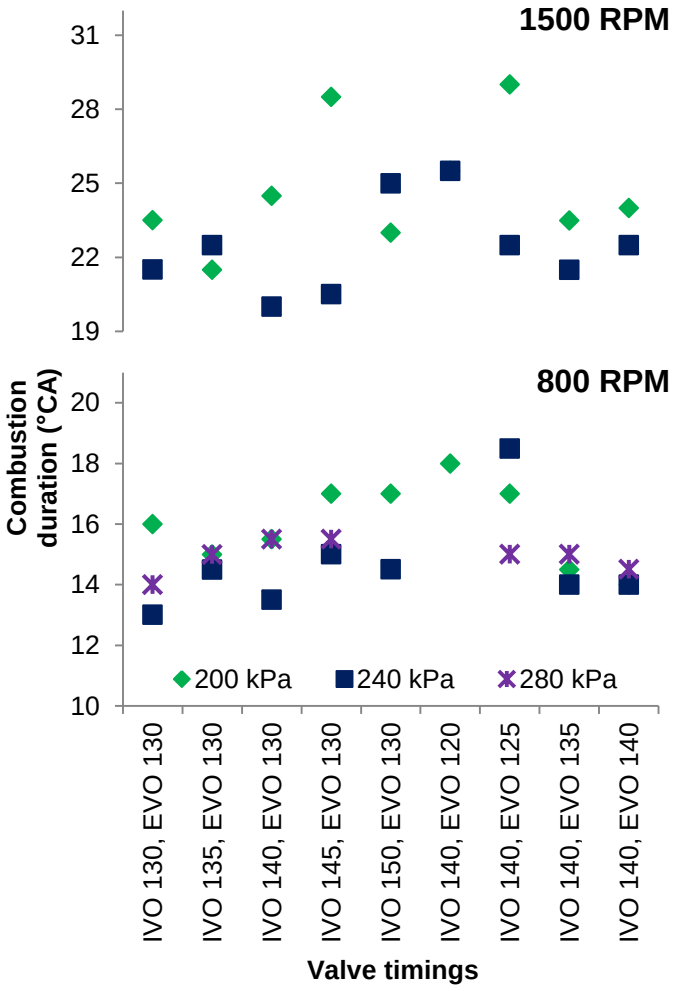

Figure 5.10 – Combustion duration at 200/240/280 kPa of intake pressure.

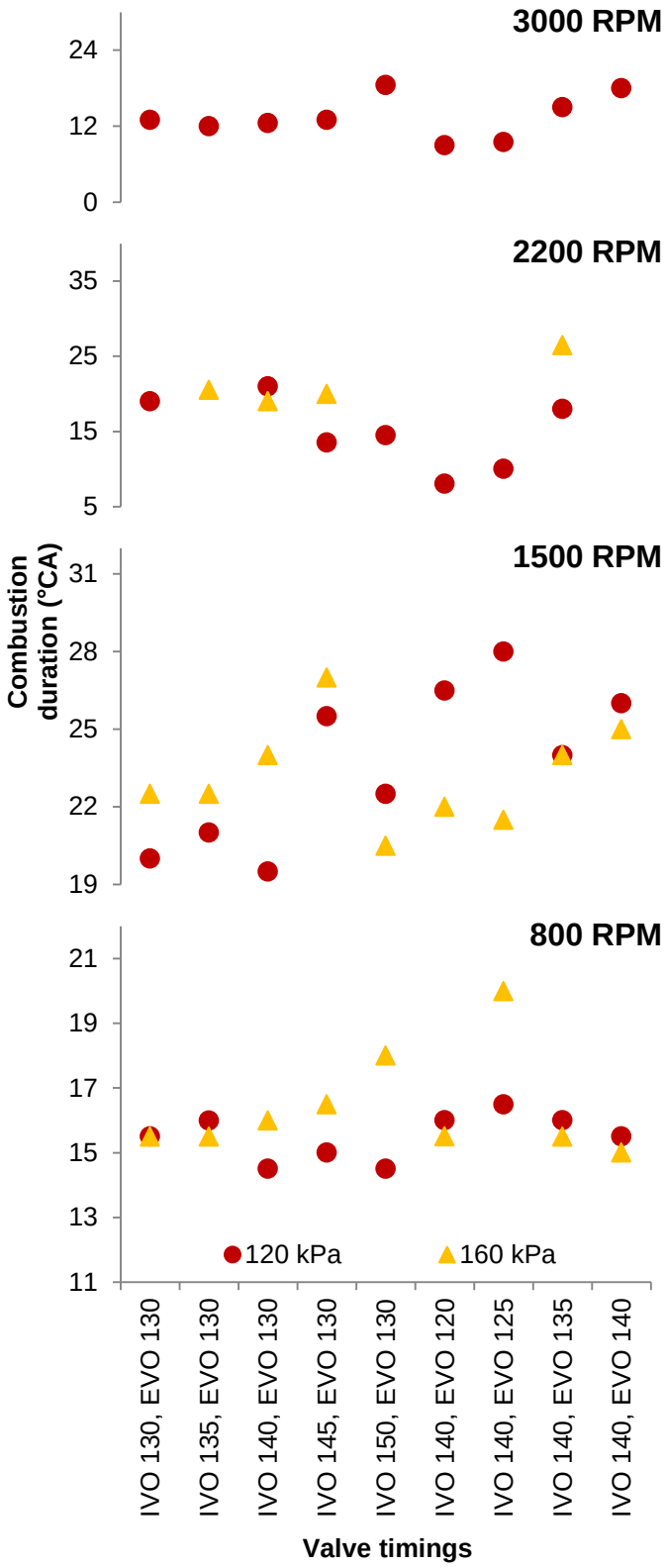

Figure 5.11 – Combustion duration at 120/160 kPa of intake pressure.

To better understand the combustion process as the engine speed increased, Figure 5.12 presents the mass fraction burnt (MFB) curves at 1500, 2200 and 3000 rpm at a constant intake pressure of 120 kPa. At 1500 rpm the gas

exchange process was favoured by the longer time available to it and thus less hot residual gas was trapped in the cylinder. The time available for heat transfer was longer as well, so the remained internal EGR cooled down. The resulting combustion process therefore relied on flame propagation initiated by the spark only, with the characteristic long “S” shape. As the engine speed increased to 2200 rpm the time available for both gas exchange and heat transfer decreased and more hot residual gas was trapped. This higher thermal load, besides the compression and temperature generated by the flame propagation initiated at the spark, increased the temperature of the end-gas up to the threshold of auto-ignition. For this reason the slow early flame propagation prevailed as the main heat release process until about 25% of the MFB (dashed line in Figure 5.12), when the auto-ignition of the end-gas took place and rapidly consumed the rest of the charge. This hybrid combustion process is sometimes referred as spark assisted compression ignition (SACI), as features of both combustion modes are combined [101][139]. At 3000 rpm, when the charging efficiency dropped significantly, high levels of hot internal EGR were trapped and triggered not only the auto-ignition of the end-gas, but the whole charge. At this speed the heat transfer was minimised and the charge achieved a high thermal state where the spark had little effect. Thus, the combustion process was governed by the charge temperature and composition only. The CAI combustion had a positive impact on the indicated efficiency (to be seen later) due to its shorter duration. Further gains would have been possible by proper phasing of the CAI combustion as it occurred too early in the cycle, as seen by the two other properly timed curves. Finally, it is notable the similar combustion rate (30-90% of the MFB slope) between pure CAI and SACI combustion, which further justified the occurrence of auto-ignition in front of the spark-ignited flame front.

At 2200 rpm and 3000 rpm stable engine operation was mainly limited to the intake pressure of 120 kPa. During such cases it was found that the spark timing had little effect on the combustion phasing and auto-ignition combustion became the dominant heat release process. This was evidenced by the very short combustion durations seen in Figure 5.11. The combustion duration remained nearly independent of IVO when EVO was set to 130° CA ATDC. In comparison, EVO had a more pronounced effect on the combustion duration as shown by the

earliest EVO (120° CA ATDC), which produced the shortest burning duration. In this case the internal EGR fraction was lower (Figure 5.5) as a result of more vigorous exhaust blowdown, which would be expected to increase the CAI combustion duration due to lower charge thermal load. However, as EVO was advanced, EVC moved by the same amount and hence the effective compression ratio (ECR) increased (Figure 5.15) and compensated the lack of hot residual gas trapped.

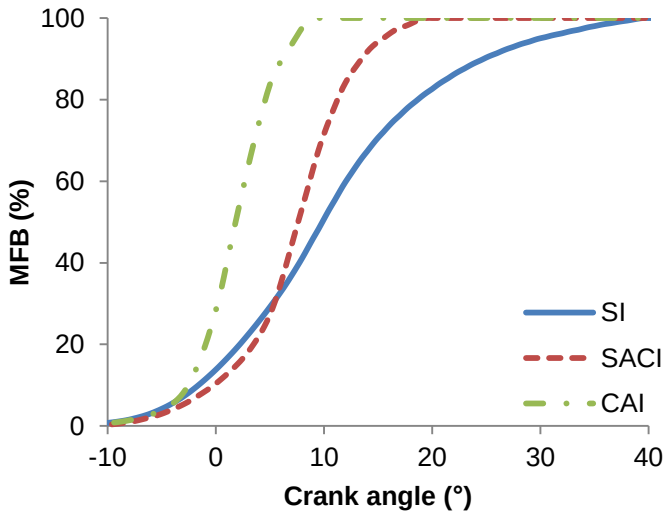

Figure 5.12 – Mass fraction burnt profile of SI, SACI and CAI combustion at 1500, 2200 and 3000 rpm, respectively (120 kPa of intake pressure).

Figure 5.13 and Figure 5.14 show the spark timings set for MBT (coloured symbols) or KLS (grey symbols) at 800 rpm and 1500 rpm, above which CAI combustion took over and the spark timing had little effect. The most retarded KLS occurred at the earliest EVO as a result of the minimum residual gas concentration and highest charging efficiency as seen in Figure 5.5. At higher charging efficiencies the level of internal EGR was reduced, so the dilution effect and charge heating capacity were both minimised. Under these conditions the heat release process became more abrupt and therefore it required retarded spark timings. The ECR also increased in this case from about 8.8:1 to 9.6:1 (Figure 5.15), which further inhibited more advanced ignition timings. In a similar fashion, the KLS timing became more retarded when IVO moved from 130° to 150° CA ATDC due to improved scavenging and less residual gas trapped. When the boost pressure was set to 120 kPa, MBT could be achieved for all valve timings at 800 and 1500 rpm. In this case even more advanced MBT

timings were realised near the middle of the x-axis when both the charging and trapping efficiencies were maximised.

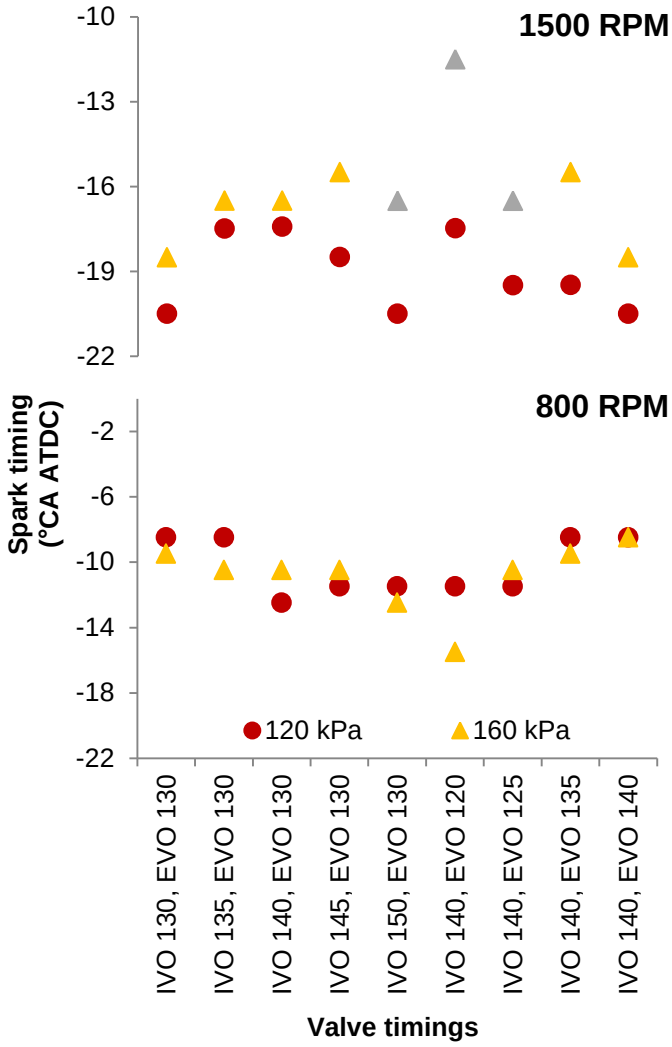

Figure 5.13 – Spark timings set for MBT (coloured symbols) or KLS (grey symbols) at 120/160 kPa of intake pressure.

Figure 5.15 shows that for a given exhaust valve timing both the effective compression and expansion ratios were constant, whilst the EER was higher than the ECR by about one unit. When EVO was retarded from 120° to 140° CA ATDC the EER increased and the ECR was reduced. The highest EER, and hence the highest expansion work, was achieved with the most retarded EVO at 140° CA ATDC. However, such increase in the useful work did not result in improved indicated efficiency (Figure 5.16) as a result of the lowest ECR amongst all points. Similarly, the case “IVO 140, EVO 120”, which presented the highest ECR, could not achieve the highest efficiency at 800 and 1500 rpm due to retarded spark timing and combustion phasing. At higher speeds, when CAI

combustion prevailed, this increment in effective compression ratio ensured indicated efficiencies as high as 0.343 at 3000 rpm.

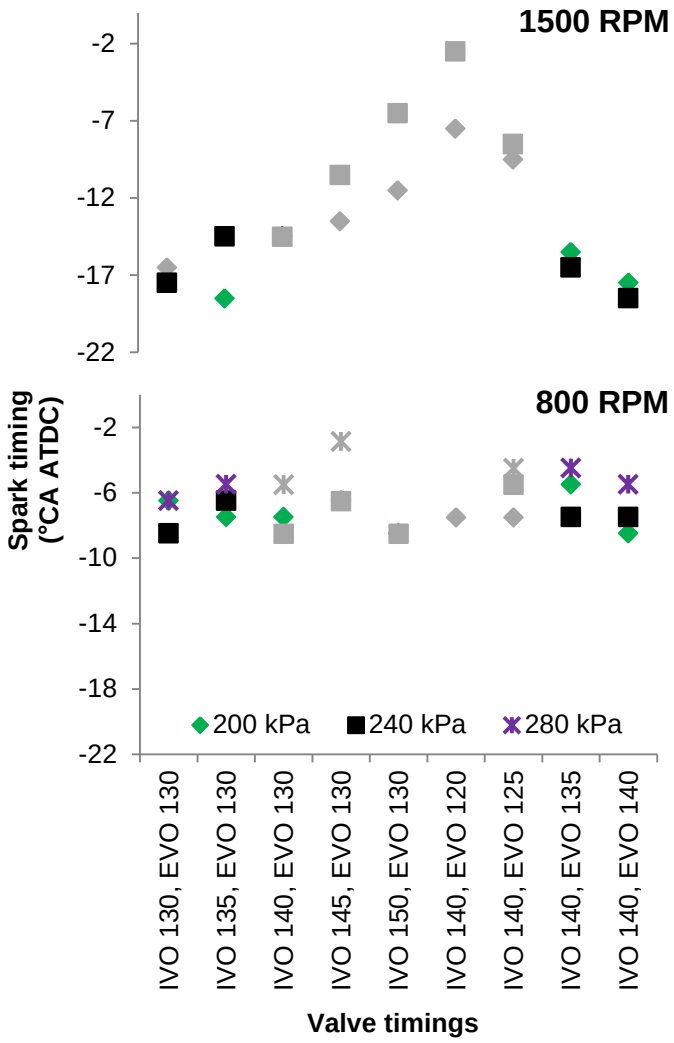

Figure 5.14 – Spark timings set for MBT (coloured symbols) or KLS (grey symbols) at 200/240/280 kPa of intake pressure.

The indicated efficiency was intrinsically linked to expansion work, charging efficiency and combustion efficiency. Therefore, there was a trade-off between higher scavenging rates through exhaust blowdown with early EVO, and higher EER achieved with late EVO but poorer scavenging. At 800 rpm the maximum indicated efficiency of 0.336 was achieved with “IVO 150, EVO 130” at nearly all boost pressures tested (Figure 5.16). The maximum indicated efficiency was attained at the same valve timing at 1500 rpm, although its value decreased with higher intake pressures. The last parameter to influence the indicated efficiency was played by the combustion process, presented in Figure 5.17.

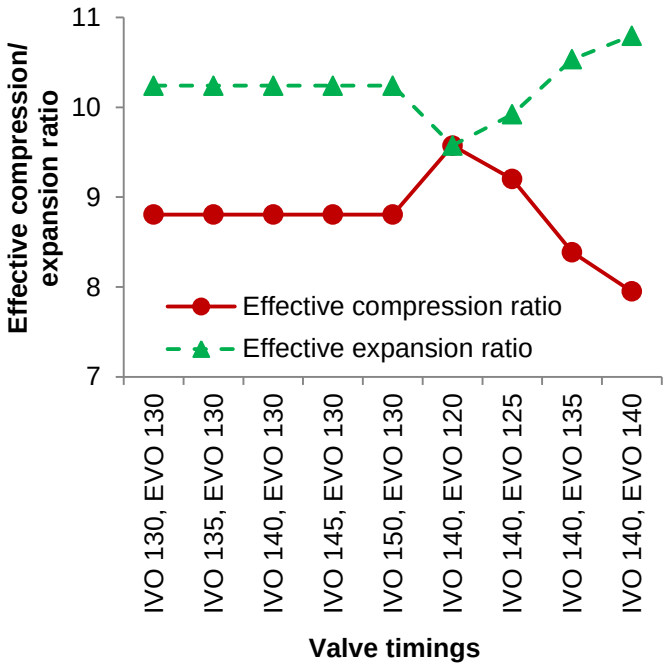

Figure 5.15 – Effective compression and expansion ratios at different valve timings.

The most significant reason of change in indicated efficiency as a function of valve timings was related to the combustion efficiency (Figure 5.17). It can be seen that the combustion efficiency results mirrored those of the indicated efficiency presented in Figure 5.16. The highest combustion and indicated efficiencies occurred in the middle of the graphs around “IVO 150, EVO 130” / “IVO 140, EVO 120”, when the charging efficiency was maximised. The combustion efficiency decreased with higher engine speeds at the same boost pressure as a result of increased charge dilution promoted by the internal EGR at lower charging efficiencies. From 1500 rpm onwards both indicated and combustion efficiencies dropped at higher boost pressures as a possible result of insufficient time available for mixture preparation. At higher loads the fuelling rate increased but the SOI was kept constant at 260° CA ATDC, which might have justified the poor air-fuel mixing. On the other hand, at 800 rpm and near the middle of the x-axis, the indicated efficiency increased at higher loads although it was not a result of the combustion efficiency. In this case the improvements were solely due to the lower levels of internal EGR, as the effective expansion and compression ratios were also kept unaltered.

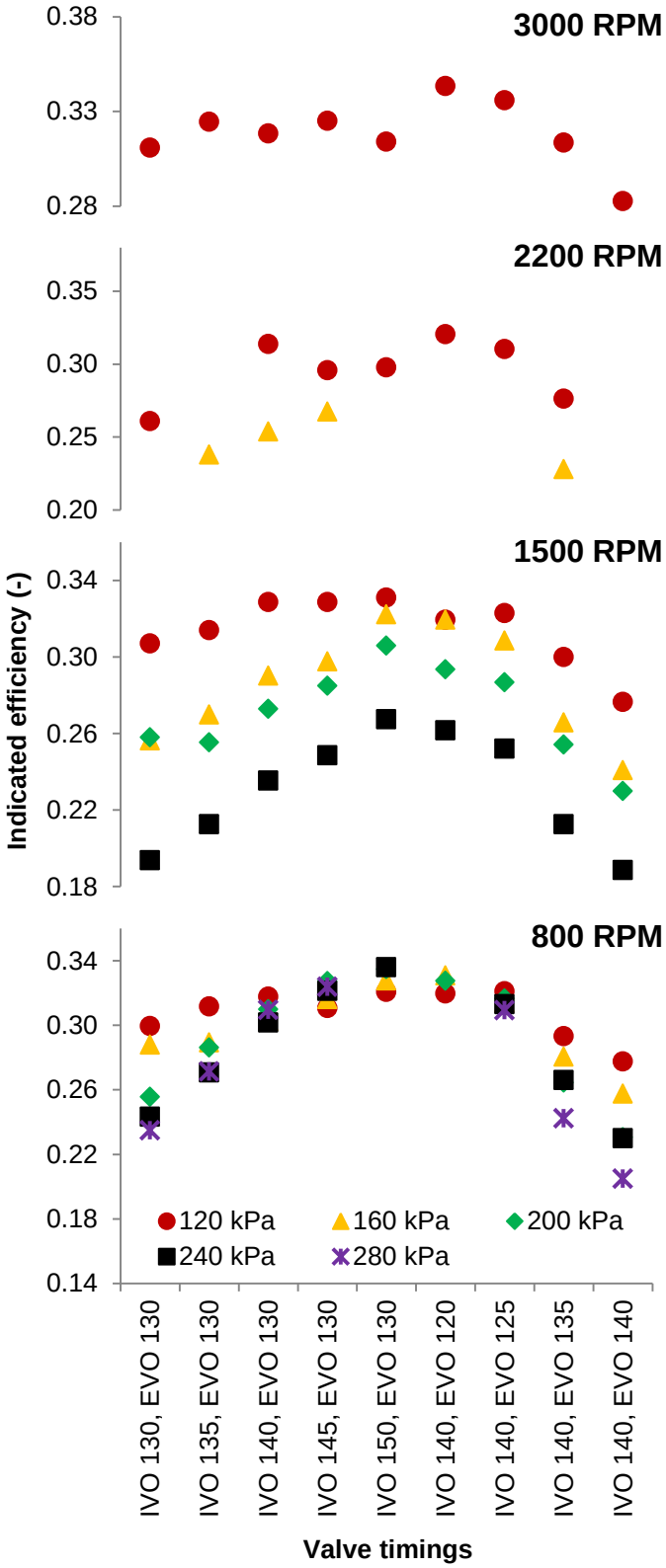

Figure 5.16 – Indicated efficiency at different engine speeds, intake pressures and valve timings.

As shown by the in-cylinder lambda values in Figure 5.18, the change in combustion efficiency with valve timings could be attributed to the variation of in-cylinder air/fuel mixture. The higher the relative air/fuel ratio (lambda) the more

complete the combustion became. The leanest mixture of near stoichiometric air/fuel ratio was reached at 800 rpm and resulted in a combustion efficiency of about 0.94. As the engine speed increased from 800 rpm to 2200 rpm, the decreased charging efficiencies led to richer air/fuel mixtures and lower combustion efficiencies. At the lowest boost pressure of 120 kPa the combustion efficiency became higher at 3000 rpm than 2200 rpm, which was attributed to the leaner mixture and faster heat release rate promoted by CAI combustion (Figure 5.11). The extremely low values of combustion efficiency at both ends of the valve timings studied were then justified by low in-cylinder lambda values. These results could have been massively improved by changing the fuelling rate, although the solely effect of valve timings alteration would have been hindered.

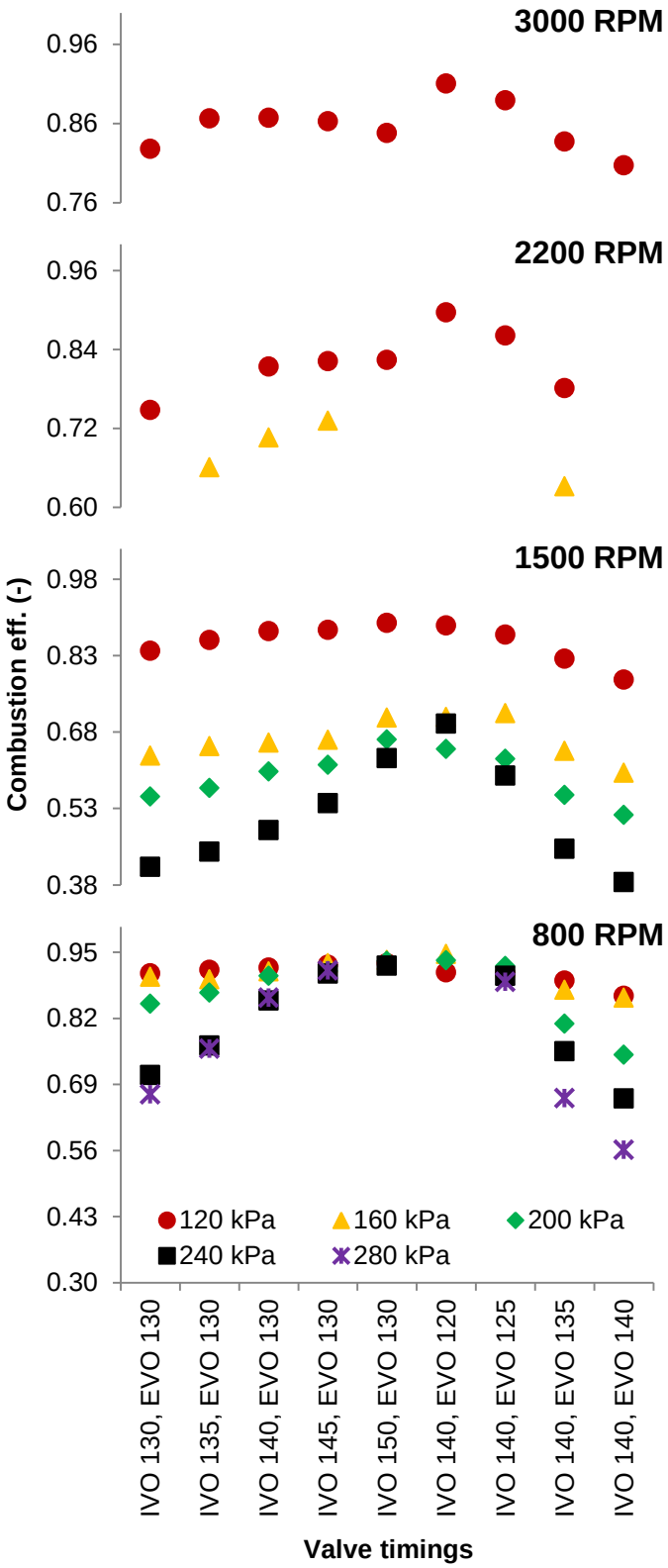

Figure 5.17 – Combustion efficiency at different engine speeds, intake pressures and valve timings.

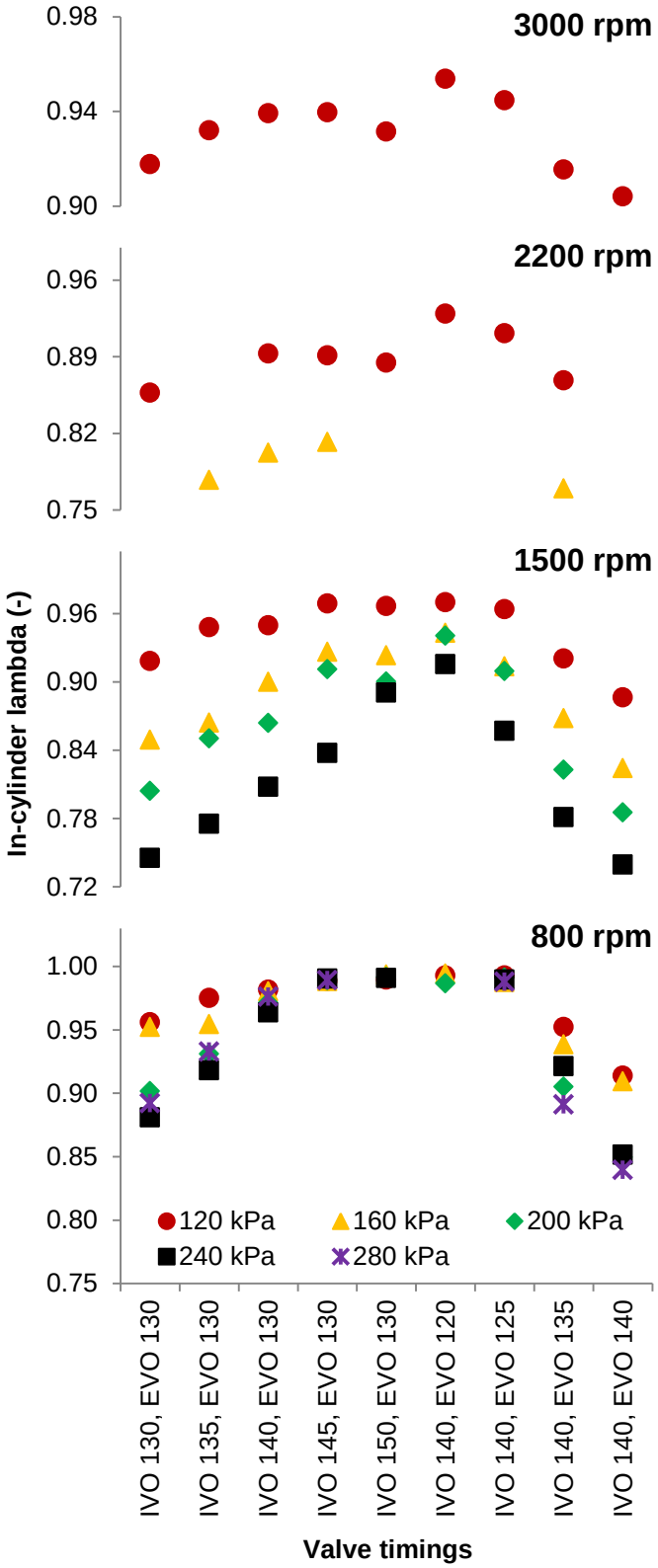

Figure 5.18 – In-cylinder lambda at different engine speeds, intake pressures and valve timings.

5.3.3 Emission analysis

As shown in Figure 5.19, CO emissions increased significantly as the mixture became richer with more advanced IVO or retarded EVO at each engine speed. Negligible CO was produced at 800 rpm when the charging efficiency and lambda were maximised. Based on the estimated in-cylinder lambda results in Figure 5.18, noticeable CO emissions were predictable by the combustion of an overall fuel rich mixture. However, the lower than expected CO level could be caused by the oxidation of CO into CO_2 by the fresh air mixed with the burnt gases during the scavenging process. As the engine speed increased, the poorer charging efficiency and combustion of richer mixtures resulted in the significant rise of CO and UHC emissions (Figure 5.20). Furthermore, the mixture was less homogeneous at higher engine speed because of the reduced time available between the end of injection and the beginning of combustion. This could have explained the very rapid rise in CO emissions when the engine speed was changed from 800 rpm to 1500 rpm. At 2200 rpm and 3000 rpm the relatively high values of CO were expected from the low temperature CAI combustion as reported in the literature [13].

The indicated specific UHC emissions (Figure 5.20) showed less dependency on valve timings (particularly at lower intake pressures) and lower correlation with the in-cylinder lambda. The UHC production was found not only dependent on the overall air/fuel ratio but also on the charge homogeneity. Compared to homogeneously charged four-stroke engines, the higher UHC emissions was likely resulted from fuel impingement as well as fuel rich combustion under late fuel injections. As the SOI took place after 260° CA ATDC, there was limited time available for a homogeneous mixture to form and very rich mixtures could be present in some regions increasing UHC emission. In addition, at higher loads the end of injection could be as late as 290° CA ATDC, when the piston was only at about 25 mm from the cylinder head. Hence, the fan shaped spray impinged onto the piston and formed pool fires on its top. For the same reasons, high soot emissions were observed as seen in Figure 5.21. Compared to UHC emissions, the soot production was noticeably more affected by the engine load and speed than by the valve timings, as the fuel impingement increased with longer injection durations.

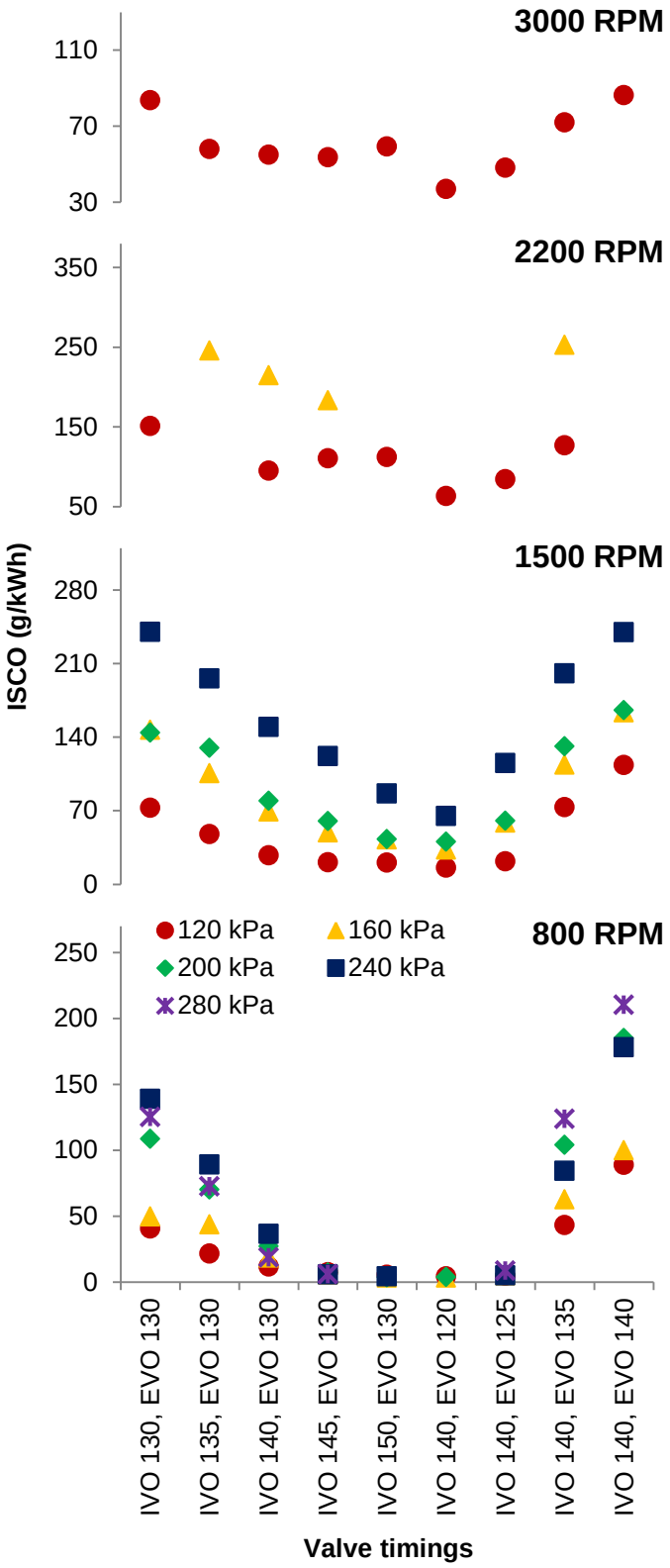

Figure 5.19 – ISCO emissions at different engine speeds, intake pressures and valve timings.

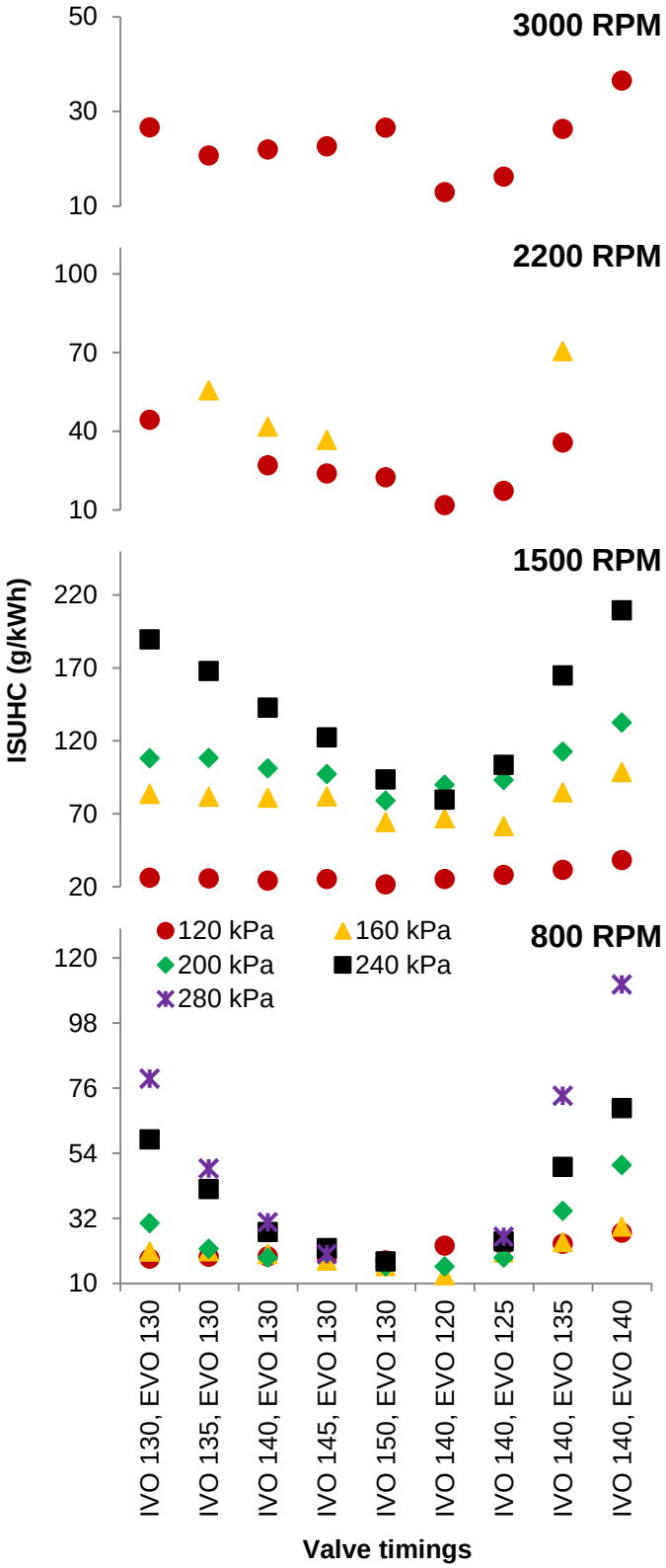

Figure 5.20 – ISUHC emissions at different engine speeds, intake pressures and valve timings.

From the results presented in Figure 5.21 it was clear that, when there was time available for the air-fuel mixing process to take place, like at 800 rpm, the levels of soot were kept relatively low even at higher loads. For the sake of comparison,

at 3000 rpm and 0.23 MPa IMEP the level of ISsoot was nearly the same of that found at 800 rpm and 1.01 MPa IMEP. The same trend was found for UHC emissions, bearing in mind that the fuelling rate increased more than four times amongst these two conditions. Additionally, at the lowest boost pressure of 120 kPa both CO and UHC emissions and smoke levels were lower at 3000 rpm than at 2200 rpm. This was attributed to the leaner mixture and faster heat release rate of CAI combustion as shown in Figure 5.11.

From Figure 5.22 it is noted that NOx emissions were more sensitive to the valve timings studied than to the load itself, especially at 800 rpm. At this speed NOx emissions increased by 20% as the boost pressure was changed from 120 to 280 kPa (0.66 to 1.22 MPa IMEP). In comparison, by retarding IVO in 10° CA from 130° to 140° CA ATDC the NOx emissions nearly doubled. The spark timing also played an important role in NOx emission as shown by the point “IVO 140, EVO 120” at 200 kPa boost. The ignition timing in this case was retarded to avoid knocking combustion (Figure 5.14), which reduced the in-cylinder peak temperature and hence NOx formation.

Moving along the x-axis from the middle to the both sides of Figure 5.22, more residual gas was trapped as a result of lower charging efficiencies. Because of the increased heat capacity of CO_2 and reduced oxygen availability by the presence of EGR, NOx formation was significantly mitigated. At 800 rpm the earlier EVO raised the charge oxygen content and increased NOx emissions to levels of downsized four-stroke engines operating at similar conditions [9]. As the speed increased, the combustion mode progressed from SI towards CAI as a result of higher levels of hot residual gas trapped (Figure 5.12). Consequently, NOx emissions progressively decreased thanks to the higher charge dilution and lower combustion temperature.

At high engine speeds and at the lowest intake pressure, pure CAI combustion took place independently of the valve timing used. At 2200 rpm NOx emissions rose rapidly as the boost pressure was increased from 120 kPa to 160 kPa. This resulted from both lower residual gas concentration and the presence of high temperature flame propagation in the spark-assisted CAI combustion.

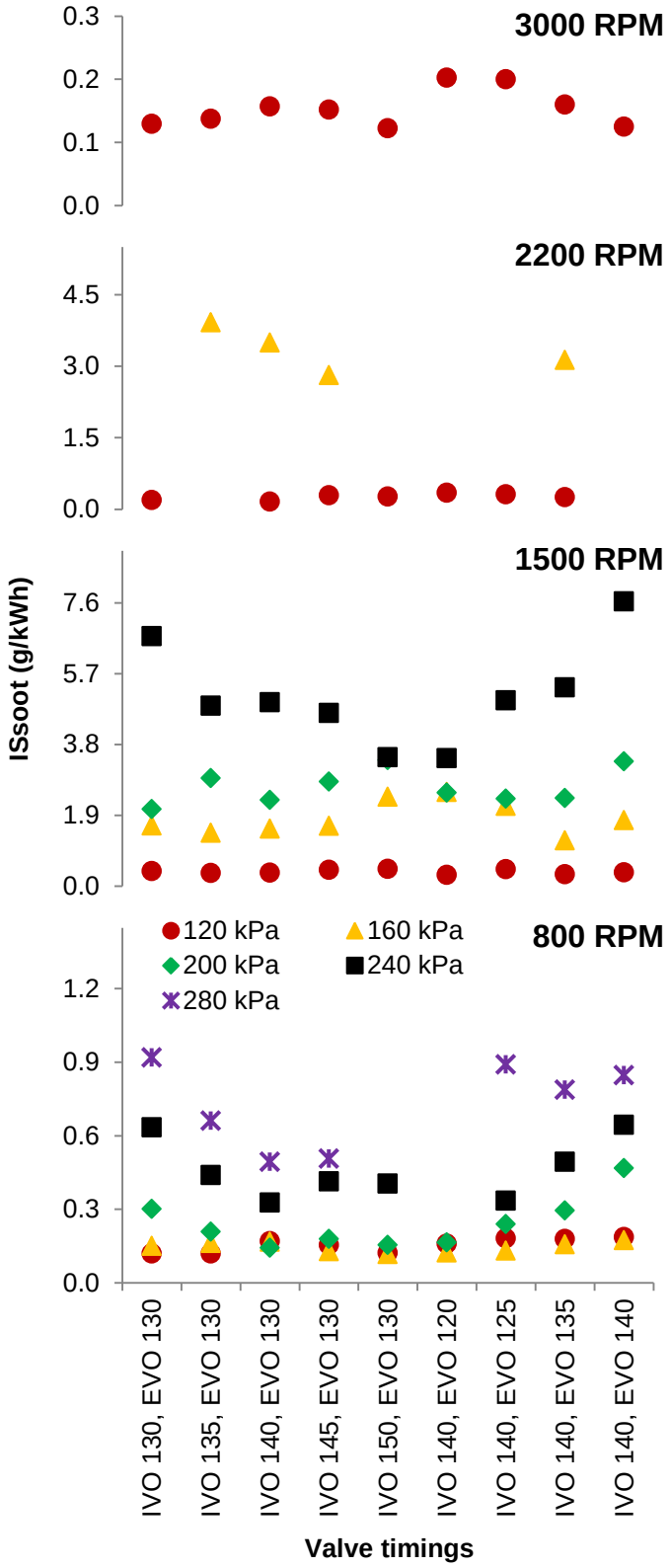

Figure 5.21 – ISsoot emissions at different engine speeds, intake pressures and valve timings.

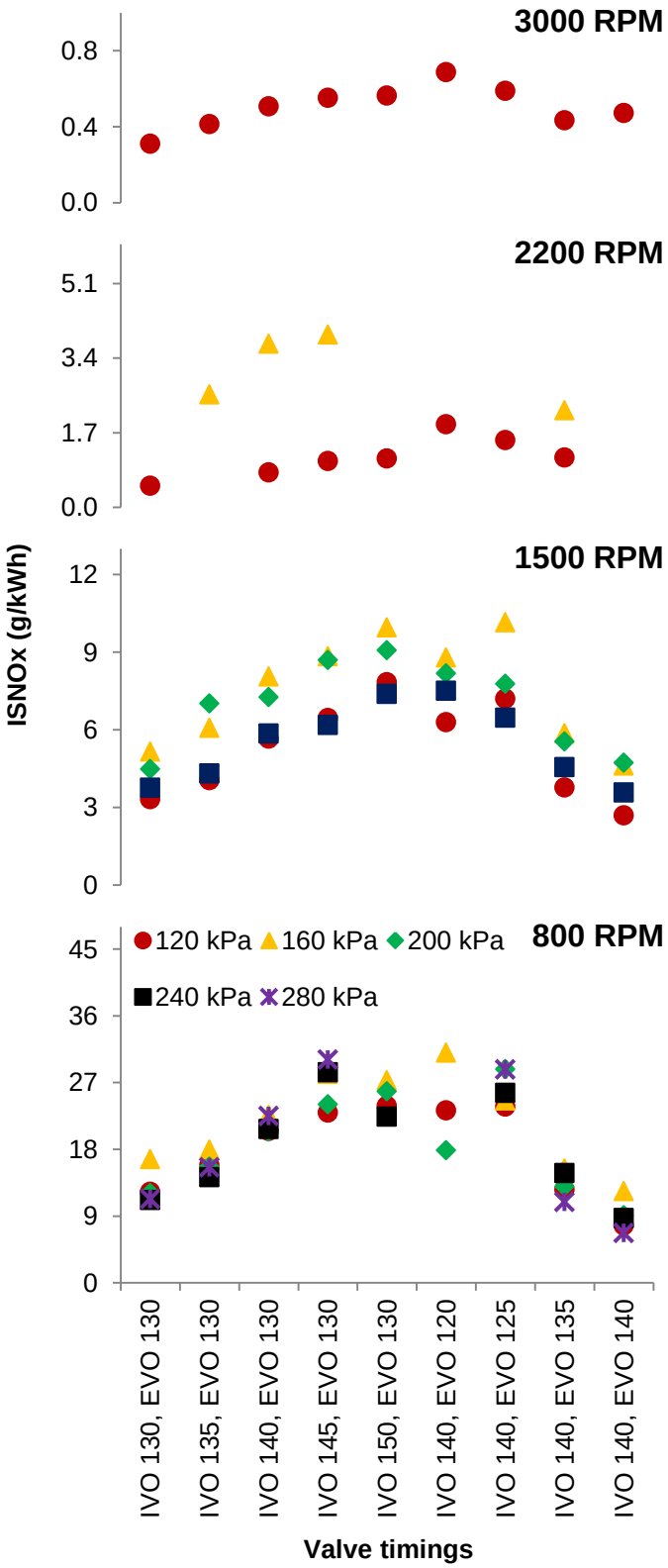

Figure 5.22 – ISNOx emissions at different engine speeds, intake pressures and valve timings.

5.4 Summary

A preliminary study in the performance of the two-stroke poppet valve engine was carried out at several engine speeds and loads. At each engine speed and intake pressure a number of intake and exhaust valve timings were tested.

The maximum IMEP was obtained with the highest charging efficiency at each engine speed. For instance, at 800 rpm the peak IMEP of 1.2 MPa was achieved at a charging efficiency of 0.95. At any given valve timing the charging efficiency dropped as the engine speed increased due to the reduced time available for the gas exchange. The large amounts of hot internal EGR at higher speeds induced abrupt heat release and limited the achievement of higher loads. Nevertheless, the trapping efficiency increased from about 0.35 to 0.70 at higher speeds.

The indicated efficiency was primarily determined by the combustion efficiency, which was related to the in-cylinder air/fuel ratio. This relative air/fuel ratio was improved by the optimisation of valve timings for maximum charging efficiency. As the engine speed increased, the combustion mode evolved from SI to SACI and finally CAI, as a result of increasing hotter residual gas trapped.

The CO emissions were directly affected by the in-cylinder lambda, whilst UHC and soot emissions were found to be more affected by the fuel impingement and local over-rich fuel regions. NOx emissions were found very low at higher engine speeds when there was high residual gas concentration and CAI combustion.

The above results have demonstrated that the scavenging process and mixture preparation were the two most important issues affecting the two-stroke poppet valve engine performance. The scavenging process could be further optimised by different valve opening durations and higher valve lifts. To improve the air-fuel mixing process it is necessary to employ a more robust stratified charge combustion system. Moreover, lower alcohol fuels could be an option to increase the oxygen content of the charge and improve knocking resistance at high loads.

Chapter Six

Investigation of the gas exchange process in the two-stroke poppet valve engine

6.1 Introduction

From the preliminary study presented in chapter five it became clear that one of the weaknesses faced by the two-stroke poppet valve engine was the gas exchange process. Therefore, in the present chapter the scavenging process was improved particularly at high engine speeds and loads. Whilst the charging efficiency was enhanced, precaution was taken to keep acceptable levels of trapping efficiency. The air trapping performance was also evaluated by means of supercharger power consumption. Intake and exhaust valve durations were independently varied until the maximum output power could be reached simultaneously at low and high engine speeds. Besides, the effect of the masked cylinder head was evaluated at two different valve lifts, so that the trade-off between air trapping efficiency and charging efficiency could be estimated. Similarly, an exhaust backpressure sweep was carried out to evaluate its effect on the engine performance and gas exchange process. In the end, the best combination of valve timing, duration and lift was tested at different engine speeds and loads, so that it could be correlated to a theoretical scavenging model. All the experimental procedures are firstly described in section 6.2.

6.2 Test procedures

In chapter five several engine speeds and loads were evaluated at the valve timings proposed, though not many different valve configurations were tested. It was shown that changes in valve timings had a similar effect on the engine load regardless of the engine speed, which was evidenced by the concave shape of all curves presented throughout the chapter. However, the effect of different engine speeds was not constant comparing to each other and hence it deserved more investigation. Therefore, further tests were carried out focusing on the high load range given by a single intake pressure of 135±4 kPa and two limiting engine speeds i.e. 800 rpm and 2000 rpm. In total, 25 different intake/exhaust

valve durations and 12 different intake/exhaust valve lifts were assessed besides an exhaust backpressure analysis. Gasoline was used in all tests and supplied by the standard double slit fuel injection system. To ensure the minimum amount of oxygen resulted from the combustion, and hence avoiding the under prediction of air trapping efficiency, the in-cylinder lambda was kept between 0.92 and 0.95 at all experiments. Thus, any free oxygen in the exhaust was expected to be resulted from scavenging inefficiencies.

6.2.1 Valve opening duration tests

Based on the preliminary studies presented in chapter five it was found that the intake valve operation should be centred around 185° CA after top dead centre (ATDC). Equally, the exhaust valve timing was optimised when centred at about 175° CA ATDC, so that improved fuel consumption, output power and gaseous emissions could be achieved from 800 rpm to 3000 rpm. Given these conditions, the intake and exhaust valve operations were centred at such points and their opening duration were varied from 50° CA to 150° CA (intake) and from 70° CA to 170° CA (exhaust) independently. An increment of 20° CA was used between each testing point as shown in Figure 6.1 and Figure 6.2 for the intake and exhaust valves, respectively. Whilst the exhaust valve opening duration was fixed at a constant value, the intake valve timing was varied between the boundaries stated above. After this, the exhaust valve timing was varied 20° CA and another set of intake durations was evaluated. The procedure was repeated until the peak torque was achieved at 800 rpm and 2000 rpm at both intake and exhaust duration sweeps. The valve lifts were set to 8 mm in all cases. The nomenclature used consists of the intake and exhaust valve opening and closing times, in this sequence. For instance, in the case “In 130/240, Ex 120/230” the intake valves opened at 130° CA ATDC and closed at 240° CA ATDC, whilst the exhaust valves opened at 120° CA ATDC and closed at 230° CA ATDC.

To avoid the interference of the air-fuel mixing process on the results, the start of injection (SOI) was set to 260° CA ATDC thoroughly, which was the latest IVC/EVC timing studied. In this case no fuel short-circuiting, as well as its backflow to the intake port, were expected to happen. Knocking combustion limited the spark timing advance (KLS) in all cases at both engine speeds.

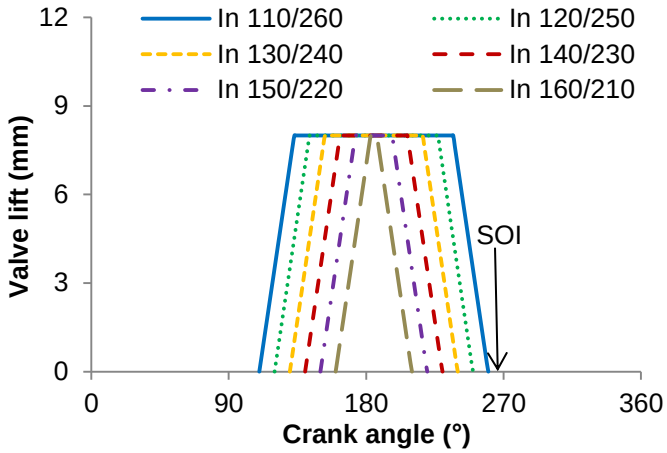

Figure 6.1 – Intake valve opening duration sweep.

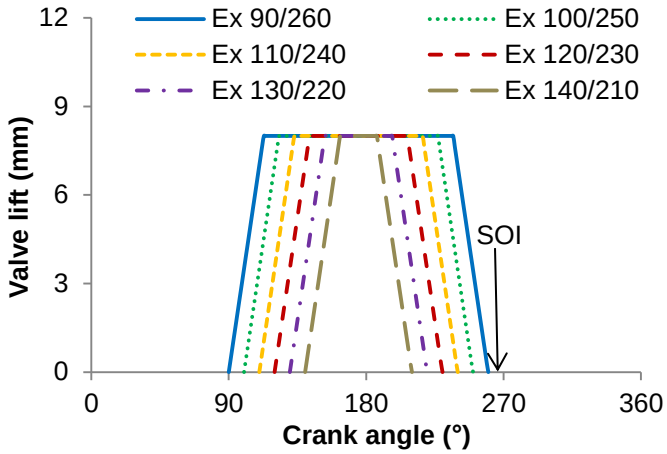

Figure 6.2 – Exhaust valve opening duration sweep.

6.2.2 Valve lift and exhaust backpressure tests

Two valve lifts of 3 mm and 8 mm were selected for further experiments at 800 rpm and 2000 rpm. The higher lift represented the maximum value achieved by the electrohydraulic valve train unit. It was also close to the dimensionless valve lift of 0.3 L/D (where “L” is the valve lift and “D” is the valve diameter), when the effective flow area reaches its maximum [8]. The 3 mm of valve lift equals to the cylinder head mask height around the intake valves as shown in Figure 4.1. In this case its influence on the gas exchange process and engine performance could be investigated. In the valve lift sweeps both intake and exhaust valves were evaluated independently at 3 mm and 8 mm of lift with the valve timing “In 130/240, Ex 120/230” (Figure 6.3). The nomenclature used in the plots indicate

firstly the intake valve lift (IVL) followed by the exhaust valve lift (EVL), with the related numbers indicating the valve lifts in millimetres.

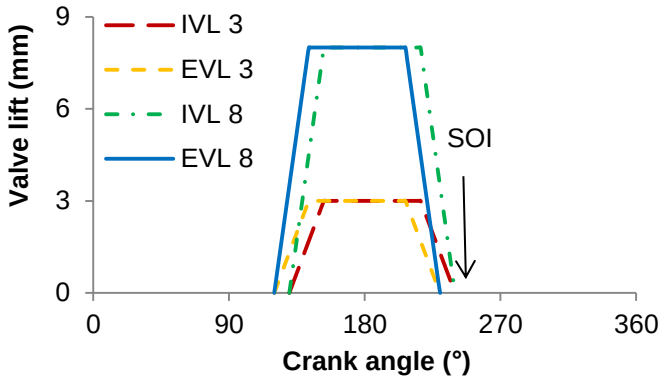

Figure 6.3 – Intake and exhaust valve lift sweeps.

For every valve lift studied, three exhaust backpressures (EBP) i.e. ~104 kPa, 110 kPa and 120 kPa were examined. The lowest exhaust backpressure tested was that of typical silencer and pipes, which remained between 103 kPa and 104 kPa depending on the valve lift used. There was also a slightly increase in the EBP when the speed raised from 800 rpm to 2000 rpm, though such difference was small compared to the effect of valve lift and it was hence omitted from the nomenclature. The pressure unit (kPa) was neglected in the plots and the abbreviation “BP” refers to backpressure. For instance, the case “IVL 3, EVL 8, BP 110” used 3 mm and 8 mm of lift in the intake and exhaust valves, respectively, with an exhaust backpressure of 110 kPa. The SOI was advanced towards IVC (240° CA ATDC) to increase the mixture homogeneity. In all cases the spark timing advance was limited by knocking combustion (KLS).

6.2.3 Procedures for estimating the in-cylinder lambda at lean conditions

In order to analyse the gas exchange process and correlate it to a theoretical scavenging model, the air trapping efficiency (TE_{air}) was acquired as a function of the scavenge ratio (SR). Such TE_{air} x SR curve depends on the cylinder head details (valves size, masked zone, port configuration) and valve operating parameters. If these parameters are kept unchanged, all the engine operation points are to be found along this curve regardless the engine load or speed tested. This trend line was obtained by means of 71 different engine operating conditions under fuel rich mixtures. The engine speed was varied from 800 rpm

to 2400 rpm and the intake pressure ranged from 104 kPa to 213 kPa. Therefore, with this TE_{air}x SR curve the in-cylinder lambda could be estimated even under fuel lean mixtures based on the values of scavenge ratio (Equation (3.42)), fuel trapping efficiency (Equation (3.45)) and exhaust lambda. The air trapping efficiency and scavenge ratio were obtained at the constant valve timing of IVO 130°, IVC 240°, EVO 120° and EVC 230° CA ATDC. The lift of 8 mm was used thoroughly for all valves. The SOI was advanced towards IVC at 240° CA ATDC to increase the mixture homogeneity. The spark timing was set for MBT or KLS based on the PRR threshold defined in section 3.3.1.

6.3 Results and discussion

The following results were averaged over 200 consecutive cycles and plotted as a function of valve duration, lift and exhaust backpressure (EBP) at 800 rpm and 2000 rpm. In the valve opening duration plots (Figure 6.4 to Figure 6.11) the dashed lines represent the trend of the exhaust valve sweep. Each of the six plots in the figures represents an individual intake valve sweep at constant exhaust valve duration (Intake S1, S2…). The exhaust valve opening duration increases from the left to the right in each figure, whilst the intake opening duration increases from the left to the right in each plot. In the valve lift and EBP results (Figure 6.12 to Figure 6.18), the dashed lines represent the exhaust backpressure sweeps increasing from the left to the right. Each of the three plots denotes the intake and exhaust valve lift sweeps at a constant EBP.

6.3.1 Effects of valve opening duration

For all the 25 valve opening durations tested, the indicated specific torque was found in the range from 76 Nm/dm^3 to 185 Nm/dm^3 as shown in Figure 6.4. In values of indicated mean effective pressure (IMEP) the load spanned from 0.48 MPa to 1.16 MPa at a constant intake pressure of 135±4 kPa. This means that a four-stroke engine of the same swept volume would need to operate from 0.96 MPa to 2.32 MPa to deliver the same torque at the same speed. Combining Equations (3.10) and (3.11) the indicated specific torque is better presented by:

$$T_{is} = \eta_i m_{air} \left(\frac{LHV}{2\pi V_d AFR} \right) \tag{6.1}$$

Whilst the intake air mass (m_{air}) corresponds to the charging efficiency defined in Equation (3.43), the indicated efficiency (η_i) is mostly a function of the combustion efficiency, combustion duration and phasing, effective expansion ratio (EER) and effective compression ratio (ECR). From the variables influencing the indicated efficiency, the ones which presented significant variation during the experiments were the ECR and EER seen in Figure 6.5.

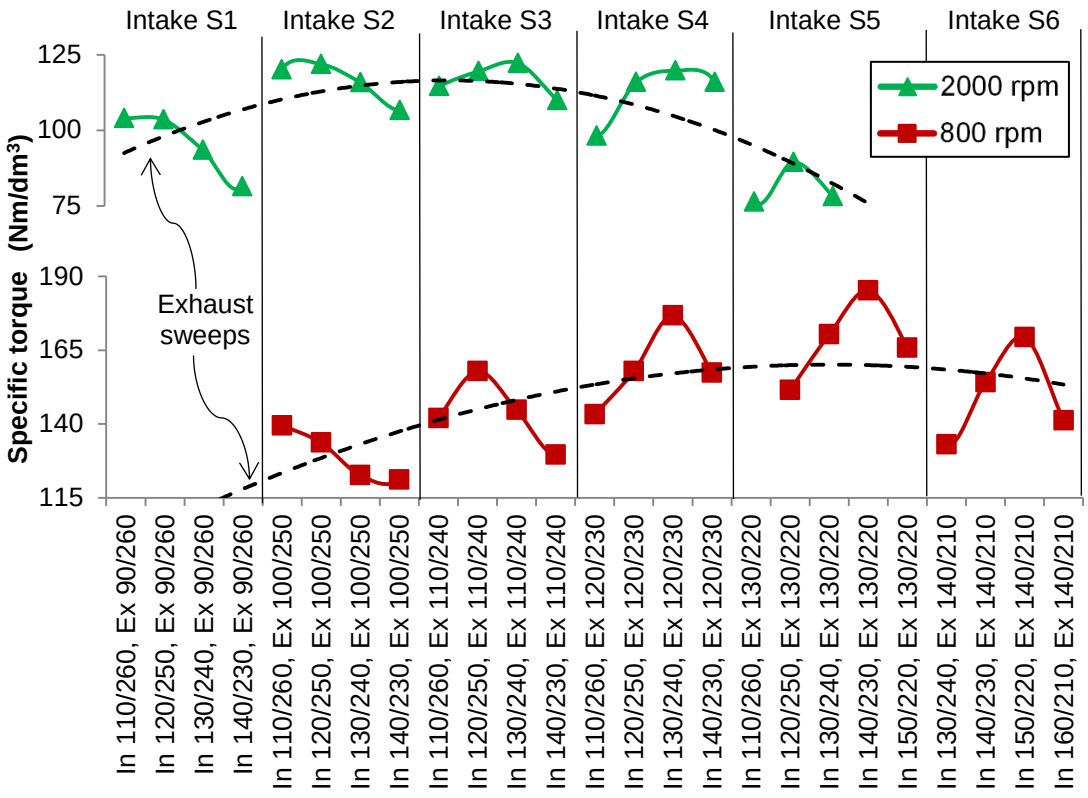

Figure 6.4 – Indicated specific torque results for the valve duration sweep.

At 800 rpm the specific torque increased at shorter exhaust valve opening durations as seen from the left to the right side along the X-axis in Figure 6.4. This was a result of the increasing ECR at more advanced EVC, although at extremely short exhaust durations the ECR effect was offset by the shorter time available for scavenging. This inflexion point was found around 90° CA of exhaust valve duration (In 140/230, Ex 130/220"). Therefore, other than this operating point, the engine torque deteriorated with either longer or shorter exhaust valve opening durations. In contrast, at 2000 rpm longer exhaust durations were made necessary to allow an effective scavenging process as the time available to do so was reduced. Besides the greater frictional flow losses at

2000 rpm, the scavenging process also suffered from the smaller effective flow area resulted from the actuation speed of the electrohydraulic valve train (Figure 5.8). Excessively long exhaust valve durations also decreased the specific torque as seen in the intake valve sweep number one (S1, first plot in Figure 6.4). The lower ECR (Figure 6.5) in this case reduced the specific torque, although it could be partially improved by higher charging efficiencies (Figure 6.6) at longer intake durations as in the case “In 110/260, Ex 90/260”.

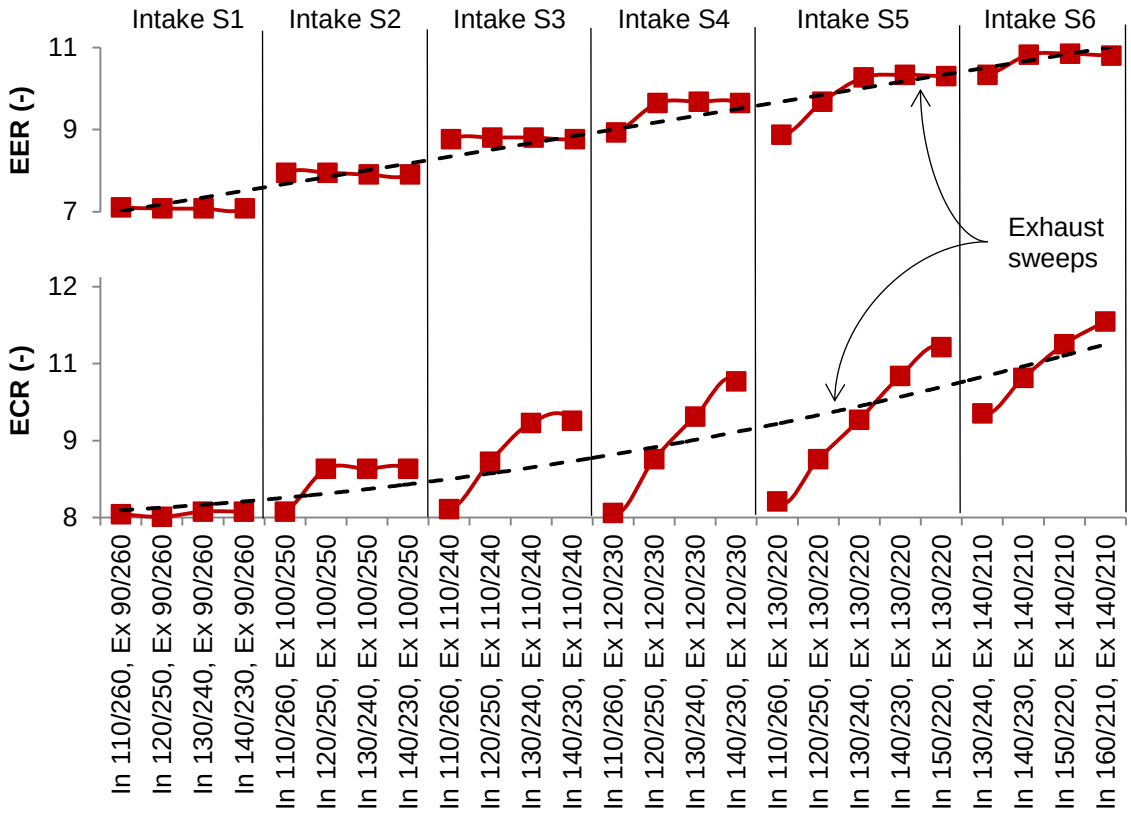

Figure 6.5 – Effective compression and expansion ratio results for the valve duration sweep.

An interesting observation drawn from the intake valve sweep two (S2) in Figure 6.4 was the specific torque behaviour at the first two valve timings i.e. “In 110/260, Ex 10/250” and “In 120/250, Ex 100/250”. At 800 rpm the highest load was achieved by closing the intake valve 10° CA after the exhaust, whilst at 2000 rpm this configuration produced poorer torque. It suggests that at higher speeds the scavenging process benefited from later EVC as observed in high speed ported two-stroke engines, where the exhaust port closes about 10° CA after the transfer ports. On the other hand, at lower engine speeds there was more time

available for scavenging and hence it was better to delay IVC to after EVC. This procedure avoided the fresh charge from exiting the cylinder through the exhaust valves. In conventional two-stroke engines, where the symmetric port arrangement makes it prohibitive to close the intake port(s) after the exhaust port(s), some of the fresh charge leaves the cylinder during the scavenging process. This shortcoming is often improved by exhaust timing valves or, at higher engine speeds, by wave propagation in tuned exhaust pipes [28].

As the exhaust valve opening was retarded towards bottom dead centre (BDC), the effective expansion ratio (EER) increased and a higher indicated efficiency was expected. However, as the in-cylinder pressure decreased close to BDC, the pressure ratio across the exhaust valves also dropped at EVO and the overall scavenging process was hindered by the weak exhaust blowdown. The highest specific torque of 185 Nm/dm^3 was achieved at 800 rpm with the valve timing “In 140/230, Ex 130/220”. At 2000 rpm the maximum torque of 122 Nm/dm^3 was reached with “In 130/240, Ex 110/240”. At lower speeds the longer time available for the gas exchange enabled earlier EVC and hence higher ECR, such as the peak torque case mentioned above where it reached 10.3:1. Meanwhile, at 2000 rpm the time available for the gas exchange deteriorated and EVC took place later in the cycle, which reduced the ECR to about 8.8:1. This reduction in ECR is not desirable and the higher the speed the poppet valve engine is to achieve, the lower it will be due to the increased valve opening duration required. For the sake of comparison, high speed ported two-stroke engines operate with a constant ECR of about 6-7:1 [23].

The specific torque (Figure 6.4) and charging efficiency (Figure 6.6) results suggested that the shorter the exhaust duration, the shorter should be the intake duration as well. This effect was observed by the moving “peak” in the curves at both engine speeds tested, although at 800 rpm it was more pronounced. At 800 rpm and in the second intake valve sweep, the peak torque was near the first point investigated of “In 110/260, Ex 100/250”. As the exhaust valve duration decreased, the peak torque moved towards shorter intake durations as seen in the third intake valve sweep in the case “In 120/250, Ex 110/240”. Between these two cases the exhaust duration was shortened by 20° CA, whilst the intake

duration was reduced by the same amount to produce the maximum torque. The trend was repeated for the other valve sweeps investigated and the common characteristic amongst all the peak torque points was that EVO took place 10° CA before IVO, which ensured an effective exhaust blowdown phase. When the intake valve was opened before this 10° CA limit, intake backflow occurred and the charge purity decreased. Conversely, when IVO took place long after EVO, the exhaust blowdown weakened and the pressure ratio across the exhaust valves dropped excessively until the scavenging process could start.

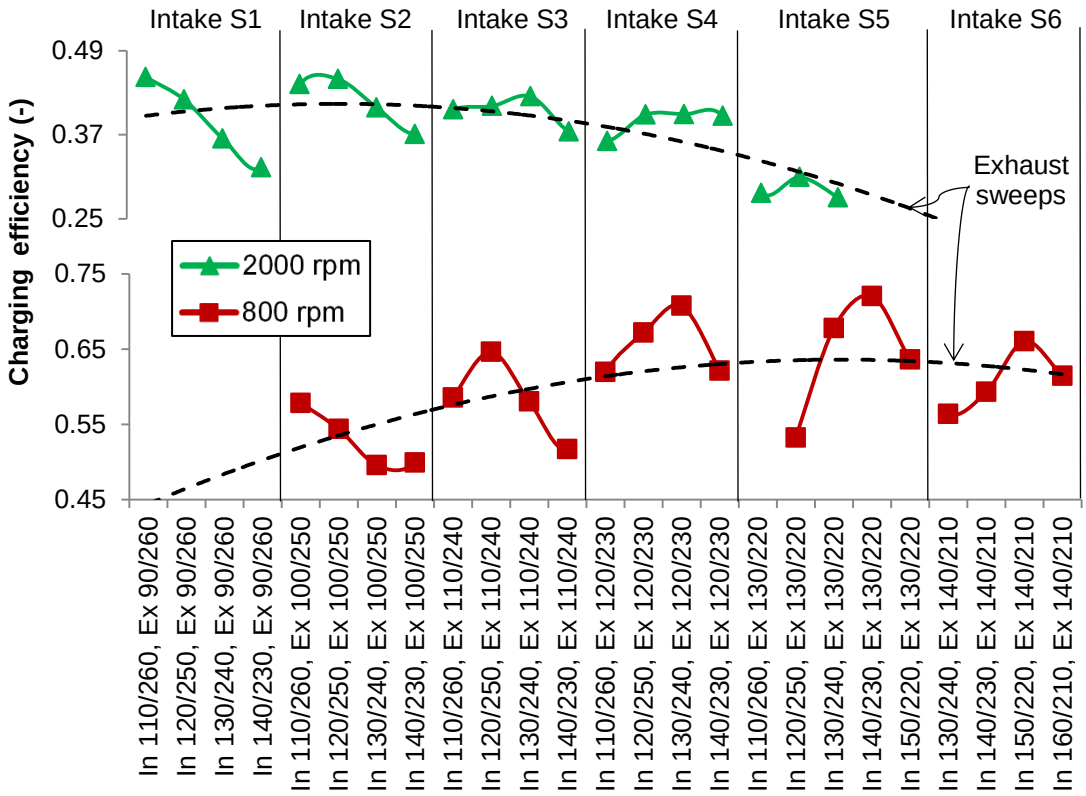

Figure 6.6 – Charging efficiency results for the valve duration sweep.

Another common feature amongst the highest torque points was that IVC took place 10° CA after EVC. This increased the charging efficiency (Figure 6.6) by providing a “supercharging” effect at the onset of compression [23]. This retarded IVC is an important advantage of two-stroke poppet valve engines compared to ported two-stroke engines. In those engines the symmetric arrangement of the ports obligates the exhaust to open before the intake and close after it. When IVC took place long after EVC, then backflow occurred as the in-cylinder pressure became higher than the intake pressure at IVC. The case “In 110/260,

Ex 110/240” was such an example where the backflow reduced the changing efficiency and consequently the output torque.

From Figure 6.4 and Figure 6.6 it is evident the strong correlation between charging efficiency and output torque as also reported in the literature [27][31]. An interesting event seen in Figure 6.6 was the reduction in charging efficiency when intake and exhaust valves opened at the same time as in the cases “In 120/250, Ex 120/230” and “In 130/240, Ex 130/220”. Both cases preceded the highest charging efficiencies points at 800 rpm, although the reduction in torque by opening all the valves at the same time was around 10%. In these cases not only the effectiveness of the blowdown was reduced but a higher in-cylinder pressure at IVO also hindered the initial phase of the scavenging process. At 2000 rpm the difference in torque (or charging efficiency) between opening intake and exhaust valves at the same time decreased to about 4% compared to the highest torque case. This behaviour suggested that the exhaust blowdown phase was not very critical in the scavenging process at such high load under high values of scavenge ratio as observed in Figure 6.7. Furthermore, the first portion of air entering the cylinder is usually mixed with burnt gases and expelled in the exhaust [23]. Thus, the air contamination in the intake ports at IVO had little effect on the purity of the trapped charge, as the cylinder was actually filled with a later portion of the inducted air at the onset of compression.

The results presented in Figure 6.6 revealed that improved valve durations and higher valve lifts could enhance the charging efficiency up to 0.72 at 800 rpm and 0.45 at 2000 rpm. Compared to the initial results presented in chapter five, the same values of charging efficiency were here obtained with 48% lower intake pressure (from 200 kPa to 135 kPa). Nevertheless, there was still a sharp drop in the scavenging process as the engine speed increased from 800 rpm to 2000 rpm. This resulted from the shorter time available for the gas exchange and greater frictional flow losses. From the exhaust sweep at 2000 rpm presented in Figure 6.6 it was clear that even with an intake and exhaust durations as long as 150° CA and 170° CA, respectively, the charging efficiency could not increase above 0.45. The same impossibility of improving the scavenging process was found at 800 rpm as the intake and exhaust valve durations increased beyond

110° CA. At both speeds there was plenty of air supply as seen by the high scavenge ratio values in Figure 6.7. For the sake of comparison, at 800 rpm the scavenge ratio reached a maximum of 3.71, whilst in ported two-stroke engines this value rarely overtakes 1.5 at full load [28]. Under these circumstances the excess of air supplied was not efficiently scavenging the burnt gases. Instead, it was actually being lost to the exhaust system. This fact was confirmed by the low values of air trapping efficiency found for these valve opening durations in Figure 6.8, especially at 800 rpm. It is important to clarify that not all of the air present in the exhaust, assessed via trapping efficiency calculation at fuel-rich in-cylinder conditions, resulted from air short-circuiting. Part of the intake charge mixed with the burnt gases during the mixing-scavenging process, so it was not possible to distinguish the portions of short-circuited air from those mixed during the scavenging. The mixing-scavenging is still a form of scavenging, though it is not as efficient as perfect displacement. It is still better than pure short-circuiting, when the burnt gases are definitely not expelled from the combustion chamber.

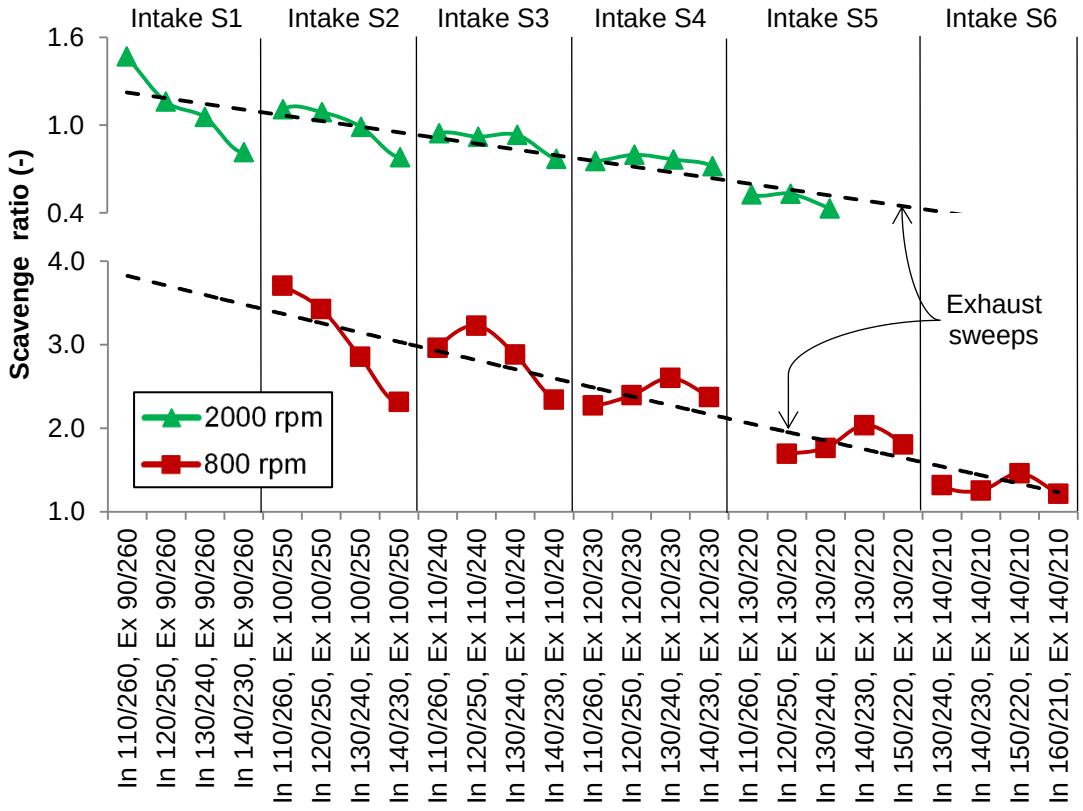

Figure 6.7 – Scavenge ratio results for the valve duration sweep.

The scavenge ratio increased linearly with the valve opening durations and showed its highest values when IVO took place 10° after EVO, so the exhaust blowdown phase could efficiently reduce the in-cylinder pressure at IVO. At 2000 rpm the engine operation was not possible at intake and exhaust valve opening durations below 110° CA and 90° CA, respectively. This was a consequence of scavenge ratios as low as 0.43 and air trapping efficiencies of up to 0.65. Under idealised flow conditions discussed in section 3.3.4, this caused the internal EGR to reach up to 0.71. The presence of large amounts of hot residual gas trapped elevated the in-cylinder charge temperature and resulted in abrupt combustion, with a PRR above 5 MPa/°CA.

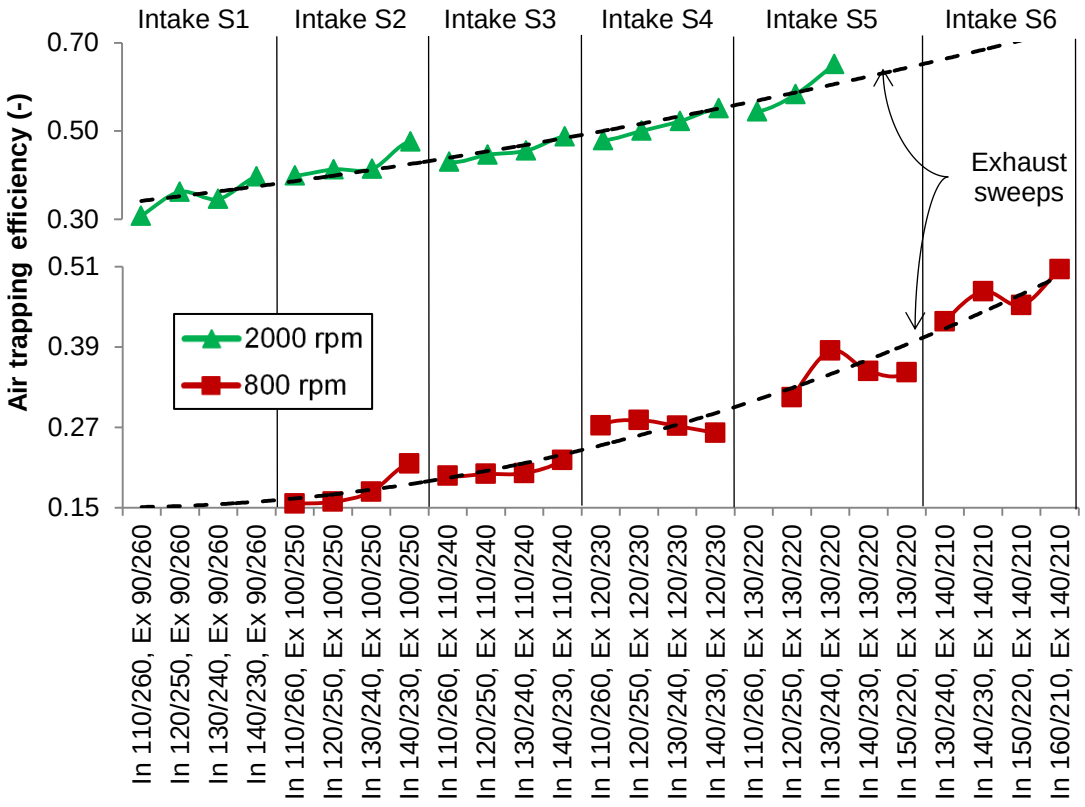

Figure 6.8 – Air trapping efficiency results for the valve duration sweep.

Figure 6.8 shows the clear correlation between the air trapping efficiency and the exhaust valve sweeps at both engine speeds, though at 2000 rpm it was more evident. Comparatively, the intake valve duration sweeps had a less pronounced effect on the trapped air mass. An initial thought about the trend in air trapping efficiency was based on the valve overlap period seen in Figure 6.9. It seemed obvious to link the probability of air short-circuiting to the length of time both

intake and exhaust valves were opened simultaneously. A similar explanation for the trapping efficiency in two-stroke poppet valve engines was also mentioned by [169]. However, by analysing the valve overlap period it became evident that the air trapping efficiency correlated better to the exhaust valve opening duration than to the valve overlap itself. For instance, in the third intake valve sweep (S3) the valve overlap reduced from 130° CA to 90° CA, although the air trapping efficiency presented lower increments around 10% at both speeds.

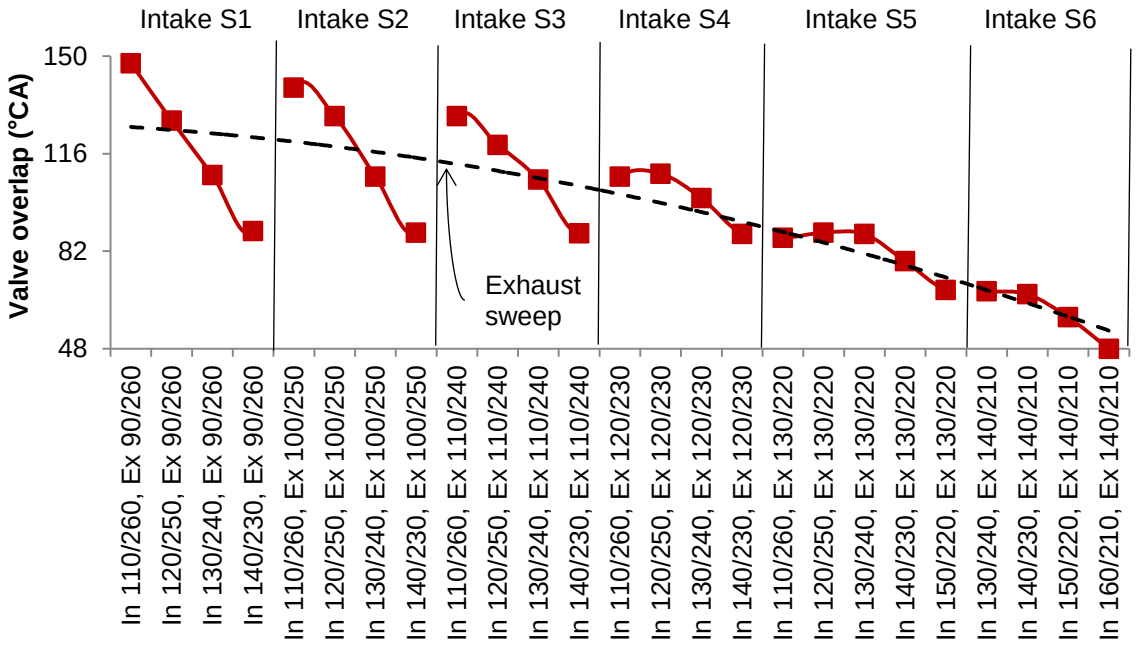

Figure 6.9 – Intake and exhaust valve overlap results for the valve duration sweep.

Whilst the engine load was directly linked to the charging efficiency, high values of air trapping efficiency were also desirable to ensure that the fresh charge was not lost in the exhaust. As seen in Equation (3.43), the charging efficiency is the product of air trapping efficiency and scavenge ratio. Thus, a higher output torque could not be achieved by only increasing the scavenge ratio at low values of trapped air mass. This was the case of very long exhaust valve durations, so the power consumed by the supercharger was considerably large as shown by its ratio to the indicated power in Figure 6.10.

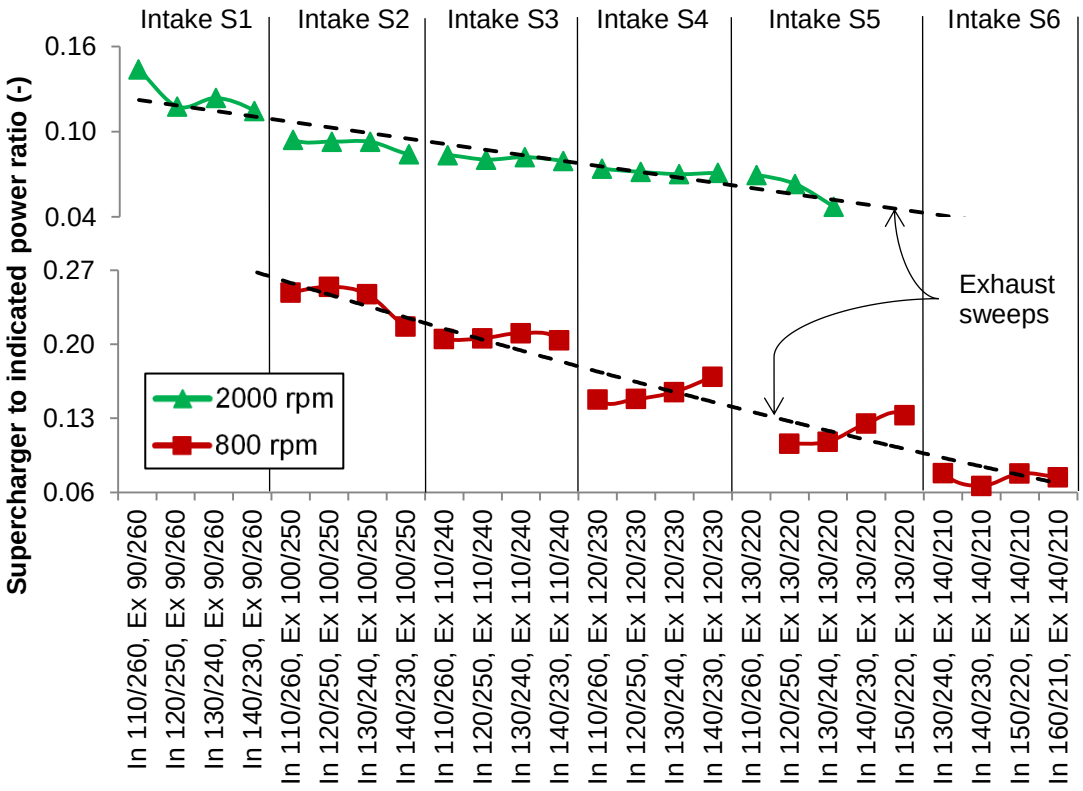

Figure 6.10 – Ratio of supercharger power requirement to engine indicated power for the valve duration sweep.

As the exhaust valve opening duration increased, the air trapping efficiency dropped and a large fraction of the supplied air was lost in the exhaust. This waste of energy, particularly visible at 800 rpm when the scavenge ratio was also noticeable, explained the great values of supercharger power consumption in the first intake valve sweeps seen in Figure 6.10. At both engine speeds the trend for this power ratio was considerably similar to the exhaust sweeps, and the intake sweeps had again a less important role. Due to the lower scavenge ratio and higher indicated power at 2000 rpm, the fraction of power consumed by the supercharger remained between 5% and 14%. At 800 rpm the supercharger to indicated power ratio reached values as high as 25%. Figure 6.11 reveals the best intake and exhaust valve durations to produce the highest possible net power, which resulted from the subtraction of the supercharger power consumption from the indicated power.

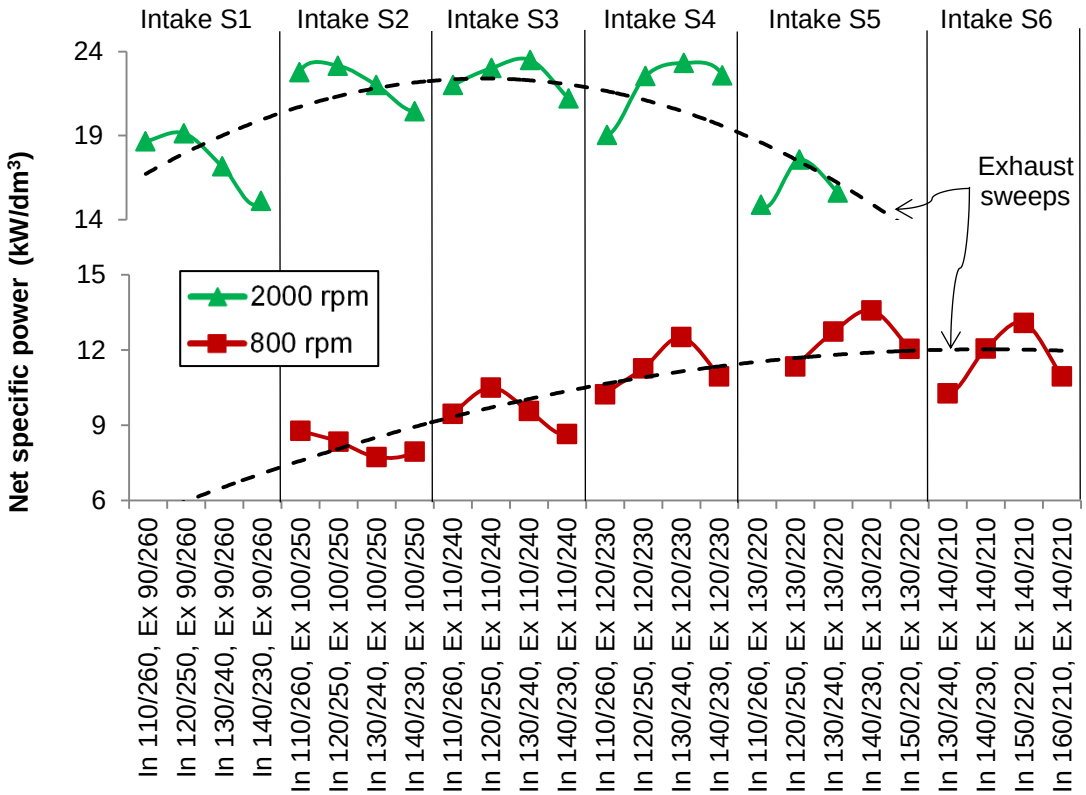

Figure 6.11 – Net indicated specific power considering the supercharger power consumption for the valve duration sweep.

At 800 rpm the valve timing “In 140/230, Ex 130/220” made it possible to achieve 13.6 kW/dm^3, whilst the cases “In 150/220, Ex 140/210” and “In 130/240, Ex 120/230” reached 4% and 8% less power, respectively. At 2000 rpm nearly the same net specific power was obtained at the three “peaks” in intake sweeps S2, S3 and S4. A value of 23.3 KW/dm^3 (±2%) was acquired at “In 120/250, Ex 100/250”, “In 130/240, Ex 110/240” and “In 130/240, Ex 120/230”. This result showed a certain flexibility of the engine for different valve configurations at higher speeds. At lower speeds the valve duration effect was more severe and even different intake opening durations at constant exhaust valve durations (S1, S2, S3…) resulted in expressive drop in output power. With the goal to produce a single valve duration to be tested with different valve lifts and backpressures, the case “In 130/240, Ex 120/230” was chosen for its adequate performance at both speeds. At 800 rpm this case represented a reduction of about 8% in the net specific power, though at 2000 rpm the decrease was irrelevant.

6.3.2 Effects of valve lift and exhaust backpressure

The evaluation of different intake valve lifts focused on the role played by the masked cylinder head during the scavenging process. Moreover, the exhaust valve lift and backpressure were also considered to demonstrate the exhaust flow restriction resulted from the possible application of a turbocharger. The valve timing used was that obtained in the previous section, which simultaneously suited the engine operation at 800 rpm and 2000 rpm i.e. “In 130/240, Ex 120/230”.

From Figure 6.12 it is noticeable that any reduction of intake and exhaust valve lifts from the maximum value of 8 mm resulted in less torque at all speeds. At 2000 rpm, when this effect was more pronounced, there was a continuous rise of specific torque by increasing the intake and exhaust valve lifts from 3 mm to 8 mm. The interesting detail was that “IVL 8, EVL 3” produced higher torque than “IVL 3, EVL 8” at any value of EBP and at both speeds. It suggested that the intake restriction posed by the masked region affected more the scavenging process than the flow restriction imposed by the lower exhaust valve lift. It is known that the scavenging process in ported two-stroke engines is strongly dependent on the exhaust port details. For the same reason, the two-stroke poppet valve engine has exhaust valves larger than intake valves. However, there was no apparent gain in scavenging by fully opening the exhaust valves if the intake flow was restricted at 3 mm of valve lift as in the case “IVL 3, EVL 8”. Though the masked region around the intake valves was supposed to reduce the air short-circuiting, the decrease in charging efficiency was more pronounced (Figure 6.13) and hence the output power dropped. This fact was further evidenced by the gain in specific torque and charging efficiency when comparing the three last cases in the first lift sweep (Lift S1). When the IVL was increased from 3 mm to 8 mm and the EVL reduced from 8 mm to 3 mm, the output torque increased by 20% at 2000 rpm. However, when the EVL was raised from 3 mm to 8 mm at a constant IVL of 8 mm, the improvement in torque was around 4%.

The specific torque trend at 800 rpm was not as linear as that at 2000 rpm, as the case with a higher EVL presented poorer performance than that with 3 mm of EVL. This fact only happened at low speed and might be a result of the lower in-

cylinder trapped mass at the onset of compression. Even though in both cases the intake valves closed after the exhaust valves by 10° CA, it is believed that the greater exhaust valve area at 8 mm of lift allowed more charge to leave the cylinder prior to IVC. Under low values of intake valve lift and the consequent restriction to the intake air flow, the incoming charge could not compensate for the lack of filling in only 10° CA between EVC and IVC. Hence, the in-cylinder pressure at IVC could not be recovered.

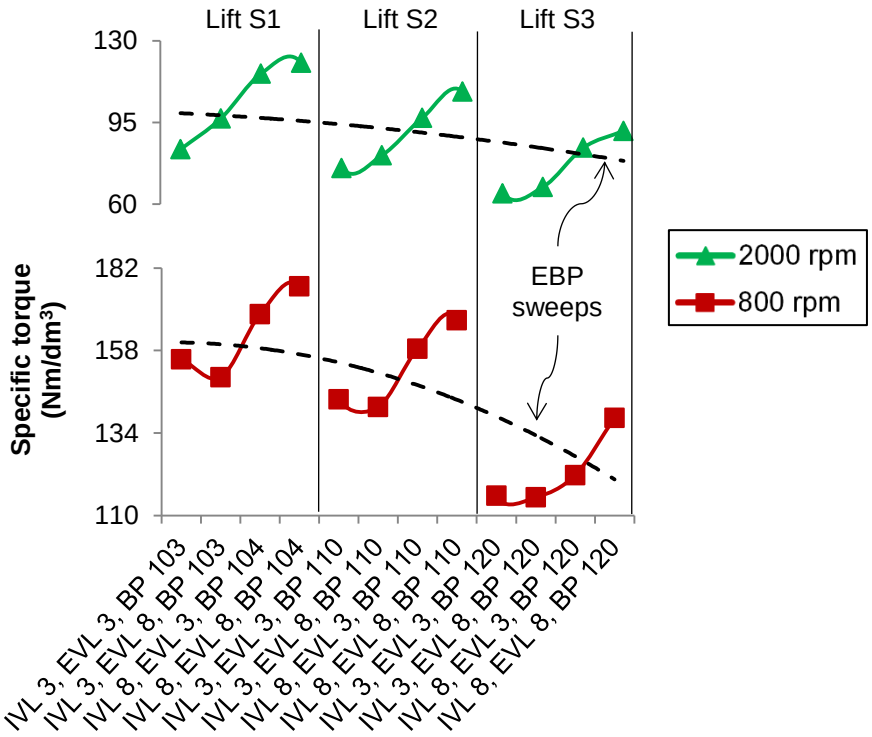

Figure 6.12 – Indicated specific torque results for the valve lift and exhaust backpressure sweeps.

As the exhaust backpressure increased, seen from the left to the right in the plots, the output torque gradually deteriorated at both engine speeds by about the same proportion. There was a uniform load reduction of about 28% between the lowest and the highest EBP at both speeds. The increase in EBP also hindered the effect of lower valve lifts at both speeds due to the reduction in the pressure ratio across the valves. This was evidenced by the less steep curves in the specific torque and charging efficiency plots in Figure 6.12 and Figure 6.13, respectively. As previously discussed, the charging efficiency followed very closely the output torque profile. However, an interesting behaviour was found in the second valve lift sweep (Lift S2) for the case “IVL 8, EVL 8, BP 110”. At 800

rpm this case provided similar values of charging efficiency than the last two cases in “Lift S1” where no exhaust backpressure was applied. It indicated that a moderate EBP of 110 kPa, as well as 3 mm of exhaust valve lift, resulted in the same charging efficiency of the best valve configuration for maximum torque (IVL 8, EVL 8, BP 104). At 2000 rpm any exhaust throttling resulted in lower charging efficiency, although similar results of charging efficiency were obtained with 3 mm or 8 mm of exhaust valve lift without EBP. This performance indicated that the exhaust was more efficient than the intake during the scavenging process, so the exhaust valves were oversized for the range of speeds evaluated. The poorer intake performance resulted from the smaller intake valve diameter and the masked region around them.

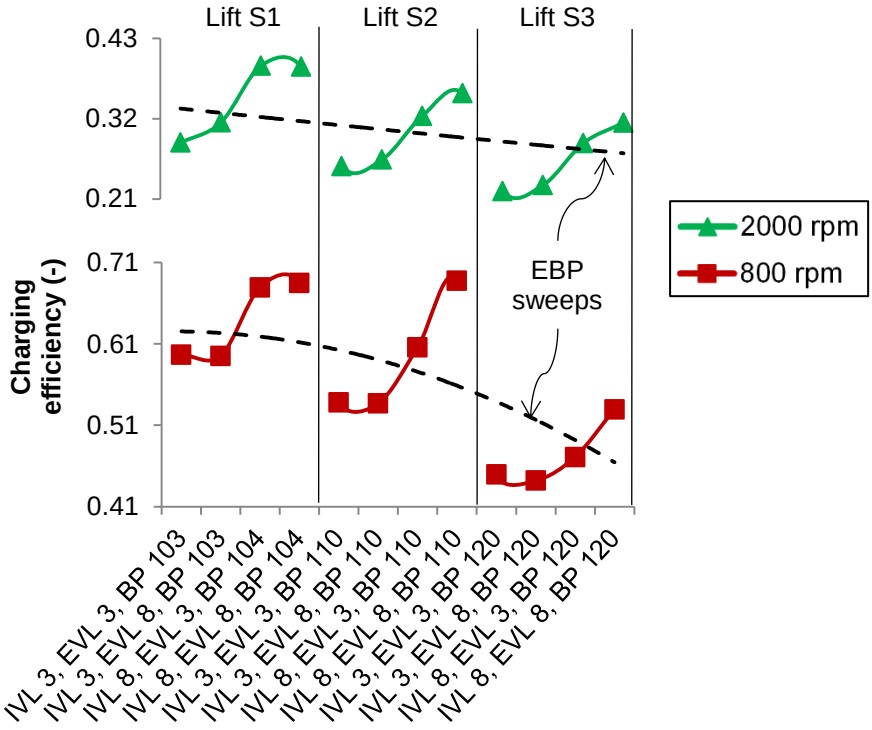

Figure 6.13 – Charging efficiency results for the valve lift and exhaust backpressure sweeps.

Whilst the charging efficiency remained similar in the two last cases of “Lift S1” and in the last case of “Lift S2”, lower torque was observed at any valve lift or EBP other than the optimum case of “IVL 8, EVL 8, BP 104”. This reduction in output torque was attributed to a higher in-cylinder charge temperature and hence a more retarded spark timing necessary to minimise the PRR. In Figure 6.14 it is observed that a higher scavenge ratio was found for the case “IVL 8,

EVL 8, BP 104". This meant that even at the same value of charging efficiency a larger portion of fresh air mass was delivered to the engine and reduced the charge temperature. The spark timing in this case was assessed and it was found that the ignition timing was advanced by 2° CA at 800 rpm and 4° CA at 2000 rpm towards MBT. At a constant value of charging efficiency and by increasing the scavenge ratio, the air trapping efficiency was expected to drop according to Equation (3.43). This was exactly the situation as seen in Figure 6.15, once it dropped by about 11% due to the use of 8 mm of exhaust valve lift.

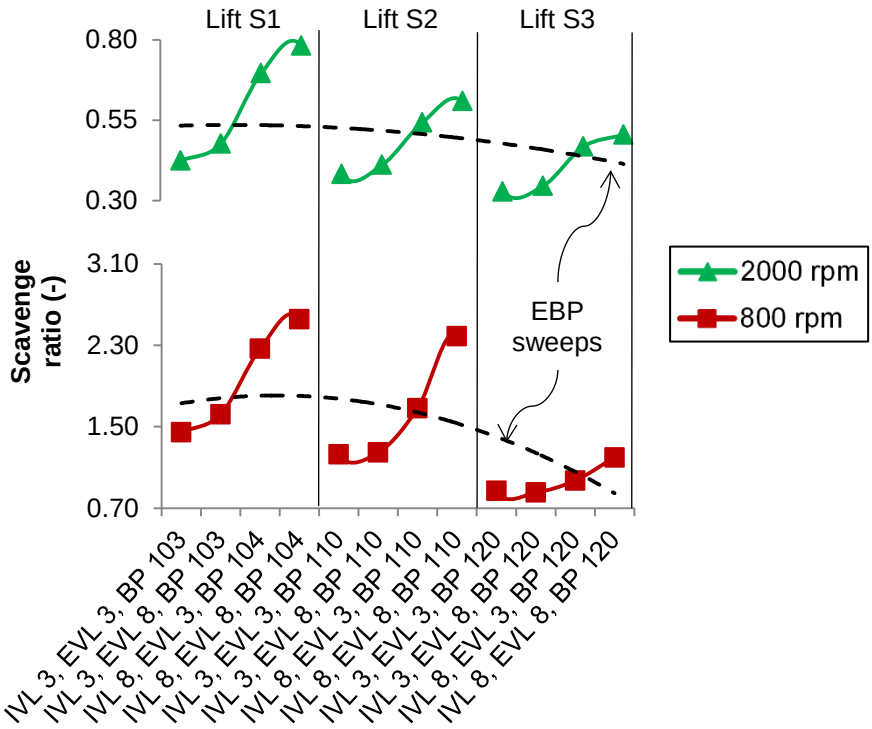

Figure 6.14 – Scavenge ratio results for the valve lift and exhaust backpressure sweeps.

At both engine speeds the scavenge ratio dropped as the EBP increased. This was evident considering that the lower intake-exhaust pressure ratio drove less fresh air through the engine. The same tendency was observed for the reduction in valve lift as the valves' discharge coefficient dropped proportionally. The reduction in scavenge ratio had a positive impact on the air trapping efficiency at both speeds as seen in Figure 6.15. This was particularly the case when the IVL was reduced from 8 mm to 3 mm and/or the EBP was set to its maximum of 120 kPa. The 110 kPa exhaust backpressure had little effect on the air trapping efficiency at 800 rpm. At 2000 rpm and 8 mm of IVL and EVL, the air trapping

efficiency increased by 17% with 110 kPa of EBP compared to the natural exhaust backpressure offered by the pipes and silencer.

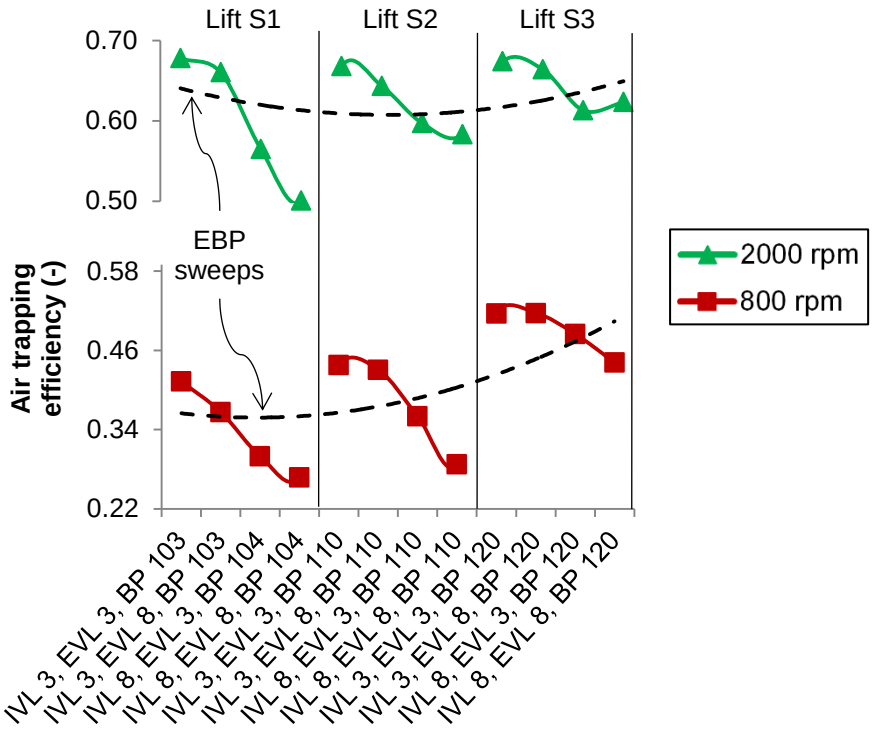

Figure 6.15 – Trapping efficiency results for the valve lift and exhaust backpressure sweeps.

The charging and air trapping efficiencies were less affected by the exhaust backpressure at higher engine speeds as seen in Figure 6.13 and Figure 6.15. It may indicate that the exhaust backpressure offered by a turbocharger at higher engine speeds would not excessively hinder the scavenging process, so part of the exhaust gas energy could be recovered. Results presented by [49] for a two-stroke poppet valve diesel engine suggested the use of a large turbocharger for scavenging the burnt gases at high engine speeds only. Meanwhile, the low speed charging was ensured by a crankshaft driven supercharger. This configuration guaranteed a minimum EBP at low speeds whilst a moderate EBP at higher engine speeds. At 2000 rpm the exhaust enthalpy increased due to the shorter time available for mixing between the fresh charge and burnt gases as evidenced by the greater air trapping efficiency. Moreover, at higher engine speeds the exhaust mass flow rate increased and less time was available for heat transfer.

The masked region around the intake valves played an important role at 3 mm of IVL, which was exactly the mask height. However, at 8 mm of intake valve lift the mask capacity of maintaining high values of air trapping efficiency deteriorated. For instance, at 2000 rpm it dropped by 17% when the intake valve lift increased from 3 mm to 8 mm as shown in the plot “Lift S1” in Figure 6.15. At the same speed the trapping efficiency dropped further 12% when the exhaust valve lift increased from 3 mm to 8 mm, as a result of the increased valves’ discharge coefficient. There was also a peculiarity that further reduced the air trapping efficiency when all valves were operate at maximum lift, as presented in the last quadrant of Figure 6.16. Due to the increased pent-roof angle of the combustion chamber (126°), necessary to accommodate the four valves, fuel injector and spark plug, there was a short path defined between the intake and exhaust valves at full lift. This region enhanced the air short-circuiting and decreased the air trapping efficiency, whilst 3 mm of IVL greatly minimised the air short-circuiting regardless the EVL employed. When 3 mm of lift was used for all valves (first quadrant in Figure 6.16), there were fewer paths for air short-circuiting to occur. Nevertheless, the increased flow restriction hindered the output torque at higher speeds by means of reduced charging efficiency.

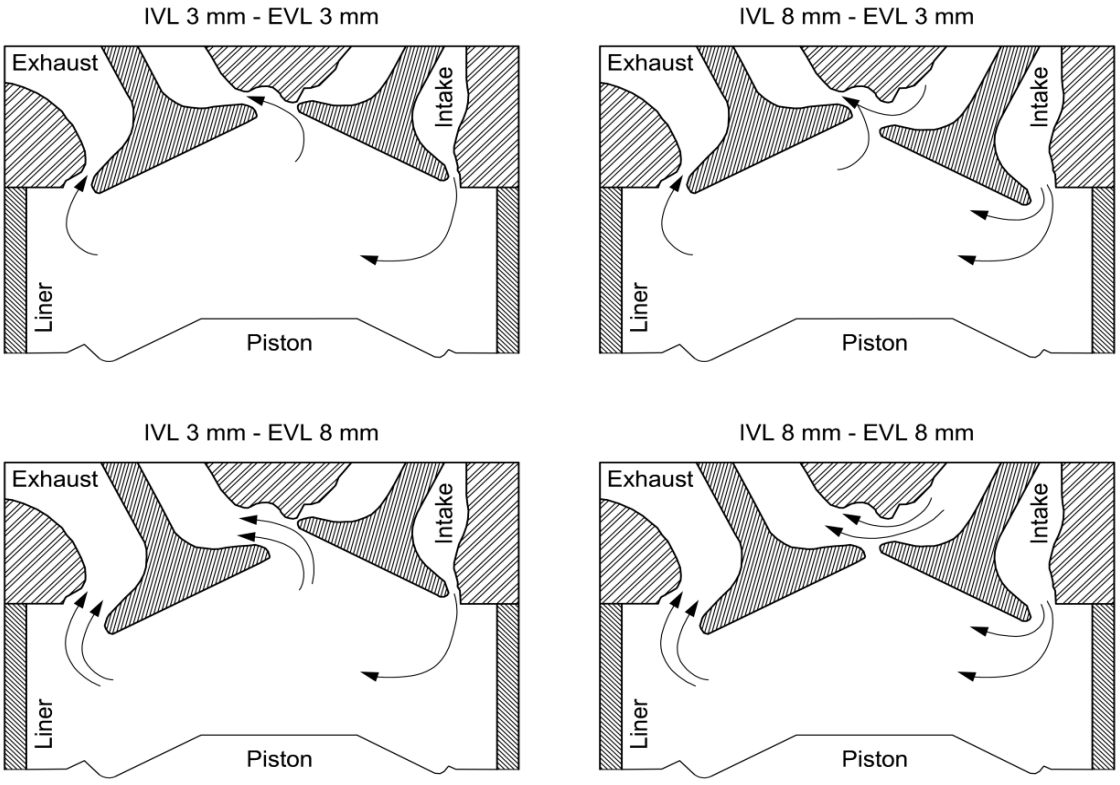

Figure 6.16 – Schematic in-cylinder flow pattern at different intake and exhaust valve lifts.

At full intake and exhaust valve lift the problem of air short-circuiting became apparent and resulted in poor air trapping efficiency. The short-circuiting itself was a problem once no exhaust gas was displaced, though the increase in exhaust pressure resulted from this issue reduced even more the charging efficiency. In the plot “Lift S1” in all figures it could be observed that the exhaust backpressure raised by 1 kPa as the IVL increased from 3 mm to 8 mm, which justified this secondary effect. The air short-circuiting had also a negative impact over the supercharger power consumption as seen in Figure 6.17, as the air flow rate increased at a lower restriction imposed by the full valve lift.

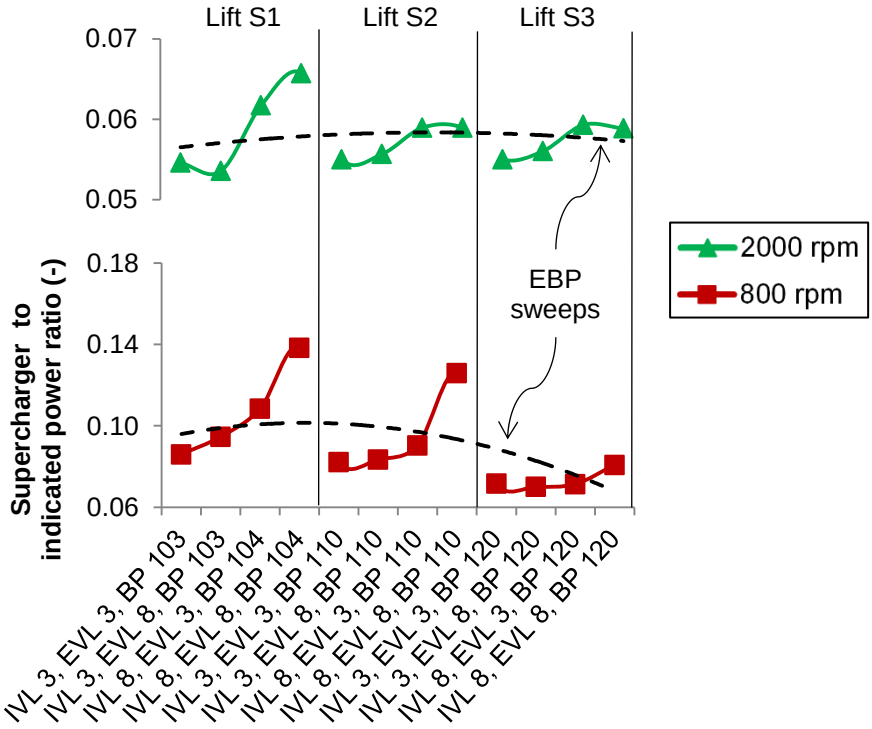

Figure 6.17 – Ratio of supercharger power requirement to engine indicated power for the valve lift and exhaust backpressure sweeps.

It is interesting to note the steep rise in supercharger power consumption as the exhaust valve lift was increased from 3 mm to 8 mm at 800 rpm. Such raise was caused by the short air path seen in Figure 6.16, even though its effect was attenuated as the EBP increased. At 2000 rpm the most perceptible difference in the supercharger power consumption took place as the IVL increased from 3 mm to 8 mm regardless the EVL used. This resulted from air trapping efficiency losses as the intake valves uncovered the masked region, which particularly imposed severe flow restrictions at higher engine speeds. A reasonably choice

for best valve configuration in Figure 6.17 would be one of the cases with higher exhaust backpressure, where a smaller fraction of the engine output power was absorbed by the supercharger. However, in those cases the indicated power was lower due to the modest charging efficiency and hence the net specific power was inferior. The net indicated specific power, presented in Figure 6.18, was calculated by subtracting the supercharger power consumption from the indicated power and dividing it by the engine displacement. At both engine speeds the maximum net power achieved was that of using no exhaust backpressure and the highest possible valve lifts (IVL 8, EVL 8, BP 104). However, the difference to the case with 3 mm of EVL (IVL 8, EVL 3, BP 104) remained low at both engine speeds, so a reduced EVL could increase the air trapping efficiency without significantly deteriorating the output power. At 800 rpm the difference in net power between these two configurations was found below 1.5%, whilst at 2000 rpm it increased to about 3% due to the shorter time available for gas exchange.

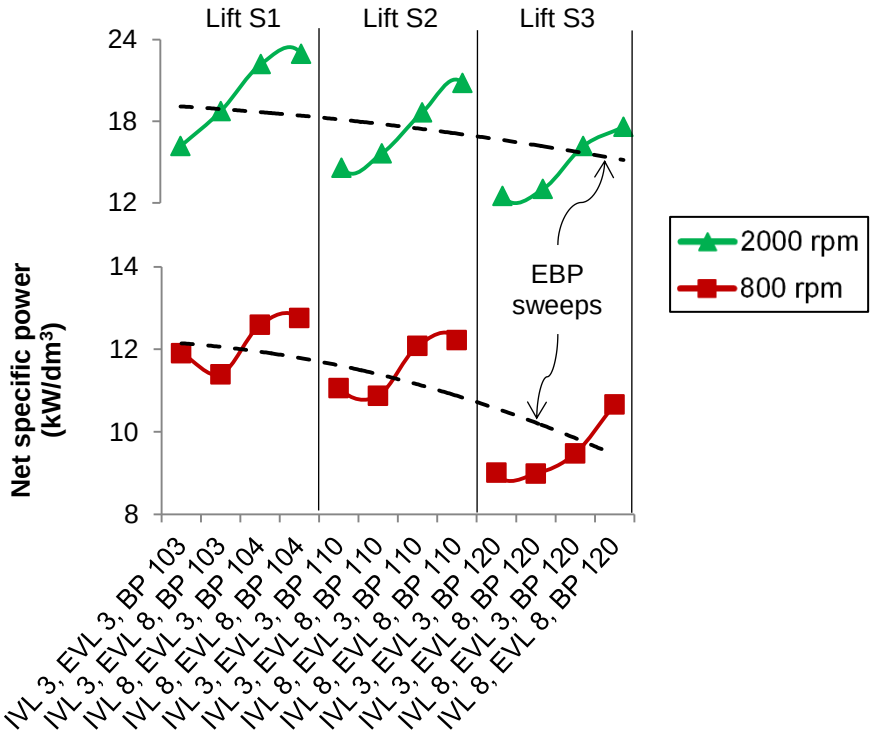

Figure 6.18 – Net indicated specific power results for the valve lift and exhaust backpressure sweeps.

The net specific power was virtually not influenced by the exhaust valve lift at the lowest EBP, though it increased the air trapping efficiency in about 12% at both

speeds. The reduction in exhaust gas dilution is interesting from the point of view of exhaust aftertreatment systems. In this case the higher the burnt gases dilution, the higher is the exhaust oxygen content and the lower is the exhaust gas temperature. This affects not only the conversion efficiency of catalysts but also reduces the energy available for the application of a turbocharger.

6.3.3 Estimation of the in-cylinder lambda at lean-burn conditions

A simple way to assess the in-cylinder lambda in two-stroke engines is by evaluating the exhaust lambda and air/fuel trapping efficiencies as presented in Equation (3.44) for in-cylinder fuel rich conditions. However, in order to obtain higher thermal and combustion efficiencies, lean-burn combustion should be employed as will be seen in chapter eight. Therefore, it is proposed to estimate the in-cylinder lambda based on the exhaust lambda, scavenge ratio and fuel trapping efficiency. To do so, the experimental data obtained at in-cylinder fuel rich conditions was fitted with the Benson-Brandham scavenging model [168].

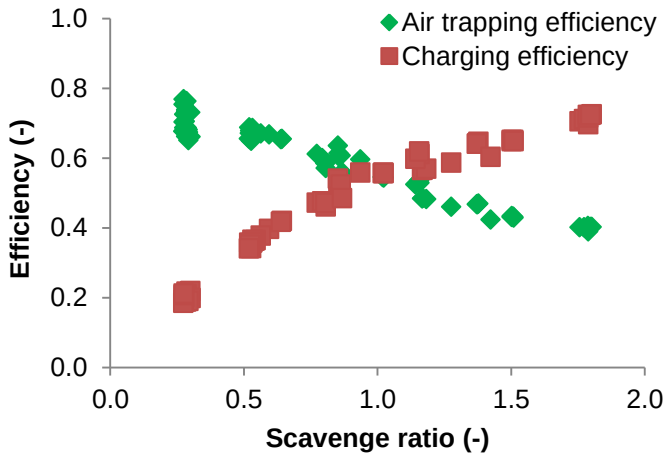

Figure 6.19 – Air trapping and charging efficiencies as a function of scavenge ratio.

The two-stroke poppet valve engine was tested at several speeds and loads following the procedures described in section 6.2.3. The operating points are plotted in Figure 6.19 as a function of scavenge ratio, air trapping efficiency and charging efficiency. As the scavenge ratio increased, the charging efficiency improved due to the larger fraction of air delivered on a time basis. However, the air trapping efficiency dropped as more air was mixed with the burnt gases and short-circuited to the exhaust. It can be seen that the air trapping and charging

efficiencies were solely dependent on the scavenge ratio irrespective of the engine speed or load. At a constant valve configuration and intake pressure, the higher the engine speed the shorter was the time available for the gas exchange, and hence the scavenge ratio dropped. On the other hand, at higher engine loads (higher intake pressures) the scavenge ratio and charging efficiency increased at the expense of air trapping efficiency.

The mixing-displacement two-zone two-phase model of Benson-Brandham [168] was developed in 1969 and successfully applied to loop, cross and uniflow scavenged two-stroke engines. Although the scavenging process is strongly dependent on the ports geometry and their orientation, this model allows the tuning of two engine-dependent empirical parameters. The Benson-Brandham model assumes that the scavenging process occurs at uniform in-cylinder pressure and volume with no heat transfer between the zones, so the temperatures are uniform across these zones. The term “zones” refers to the in-cylinder regions containing fresh charge, combustion products, and a mixture of both. Meanwhile, the term “phases” denotes the sequence of events in time i.e. displacement, mixing, and short-circuiting. To apply this scavenging model to the poppet valve engine the cylinder was divided into two zones: a mixing zone near the intake valves and a burnt gas zone close to the exhaust valves. The fresh charge mixed with the burnt gas adjacent to the intake valves, although close to the exhaust valves the burnt gas zone remained unaffected whilst leaving the cylinder. By the time that all the burnt gas contained in this region close to the exhaust valves had left the cylinder, the second phase of the Benson-Brandham model started and only mixing-scavenging occurred. Apart from the two zones mentioned (mixing and burnt gas zones), a third zone, the air short-circuiting, was considered throughout the phases. In the original work of Benson and Brandham the short-circuiting term was not considered, although the work of [24][28] added this parameter which was particularly important in this study. Figure 6.20 shows a schematic view of the extended Benson-Brandham model applied to the two-stroke poppet valve engine.

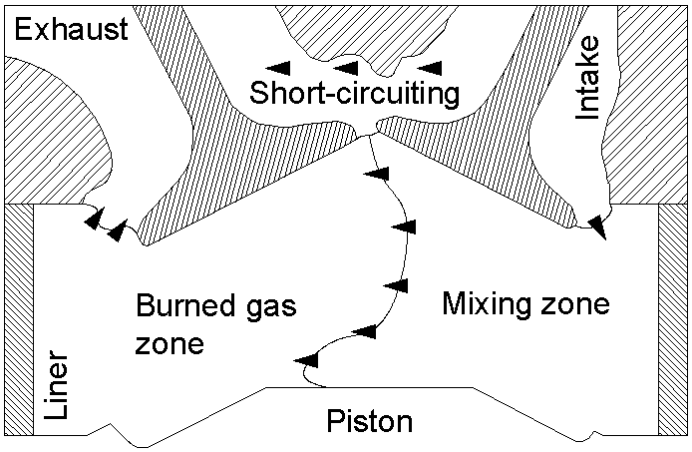

Figure 6.20 – Schematic representation of the extended Benson-Brandham scavenging model in the two-stroke poppet valve engine.

The end of the first phase of the scavenging process, called perfect displacement, occurred at an engine-dependent value of scavenge ratio (SR) known as the scavenge ratio of perfect displacement (SR_{pd}). After this instant the scavenging process was conducted under perfect mixing between the incoming charge and the burnt gases. Hence, there were two equations used to calculate the air trapping efficiency:

When: $$SR \leq \frac{SR_{pd}}{(1 - SC_{air})} \tag{6.2}$$

Then: $$TE_{air} = 1 - SC_{air} \tag{6.3}$$

And when: $$SR \geq \frac{SR_{pd}}{(1 - SC_{air})} \tag{6.4}$$

Then: $$TE_{air} = \frac{1 - \left(1 - SR_{pd}\right)e^{(SR_{pd} - (1 - SC_{air})SR)}}{SR} \tag{6.5}$$

Equation (6.3) was used for SR values below the SR_{pd}, whilst Equation (6.5) was employed for SR values above the SR_{pd}. The air short-circuiting term (SC_{air}) was included as a reducer of the scavenge ratio.

From the experimental data presented in Figure 6.19 it was possible to correlate scavenge ratio and air trapping efficiency with the extended Benson-Brandham

model. As there were no direct measurements of the scavenge ratio of perfect displacement and air short-circuiting, an iterative process was applied to fit the trend line resulted from Equations (6.3) and (6.5) to the experimental data. The coefficient of determination (R^2) was then used to indicate the most appropriate values of SR_{pd} and SC_{air} resulting in the lowest residual between the extended Benson-Brandham curve and the data acquired in the tests. The most suitable trend line is presented in Figure 6.21 alongside the experimental results.

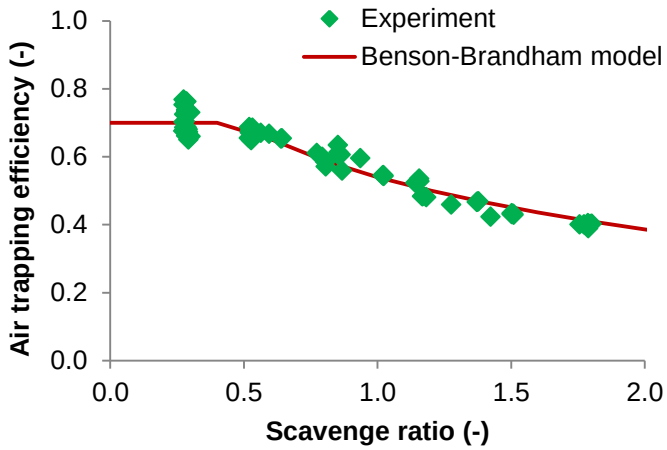

Figure 6.21 – Application of the Benson-Brandham scavenging model to the experimental results.

In Figure 6.21 it is possible to identify the transition from displacement scavenging to mixing scavenging, given by the inflexion in the Benson-Brandham curve. The correlation between this scavenging model and the data acquired was considered satisfactory, with a R^2 better than 0.946 for the 71 testing points obtained. The optimum value of the constants SR_{pd} and SC_{air} to be used in Equations (6.3) and (6.5) were found to be 0.342 and 0.300, respectively. Therefore, the air trapping efficiency became a function of the scavenge ratio only, which was easily calculated by the intake air mass flow rate and its density as presented in Equation (3.42).

Alongside the scavenge ratio, the fuel trapping efficiency (TE_{fuel}) and the exhaust lambda were the two remaining parameters necessary to estimate the in-cylinder lambda regardless the engine operating conditions. By using direct fuel injection only air was employed to scavenge the burnt gases and hence higher values of TE_{fuel} were expected in comparison to mixture scavenged two-

stroke engines. However, it is sometimes convenient to set the SOI before IVC and EVC to improve the mixture formation, but at the expense of poorer fuel trapping efficiency as will be seen in chapter eight. Figure 6.22 presents the in-cylinder lambda prediction according to the scavenge ratio at fuel trapping efficiencies of 0.9 (left) and 1.0 (right).

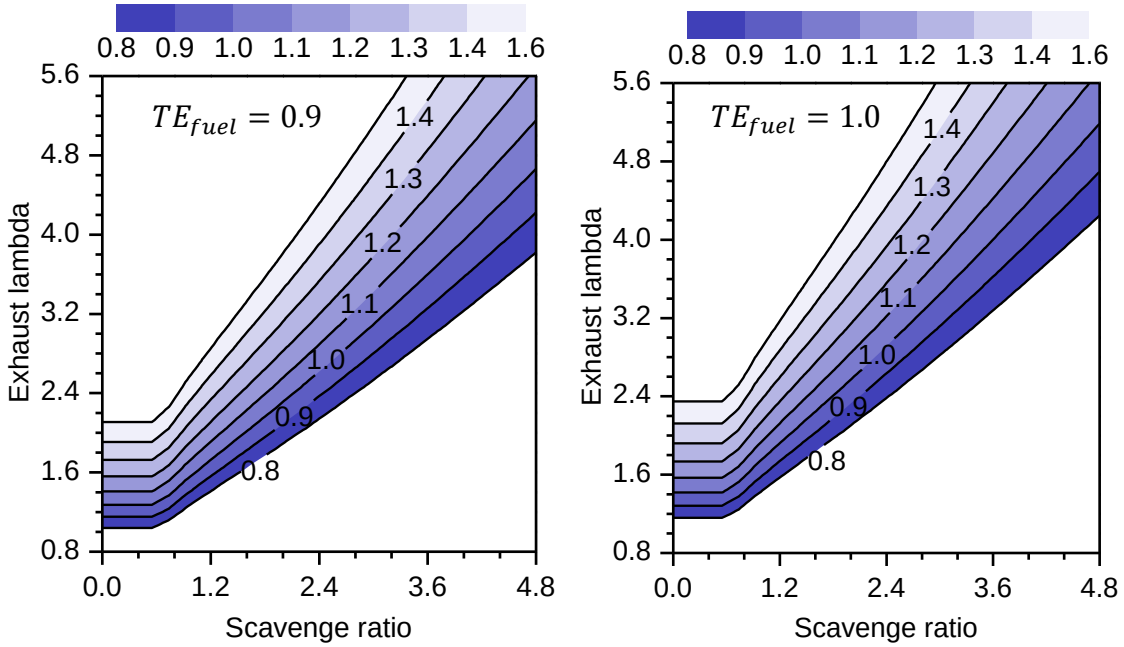

Figure 6.22 – In-cylinder lambda estimation as a function of the exhaust lambda and scavenge ratio at different fuel trapping efficiencies.

It can be seen in Figure 6.22 the linear correlation between exhaust lambda and in-cylinder lambda until the critic scavenge ratio of 0.49. At this point the mixing phase of the scavenging process begun and the air trapping efficiency started dropping from its constant value. A constant air short-circuiting value of 0.3 was considered in the determination of the transitional SR in Equations (6.2) and (6.4). After this transition the exhaust lambda increased linearly with the scavenge ratio, though the curves were proportionally shifted downwards as the fuel trapping efficiency decreased. The relationship between scavenge ratio, exhaust lambda, fuel trapping efficiency, and in-cylinder lambda presented in Figure 6.22 can be analytically expressed as:

When: $SR \leq 0.49$ (6.6)

Then: $$\lambda_{cyl} = \lambda_{exh} \left(\frac{0.7}{TE_{fuel}} \right) \quad (6.7)$$

And when: $$SR \geq 0.49 \quad (6.8)$$

Then: $$\lambda_{cyl} = \lambda_{exh} \left(\frac{1 - 0.658e^{(0.342 - 0.7\,SR)}}{TE_{fuel}\,SR} \right) \quad (6.9)$$

Therefore, for this particular engine operating with a constant valve timing and lift, the in-cylinder lambda can be estimated even under fuel lean conditions as will be presented in chapter eight. The requirements in this case are the exhaust lambda (λ_{exh}), scavenge ratio (SR) given by Equation (3.42) and fuel trapping efficiency (TE_{fuel}) given by Equation (3.45).

6.4 Summary

The performance and gas exchange process of the two-stroke poppet valve engine were investigated in the high load range at different engine speeds under fuel-rich operation. Valve defined parameters, such as effective expansion and compression ratios and valve overlap, were correlated to the experimental results. The supercharger power consumption was also considered so that a more realistic estimation of the net indicated power could be presented. Finally, a formulation was derived to allow the estimation of in-cylinder lambda under lean-burn combustion regardless the engine speed and load employed.

A series of different intake and exhaust valve opening durations were tested until the peak engine power could be achieved at 800 rpm and 2000 rpm. Lower engine speeds benefited from shorter valve opening durations, whilst at higher speeds the time available for gas exchange reduced and longer valve durations were required. Very long intake and exhaust opening durations minimised the effective compression ratio and air trapping efficiency, so the indicated power reduced and the supercharger power consumption increased. Similarly, excessively short valve opening durations resulted in poor charging efficiency and hence torque, especially at 2000 rpm.

The single valve timing IVO 130°, IVC 240°, EVO 120°, EVC 230° CA ATDC was able to develop reasonable engine performance at both engine speeds tested. The 10° CA between EVO and IVO enabled an effective exhaust blowdown phase to take place without intake backflow. The 10° CA between EVC and IVC improved the charge purity at the onset of compression. This optimised valve configuration was further evaluated regarding different intake and exhaust valve lifts and the effect of exhaust backpressure.

Any combination of intake and exhaust valve lifts, apart from 8 mm, resulted in torque deterioration at both speeds but particularly at 2000 rpm. At low intake valve lifts there were modest gains by opening the exhaust valves beyond the same values of lift. In addition, the air trapping efficiency was greatly improved by limited valve openings. As the exhaust backpressure increased, the output torque gradually deteriorated at both engine speeds by about the same proportion. Nevertheless, the charging and trapping efficiencies were less affected by the exhaust backpressure at higher engine speeds.

With the optimised valve timing and lift, the extended Benson-Brandham mixing-scavenging model was used to estimate the air trapping efficiency at different engine speeds and loads. With this model the in-cylinder lambda could be evaluated at lean-burn conditions by means of the scavenge ratio, exhaust lambda and fuel trapping efficiency, regardless the engine operating conditions.

Chapter Seven

Numerical analysis of the in-cylinder mixture formation in the two-stroke poppet valve engine

7.1 Introduction

The results presented in chapter five demonstrated that irregular fuel stratification occurred as a consequence of the short time available for mixture preparation. The late SOI also led to severe fuel impingement on the piston surface since the original side mounted fuel injector had a more vertical spray pattern as required by four-stroke engines with early injections. These drawbacks affected the combustion and thermal efficiencies and resulted in high values of CO, UHC and soot emissions. Therefore, the fuel injection system was modified accordingly so the spray penetration was directed horizontally towards the cylinder head instead of the piston top. This configuration was expected to reduce fuel impingement on the piston top at late SOIs. It could also take advantage of the large engine's bore-to-stroke ratio (1.22) and keep fuel impingement on the liner at its minimum. To evaluate the proposed fuel injection system a numerical analysis was performed for several injection strategies with gasoline and ethanol, so the mixture formation could be investigated in a 3-D CFD environment. The main objective of the study was to minimise fuel impingement whilst concentrating a fuel rich mixture in the vicinity of the spark plug (intentional charge stratification) to facilitate the initial flame propagation. In the last section of this chapter some of the injection strategies were experimentally tested and compared to the numerical results.

7.2 Modelling and test procedures

Fourteen different fuel injection strategies, including single and double injections of gasoline and ethanol, were simulated using the multi-hole solenoid type injector side mounted in the combustion chamber. The minimum dwell time between two successive injections was set to 1.5 ms (13.5° CA @ 1500 rpm) to ensure a full injector needle recovery and a proper separation between first and second injections [170].

7.2.1 Simulation case setup

After the spray model validation in section 4.5.2 the spray details were updated to the engine geometry and mesh. The original fuel injector position was swapped with the in-cylinder pressure transducer location so the fuel spray could have a more horizontal penetration. Whilst the original fuel injector boss in the cylinder head was set at about 50° with the cylinder axis, the pressure transducer boss had an angle of 65° with the same axis. These extra 15° were enough to give a nearly horizontal spray penetration without the need of machining the cylinder head and hence justified the injector position alteration. Figure 7.1 presents the final injector location and the spray pattern in a cross section view and bottom view. In the bottom view, the intake valves are seen below the exhaust valves with the old injector position between them.

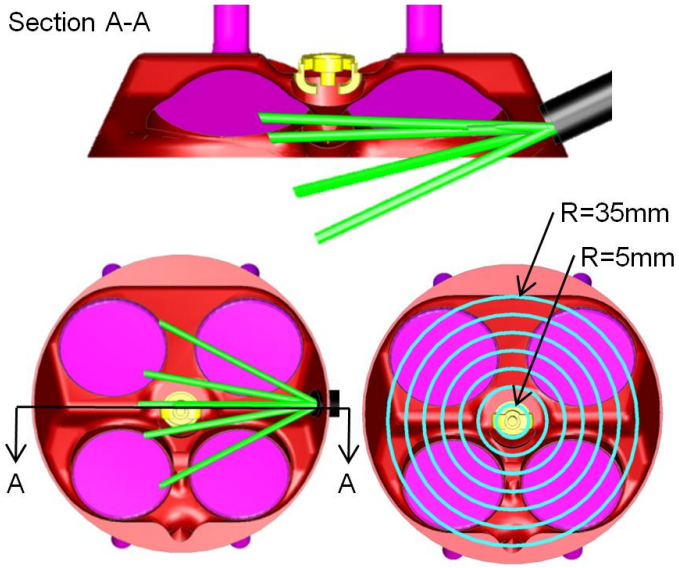

Figure 7.1 – Multi-hole injector position and classified regions for the equivalence ratio analysis.

The air-fuel mixture formation was evaluated by several in-cylinder parameters i.e. stratification index at TDC, spatial equivalence ratio distribution around the spark plug, global equivalence ratio, turbulence effects, averaged in-cylinder temperature, fuel impingement, and spark window duration.

The stratification index compared the species mass fraction in each in-cylinder cell to the averaged value over the whole domain, accounting for the number and volume of elements at TDC. To quantify the spatial distribution of fuel seven

spheres were concentrically located around the spark plug with radii varying from 5 mm to 35 mm as shown in Figure 7.1. The local equivalence ratio was then calculated and averaged by the number and volume of the elements inside each sphere. The effect of turbulence on the mixture preparation was evaluated by means of the turbulent kinetic energy (TKE) and reverse tumble flow, computed from Equations (4.7) and (4.16), respectively. The fuel impingement was determined by the maximum fuel mass impinged on the piston, liner and cylinder head at any time during the engine cycle and normalised by the total fuel mass injected. And finally, the spark window duration was used to quantify how long a rich mixture could be found close to the spark plug to enable stratified combustion. In this case an equivalence ratio between the burning limits of 0.8 and 1.6 was considered in the vicinity of the spark plug, represented by the smallest sphere of 5 mm radius. The duration, in crank angle degrees, of a flammable mixture inside this sphere indicated the degree of freedom the spark ignited flame kernel could be realised.

7.2.2 Boundary and initial conditions

The CFD simulations were carried out under similar initial and boundary conditions to those found in the cold flow study in section 4.4. The cold flow model of the engine was run until the first SOI studied i.e. 235° CA ATDC was reached, so the simulation was stopped and 14 copies of the engine model were created. Each of them had the same initial in-cylinder and port conditions prior to the fuel injections, so the simulation did not have to start from the beginning of the engine cycle for each injection strategy tested. The SOI took place after EVC and IVC to avoid fuel short-circuiting or its backflow to the intake ports, respectively. Single fuel injections at 235°, 260°, 285°, 310° and 335° and split injections at 235°/285°, 235°/310°, 235°/335° and 310°/335° CA ATDC with fuel mass distributions of 50/50%, 70/30% and 85/15% were evaluated. Some of the parameters used in the numerical simulations can be found in Table 7.1.

In the first part of the mixture formation study only gasoline (mixture of n-octane and n-heptane) was used to evaluate the fuel injection strategies proposed. Three of the most prominent cases amongst the 14 studied were chosen to be tested with ethanol (E100) under the same boundary and initial conditions of

gasoline. The mass of ethanol injected was estimated based on the difference between its lower heating value (LHV) and that of gasoline, so the energy input could be kept constant. In this case the mass of ethanol injected was 64% higher than that of gasoline, which resulted in proportionally longer injection durations considering a nearly constant injector flow rate amongst the fuels.

Table 7.1 – Boundary and initial conditions used in the fuel spray simulations.

Effective compression ratio (-)	11:1
Engine speed (rpm)	1500
EVC (°CA ATDC)	196
EVO (°CA ATDC)	153
Exhaust pressure (kPa)	103.2
Exhaust temperature (K)	503
Fuels temperature (K)	293
IMEP (MPa)	1.9
Initial in-cylinder pressure (kPa)	103.2
Initial in-cylinder temperature (K)	503
Initial velocity components (m/s)	1.0
Injection duration (ms)	0.56
Intake pressure (kPa)	126.9
Intake temperature (K)	289
IVC (°CA ATDC)	216
IVO (°CA ATDC)	164
Simulation duration (°CA)	235 to 360
Valve lift (mm)	2.9

7.2.3 Experimental testing conditions

To understand the effect of charge stratification on the engine performance and emissions some of the fuel injection strategies were experimentally investigated. The engine operating conditions were set as close as possible to those values presented in Table 7.1 with deviations below 5%. A sweep of 16 single injections of gasoline was performed from 180° to 330° CA ATDC in steps of 10° CA. The new multi-hole side mounted fuel injector was employed with a constant fuelling rate throughout the experiments.

7.3 Results and discussion

The simulation results presented in section 7.3.1 were named by the start of injection (SOI) timings in °CA ATDC, followed by the fuel mass distribution amongst first and second injections between brackets. For instance, the case

“235°(70%), 335°(30%)” had a first fuel injection at 235° CA ATDC and the second at 335° CA ATDC, with a mass distribution of 70% in the first injection and 30% in the second. A similar approach was used for the cases with a single injection as represented by the fuel distribution of 100%. The same nomenclature was used in section 7.3.2 added by the suffixes “G” and “E” to distinguish between the cases employing gasoline or ethanol, respectively. The experimental results were averaged over 200 consecutive cycles and presented as a function of the SOI for the single injections tested.

7.3.1 In-cylinder mixture formation

To avoid fuel short-circuiting to the exhaust the start of injection (SOI) took place in the narrow window between EVC/IVC and TDC, which implied higher levels of fuel stratification compared to conventional four-stroke engines. From the fuel stratification results at TDC shown in Figure 7.2, the later the SOI the greater was the charge stratification when using a single injection. The exception was the case “285°(100%)”, which presented a more homogeneous charge due to improved fuel vaporisation at nearly zero impingement as will be seen later. The lowest values of charge stratification were achieved with 85/15% fuel mass distribution and first injection at 235° CA ATDC. The largest stratification was obtained at the latest single injection due to reduced spray dispersion under high in-cylinder pressures. The higher in-cylinder pressure in this case increased the gas density and therefore the fuel droplets experienced greater drag forces, which minimised the plume penetration and diffusion. When split injections were employed, the levels of charge stratification were found lower in cases with more fuel injected at the first time (85/15%) compared to a more even fuel balance (50/50%). Greater charge stratifications took place with retarded first injections due to the shorter time available for air-fuel mixing prior to the second injection, as in the case “310°(70%), 335°(30%)”.

In addition to the shorter time available for air-fuel mixing at later single fuel injections, the higher levels of stratification were also a result of lower reverse tumble ratios as seen in Figure 7.3. As the piston approached TDC the large turbulence scales dissipated into heat by friction at the chamber walls and into small scales of turbulence in the cylinder core, therefore reducing the potential

for air-fuel mixing. For split injections this effect was more evident in the cases when the second injection took place later in the cycle. It could be observed that every 25° CA closer to TDC the reverse tumble ratio dropped about 3 times. This partially explained the continuous increase in charge stratification in the first three injection strategies in Figure 7.2, even though these three cases had the same fuel distribution and equal first injection timings.

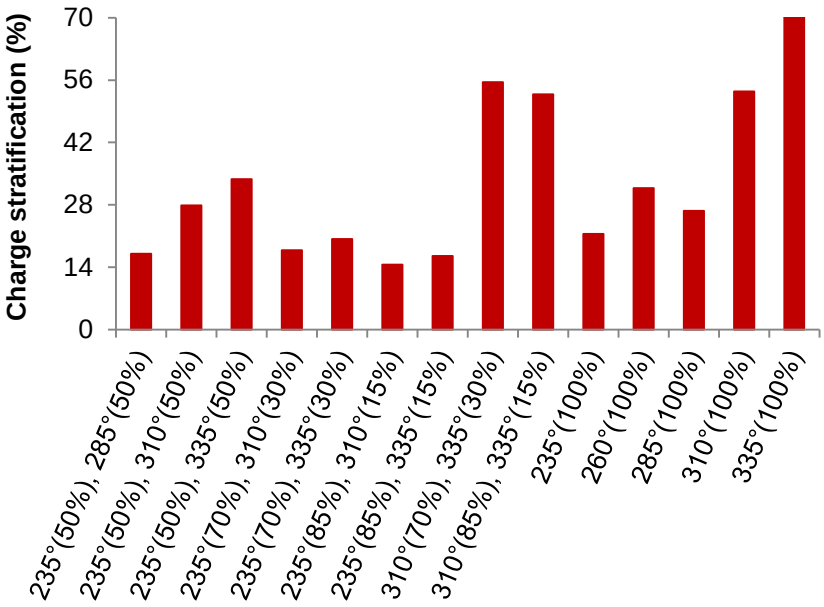

Figure 7.2 – Overall charge stratification at TDC.

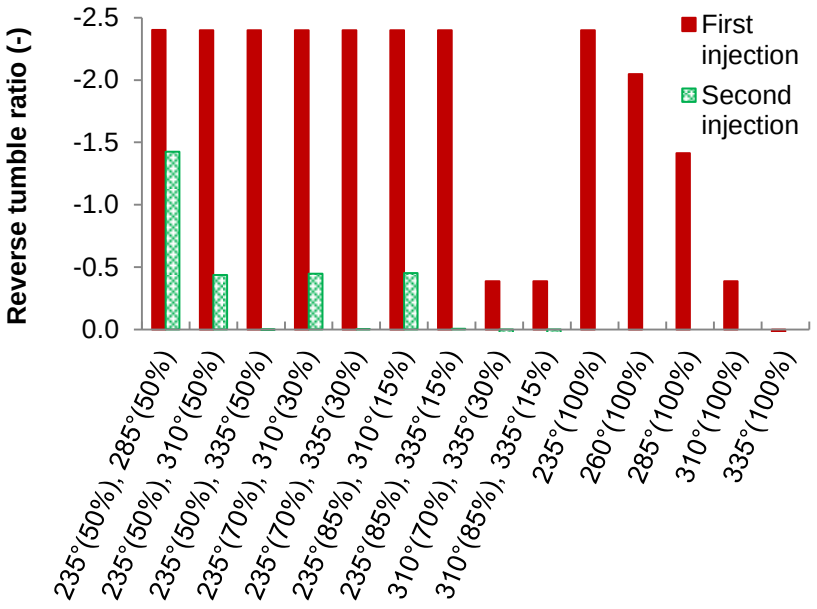

Figure 7.3 – Reverse tumble ratio at the start of injections.

An interesting event that could not be observed in the reverse tumble ratio plot was the influence of the first injection on the mixing process of the second injection. As shown in Figure 7.4 the first fuel injection increased the turbulent kinetic energy (TKE) at the start of the second injection, which resulted in improved air-fuel mixing of the second spray. By comparing the injections at 235°/335° and 310°/335° CA ATDC at 70/30% fuel mass balance, it could be seen that the TKE at the start of the second injection in the closely spaced case (310°/335° CA ATDC) was about 20% higher. This increase in TKE, although, did not strongly affect the charge stratification as seen in Figure 7.2. Hence it is concluded that the time available for air-fuel mixing in this case (32% longer) played a more important role than the in-cylinder turbulence.

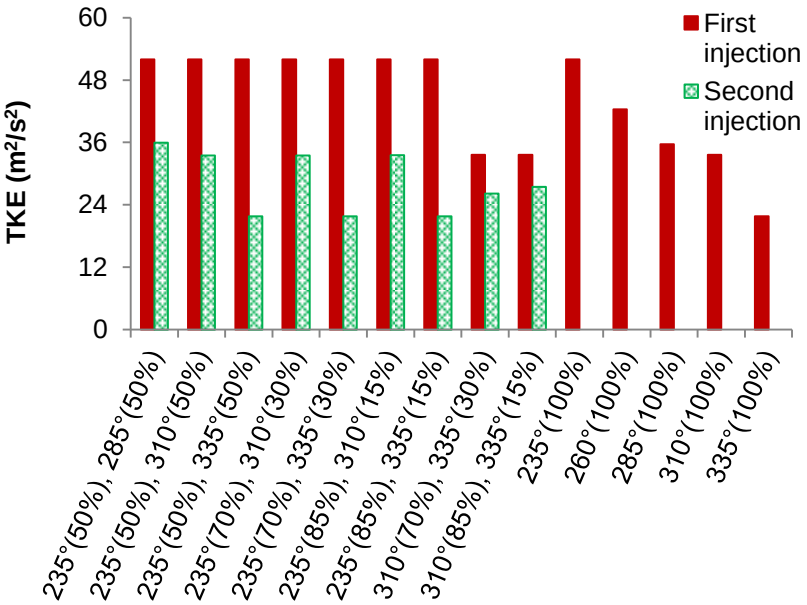

Figure 7.4 – In-cylinder turbulent kinetic energy at the start of injections.

The charge stratification at TDC presented in Figure 7.2 was useful to evaluate the overall mixing process, although it could not provide any details regarding local mixture conditions. Therefore, Figure 7.5 presents the averaged equivalence ratios inside each of the concentric spheres defined in Figure 7.1, as well as the global equivalence ratio throughout the chamber. From the local air/fuel ratio distributions it is clear the weak charge stratification achieved with early second injections, even in the case of large fuel distributions as 50/50% at 285° and 310° CA ATDC. This behaviour was attributed to the longer time available for fuel vaporisation and mixing under high values of reverse tumble

ratio and TKE seen in Figure 7.3 and Figure 7.4. In contrast, the second injection in the case “235°(50%), 335°(50%)” had enough momentum to reach the spark plug region whilst the lower levels of turbulence were not able to disperse the spray. This injection strategy, besides the injections at 310° and 335° CA ATDC with 70/30% and 85/15% fuel distribution, showed reasonably stratification results nearby the spark plug with an overall lean region. Single injections at 260° and 310° CA ATDC also demonstrated potential for stratified operation due to the reduced spray penetration given by higher in-cylinder charge densities. The 1.4% standard deviation in the global equivalence ratio was attributed to numerical errors during the simulations, as the air and fuel flow rates were kept unchanged throughout the study.

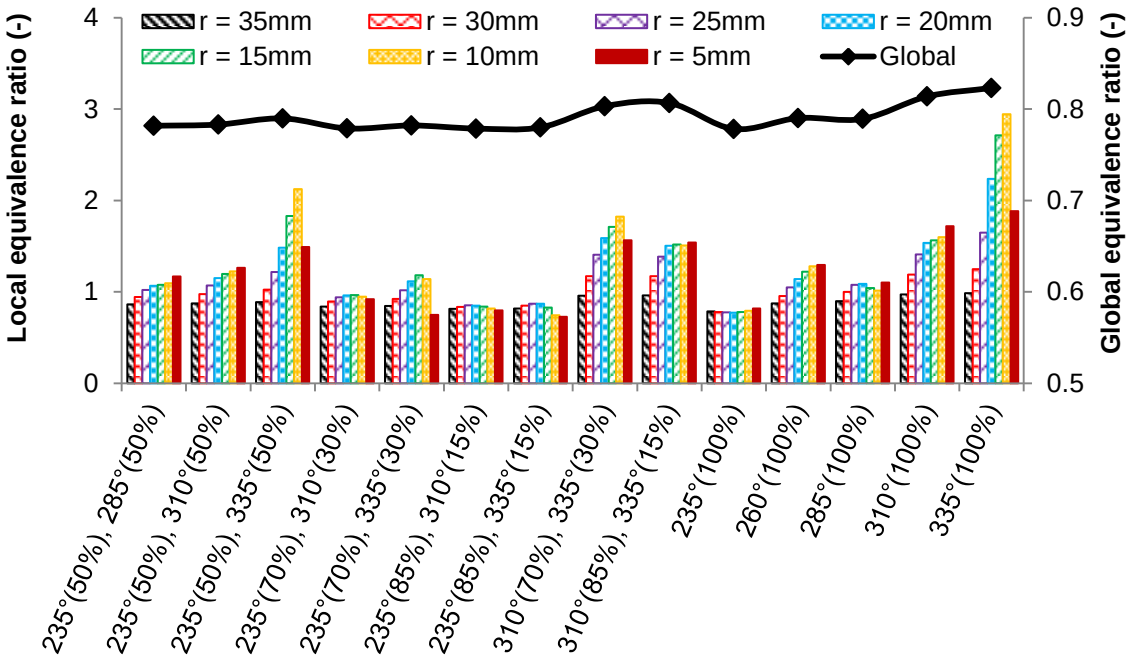

Figure 7.5 – Local and global equivalence ratio distributions at TDC.

The in-cylinder temperature at TDC was found around 830 K regardless the fuel injection strategy used in the simulations as presented in Figure 7.6. This was a result of constant fuelling rates besides the fact that SOI took place after IVC, so the fuel vaporisation and expansion could not displace the intake air flow as normally occurs in PFI engines. A slightly higher temperature was achieved at the latest single injection at 335° CA ATDC as part of the fuel could not vaporise due to the short time available to do so.

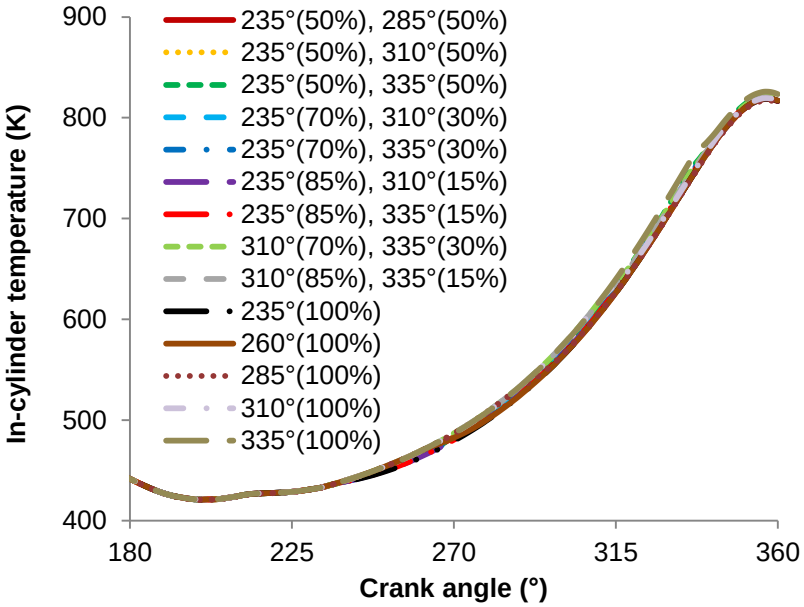

Figure 7.6 – Cycle-resolved in-cylinder temperature.

From the fuel impingement results presented in Figure 7.7 it could be observed that early single injections and early first injections with greater fuel distributions were responsible for larger fuel impingement. When the single injections were retarded, the higher in-cylinder gas density minimised the spray penetration and both liner and cylinder head were not impinged by the spray. However, the piston position at such late injections was closer to TDC and therefore impingement on its surface was inevitable even with the predominantly horizontal spray pattern. The same situation took place during split injections using 50/50% and 70/30% fuel distribution with the second injection at 335°. When the first and second injections occurred relatively early i.e. 235°/285° and 235°/310°, less than 5% of the total fuel injected impinged on the walls. Surprisingly, the same promising results were found for single injections at 260° and 285° when nearly zero impingement was observed. Although fuel impingement is not desirable, its occurrence on the piston surface is less problematic compared to the liner. The higher surface temperature of the piston provides a higher rate of vaporisation and hence the incidence of pool flames during the combustion is minimised. Meanwhile, any fuel remained on the liner at the time the piston is moving towards TDC can result in lubricant oil dilution.

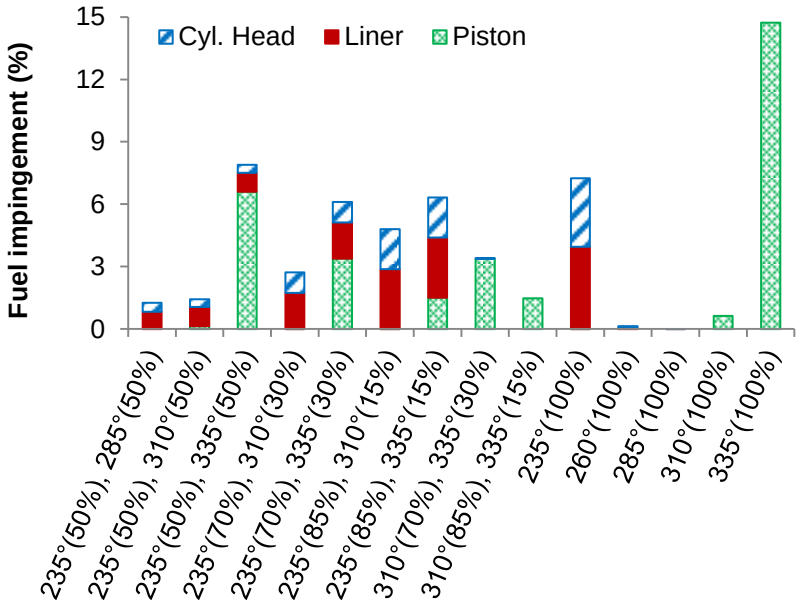

Figure 7.7 – Fuel impingement on the cylinder head, liner and piston surfaces.

The satisfactory values of fuel impingement for all injection strategies tested, despite of the latest single injection, were also a result of the injector assembly position and its spray orientation. By mounting it nearly aligned to the reverse tumble flow axis, the fuel vaporisation was enhanced by the hot residual gas left in the core of this large flow scale as seen in Figure 7.8. In this cross section of the combustion chamber at the valves plane, with the intake on the right and the exhaust on the left, it is possible to see a thermal stratification of about 50 K between the in-cylinder core and the outer region. In this representation only the cold flow was simulated so there was no evaporative cooling effect resulted from fuel injection. Therefore, only a small portion of fuel was able to remain liquid and keep migrating towards the chamber walls, whilst the larger portion vaporised in the hot region thanks to the wide spray distribution shown in Figure 4.11.

Considering the charge stratification in the vicinity of the spark plug (r = 5 mm), the spark window duration presented in Figure 7.9 decreased for later single injections and even split injections with late secondary SOIs. When early single injections were employed a larger spark window was observed. However, modest results in charge stratification due to the improved mixture homogeneity were obtained as seen in Figure 7.5. At very late single injections the charge became excessively rich in the vicinity of the spark plug (**R**), which could lead to electrode wetting and spark plug fouling. The split injection with 50/50% fuel

mass distribution presented the overall best results for all second injection timings i.e. 285°, 310° and 335° CA ATDC. Meanwhile, the 70/30% fuel balance performed well only when the second injection timing was set to 310° CA ATDC. In the case “235°(70%), 335°(30%)” the higher in-cylinder pressure held the spray midway between the nozzle and the centre of the chamber, so a very lean mixture was formed around the spark plug (**L**). In this case when the second injection timing was advanced to 310° CA ATDC, the lower background density allowed a longer spray penetration towards the spark plug. Alongside the remarkable results of fuel impingement given by the start of single injections at 260° and 285° CA ATDC, the spark window duration in both cases was found satisfactory wide at 29° and 25° CA, respectively.

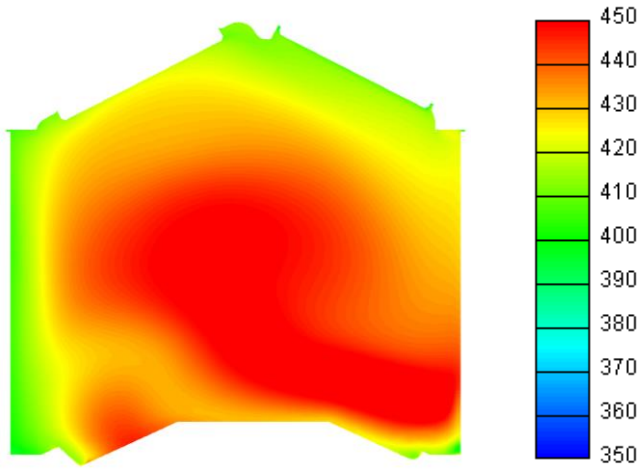

Figure 7.8 – In-cylinder average temperature (K) distribution in the valve plane section at 240° CA ATDC.

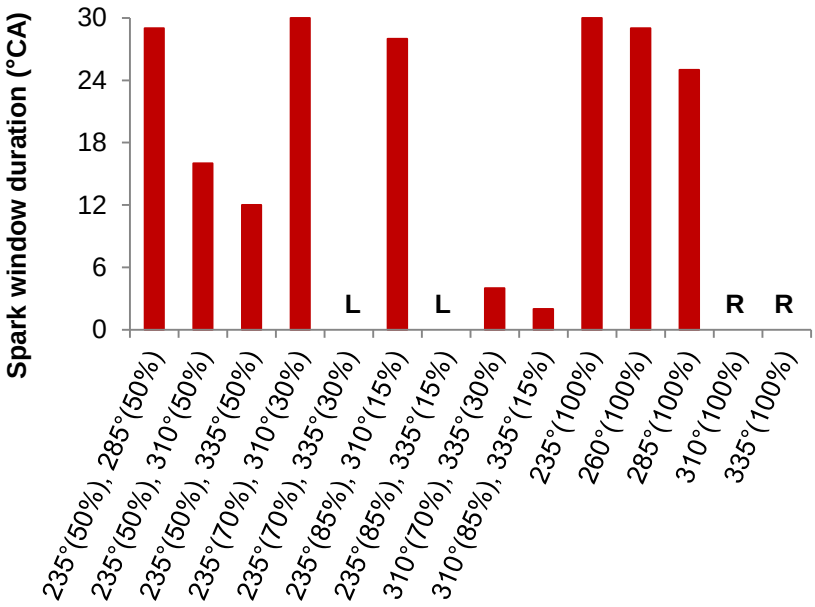

Figure 7.9 – Spark window duration from 330° to 360° CA ATDC.

Amongst the split injection strategies the cases “235°(50%), 335°(50%)” showed the richest region near the spark plug with 12° of spark window duration, although the fuel impingement in this case was about 8%. The case “235°(50%), 310°(50%)” presented about 21% less charge stratification though a 33% wider spark window duration and less than 2% of fuel impingement. This last case also provided a richer mixture near the spark plug with a lean charge elsewhere (Figure 7.10). Overall, the single injection at 260° CA ATDC presented the best results considering fuel stratification and spark window duration, with fuel impingement below 0.1%. This prominent case was also presented frame by frame in Figure 7.11, where it is possible to see the multi-electrode spark plug at the top and the piston moving towards the cylinder head at the bottom.

From the cases “235°(50%), 310°(50%)” and “260°(100%)”, the single injection clearly presented a richer region in the core of the fuel spray compared to the split injection. This was a result of a larger amount of fuel injected at once, which was not the case of the split injection where the total fuel mass was equally distributed between two injections. However, because the split injection had its first spray so early in the cycle its penetration could not be held by the high gas density and fuel impinged on the cylinder liner as seen around 260° CA ATDC. In both injection strategies it could be seen that a small fraction of fuel reached the crevice region in the bottom left corner of the pictures, which could compromise the first piston ring lubrication. In the single injection case shown in Figure 7.11 it was possible to identify the stretching effect provided by the reverse tumble ratio on the spray plume, particularly between 280° and 300° CA ATDC. Differently from the case with split injections where the reverse tumble flow blown the spray towards the liner, in the single injection case the energy present in the reverse tumble decayed enough to not have momentum to disperse the spray. Moreover, due to the larger fuel mass injected, the spray plume inertia was higher and it better resisted to the in-cylinder air motion. It is also worth noting the uniform equivalence ratio gradient from the in-cylinder core towards the walls found in the single injection case in Figure 7.11, achieving the expected stratification results. Finally, in both injection strategies the formation of a slightly rich region on the top of the piston and cylinder head was observed. This could contribute to the occurrence of pool fires and thus increased UHC and soot emissions [86].

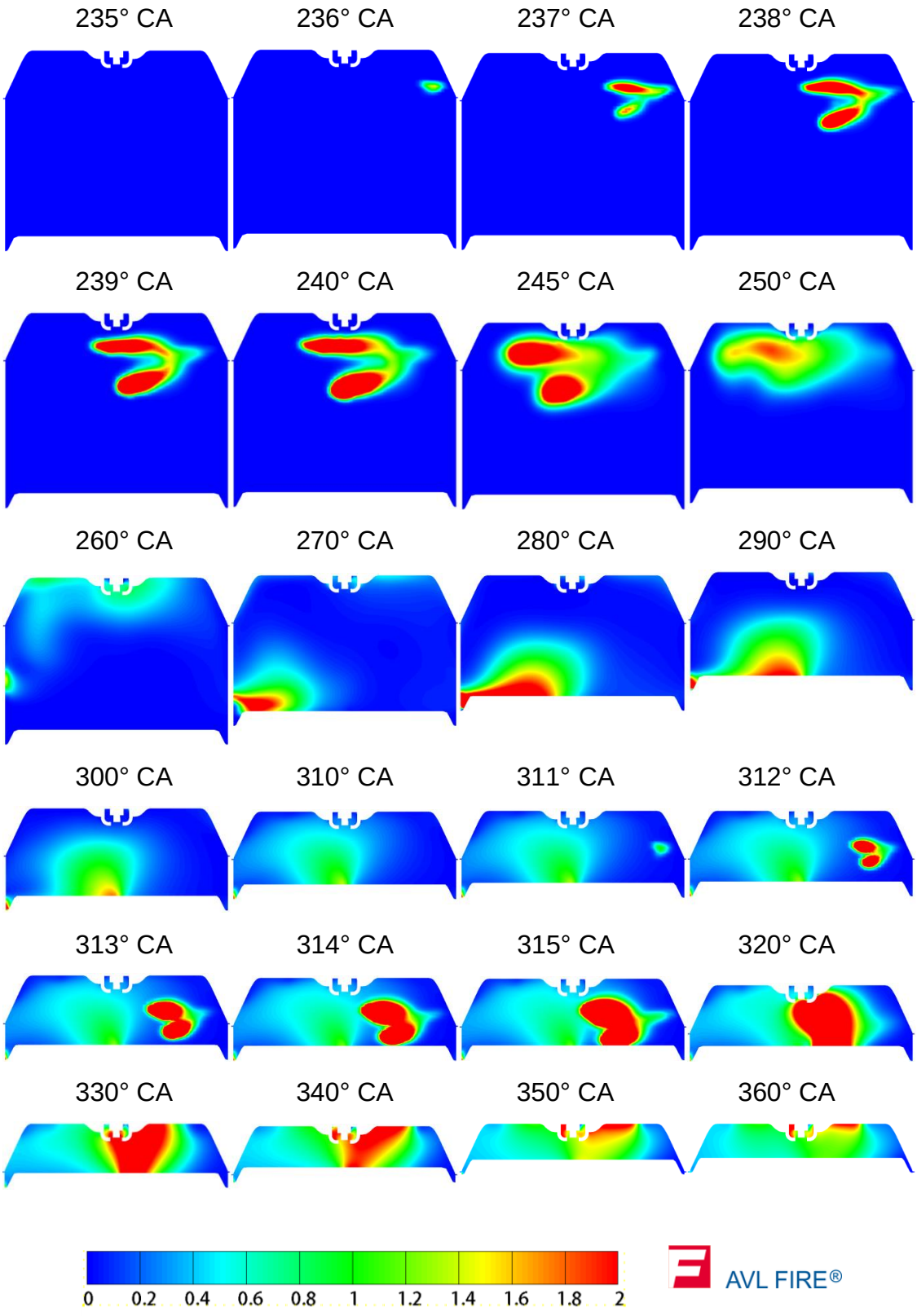

Figure 7.10 – In-cylinder equivalence ratio at the spark plug section plane for the selected injection strategy of “235°(50%), 310°(50%)”.

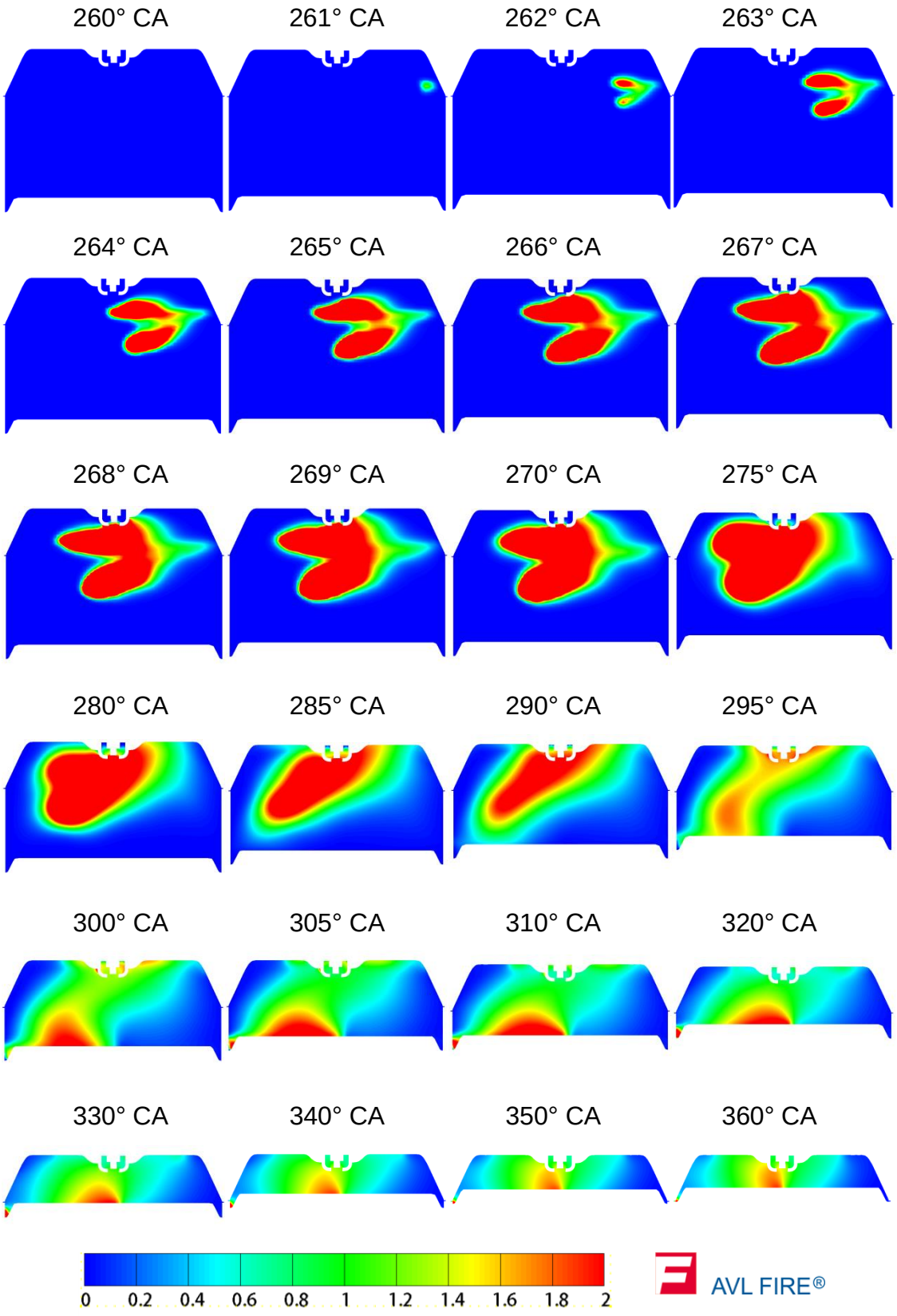

Figure 7.11 – In-cylinder equivalence ratio at the spark plug section plane for the selected injection strategy of “260°(100%)”.

7.3.2 Charge stratification with gasoline and ethanol

Amongst the injection strategies evaluated in the previous section three of them were further analysed using ethanol i.e. “235°(50%), 310°(50%)”, “310°(70%), 335°(30%)” and “260°(100%)”. From the charge stratification results presented in Figure 7.12 it is noted that the charge homogeneity did not change considerably between gasoline and ethanol, though the mass of ethanol injected was 64% greater for the same energy input. In the case “310°(70%), 335°(30%)”, for instance, the charge stratification was reduced by 9%, whilst in the others the difference remained below 2%.

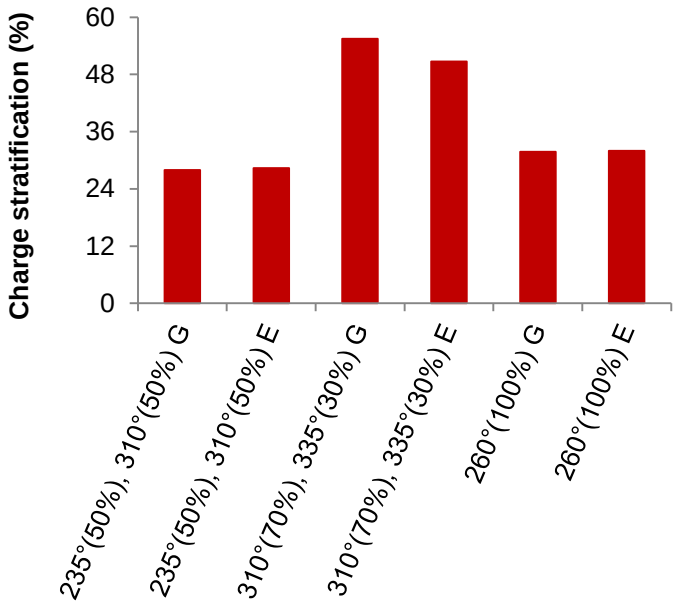

Figure 7.12 – Overall charge stratification at TDC with gasoline and ethanol.

In the case of closely spaced split injection of ethanol the amount of fuel in the first spray was greater than that of gasoline, so the in-cylinder TKE increased by the time the second spray took place and improved the charge mixing. The difference in TKE between gasoline and ethanol in this case was found at 7% as seen in Figure 7.13. The reverse tumble ratio was not affected by the fuel swap due to its larger turbulence length scale.

Whilst the overall charge stratification was slightly affected by the use of ethanol, the local equivalence ratio (Figure 7.14) showed improvements regarding the mixture conditions next to the spark plug. The larger spray momentum resulted from the greater mass of ethanol injected allowed its further penetration towards

the spark plug, so richer mixtures could be formed next to it even with later injections. The global equivalence ratio seen in Figure 7.14 was kept constant throughout the tests as a result of the constant energy substitution amongst the fuels, despite of 1% standard deviation due to numerical inaccuracies.

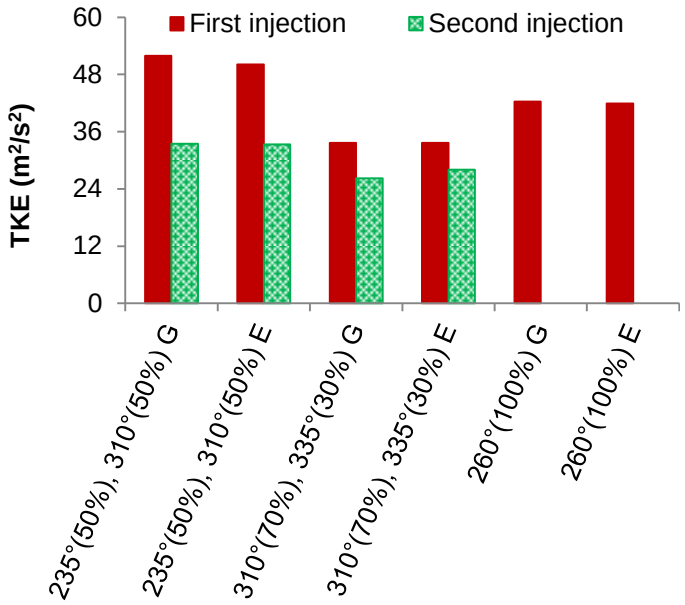

Figure 7.13 – Turbulent kinetic energy at the SOI with gasoline and ethanol.

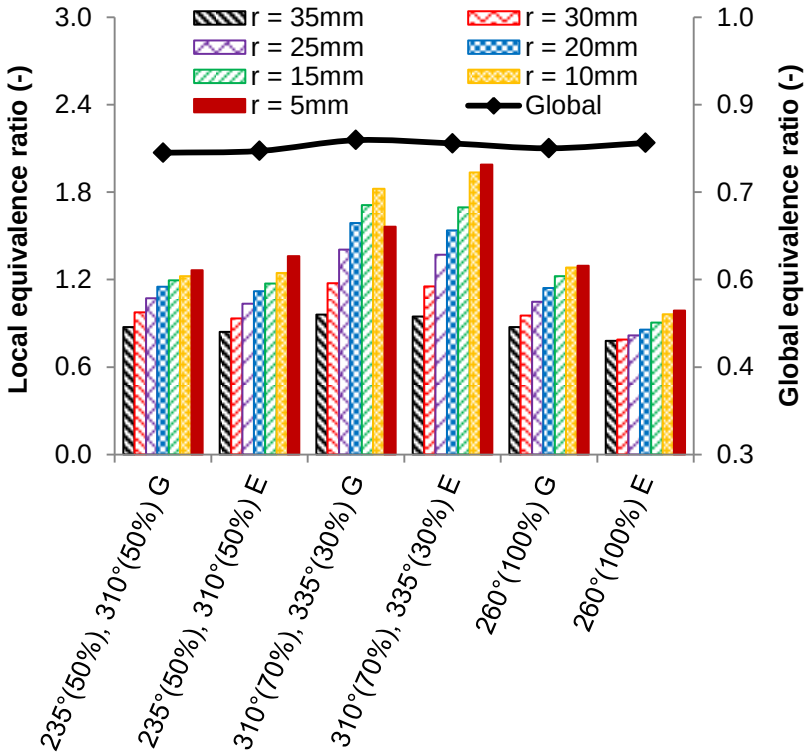

Figure 7.14 – Local and global equivalence ratio distributions at TDC with gasoline and ethanol.

Due to the higher heat of vaporisation of ethanol the in-cylinder temperature was reduced from about 820 K to 640 K at TDC. In the latest injection strategy of 310°(70%) and 335°(30%) the in-cylinder temperature was found slightly higher amongst the cases fuelled with ethanol as a result of remaining liquid fuel at TDC. This great reduction in the in-cylinder temperature seen in Figure 7.15 is expected to mitigate the knocking tendency at higher loads allowing more advanced spark timings towards MBT. Moreover, the lower in-cylinder pressure found at lower temperatures can minimise the compression work from the piston to the in-cylinder gases and further increase the engine thermal efficiency.

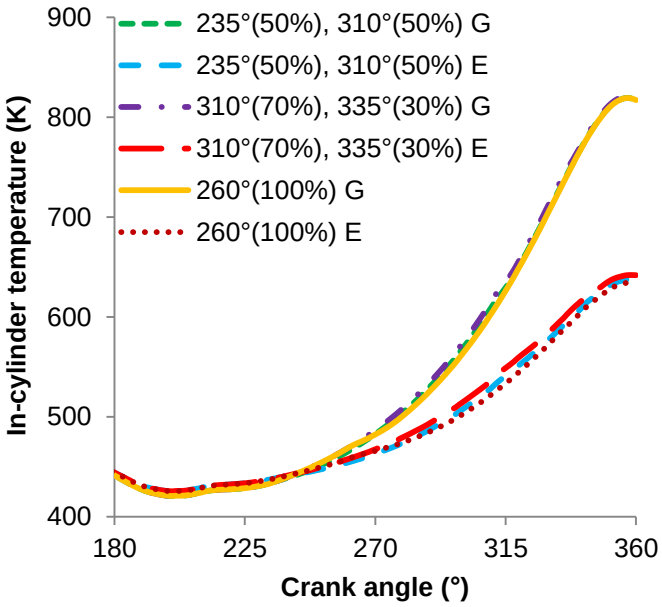

Figure 7.15 – Cycle-resolved in-cylinder temperature with gasoline and ethanol.

The injection of a larger amount of fuel led to greater fuel impingement when comparing ethanol and gasoline as shown in Figure 7.16. The cases “260°(100%)” and “235°(50%), 310°(50%)” presented the most severe impingement as a result of lower in-cylinder gas density with associated greater spray penetration. At early split injections the ethanol impingement was found about 12 times higher than gasoline, whilst in the case “310°(70%), 335°(30%)” it increased by three times. In this latter case only the piston was actually hit by the fuel considering its advanced position towards the cylinder head. In this study the chamber wall temperatures were estimated according to the experiments carried out in a four-stroke engine [155]. Thus, in real engine conditions the chamber wall temperature is expected to be higher in the two-stroke cycle due to the

shorter time available for heat transfer under the doubled firing frequency. Therefore, the numerical fuel impingement results may not indicate severe UHC emissions in this case considering the greater vaporisation rate of the fuel resting on these surfaces. The fuel impingement on the liner, although, was still a concern particularly in the case of ethanol where the risk of oil dilution and consequent reduction in engine durability is eminent [126].

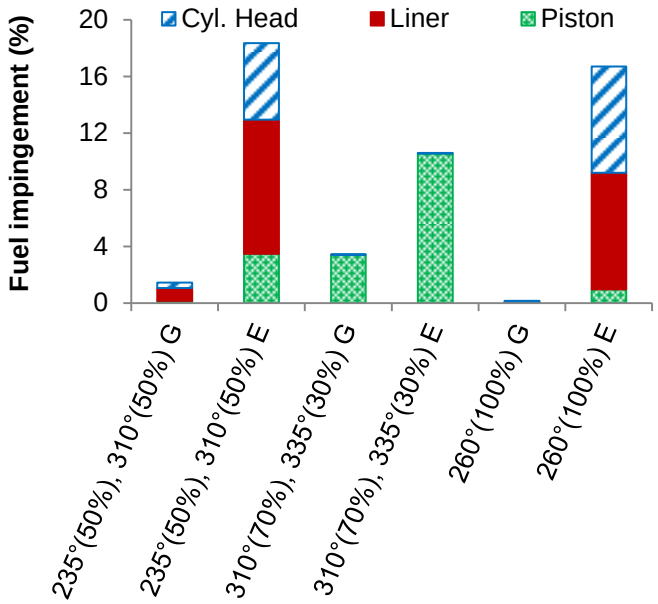

Figure 7.16 – Fuel impingement on the cylinder head, liner and piston surfaces using gasoline and ethanol.

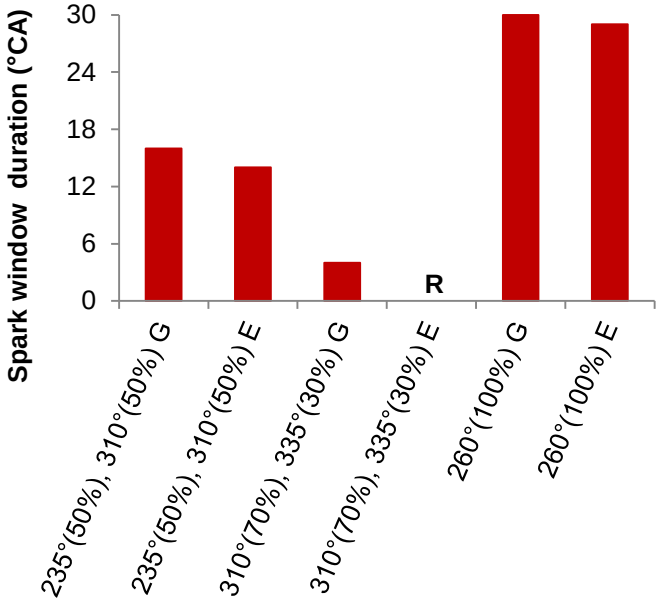

Figure 7.17 – Spark window duration from 330° CA to 360° CA with gasoline and ethanol.

The use of ethanol was characterised by a slight reduction in the time available to obtain stable ignition and combustion in the vicinity of the spark plug as presented in Figure 7.17. In the case “235°(50%), 310°(50%)” the use of ethanol reduced the spark window duration from 16° to 14° as a result of excessive enrichment. As the split injections were delayed, the mixture next to the spark plug became so rich that the initial flame development could not be realised with ethanol in the case “310°(70%), 335°(30%)”. Nevertheless, the single injection of ethanol at 260° CA ATDC performed nearly as well as gasoline in providing sufficient conditions for the initial flame kernel development.

7.3.3 Correlation between simulation and experiments

The simulation results presented in the previous sections provided an insight about the in-cylinder mixture conditions under different injection strategies. However, the absence of combustion modelling in the CFD simulations led to the study of the effects of fuel injection strategies on the engine performance and emissions by means of experiments. In this case a sweep of single injections was performed from 180° to 330° CA ATDC whilst all the other engine parameters were kept constant. The multiple injections were not experimentally evaluated because of the limited ability of the ECU employed, which was also responsible for the valve parameters and spark timing computations.

From the IMEP results presented in Figure 7.18 it is noted the reduction in output power as the SOI was delayed towards TDC particularly after 260° CA ATDC. As the fuelling rate was held constant throughout the tests, this reduction in output power deteriorated the indicated efficiency at the same rate as shown in the same plot. At the latest SOI tested of 330° CA ATDC the efficiency dropped by about 27% compared to early injections between 210° and 240° CA ATDC. The engine performance deterioration at late start of injections was attributed to several factors, amongst which the combustion stability seen in Figure 7.19 was the most prominent.

It is also interesting to note the reduction in IMEP and indicated efficiency at earlier injections in Figure 7.18 due to the prominence of fuel short-circuiting to the exhaust. Since EVC and IVC took place at 196° and 216° CA ATDC,

respectively, it became clear that any SOI before about 210° CA ATDC resulted in fuel losses either to the exhaust or intake ports. It was discussed earlier that at certain operating conditions, when the in-cylinder pressure was higher than the intake pressure at IVC, some fuel could escape to the intake port and be short-circuited to the exhaust during the scavenging process in the following cycle. The occurrence of such fuel short-circuiting could be the reason why the IMEP at the start of injections of 190° and 200° CA ATDC reduced by 2-3% compared to the results obtained with SOIs between 210° and 240° CA ATDC. At 190° and 200° CA ATDC the exhaust valves were closed (or nearly) and hence the only place fuel could escape was to the intake ports. However, when the SOI was further advanced to 180° CA ATDC severe fuel losses to the exhaust resulted in 16% reduction of IMEP and indicated efficiency.

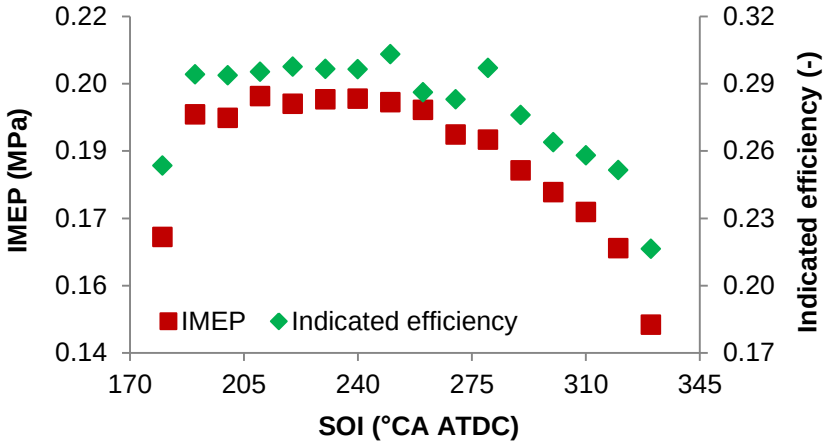

Figure 7.18 – IMEP and indicated efficiency for the SOI sweep.

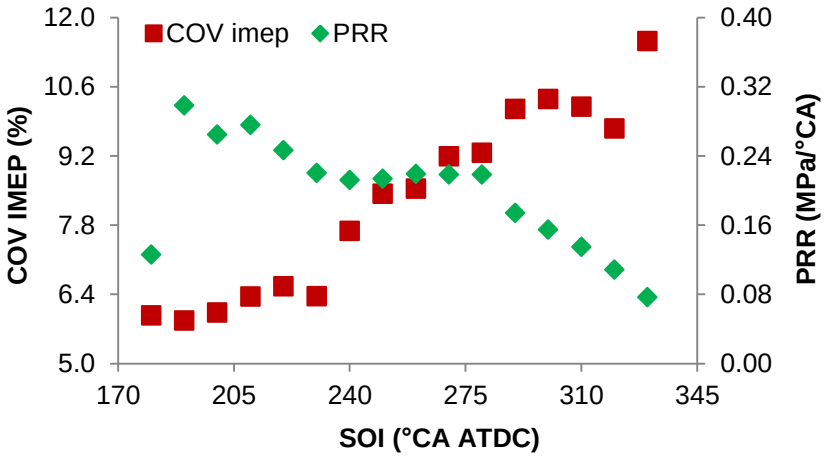

Figure 7.19 – COV of IMEP and PRR for the SOI sweep.

The formation of over rich regions due to the short time available for air entrainment in the fuel cloud resulted in diffusive and partial burning alongside the premixed flame propagated combustion. Such hybrid heat release process led to combustion instabilities as shown by the linear increase of COV of IMEP in Figure 7.19. At the latest SOI of 330° CA ATDC the limit of 10% stipulated in section 3.3.2 was exceeded, whilst for earlier injections (before 240° CA ATDC) it remained below 6.5%. Some of the simulation results presented in Figure 7.5, as the case 335° CA ATDC, could not ensure a rich mixture next to the spark plug at TDC. This occurred when the spray plume was held halfway between the injector tip and the spark plug due to the increased charge density at higher values of in-cylinder pressure. This may also explain the high values of combustion instability obtained in the experiments due to the weak initial flame propagation. Similarly, the continuous decrease in pressure rise rate (PRR) at later SOI revealed the strong charge stratification taking place in the combustion chamber and resulting in partial burn. This reduction in PRR correlates well with the lower IMEP and efficiency found for late injections in Figure 7.18. At the earliest SOI the PRR dropped as a result of less fuel trapped in the cylinder due to short-circuiting, although the COV of IMEP remained low at 6% as a result of the homogeneous mixture formed.

As shown in Figure 7.20 the combustion efficiency increased from 0.75 at the earliest SOI to a maximum of 0.95 when fuel short-circuiting was avoided by later injections. Overall, the combustion efficiency did not deteriorate excessively even at very late values of SOI, reaching a minimum of 0.88 at 330° CA ATDC. The averaged combustion efficiency result of 0.93 is in the range of values achieved in four-stroke gasoline engines, either port fuel injected or direct injected [9].

The maximum combustion efficiency of 0.95 coincided with the lowest indicated specific unburnt hydrocarbon (ISUHC) emissions of 13.9 g/kWh at 260° CA ATDC. According to the simulation results, the lowest fuel impingement for single injections was achieved with start of injections between 260° and 285° CA ATDC (Figure 7.7). At both ends of the SOI sweep in Figure 7.20, the ISUHC emissions increased in accordance with the simulation trade-off regarding fuel impingement at early and late injections. The peak UHC at the earliest SOI (80 g/kWh) was

attributed to fuel short-circuiting. The ISUHC decreased as the SOI advanced towards 260° CA ATDC. Such reduction was attributed to less fuel impingement on the cylinder head and liner due to shorter fuel spray penetrations in a denser charge. As the SOI passed 260° CA ATDC less fuel impinged on the liner but more fuel spray hit the piston resulting in pool flames.

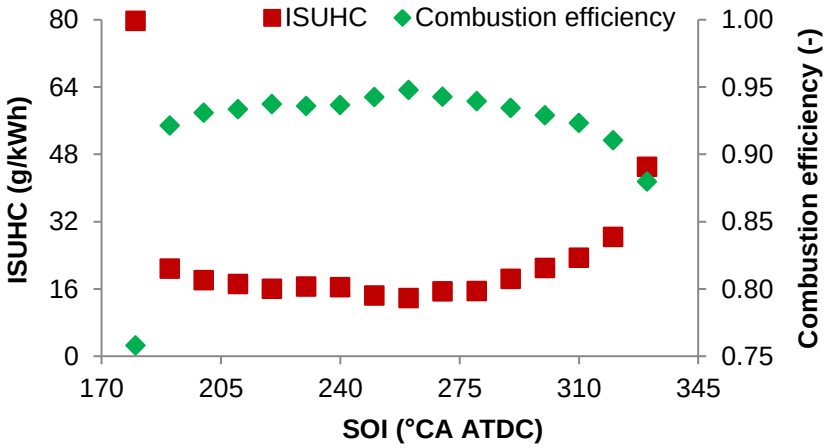

Figure 7.20 – ISUHC emissions and combustion efficiency for the SOI sweep.

Emissions of CO and NOx exhibited similar trends with the injection timings and had the lowest values at the SOI of 260° CA ATDC (ignoring the fuel short-circuiting case of the earliest SOI when the in-cylinder mixture became leaner). The overall low ISNOx results seen in Figure 7.21 indicated the occurrence of diluted combustion with high values of internal residual gas, which is inherent of two-stroke engines operating at low values of scavenge ratio. The larger heat capacity of the burnt gases and the minimum in-cylinder oxygen concentration were therefore the main responsible for mitigating NOx production. Nevertheless, the lower combustion temperature resulted in poor post-flame oxidation and relatively high values of CO emissions.

The trade-off between early injections with fuel impingement on the liner and late injections with impingement on the piston were the main reason for the “V” shaped trend in the NOx and CO plots. In both circumstances the occurrence of pool fires hindered the mixture formation and resulted in long partial burn at lower global temperatures, which therefore increased CO emissions. On the other hand, the rise in NOx production towards both ends of the plots was attributed to the diffusive combustion given by the over rich stratified regions.

Comparable to compression ignition engines where the majority of the heat release process takes place in the interface between the fuel spray and air, the local high temperature gradients were responsible for increasing ISNOx in this case. This event was mainly visible when the SOI was delayed from 320° to 330° CA ATDC resulting in about 20% higher ISNOx.

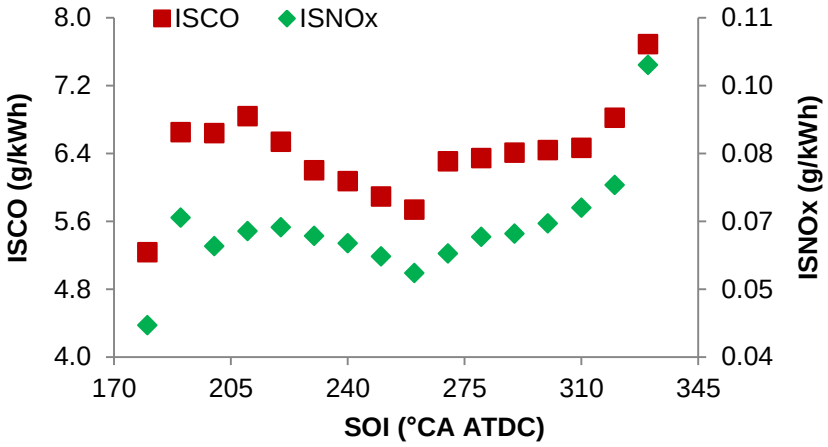

Figure 7.21 – ISCO and ISNOx emissions for the SOI sweep.

7.4 Summary

The in-cylinder mixture formation was analysed via 3-D CFD simulation in the two-stroke poppet valve engine. Gasoline and ethanol were fuelled through a multi-hole side mounted fuel injector. Several parameters were employed to characterise the charge stratification, as well as fuel impingement and spark window duration. It was shown that the mixture formation was mainly dependent on the spray momentum, determined by the fuel mass injected and in-cylinder pressure at SOI, as well as the time available for air-fuel mixing. The in-cylinder turbulence played a secondary role due to the energy dissipation of the reverse tumble flow at late injections near TDC. Nevertheless, the TKE was still important on enhancing the air-fuel homogeneity, particularly when split injections where employed and the first injection increased the TKE in the region nearby the second injection.

The fuel impingement was mainly caused by over penetration of the fuel spray resulting from lower in-cylinder pressure and density at early start of injections. For split injections the fuel impingement was driven exclusively by the first

injection, as the second injection took place in a higher density environment. A single injection of gasoline at 260° and 285° CA ATDC was able to produce appreciable charge stratification with near zero fuel impingement.

The use of ethanol increased fuel impingement as a result of a larger fuel mass injected for the same energy replacement, though the use of split injections minimised this shortcoming. Ethanol's higher heat of vaporisation reduced the in-cylinder temperature by 28% at TDC with similar stratification levels and spark window durations compared to gasoline operation.

The experimental evaluation of some injection strategies showed that the output power and indicated efficiency decreased as the SOI was retarded beyond 260° CA ATDC. At later fuel injections the formation of over rich regions, due to the short time available for charge mixing near the spark plug, resulted in diffusive and partial burn. This poor combustion led to increased values of COV of IMEP and lower PRR, whilst the emissions of UHC, CO and NOx increased simultaneously. Gaseous emissions also increased at early injections when fuel impingement resulted in pool fires and lower post-oxidation temperatures. Nevertheless, the combustion efficiency did not deteriorate and remained at about 0.93, with a peak of 0.95 at the SOI of 260° CA ATDC.

The correlation between experiment and simulation was found satisfactory and the possibility of stratifying the in-cylinder charge whilst reducing fuel impingement was confirmed.

Chapter Eight

Gasoline and ethanol operation in the two-stroke poppet valve engine

8.1 Introduction

From the results presented in chapters five and six, a combination of intake and exhaust valve parameters was identified for optimum operation at 800 rpm and 2000 rpm. In chapter seven the proposed fuel injection system was numerically analysed and correlated to experiments, which demonstrated potential for fuel stratification with low impingement on the chamber walls. The use of ethanol instead of gasoline also presented significant advantages on reducing the in-cylinder temperature, which could mitigate knocking combustion at higher engine loads and speeds. Therefore, the present chapter experimentally exploits the engine performance, combustion and emissions in a variety of speeds from low to high loads using both gasoline and ethanol fuels. The gas exchange parameters were estimated based on the correlation proposed in section 6.3.3 under lean-burn conditions. Thus, improved efficiencies could be achieved as a fuel rich in-cylinder condition was no longer required. Before the presentation and discussion of the results, the test procedures are described in section 8.2. Special attention was given to the start of injection due to the trade-off between fuel short-circuiting, charge stratification and fuel impingement discussed in chapter seven.

8.2 Test procedures

Twenty-five operation points were tested with gasoline and ethanol from 0.2 MPa to 1.0 MPa IMEP with increments of 0.2 MPa. The engine speed was varied from 800 rpm to 2400 rpm in steps of 400 rpm. Speeds beyond this point were not tested due to the great reduction in the intake and exhaust valve effective opening areas as seen in Figure 5.8. Moreover, at speeds between 2400 rpm and 3000 rpm (the maximum supported by the setup), the full valve lift of 8 mm could not be sustained due to the insufficient response time of the VVA system.

Engine loads below 0.2 MPa IMEP could not be investigated as the injector chosen had a minimum opening duration of 0.48 ms. At such duration its flow rate was excessively large to allow for a further reduction in the engine load. If the injection pressure was reduced in an attempt to minimise the fuel flow rate, then the spray vaporisation would be compromised and higher emissions of CO and UHC could be expected. Based on commercial gasoline DI injectors this one was amongst the smallest fuel flow rates available as it came from a four-cylinder 1400 cm^3 DI engine. The engine's unitary displacement matched the one used in this research, 350 cm^3, although the doubled firing frequency of the two-stroke cycle required about half the fuelling rate for the same output torque. It may explain why the Toyota S-2 two-stroke poppet valve engine [22] had two DI injectors in the cylinder head, being one for stratified charging at low loads and the other for homogeneous charging at high loads. The need for two injectors relied on the accommodation of a wide range of fuel flow rates from low to high loads. A contemporary solution for this limitation would be the use of a piezoelectric injector.

The intake and exhaust valve parameters were set according to the best results achieved in chapters five and six, so the intake and exhaust valve lifts were set to their maximum (8mm) and no backpressure was employed. IVO and IVC were set to 130° and 240° CA ATDC, respectively. EVO and EVC occurred at 120° and at 230° CA ATDC, respectively. The intake pressure was varied from 104 kPa to 222 kPa as a way to control the engine load. The fuelling rate was adjusted for best fuel economy so a leaner than stoichiometric in-cylinder mixture was obtained in the majority of testing conditions. Hence, the gas exchange parameters could not be calculated using the oxygen value measured in the exhaust. Instead, the Benson-Brandham scavenging model described in section 6.3.3 was used to estimate the air trapping and charging efficiencies based on the measured scavenge ratio. The in-cylinder lambda was estimated by means of the exhaust lambda, fuel trapping efficiency and scavenge ratio as given by Equations (6.6) to (6.9). The spark timing was adjusted for MBT or KLS depending on each operating condition and fuel used.

From the mixture formation process investigated in chapter seven by means of CFD simulation and experiments, it became clear the existence of a trade-off in the SOI timing. At early injections the in-cylinder pressure and gas density were lower, so excessive fuel spray penetration towards the liner and cylinder head resulted in fuel impingement. At even earlier injection timings, before IVC and EVC, fuel short-circuiting took place and reduced the indicated efficiency. Emissions of UHC greatly increased in these circumstances and contributed to reduce the combustion efficiency. On the other hand, later fuel injections led to fuel impingement on the piston and formation of over rich regions due to the short time available for charge homogeneity. Poorer combustion characteristics were realised in these conditions and led to lower indicated efficiencies and combustion instabilities. Therefore, the proper SOI timing had to be investigated in all 25 operation points with gasoline and ethanol for each engine speed and load. A window of about 40°CA around IVC was firstly evaluated in steps of 10° CA and then a finer variation of 5° CA was used to optimise the SOI. The larger amount of ethanol injected for the same output power than gasoline required different injection timings considering charge homogeneity and fuel impingement.

8.3 Results and discussion

The results of SOI timing optimisation for ethanol and gasoline are firstly presented, being followed by the engine performance, combustion and gas exchange analysis. Finally, engine-out gaseous and soot emissions are presented and discussed. Despite of Figure 8.1 and Figure 8.2, in all plots the X-axis corresponds to the engine speed whilst the Y-axis shows the engine load. On the left side of the plots the load is shown in values of IMEP (MPa) and on the right it is presented in specific torque units (Nm/litre). The plots on the left represent the results found for gasoline operation and on the right those for ethanol. The relevant variables and their units are described in the captions. All test results were averaged over 200 consecutive engine cycles.

8.3.1 Determination of optimum start of injection timings

Amongst the 25 points studied for each fuel, a sweep of injection timings was carried out to find the trade-off between early and late SOIs. In all cases the indicated efficiency reached a maximum at a specific start of fuel injection. In

most of the conditions this SOI matched the highest combustion efficiency and thus the lowest emissions of UHC and CO. Advancing or retarding the start of injection point from this best timing deteriorated the engine performance.

Figure 8.1 presents the indicated efficiency as a function of the SOI at the limiting speeds and loads evaluated i.e. 800 rpm and 2400 rpm and 0.2 MPa and 1.0 MPa IMEP. To avoid clustering only four operating points around the maximum indicated efficiency were presented for each case using gasoline. It could be observed that the engine speed had the major impact on the optimum SOI timing. Even though the engine load increased by five times amongst the cases presented, which meant the fuelling rate increased proportionally, the SOI for best indicated efficiency remained nearly constant.

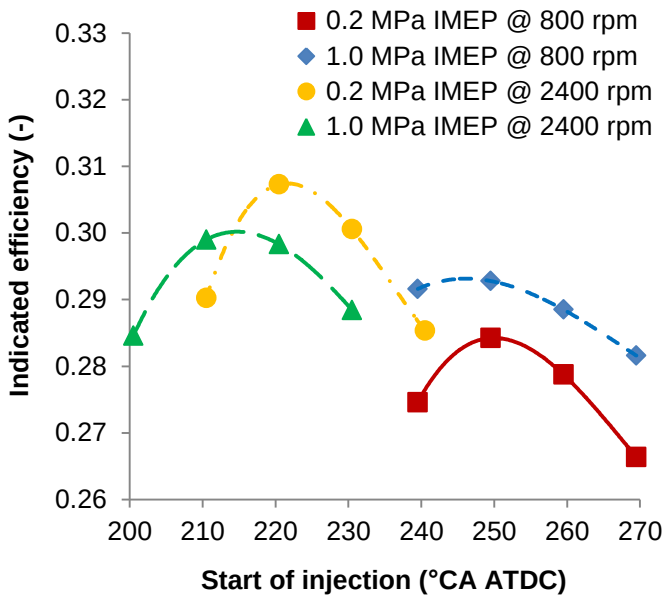

Figure 8.1 – Indicated efficiency during the injection sweeps with gasoline at 800/2400 rpm and 0.2/1.0 MPa IMEP.

A similar trend to the indicated efficiency was observed in the combustion efficiency results shown in Figure 8.2. At the lower engine speed the time available for air-fuel mixing increased and later start of injection could be used, with associated lower spray penetration and less fuel impingement. However, as the engine speed increased to 2400 rpm the time available for charge homogeneity dropped and the SOI had to be advanced by about 30° CA. In this case it could be inferred that any possible fuel impingement given by earlier injections, particularly on the cylinder liner, was offset by the gains in mixture

preparation at longer mixing times. The higher wall temperatures at 2400 rpm resulted from the shorter time available for heat transfer also contributed to accelerate the vaporisation of any impinged fuel. Figure 8.1 and Figure 8.2 also show that the indicated and combustion efficiencies were more sensitive to the SOI at the higher engine speed. This was attributed not only to the shorter time available for mixture formation, but also to the eminence of fuel short-circuiting at start of injections before 210°-220° CA ATDC.

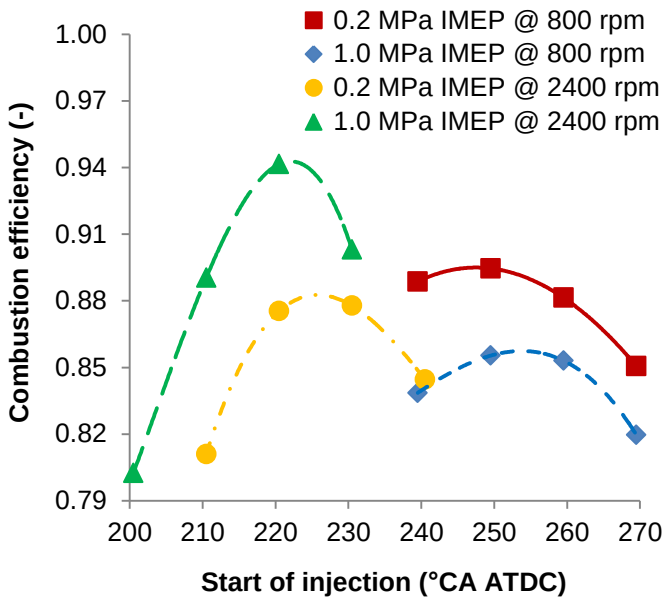

Figure 8.2 – Combustion efficiency during the injection sweep with gasoline at 800/2400 rpm and 0.2/1.0 MPa IMEP.

Similar results were obtained with ethanol, although the SOI timings were advanced by about 5°-10° CA towards BDC due to a larger fuel mass injected. The optimised SOI results obtained for gasoline and ethanol in the range of engine speeds and loads considered are presented in Figure 8.3. At 2400 rpm the SOI timings of gasoline were in the range of 220°-230° CA ATDC, whilst for ethanol it was found between 210°-220° CA ATDC. Furthermore, the optimum gasoline SOI timings were more sensitive to variations in load than ethanol, particularly at engine speeds beyond 1200 rpm. At the lowest engine speed and load tested of 800 rpm and 0.2 MPa IMEP both fuels had similar injection timings for best fuel economy. These were found between 260° and 270° CA ATDC, which were later than EVC and IVC timings. In this condition the amount of fuel injected was so small that later injections might have helped to form a more combustible mixture near the spark plug for a more complete combustion.

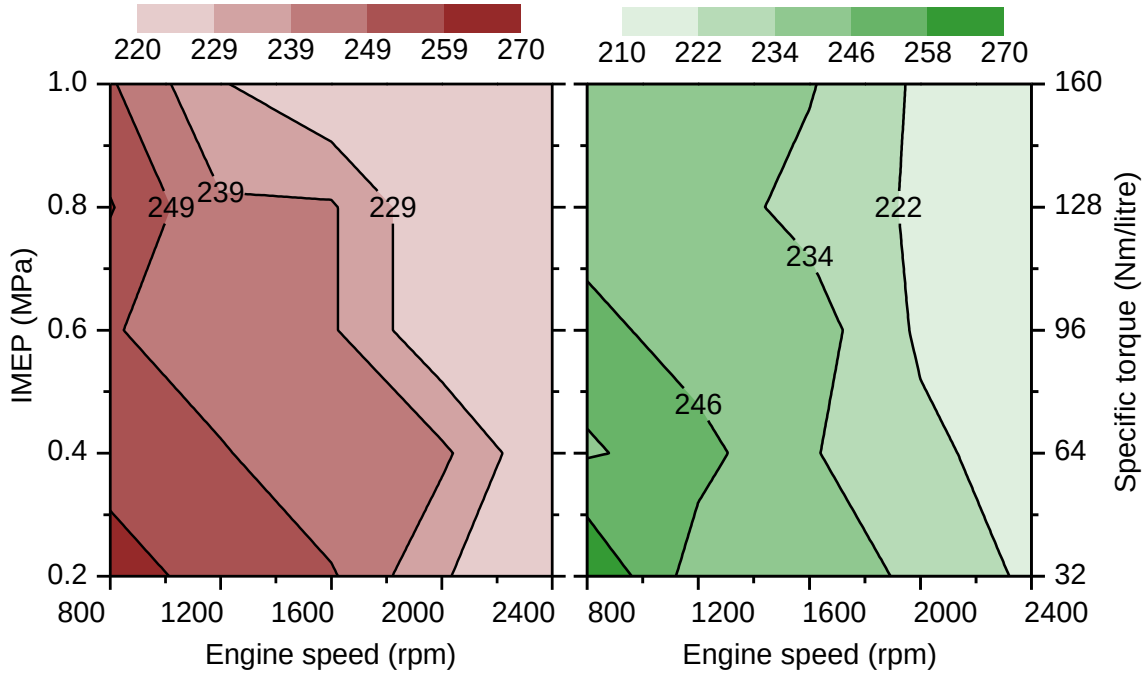

Figure 8.3 – Injection timing (°CA ATDC) versus engine speed and load with gasoline (left) and ethanol (right).

8.3.2 Engine performance, combustion and gas exchange analysis

Gasoline and ethanol operation were compared side-by-side in this chapter under the same engine speeds and loads. The first result presented is the corrected indicated efficiency ($\eta_{i\,corr}$) in Figure 8.4, which considers the supercharger power consumption in the calculation of the net power. Regardless the fuel used, the maximum efficiency was achieved from 800 rpm to about 1600 rpm and in the load range between 0.4 MPa and 0.6 MPa IMEP. With gasoline $\eta_{i\,corr}$ stayed between 0.31 and 0.33, whilst using ethanol it increased by about 10% to 0.32 and 0.35. Compared to a four-stroke 850 cm^3 two-cylinder GDI downsized engine presented by [17], very similar efficiencies were observed with both engines running on gasoline.

As the engine load increased, the supercharger power consumption increased in a larger rate as seen in Figure 8.5, so less net power was available and the $\eta_{i\,corr}$ dropped. At 1600 rpm and 0.8 MPa IMEP, which is equivalent to 128 Nm/dm^3, the engine presented a corrected indicated efficiency around 0.30 for gasoline and 0.31 for ethanol. At a similar engine speed and load, another study

carried out in a four-stroke highly boosted single cylinder 400 cm^3 engine [171] registered around 12% lower fuel consumption with gasoline. Therefore, there was a trade-off between output power and supercharger power consumption, which deteriorated beyond 0.8 MPa IMEP at all speeds and fuels tested. The higher energy consumption by the supercharger resulted from the higher scavenge ratio required to improve the charge purity. At this load it could be observed that the supercharger to indicated power ratio was nearly doubled for both fuels, going from 6% to 11% of the total power.

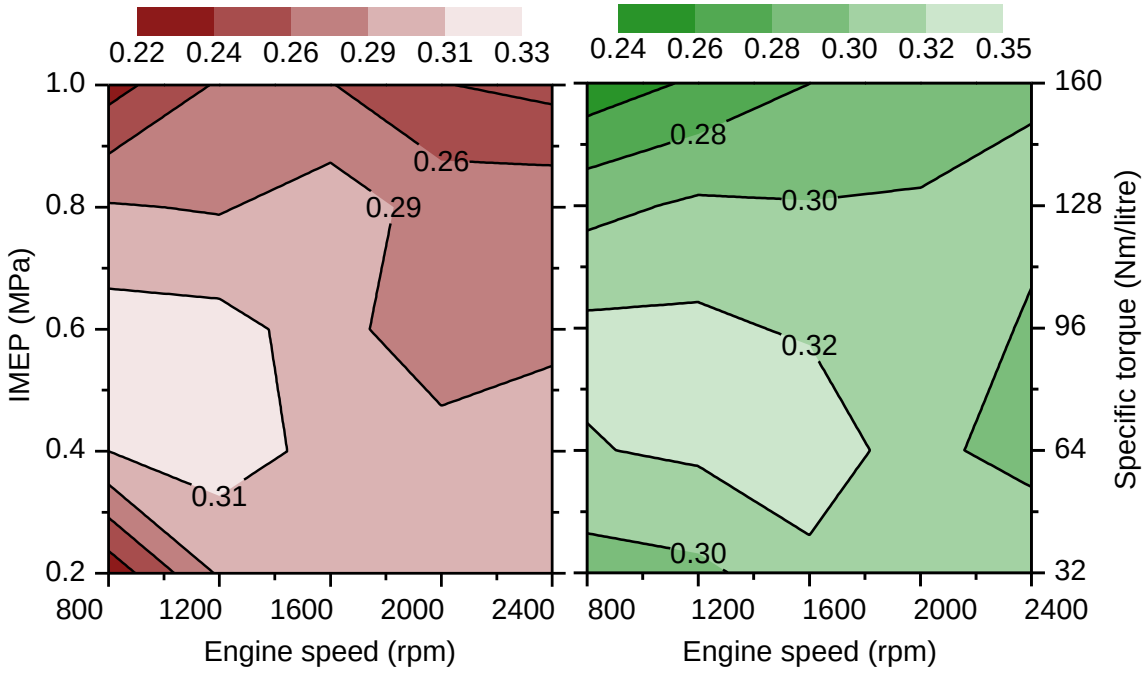

Figure 8.4 – Corrected indicated efficiency (-) versus engine speed and load with gasoline (left) and ethanol (right).

At lower engine loads the larger amount of residual gas trapped resulted in excessive dilution, so the fuelling rate had to be increased to keep an acceptable level of combustion stability. This was particularly noticeable in the gasoline operation at 800 rpm, when the longer time available for heat transfer further reduced the residual gas temperature. At 0.2 MPa and 800 rpm the minimum corrected indicated efficiency of 0.22 was registered. With ethanol this problem was significantly improved by its oxygen content, so the indicated efficiency remained close to 0.3 in this region. In this case, ethanol carried part of its oxidant, nearly 35% by mass, so the highly diluted in-cylinder charge could not hinder the oxygen availability required for a more stable combustion.

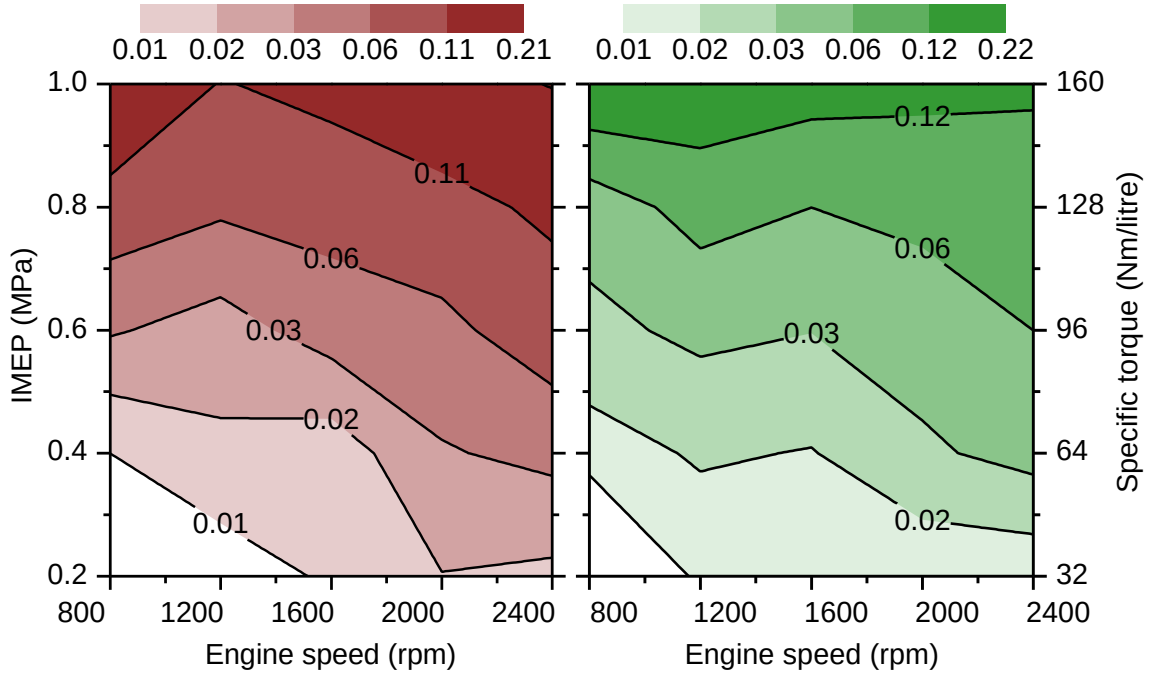

Figure 8.5 – Supercharger to indicated power ratio (-) versus engine speed and load with gasoline (left) and ethanol (right).

As the engine speed increased, the $\eta_{i\,corr}$ tended to slightly decrease due to higher supercharger power consumption as seen in Figure 8.5. At higher engine speeds the time available for the gas exchange shortened and thus higher intake pressures were necessary to keep up the engine load as shown in Figure 8.6. In the same plot it is noted that both speed and load had a similar result over the intake-exhaust pressure ratio as given by the diagonal isolines. The supercharger to indicated power ratio actually behaved similarly from 1600 rpm onwards, although at lower speeds the poor output power was hindered by the higher compressor power demand. At lower engine speeds the time available for gas exchange increased and scavenging losses prevailed for both fuels.

Although the maximum intake to exhaust pressure ratio was detected at full speed and load, the supercharger to indicated power ratio did not increase in the same rate as the output power was maximised in such region. The greater intake pressure required at higher engine speeds also resulted from the incapacity of the electrohydraulic valve train unit to maintain a constant valve opening area throughout the engine speeds, previously seen in Figure 5.8. It is also worth mentioning the lower intake pressure needed at full speed and load operation of

ethanol, which improved the corrected indicated efficiency by about 16% compared to equivalent gasoline operation. Furthermore, the higher efficiency of the ethanol tests benefited from more advanced spark timings towards MBT. In comparison, the gasoline operation was mainly limited by knocking combustion due to the presence of hot residual gas trapped.

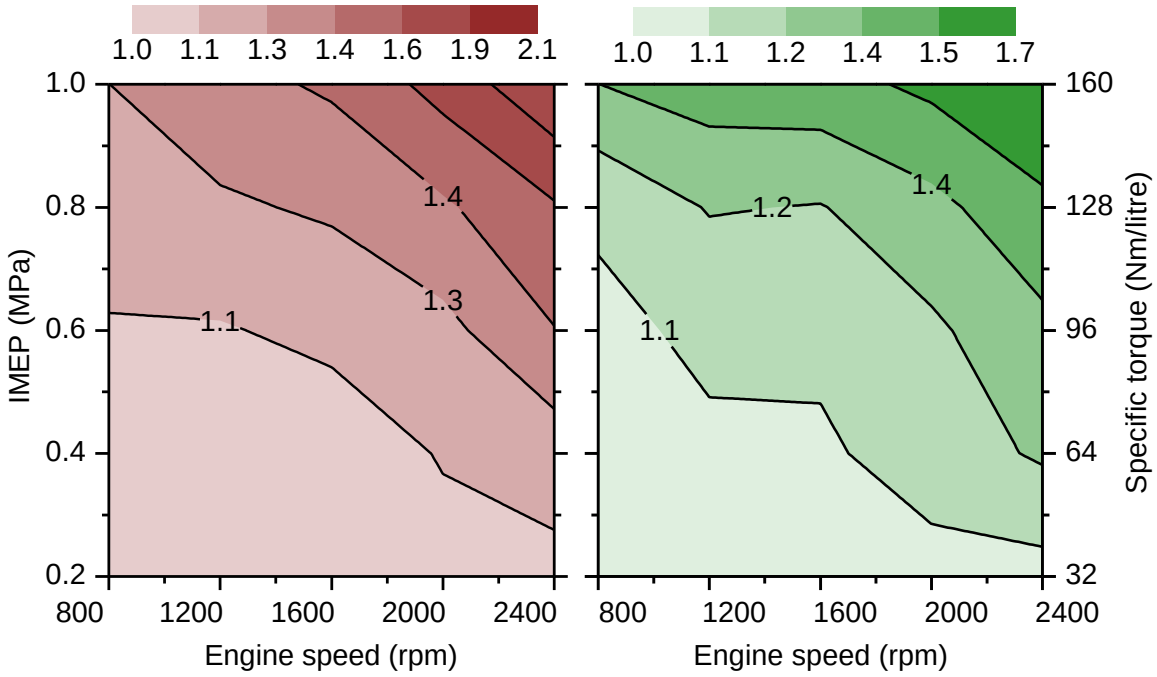

Figure 8.6 – Intake to exhaust pressure ratio (-) versus engine speed and load with gasoline (left) and ethanol (right).

Besides the higher supercharger power consumption at higher engine speeds, the $\eta_{i\,corr}$ values were also affected by the combustion efficiencies seen in Figure 8.7. As the engine speed increased, the time available for air-fuel mixing reduced and over-rich regions were formed particularly at higher loads. By further advancing the SOI could not help the mixture preparation but increase the fuel short-circuiting to the exhaust port. Under these conditions the only way to improve the charge preparation would be adopting higher injection pressures. Interestingly though, the combustion efficiency did not deteriorate continually as the engine speed and load increased. Actually, with both fuels the combustion efficiency remained at 0.9 at full speed and load, which could be explained by the highest combustion temperature and shortest time available for heat transfer. Similarly, the optimum $\eta_{i\,corr}$ values were achieved when the combustion efficiency was maximised between 0.4 MPa and 0.8 MPa and below 1600 rpm.

In this case there was a trade-off between charge stratification at high loads, when the SOI could not be further advanced because of fuel short-circuiting, and combustion dilution at minimum values of charging efficiency at low loads. At minimum loads the ethanol operation showed around 3% improvement in combustion efficiency even at internal EGR levels above 0.7. This higher tolerance of ethanol to EGR was attributed to its higher flame speed and oxygen content compared to gasoline, which improved the combustion process [47].

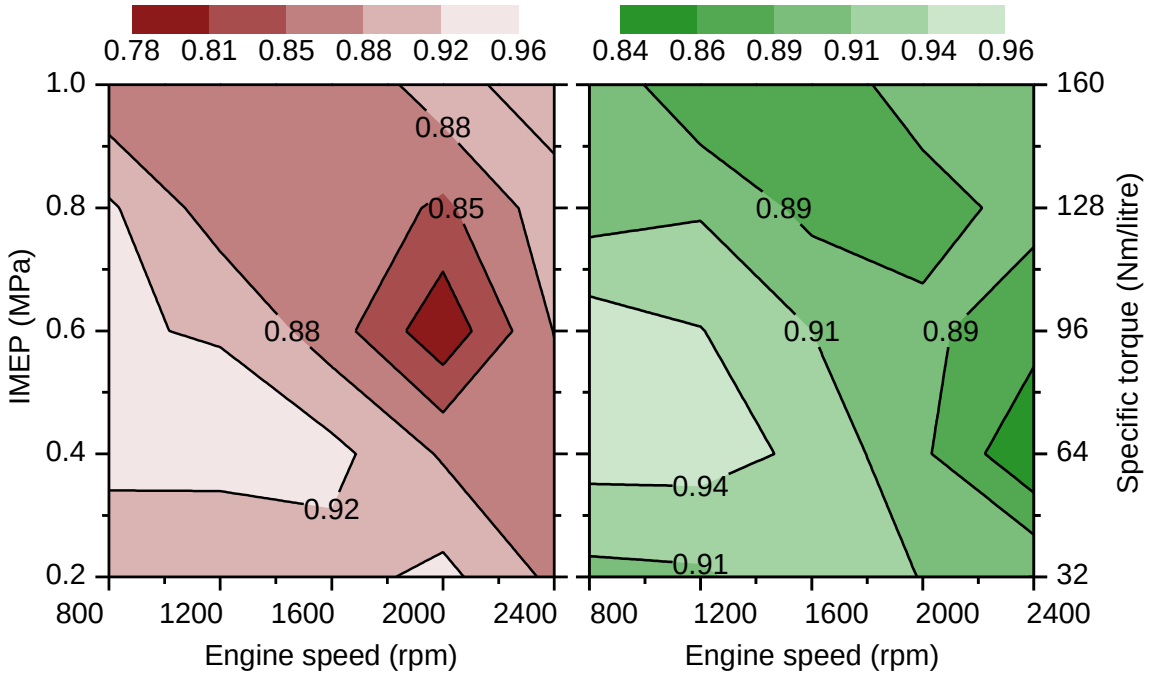

Figure 8.7 – Combustion efficiency (-) versus engine speed and load with gasoline (left) and ethanol (right).

Although ethanol improved the global combustion efficiency by about 2%, both fuels presented some regions where it was severely deteriorated i.e. 0.6 MPa IMEP at 2000 rpm (gasoline) and 0.4 MPa at 2400 rpm (ethanol). With gasoline the combustion efficiency dropped to around 0.8 in this condition, whilst the ethanol fuelled case was found at 0.84. In both cases this poor combustion resulted from a transition between spark ignition (SI) flame propagated combustion and spark assisted compression ignition (SACI) combustion as presented in Figure 8.8. It was already explained in chapter five and exemplified in Figure 5.12 that the SACI concept is a hybrid combustion mode composed of flame propagation and subsequent auto-ignition of the end-gas. As the flame front consumed the in-cylinder charge it compressed the outer regions occupied

by unburnt mixture until the auto-ignition temperature was reached. At this condition multiple ignition points initiated a faster heat release process in the end-gas. The occurrence of this hybrid combustion mode in the two-stroke cycle was related to the large amount of hot residual gas trapped at higher engine speeds, when the time available for gas exchange and heat transfer was reduced. For the fixed intake and exhaust valve timings used, the transition from SACI to SI was not controlled.

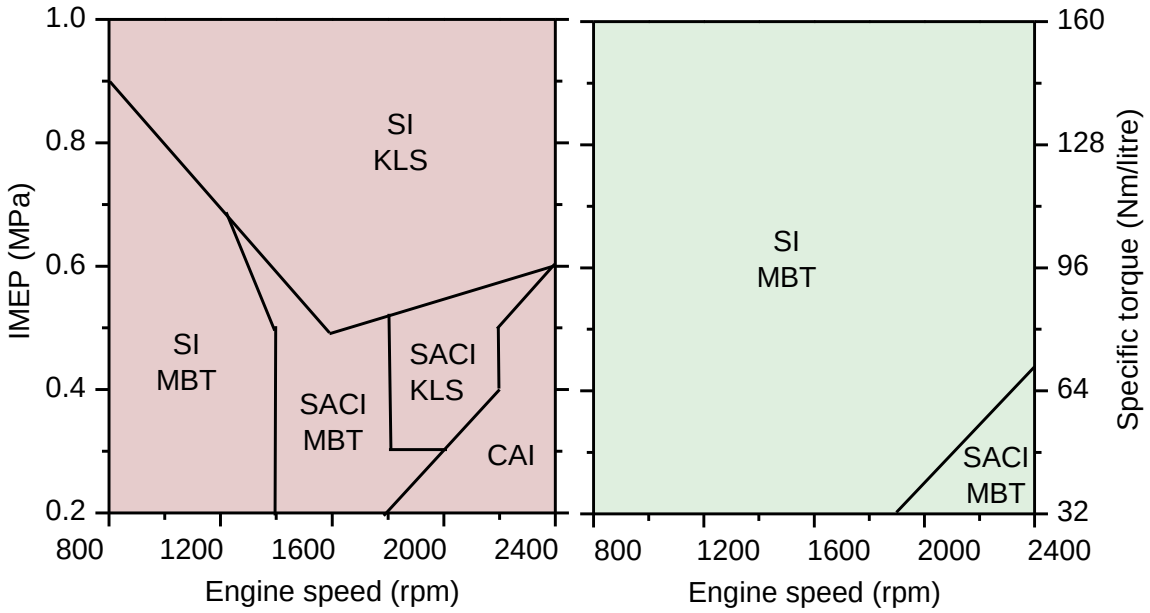

Figure 8.8 – Approximate scheme of combustion modes versus engine speed and load with gasoline (left) and ethanol (right).

The transition from SACI to SI with ethanol took place beyond 1800 rpm due to its higher heat of vaporisation and higher RON. With gasoline this switch was harder to execute because the SACI combustion was limited by excessive heat release rate in the same region. As shown in Figure 8.8, KLS was detected between SACI MBT and CAI combustion. This sequence of events resulted from the increasing temperature of the residual gas at higher engine speeds, so the in-cylinder radius at which the flame propagated heat release triggered the auto-ignition of the end-gas shortened. From 2000 rpm onwards at 0.2 MPa IMEP this radius disappeared and pure controlled auto-ignition (CAI) combustion took place with gasoline. Until about 1400 rpm MBT could be realised from 0.2 MPa to 0.8 MPa IMEP with gasoline due to the larger time available for heat transfer and gas exchange, so the residual gas and end-gas were kept at lower

temperatures. Nevertheless, gasoline operation was mainly dominated by knock limited spark advance (KLS) SI combustion, so the maximum efficiency could not be achieved due to the abrupt heat release particularly at higher engine speeds and loads.

The occurrence of knocking combustion and hence KLS during gasoline operation reduced the in-cylinder peak pressure at higher engine speeds as seen in Figure 8.9. This is clearly visible by the deviation of the horizontal peak pressure contours around 1600 rpm, where the division between MBT and KLS was located. In comparison, ethanol operation was characterised with SI MBT in most regions and SACI MBT in a small area of high speeds and low loads. This fact allowed the achievement of the maximum indicated efficiency as the combustion event could be properly phased as presented in Figure 8.10. Overall, the in-cylinder peak pressures between gasoline and ethanol operation varied between 2 MPa and 6 MPa in the range of loads and speeds analysed. Ethanol presented a lower global peak pressure due to its greater charge cooling effect at a higher heat of vaporisation than gasoline [172].

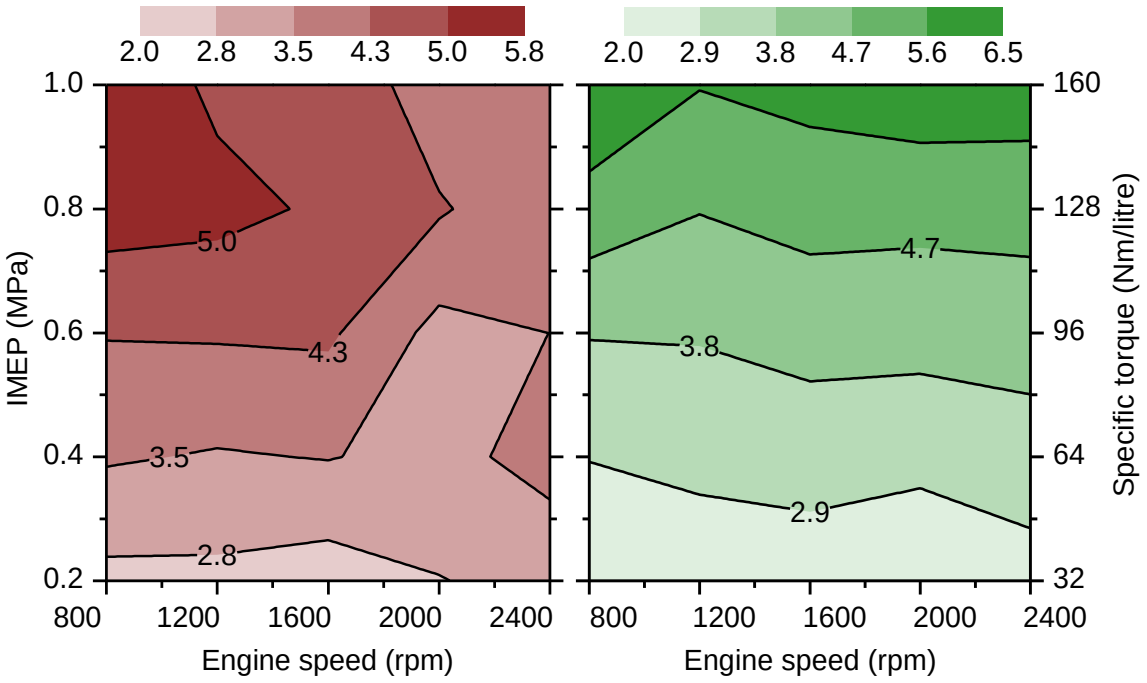

Figure 8.9 – In-cylinder peak pressure (MPa) versus engine speed and load with gasoline (left) and ethanol (right).

Compared to a downsized four-stroke GDI engine [69] running at 126 Nm/dm^3 and 1000 rpm, the peak in-cylinder pressure was found about 30% lower in the two-stroke engine. At a higher load of 160 Nm/dm^3 and 1200 rpm the decrease in in-cylinder pressure reached 50%. The lower in-cylinder peak pressure does not only reduce structural stresses but also enables the optimisation of combustion phasing towards MBT. Therefore, higher indicated efficiencies can be obtained without knocking combustion especially in the case of gasoline combustion.

Figure 8.10 presents the combustion phasing (CA50) given by the crank angle where 50% of the mass fraction burnt (MFB) took place. When comparing both fuels it is clear the advantage of a greater RON of ethanol by allowing a proper combustion phasing throughout the whole operation map. Meanwhile, gasoline was limited by knocking combustion particularly after 1600 rpm. In this case the spark timing had to be retarded so that the middle of the fast burning region (10-90% of the MFB) was shifted towards the expansion phase. According to [8] the maximum torque occurs when half of the charge is burnt around 10° CA ATDC, which was the overall case of ethanol operation. With gasoline this optimum timing was restricted to a small region in the middle of the map, before the higher charge temperature and pressure induced abrupt auto-ignition of the end-gas and the spark timing had to be retarded.

It is interesting to note the advanced CA50 towards TDC at lower engine speeds and loads found between 1° and 7° CA ATDC for both fuels. The relatively large amount of residual gas at lower temperatures reduced the combustion heat transfer to the cylinder walls, which is pointed out as the main cause advancing the CA50 timing [173]. The same work reported that under ideal conditions of adiabatic cylinder walls, half of the MFB would be located at TDC and the peak in-cylinder pressure would be between 5° and 10° CA ATDC to maximise thermal efficiency. In the case of gasoline operation the region between 0.2 MPa and 0.5 MPa from 1800 rpm onwards was also subjected to advanced combustion phasing. Although the residual gas trapped in this condition was at a greater temperature due to the shorter time available for heat transfer, the CA50 remained about 7° CA more advanced than the expected value for MBT. This was actually a result of pure CAI combustion (Figure 8.8), so the combustion

event was mainly driven by the mixture composition and charge temperature history [13], whilst the spark had little effect on the combustion timing.

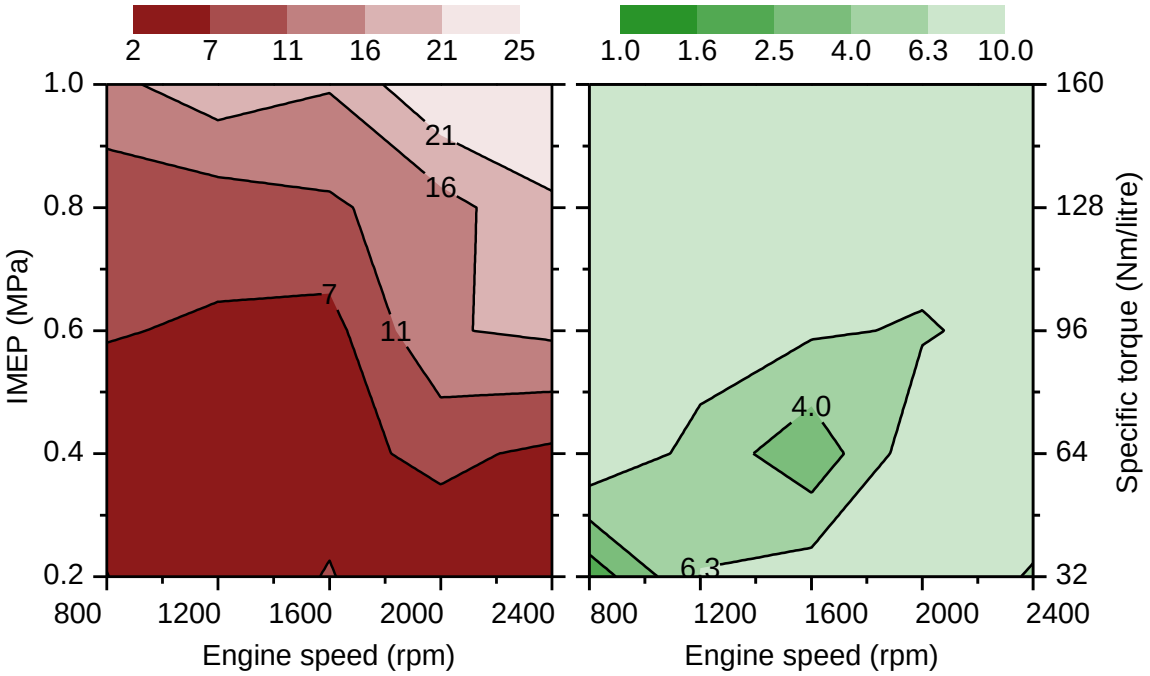

Figure 8.10 – Combustion phasing (°CA) given by 50% of the MFB versus engine speed and load with gasoline (left) and ethanol (right).

The advanced combustion phasing during ethanol operation was found quite symmetric to the load and speed axis. Hence, the same effect of higher charging efficiencies on reducing the residual gas trapped at higher loads was comparable to the effect of higher engine speeds with shorter time available for heat transfer and gas exchange. In both cases either the residual gas trapped level dropped or its temperature increased, so the combustion phasing was retarded at higher values of heat losses. Other operation parameters such as the combustion duration and air/fuel ratio have a smaller effect on the combustion phasing [174].

The occurrence of CAI combustion with gasoline at higher engine speeds resulted from poorer charging efficiencies and shorter time available for heat transfer. This combustion mode had a positive impact on the indicated efficiency due to the quick heat release rate, represented in Figure 8.11 by the short combustion duration calculated from 10-90% of the MFB. Combustion durations as short as 6° CA were registered at the maximum speed and lowest load tested with gasoline, whilst using ethanol this value more than doubled to 14° CA.

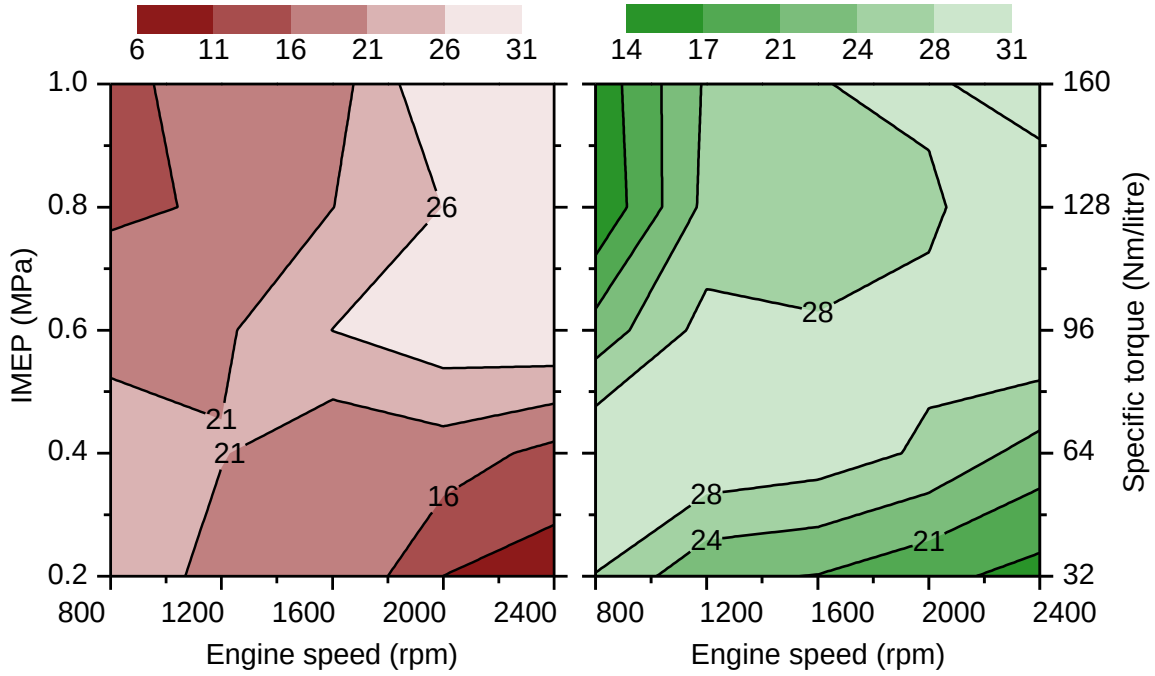

Figure 8.11 – Combustion duration (°CA) versus engine speed and load with gasoline (left) and ethanol (right).

The combustion durations with both gasoline and ethanol fuels presented a visible symmetry around the diagonal line joining the lowest load/speed (bottom left) to the highest load/speed (top right) as seen in Figure 8.11. As the operation points moved away from this line their combustion durations decreased. The longer combustion durations alongside this diagonal resulted from the relatively higher concentration of burnt gas at lower temperatures. This residual gas trapped could not promoted SACI/CAI neither it could be completely scavenged to improve the flame propagation process. From the charging efficiency results presented in Figure 8.12 it can be seen that this diagonal line is located around 50% of residual gas (under ideal conditions).

The short combustion durations achieved with both fuels at higher engine speeds and low loads was attributed to CAI/SACI combustion led by a large amount of hot residual gas trapped. As the load increased at such high speeds, the residual gas trapped level dropped and conventional SI combustion took over. On the other hand, at lower engine speeds and higher loads, the flame speed was accelerated by the higher combustion pressure and temperature as normally obtained in four-stroke engines. The longer time available for the gas

exchange at lower speeds also enhanced the reverse tumble ratio, so the in-cylinder turbulence further improved the combustion process. The better charge homogeneity resulted from the longer air-fuel mixing time also shortened the burning duration in this condition.

The burning durations of ethanol were found slightly longer than those of gasoline due to the larger charge cooling effect, which reduced the in-cylinder temperature and pressure as already pointed out. Interestingly, the lower combustion temperature of ethanol prevailed over its faster laminar flame speed compared to gasoline since a shorter combustion of the oxygenated fuel would be expected a priori. This is a particular feature of ethanol DI engines, whilst in PFI engines part of the fuel vaporises in the intake ports/runners so a hotter charge is inducted and usually promotes a faster combustion process [87][172].

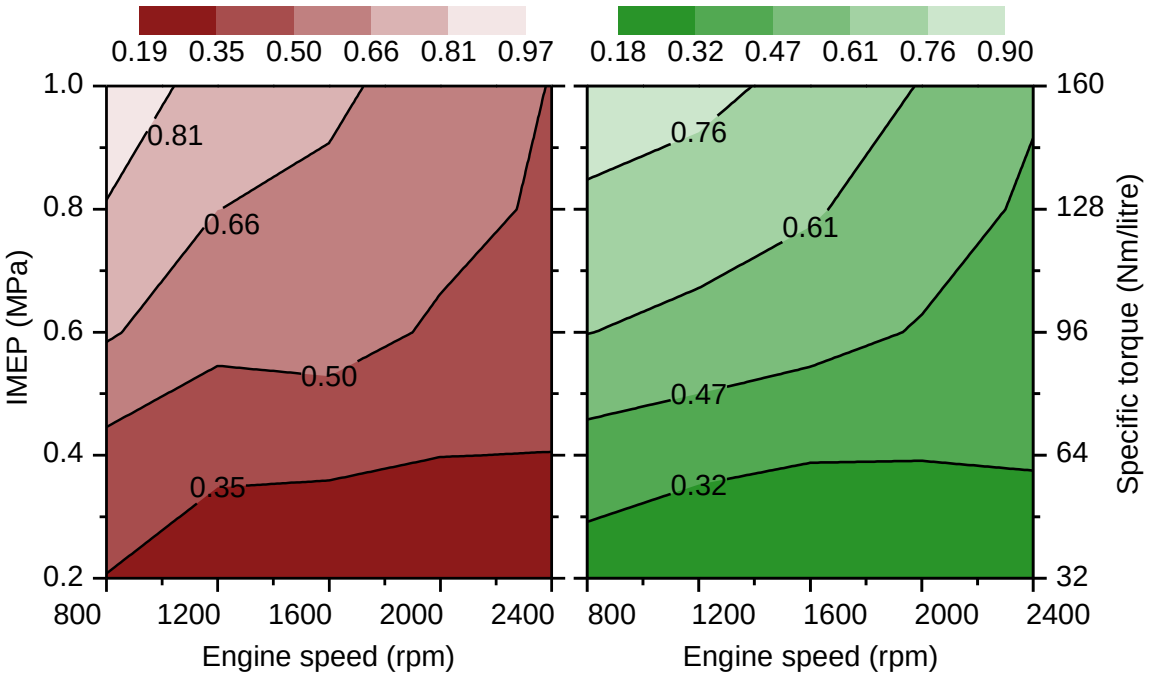

Figure 8.12 – Charging efficiency (-) versus engine speed and load with gasoline (left) and ethanol (right).

In the two-stroke poppet valve engine the SOI took place so close to IVC/EVC that the fuel vaporisation had negligible effect on the induced air mass regardless the use of ethanol or gasoline. With ethanol a slightly lower charging efficiency was required to achieve the maximum power at 800 rpm, which was attributed to its inherent oxygen content particularly at larger fuelling rates. At a

lower charging efficiency the scavenge ratio (Figure 8.13) was also reduced, which in this case improved the corrected indicated efficiency as the supercharger power consumption was minimised.

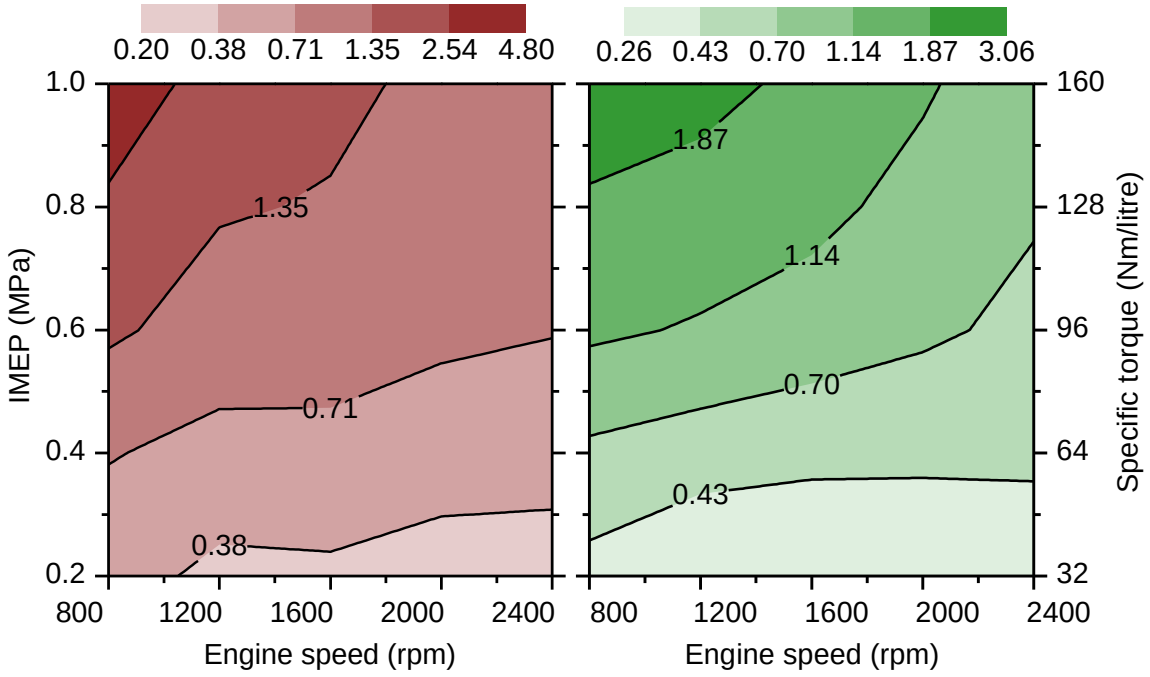

Figure 8.13 – Scavenge ratio (-) versus engine speed and load with gasoline (left) and ethanol (right).

Other than the difference at full load and minimum engine speed, the overall scavenging performance of gasoline and ethanol operations was found similar to each other. At lower engine speeds the scavenge ratio increased more rapidly due to the longer time available for the gas exchange and hence greater air short-circuiting. Similar air trapping efficiency (TE_{air}) results (Figure 8.14) were obtained for gasoline and ethanol operations in most regions despite the full load points around 800 rpm. In this region the air trapping efficiency dropped to only 20% with gasoline and 29% with ethanol because of significant air short-circuiting over longer gas exchange durations. As the engine speed increased, the time available for the gas exchange shortened and the air trapping efficiency improved. Nevertheless, even at higher engine speeds and lower loads the TE_{air} could not exceed 70% as a result of the constant air short-circuiting of 30% imposed by the Benson-Brandham model described in section 6.3.3.

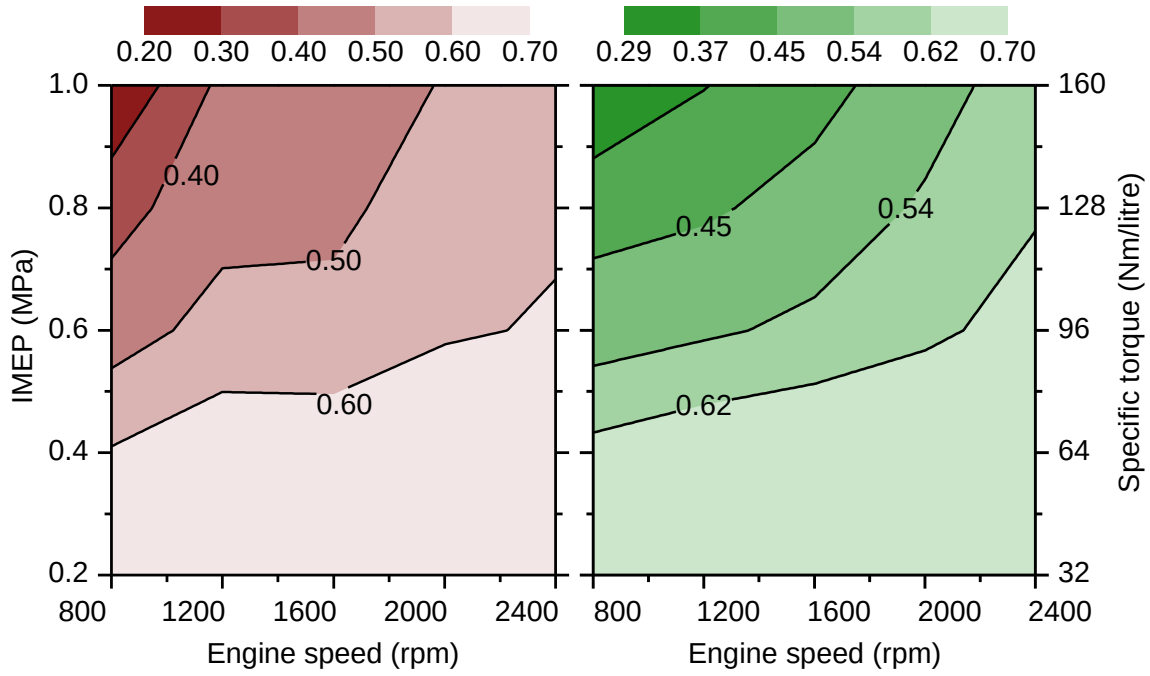

Figure 8.14 – Air trapping efficiency (-) versus engine speed and load with gasoline (left) and ethanol (right).

The fuelling rate was adjusted for maximum indicated efficiency throughout the tests, so the in-cylinder lambda was unknown until the post-processing of the results. It is recognised that maximum fuel economy is achieved with slightly lean mixtures around lambda 1.10, so the excess of oxygen can ensure the combustion of as much as possible fuel [27]. Richer air-fuel mixtures are able to produce higher output power, but at the expense of poorer combustion efficiency and emissions of UHC and CO. On the other hand, excessively lean charges have a negative effect on the combustion completeness due to the lower temperature and poor post-flame oxidation. Therefore, it was expected that the in-cylinder lambda would be around 1.10 all over the operating conditions tested, and this was partially the case for both fuels as seen in Figure 8.15. As the engine load increased at lower speeds, the minimum levels of residual gas trapped and the greater in-cylinder temperatures enabled the achievement of leaner in-cylinder mixtures. Moreover, the higher charge turbulence generated by the larger reverse tumble ratio at such speeds also contributed to increase the lean-burn limit. In the case of gasoline the in-cylinder lambda reached 1.34 from 0.5 MPa to 1.0 MPa IMEP, whilst with ethanol this lambda value was only achieved near full load. The larger heat of vaporisation of ethanol reduced the in-

cylinder temperature so the maximum efficiency was obtained with richer mixtures at about lambda 1.15. At higher engine speeds the amount of residual gas trapped raised and the charge heat capacity also enlarged for both fuels. Therefore, the charge temperature dropped and fuel economy was maximised at gradually richer mixtures, resulting in lambda values between 1.00 and 1.10 in the largest portion of the operation map.

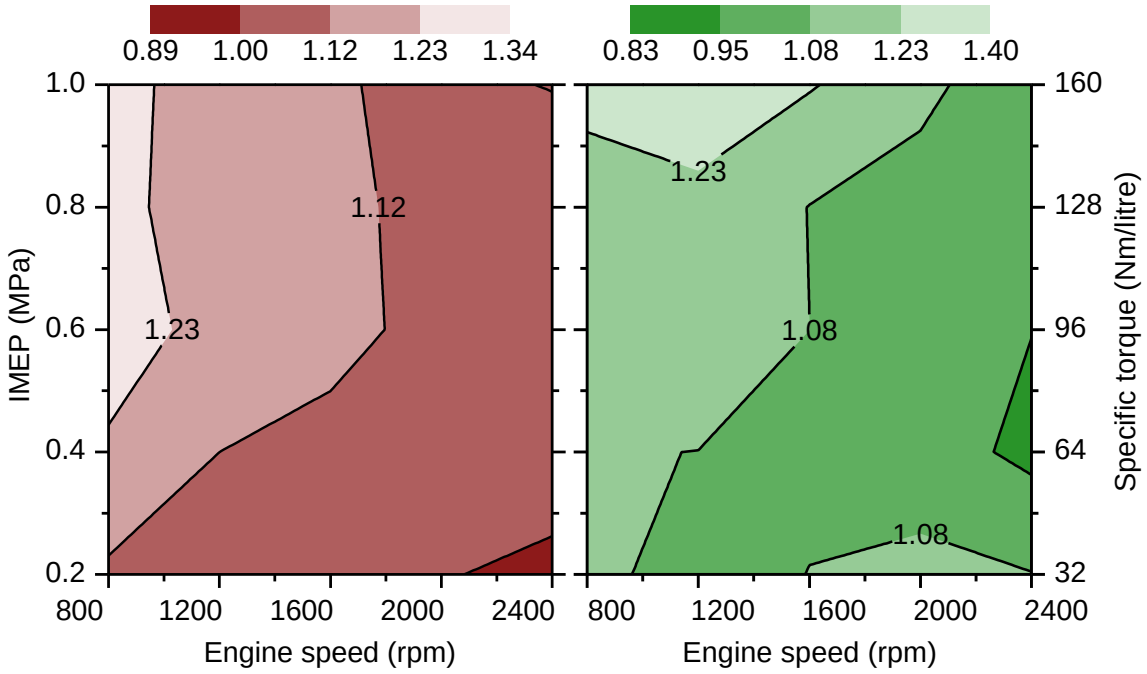

Figure 8.15 – Approximated in-cylinder lambda (-) versus engine speed and load with gasoline (left) and ethanol (right).

Despite the overall lean engine operation with gasoline and ethanol, there were some regions where richer mixtures were employed. At the extremely diluted CAI combustion with gasoline at 2400 rpm and 0.2 MPa IMEP, the in-cylinder lambda was reduced to about 0.90 to improve combustion stability. In comparison, ethanol tolerated leaner mixtures in this region as a result of its higher oxygen content and faster laminar flame speed as previously commented. During ethanol operation the in-cylinder lambda deteriorated in the transition from SACI to CAI combustion at around 0.4 MPa IMEP and 2400 rpm. In this case the larger fuelling rate was required to reduce the in-cylinder temperature through cooling effect so that the heat release process could be better controlled.

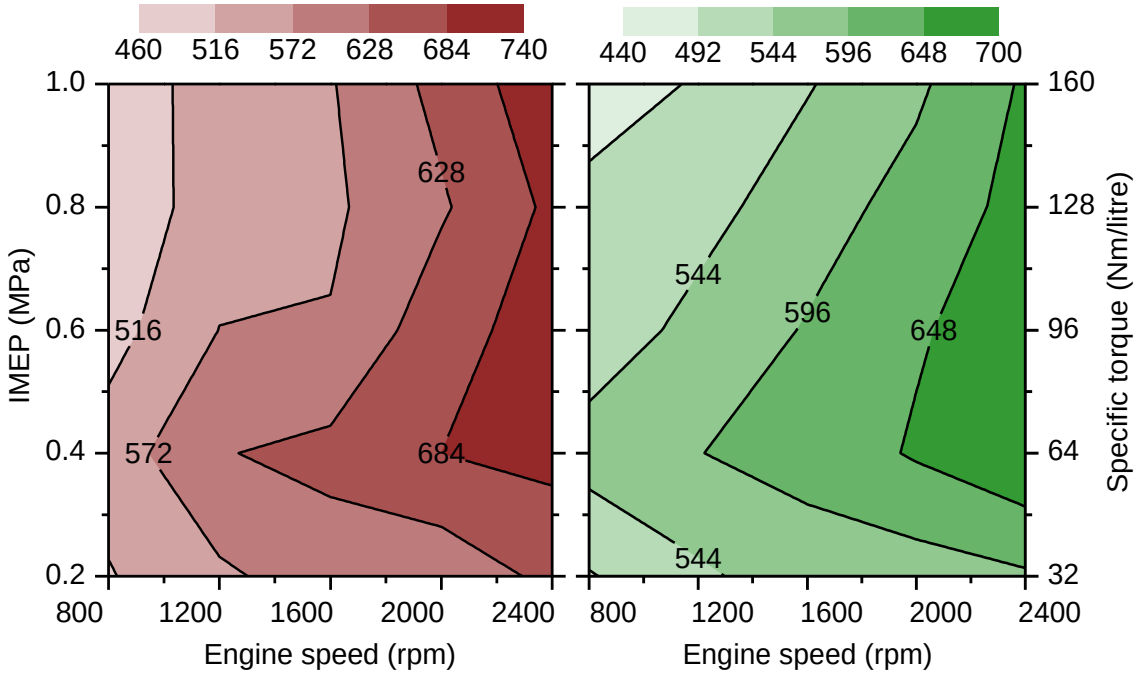

Figure 8.16 – Exhaust temperature (K) versus engine speed and load with gasoline (left) and ethanol (right).

Finally, it is worth mentioning the exhaust temperature trend seen in Figure 8.16 for both fuels. The 0.4 MPa IMEP load showed the highest temperature throughout the operation map regardless the engine speed, which was attributed to the competition between air trapping efficiency and engine load. Until 0.4 MPa IMEP the exhaust temperature increased linearly with the engine load due to the improved combustion rate. In this range the air trapping efficiency remained at about 70% according to the air short-circuiting term found via the Benson-Brandham scavenging model (section 6.3.3). Therefore, a constant fraction of the supplied intake air mass was trapped at all speeds until this value of TE_{air} was achieved, indicating that the exhaust temperature was mainly a function of the engine load. After this load the air trapping efficiency started reducing, so any increase in engine load could not recover the dominant air dilution effect on the exhaust flow. The more uniform temperature distribution with ethanol operation was attributed to the MBT operation throughout the whole map, whilst the gasoline operation was largely knocking limited. The minimum temperature of 440 K was registered at 800 rpm and full load, whilst the maximum of 740 K was found at 2400 rpm and 0.4 MPa IMEP. In average, ethanol exhibited 20 K lower exhaust temperature than gasoline, which was attributed to the lower combustion

temperature with improved overall efficiency. The overall low exhaust enthalpy compared to four-stroke engines may implicate some restriction regarding exhaust after-treatment and turbocharging. Nevertheless, the lower exhaust temperature of the two-stroke poppet valve engine at full load could reduce the need for fuel enrichment to prevent aftertreatment and/or turbine damage [16][17][73].

8.3.3 Exhaust emissions

The emissions of CO, soot and UHC were largely influenced by the start of fuel injections. As the SOI delayed towards TDC the time available for charge preparation shortened and the emissions of CO maximised as a result of poor oxidation of over-rich regions. Conversely, the probability of fuel short-circuiting with SOI after IVC/EVC was minimised and UHC emissions decreased. Similarly, when the SOI was advanced towards BDC more fuel was prone to short-circuit and hence UHC increased, although the mixture formation was improved and CO emissions dropped. This trade-off also affected the soot formation, which increased for late SOIs as a result of diffuse combustion in over-rich regions and pool fires. The NOx formation was less sensitive to the fuel injection strategy and remained strongly linked to the engine load and speed.

From the ISCO emissions of gasoline presented in Figure 8.17 it is clear the poor results around low loads in a variety of engine speeds. The presence of large portions of residual gas in this case inhibited a more complete oxidation of CO into CO_2, particularly when the averaged combustion temperatures dropped below 1500 K [106]. As the engine load increased, the residual gas trapped was minimised and higher combustion temperatures were obtained. This improved CO emissions for both fuels particularly between 0.3-0.7 MPa IMEP. Both gasoline and ethanol operation demonstrated significant emissions at full speed/load due to the short time available for mixture preparation. Although ethanol presented improved CO emissions at lower loads regardless the engine speed, the full speed operation registered poorer values compared to gasoline. This was attributed to the larger fuel mass injected for the same energy substitution at relatively short time available for mixture preparation. Overall, both fuels demonstrated similar CO results varying from 4 to 60 g/kWh. Ethanol

presented 8% more emissions than gasoline in average due to the lower combustion temperature and hence poorer oxidation of CO into CO_2.

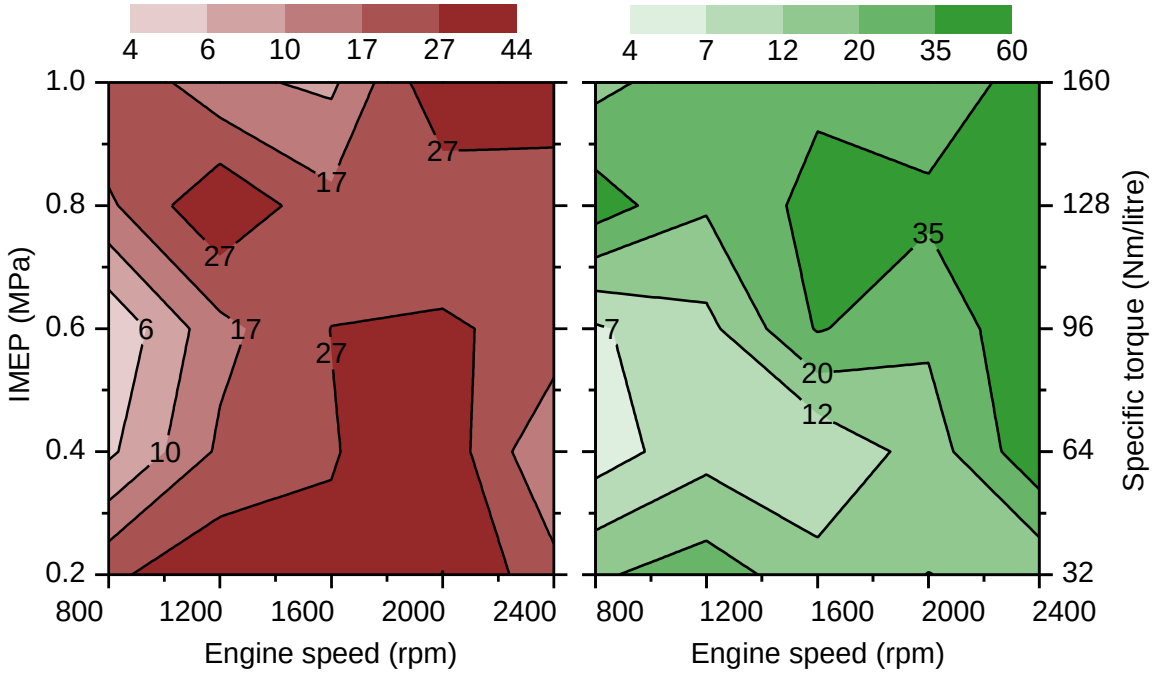

Figure 8.17 – ISCO emissions (g/kWh) versus engine speed and load with gasoline (left) and ethanol (right).

The use of DI greatly improved UHC emissions (Figure 8.18) compared to port fuel injected two-stroke engines, as the fuel trapping efficiency could be maximised independently of the air trapping efficiency obtained. For instance, in the work reported by [31] for a 400 cm^3 loop scavenged two-stroke engine, the minimum UHC emissions of 80 g/kWh was found at 3000 rpm and 0.68 MPa IMEP. At the same load condition but lower engine speed (2400 rpm), the present engine registered around 27 g/kWh with both fuels tested. Nevertheless, some regions for both ethanol and gasoline operations presented poor emissions particularly in the transition between SI and SACI/CAI combustion. Such emissions reflected the fuel enrichment required to improve the COV of IMEP and/or the pressure rise rate. At full load UHC emissions increased due to the relatively late injection of large amounts of fuel, particularly in the case of ethanol. The lower in-cylinder wall temperatures in this case, which resulted from the longer time available for heat transfer and reduced friction, also hindered the vaporisation of any impinged fuel. The possible presence of liquid gasoline/ethanol at TDC also led to partial burn and hence increased UHC

emissions. On the other hand, at full speed the greater wall temperatures favoured the vaporisation of impinged fuel droplets so the combustion became more complete.

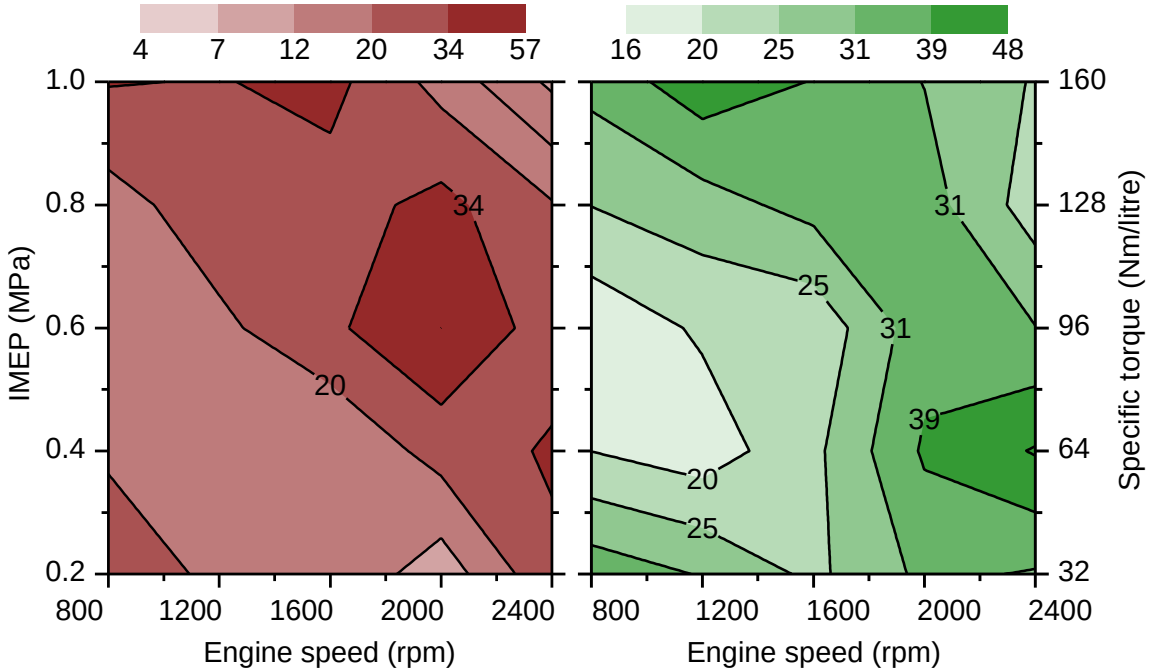

Figure 8.18 – ISUHC emissions (g/kWh) versus engine speed and load with gasoline (left) and ethanol (right).

Both fuels presented lower ISUHC emissions in the mid-low speed range and mid loads, when fuel impingement was minimised at moderate fuelling rates. The improved charge purity also ensured higher combustion temperatures, whilst the mixture formation was enhanced by higher in-cylinder turbulences resulted from the stronger reverse tumble flow. This large turbulence scale followed the scavenge ratio tendency, which was maximised at lower engine speeds when the time available for the charge motion organisation reached its peak (to be seen in chapter nine). Globally, ethanol produced about 19% more UHC than gasoline mostly resulted from the insufficient time available for air-fuel mixing with a greater fuel injected mass. The higher in-cylinder pressures resulted from knock-free operation with ethanol might have also increased the mixture entrainment in the chamber crevices and amplified these emissions [125]. Coincidently, this difference (19%) was of the same order of magnitude of the multiplication factor applied to ethanol's UHC emissions resulted from the poorer FID response to oxygenated fuels (Equation (3.24)). In the absence of this

correction of 22% the emissions of ethanol would be found below those from gasoline, which is occasionally found in the literature for four-stroke engines.

The NOx formation presented in Figure 8.19 was found very consistent and followed the charging efficiency results, which means these emissions were mostly proportional to the engine load. The maximum values of NOx were obtained at full load and lower engine speeds for both fuels, when the oxygen availability was maximised and the internal residual gas level kept at its minimum. In this case the greater combustion temperature favoured the NOx formation mechanism, which was particularly enhanced beyond ~1800 K [27]. As the engine speed increased, the charging efficiency dropped and more residual gas was trapped contributing to reduce the oxygen availability for NOx combination. Moreover, the large fraction of CO_2 in the internal EGR increased the charge heat capacity, so the combustion peak temperature dropped and further mitigated NOx formation [13].

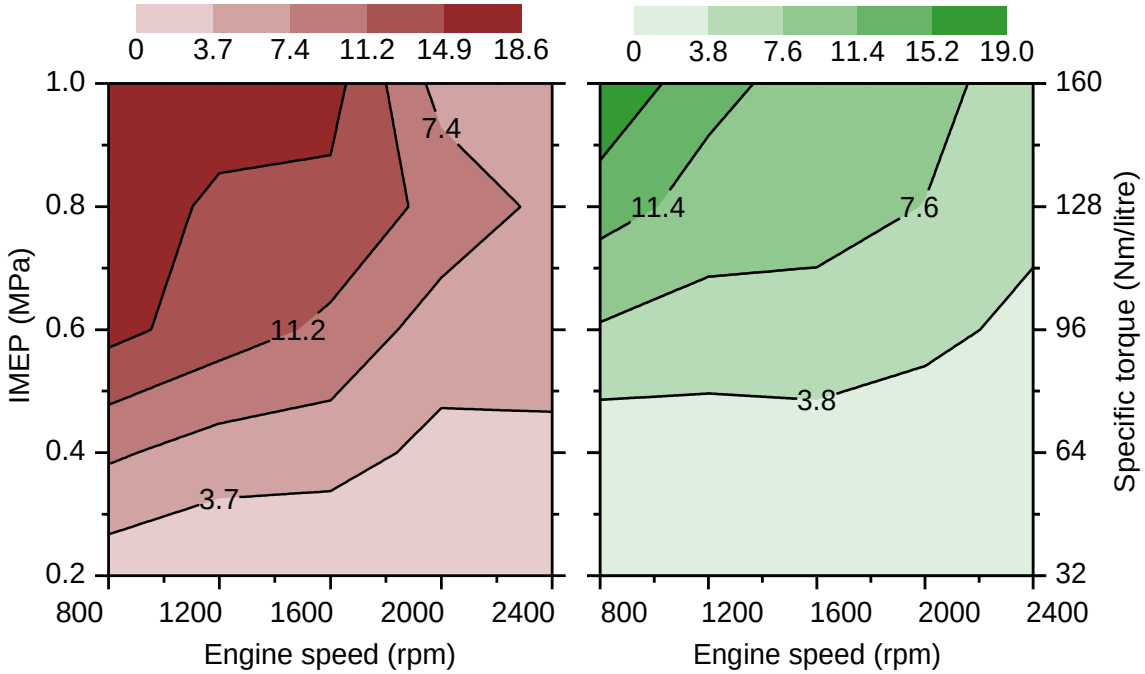

Figure 8.19 – ISNOx emissions (g/kWh) versus engine speed and load with gasoline (left) and ethanol (right).

Overall ethanol produced about 50% less NOx compared to gasoline. This resulted from ethanol's higher latent heat of vaporisation and consequent lower combustion temperature, explaining the higher CO values and longer overall

combustion duration of this fuel. In this case the charge cooling effect played a more important role than the fuel's oxygen content in the NOx formation, which is particular of DI engines [124]. The lower adiabatic flame temperature of ethanol also assisted the NOx reduction. Similarly, 35% lower NOx emissions were obtained in a four-stroke engine operating with stratified charge combustion of ethanol compared to gasoline [12].

Overall, the sum of ISNOx and ISUHC for both fuels was found around the results normally obtained in PFI four-stroke engines. The consideration of NOx and UHC together implies the possible reduction of NOx by fuel enrichment at the expense of poorer UHC emissions, or vice-versa by lean-burn operation. Values around 25 g/kWh (ISNOx + ISUHC) were reported by [27] for a four-stroke four-cylinder engine operating in the range of 0.3-0.7 MPa IMEP. Meanwhile, the equivalent load operation in the two-stroke poppet valve engine registered 24 g/kWh for gasoline and 30 g/kWh in the ethanol fuelled cases.

Alongside engine-out gaseous emissions, ISsoot was also measured for gasoline as seen in Figure 8.20. Nearly zero soot was obtained below 0.3 MPa at all speeds tested, and below 1500 rpm similar low values were found with loads up to 0.5 MPa. Beyond this region soot emissions increased proportionally to the engine load and reached up to 0.75 g/kWh at 800 rpm and full load. Interestingly though, the highest ISsoot was not found at the highest speed/load, when the short time available for the air-fuel mixing would be a problem. Instead, it took place at the lowest engine speeds when the SOI could not be advanced greatly before IVC/EVC due to fuel short-circuiting resulted from the stronger reverse tumble flow in the direction of the exhaust valves. The longer time available for heat transfer at such speeds also hindered the vaporisation of any impinged fuel, so the formation of pool fires may have been enhanced. The greater soot formation after 1600 rpm was mainly a result of shorter time available for air-fuel mixing, so partial burn took place in over-rich regions. The higher emissions after 1600 rpm also reflected the near stoichiometric in-cylinder charge seen in Figure 8.15. At lower engine speeds and loads the air-fuel mixing time increased and favoured the charge homogeneity reducing soot formation.

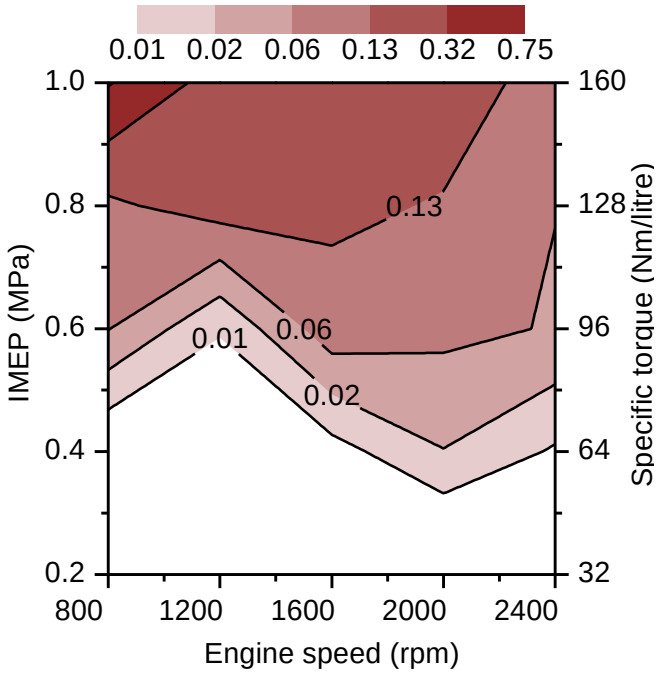

Figure 8.20 – ISsoot emissions (g/kWh) versus engine speed and load with gasoline.

Compared to a downsized GDI four-stroke engine [17], the two-stroke unit produced similar soot values until about 0.7 MPa IMEP at all speeds. For higher engine loads the combustion deteriorated and values up to 10 times greater were achieved particularly below 1600 rpm. Nevertheless, that study employed a centrally mounted multi-hole injector operating at 20 MPa and about three times longer air-fuel mixing times than the ones realised in this study.

The greatest advantage of ethanol operation in the two-stroke poppet valve engine was the total absence of soot throughout the loads and speeds evaluated. Although the lower combustion temperature of ethanol was expected to increase the soot formation, its higher oxygen content ensured a more complete carbon oxidation even at fuel rich conditions. Proportional reductions were obtained by [125] for both particulate number (PN) and particulate mass (PM) at any gasoline-ethanol blends, and not only for pure ethanol as evaluated here. Studies conducted by [124] attributed this behaviour of ethanol to its simpler molecular structure with only two carbon atoms, instead of longer chains as those found in gasoline and other fossil fuels.

8.4 Summary

A sweep of engine loads and speeds between 0.2-1.0 MPa IMEP and 800-2400 rpm, respectively, was evaluated in the two-stroke poppet valve engine using gasoline and ethanol. The fuelling rate was adjusted to provide maximum indicated efficiency, so the gas exchange parameters had to be estimated based on the Benson-Brandham scavenging model due to the lean-burn combustion.

As the engine load increased, the supercharger power consumption increased in a larger rate so the net power and indicated efficiency dropped. A trade-off between output power and supercharger power consumption was found at 0.8 MPa IMEP regardless the fuel used. Overall, ethanol presented nearly 10% better indicated efficiency than gasoline. Ethanol also enabled MBT operation in the whole engine map studied whereas gasoline had several operating points under knock limited spark advance.

The combustion efficiency was maximised at mid-loads and engine speeds below 1600 rpm, when values around 0.93 were achieved with both fuels. In some regions the combustion efficiency dropped to values as low as 0.8 as a result of combustion instabilities and fuel rich conditions. This was particularly the case during the transitions between SACI and SI combustion with both fuels.

Overall, the in-cylinder peak pressures during gasoline and ethanol operation varied from 2 MPa to 6 MPa. Ethanol presented lower values due to its greater charge cooling effect resulted from the higher heat of vaporisation. The lower in-cylinder pressure and temperature also increased the combustion duration of ethanol by a few crank angle degrees compared to gasoline. In this case its faster laminar flame speed could not prevail over the reduced combustion temperature.

Whilst gasoline operation was marked by several combustion modes (SI MBT, SI KLS, SACI MBT, SACI KLS and CAI) depending mostly on the residual gas concentrations, ethanol presented only SI/SACI MBT combustion. In several regions the minimum amounts of residual gas trapped and greater in-cylinder temperatures enabled the achievement of leaner in-cylinder mixtures, with in-

cylinder lambda values of up to 1.34 for gasoline and 1.40 for ethanol. Moreover, the higher in-cylinder turbulence generated by the large reverse tumble ratio also contributed to increase the lean-burn limit especially at lower engine speeds.

The emissions of CO, soot and UHC were largely influenced by the SOI. As the SOI delayed towards TDC the time available for charge preparation shortened and the emissions of CO and soot increased as a result of poor oxidation. Similarly, when the SOI was advanced towards BDC more fuel was prone to short-circuit before IVC/EVC and hence UHC increased. The NOx formation was found more sensitive to the engine speed and load. Ethanol operation globally increased CO and UHC emissions by about 8% and 19%, respectively. In the case of UHC it resulted from larger fuel mass injected with poor mixture preparation and possible greater impingement, whilst the rise in CO was mainly attributed to lower combustion temperature. Nevertheless, ethanol was able to reduce NOx emissions in about 50% compared to gasoline, whilst ensuring absolutely no soot emissions throughout the loads and speeds studied.

Chapter Nine

Investigation of high speed performance and brake parameters in the two-stroke poppet valve engine

9.1 Introduction

In chapter eight the two-stroke poppet valve engine operation was evaluated at several engine speeds and loads using gasoline and ethanol. The promising results compared to four-stroke engines were made possible by means of valve timings and in-cylinder mixture optimisation as described in chapters five, six and seven. As contemporary four-stroke engines often reach higher speeds than those tested, further investigations were required in the high speed range of the two-stroke engine. Furthermore, the supercharger power consumption was estimated based on a constant efficiency and its influence was only evaluated on the corrected indicated efficiency data. For these reasons, the present chapter numerically evaluates the two-stroke poppet valve engine performance at speeds up to 5000 rpm at several intake pressures. The transient CFD data was compared to experimental results to demonstrate the reliability of the model, whilst an analytical study was carried out based on the engine operation in chapter eight. A two-cylinder 700 cm^3 two-stroke poppet valve engine concept was proposed and evaluated using a mechanically driven radial flow supercharger. The supercharger power consumption was correlated to a real compressor map. The engine friction was modelled considering recurrent driven accessories so that bake power, brake torque and brake efficiency could be estimated. At the end of the chapter a low intake valve lift operation was evaluated against full lift mode at several engine speeds and mid-low loads.

9.2 Modelling conditions

The parameters used in the 3-D CFD analysis at several engine speeds and intake pressures are described first. In section 9.2.2 the methods and assumptions used to evaluate the potential of a two-cylinder two-stroke poppet valve engine concept with a mechanically driven supercharger are presented.

9.2.1 Simulation setup

In this numerical analysis a similar mesh described in chapter seven for the mixture formation study was used. The intake and exhaust valve opening and closing times were set according to the values used in chapter eight i.e. EVO 120°, IVO 130°, EVC 230° and IVC 240° CA ATDC, all of them with 8 mm of lift. Based on the mesh size and time-step independency studies presented in chapter four, the number of elements used was around 1.7 million at BDC. A constant time-step of 0.2 °CA was employed thoroughly, but reduced to 0.1° CA at IVO and IVC for about 4° CA to reduce computational instabilities. The simulations started at IVO (130° CA ATDC) and finished by the end of the scavenging process at IVC (240° CA ATDC). Forty-two different operating conditions were simulated at engine speeds varying from 1000 rpm to 5000 rpm and intake pressures in the range of 105.1-280 kPa as presented in Table 9.1. The higher the engine speed the higher were the intake pressures tested aiming at improved scavenging performance. Furthermore, 20 other cases were modelled with 3 mm of intake valve lift in the same speed range, but with intake pressures up to 115 kPa as presented in section 9.3.4.

Table 9.1 – Engine speeds and intake pressures used in the simulations.

		Intake pressure (kPa)									
		105.1	106	110	115	120	140	160	200	240	280
Engine speed (rpm)	**1000**	●	●	●	●	●	●	●			
	2000	●	●	●	●	●	●	●	●		
	3000	●	●	●	●	●	●	●	●		
	4000	●	●	●	●	●	●	●	●	●	
	5000	●	●	●	●	●	●	●	●	●	●

Other than different intake pressures and engine speeds set for each particular case, all the boundary and initial simulation conditions were kept constant. Averaged temperatures and charge composition were based on the experimental results obtained with ethanol between 800 rpm and 2400 rpm and from 0.2 MPa to 1.0 MPa IMEP. The summary of initial and boundary conditions adopted for all the cases are given in Table 9.2. The wall temperatures on the intake side (intake ports, back of intake valves and runners) were set to 320 K, whilst on the exhaust side they were set to 400 K. The piston, cylinder head and liner wall temperatures were set to 450 K, 420 K and 400 K, respectively, based on the

firedeck temperature correlation of [155]. The intake ports were initialised with pure air, whilst the cylinder and exhaust ports volumes were full filled with burnt gases at stoichiometric conditions. The reason for filling these regions with burnt gases is that neither fuel injection or combustion were simulated, so the single cold flow cycle could be initialised with approximated species concentrations. Stoichiometric conditions were employed for these zones otherwise it would have been impossible to distinguish the fresh charge from the remained air from lean-burn combustion. The in-cylinder pressure at the beginning of the simulations at IVO was considered the same as the exhaust pressure. In other words, it was assumed a successful blowdown event and associated equalisation of pressures for all cases modelled.

Table 9.2 – Boundary and initial conditions used in the CFD analysis of engine performance.

ECR and EER	9.7:1
Engine speed (rpm)	1000 - 5000
EVC (°CA ATDC)	230
EVO (°CA ATDC)	120
Exhaust pressure (kPa)	105
Exhaust temperature (K)	600
Initial in-cylinder pressure (kPa)	105
Initial in-cylinder temperature (K)	800
Initial velocity components (m/s)	1.0
Intake pressure (kPa	105.1 - 280
Intake temperature (K)	300
IVC (°CA ATDC)	240
IVO (°CA ATDC)	130
Valve lift (mm)	8.0

During the experiments presented in chapters five, six and eight, the gas exchange process was evaluated based on the air trapping efficiency, charging efficiency and scavenge ratio. In this chapter, the concept of scavenging efficiency (SE) is introduced to better describe the gas exchange process. It is defined as the ratio of in-cylinder trapped delivered air mass to the total in-cylinder trapped mass, which indicates how effectively the burnt gases have been replaced by fresh charge as presented in Equation (9.1).

$$SE = \frac{m_{trap\ del\ air}}{m_{trap}} = 1 - EGR_{in} \tag{9.1}$$

Therefore, the SE relies on the determination of the in-cylinder trapped mass (m_{trap}) at the onset of compression, which is not always experimentally possible due to the uncertainty about the residual gas fraction left [48]. In the numerical environment this variable could be easily accessed, which also enabled the calculation of the internal exhaust gas recycled (EGR_{in}) fraction.

The idea of trapped delivered air mass ($m_{trap\ del\ air}$) differs from the trapped air mass ($m_{air\ trap}$) used in the definition of air trapping efficiency in Equation (3.41). At fuel rich conditions these two parameters are identical, since the combustion should use all the available air and no free oxygen should remain for the next cycle. However, under lean conditions some of the fresh charge does not take part in the combustion process and remains inside the chamber in the following cycle. This is basically the difference between scavenging efficiency and charge purity, as the former relies on the trapped delivered air mass whilst the latter uses the trapped air mass only. Consequently, under lean-burn combustion the charge purity is always higher than the scavenging efficiency, although the two parameters match each other at stoichiometric and fuel rich conditions.

9.2.2 Analytical considerations

From the cold flow CFD results (section 9.3.1) and the ethanol fuelled operation presented in chapter eight, a two-cylinder 700 cm^3 concept of the two-stroke poppet valve engine was proposed. Brake parameters as power, torque and efficiency were estimated by subtracting the supercharger power consumption and friction losses from the indicated results. Ethanol was chosen due to its higher averaged indicated efficiency than gasoline (~10%) throughout the operation map studied. In addition, it allowed knock-free operation at all speeds and loads tested so the in-cylinder peak pressure became a function of the engine load only. This was particularly important during the estimation of the friction mean effective pressure (FMEP), which is a function of the in-cylinder peak pressure.

The FMEP was estimated based on the Chen-Flynn friction model [175], modified by [176] to be used in one-dimensional engine simulation as seen in Equation (9.2).

$$FMEP = A_f + \frac{1}{n_{cyl}} \sum_{i=1}^{n_{cyl}} \left[B_f (p_{max})_i + C_f \left(\frac{NS}{2} \right)_i + D_f \left(\frac{NS}{2} \right)_i^2 \right] \quad (9.2)$$

The term A_f corresponded to accessories friction i.e. valve train, alternator, DI fuel pump, oil pump and coolant pump. Although these parameters are known for varying with the engine speed, constant mean values of 20 kPa, 8 kPa, 6 kPa, 6 kPa and 5 kPa were respectively used based on recommendations from [8]. The factor B_f was a multiplier of the in-cylinder peak pressure contribution to the engine friction, assumed equal to 0.006. The constants C_f and D_f were both related to the piston mean speed, given by the engine speed (N) and stroke (S). The first constant (C_f) accounted for piston hydrodynamic friction and the second term was related to piston windage losses. Values of 600 Pa.min/m and 0.2 Pa.min^2/m^2 were respectively assumed for each of them. The contribution of in-cylinder pressure and engine speed to the total friction was summed up over the number of cylinders n_{cyl}. The peak in-cylinder pressure (p_{max}) was extrapolated beyond 2400 rpm using Equation (9.3).

$$p_{max}(MPa) = 4.5768 * IMEP(MPa) + 1.3579 \quad (9.3)$$

The coefficient of determination of this linear function to the 25 testing points with ethanol seen in Figure 8.9 was found at 0.98. The strong relation between p_{max} and IMEP independent of engine speed was a result of MBT operation throughout the points studied. From the friction mean effective pressure it was also possible to obtain the friction power by simply replacing the IMEP by FMEP in Equations (3.6) and (3.8).

The supercharger power consumption was calculated from Equation (3.12) but using the efficiency data provided by Rotrex for a mechanically driven radial flow compressor. This type of centrifugal supercharger, seen in Figure 9.1, usually presents higher efficiencies and lower weight than conventional roots type

blowers. Its working principle is similar to contemporary turbochargers, despite the fact the compressor shaft is driven by a pulley through a high-speed planetary drive. In the model employed in this analysis, a Rotrex C15-20, the planetary system provided a multiplication factor of 12.67 to the pulley input speed. It means that if the engine was running at 3000 rpm with a crankshaft-supercharger pulley ratio of 1:3, the compressor impeller would reach about 114000 rpm. This supercharger model presented a maximum pressure ratio of 2.94 and a limiting air flow rate of 0.15 kg/s, with a self-contained lubrication/cooling system and a total weight of about 3 kg [140].

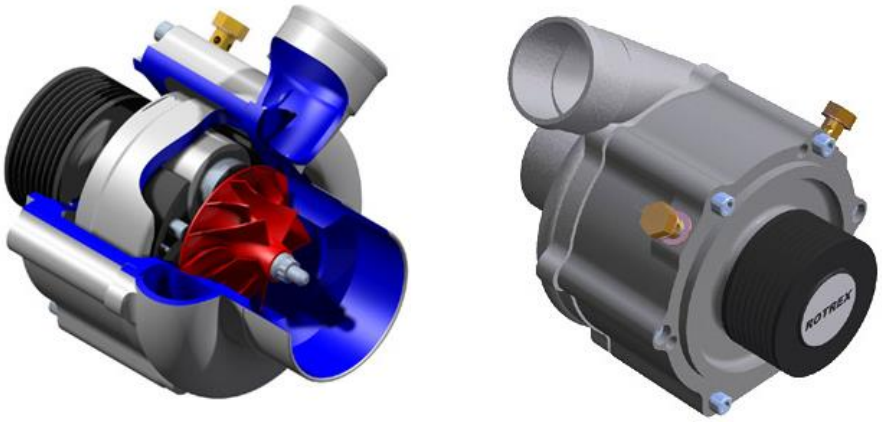

Figure 9.1 – Rotrex mechanically driven radial flow compressor, adapted from [177].

The only parameter related to the engine output performance acquired with the CFD simulations was the fresh trapped air mass. Therefore, it was necessary to assess the amount of fuel burnt so that parameters as the indicated power could be obtained. According to Equation (3.11) the indicated power is the product of indicated efficiency, fuel flow rate and the fuel's LHV (26.9 MJ/kg in the case of ethanol). The two remaining variables, the fuelling rate and indicated efficiency, were then estimated based on the averaged results over the 25 operational points studied in chapter eight. The mean indicated efficiency of 0.325 was used in this case with a standard deviation of 0.014. The fuelling rate was setup based on the averaged in-cylinder lambda of 1.09 found in the range of speeds and loads tested, with a standard deviation of 0.09. The adoption of a constant intake temperature of 300 K (Table 9.2) implied the use of an intercooler between the supercharger and the intake manifold, though its pressure drop was disregarded.

The range of engine speeds simulated was limited to 5000 rpm due to the complexity required of current valve trains to achieve higher speeds. In other words, in four-stroke engines the valve train operates at half the crankshaft speed, so commonly achieved engine speeds of 5000 rpm imply a rotational camshaft speed of 2500 rpm. However, in the two-stroke poppet valve engine the valve train and crankshaft operate at the same speed, so a an engine speed of 5000 rpm requires a similar valve train to those used in four-stroke engines able to achieve 10000 rpm. Such high speed four-stroke engine components are usually found in high performance motorbikes and racing vehicles.

9.3 Results and discussion

The first results presented are those related to the cold flow analysis of the two-stroke poppet valve engine operating in the range of speeds and intake pressures shown in Table 9.1. The gas exchange parameters are presented and compared to experimental results. Following this, the results obtained for the two-cylinder two-stroke poppet valve engine concept are introduced and the engine operation points presented on the supercharger map. In section 9.3.3 it is proposed the use of a dual drive ratio between the crankshaft and the compressor, so the engine performance could be improved. Finally, the last section presents a comparison between 3 mm and 8 mm of intake valve lift operation in the mid-low load range at several engine speeds.

9.3.1 Single cylinder results and model correlation

Figure 9.2 shows that the calculated charging efficiency decreased at higher engine speeds as experimentally observed in previous chapters. At every 1000 rpm increase in the engine speed, the charging efficiency dropped 15% in average independent of the intake pressure employed. It is also interesting to observe that above 140 kPa of intake pressure the charging efficiency levelled off regardless the engine speed, which indicated some degree of choked intake flow. The restriction of the intake air flow rate resulted from the masked cylinder head covering about 120° of the valves perimeter, besides the smaller intake valves of 28 mm in diameter compared to the exhaust valves of 30 mm in diameter. Even though the trapped air mass increased at higher intake pressures, it was offset by the greater charge density in the charging efficiency's

equation denominator (Equation (3.43)) so the charging efficiency could not increase more. Greater charging efficiencies could be obtained by larger intake valves, wave tuning and ram effect in a similar fashion to four-stroke engines [8]. In comparison, the scavenging efficiency continued to increase at higher boost pressures as seen in Figure 9.3. This resulted from the lower rate of increase of the trapped mass compared to the in-cylinder trapped delivered air mass as presented in Equation (9.1).

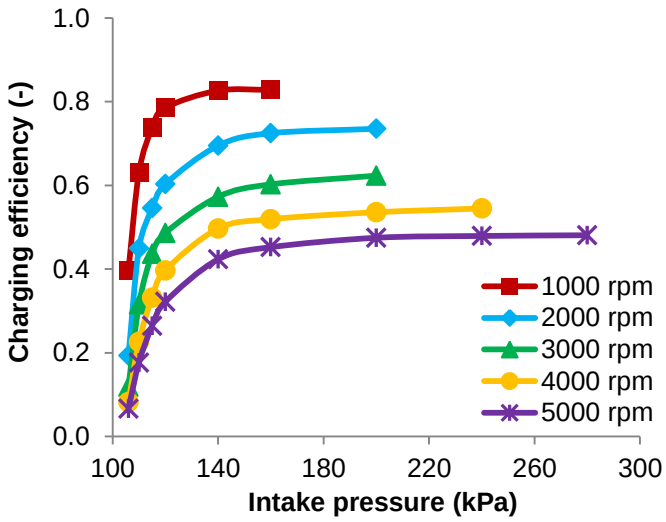

Figure 9.2 – Charging efficiency at different engine speeds and intake pressures.

In addition, Figure 9.3 shows that the scavenging efficiency decreased by about 7% for every 1000 rpm increase in the engine speed. Its rate of rise was noticeably reduced above the intake pressure of 140 kPa, indicating that the removal of burnt gases became less efficient at higher boost pressures. At 1000 rpm and 160 kPa the internal EGR fraction (right axis in Figure 9.3) was 0.12, whilst at 5000 rpm and at the same intake pressure it went up to 0.28. At this full engine speed the internal EGR remained at 0.18 even with the highest boost pressure simulated of 280 kPa. Such value of EGR_{in} is higher than 0.07 (horizontal line in Figure 9.3) usually achieved by four-stroke engines running at full load [8]. Improved scavenging could be obtained by increasing the intake/exhaust valve duration and valve overlap, although it would be at the cost of poorer air trapping efficiency as discussed in chapter six.

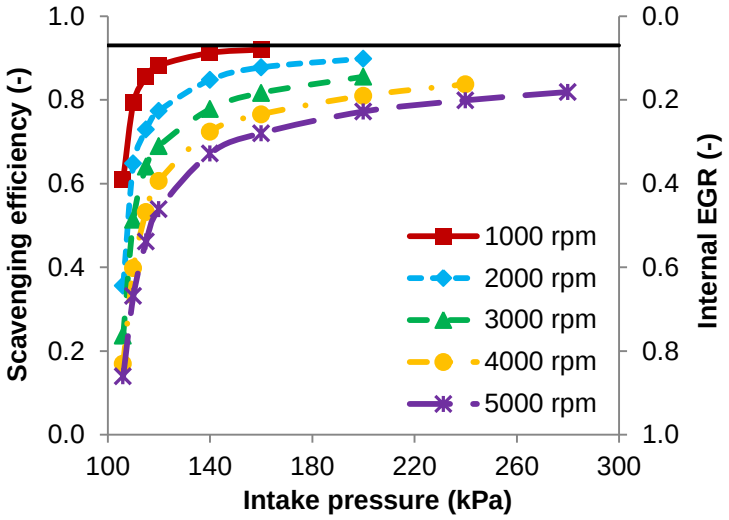

Figure 9.3 – Scavenging efficiency and internal EGR at different engine speeds and intake pressures.

The relatively lower scavenging efficiencies at engine speeds beyond 3000 rpm reflected the insufficient time available for the gas exchange with the constant valve timing adopted. The short intake and exhaust valve opening durations in this case were also mentioned by [28] and compared to crankcase scavenged engines. In externally scavenged engines a nearly constant intake pressure is applied and lasts for the majority of the time the intake valves (or ports) are opened. On the other hand, crankcase scavenged engines have a peak pressure at IVO (or intake port opening) that drops gradually towards the end of the gas exchange phase. Considering that mixing between fresh charge and burnt gases occurs after pressure equalisation, crankcase scavenged engines usually provide superior scavenging at similar operating conditions. Therefore, externally scavenged engines require longer valve/ports opening durations than crankcase scavenged engines. For the sake of comparison, conventional ported two-stroke engines have intake opening durations often around 120° CA [28]. However, in this study 110° CA of intake duration was adopted based on the low speed analysis presented in chapter six at 800 rpm and 2000 rpm.

During the combustion analysis of gasoline and ethanol in Figure 8.11 a short burning duration was found at 800 rpm and full load. It was presumed to be caused by the high levels of in-cylinder turbulence resulted from greater reverse tumble ratios at lower engine speeds. This can be confirmed by the results of averaged reverse tumble ratios as a function of the scavenge ratio during the

intake process seen in Figure 9.4. A quite linear behaviour could be observed with a coefficient of determination close to 0.98. As the engine speed increased, the time available for the gas exchange dropped and the formation of this large scale of turbulence was minimised. The maximum averaged reverse tumble ratio of -12.8 was found at the minimum speed of 1000 rpm and the highest intake pressure of 160 kPa.

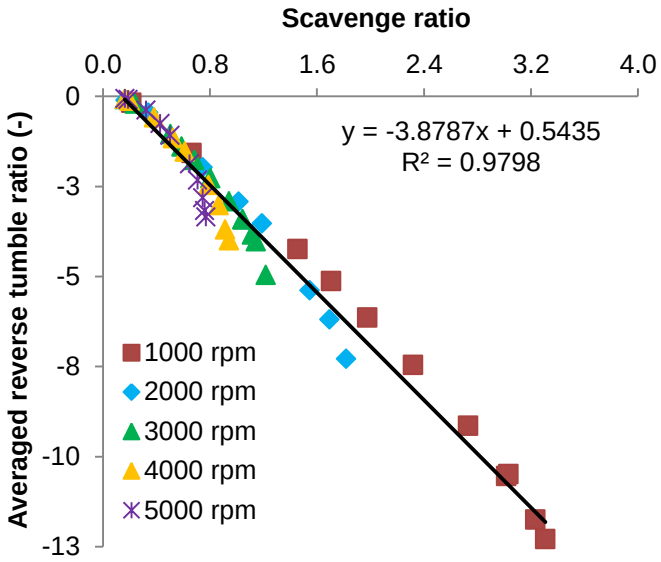

Figure 9.4 – Averaged reverse tumble ratio during the intake at different scavenge ratios and engine speeds.

To correlate the cold flow simulations with experiments the air trapping efficiency was chosen based on its acquisition at fuel rich conditions described in section 6.3.3. Figure 9.5 presents the experimental results obtained in section 6.3.3 from 800 rpm to 2400 rpm at intake pressures between 104 kPa and 213 kPa. Together, the CFD results and the Benson-Brandham scavenging model, used to estimate the in-cylinder lambda at lean conditions in chapter eight, are also presented.

The simulation results were found satisfactory for scavenge ratios beyond 0.5, which was the region of interest for most of the experiments seen in Figure 8.13. It is interesting to observe the numerical results at scavenge ratios below 0.5, which detached from the Benson-Brandham model and tended to zero. It would be expected that at nearly zero scavenge ratios an infinitesimal mass of fresh air entering the chamber could not be short-circuited without displacing or mixing

with the burnt gases. This is especially the case of ported two-stroke engines where the intake/transfer port(s) are usually located far from the exhaust port(s). However, in the two-stroke poppet valve engine the intake and exhaust valves were closely spaced and thus the preferable path for the incoming fresh air was its way to the exhaust port. As the Benson-Brandham model was developed particularly for loop and cross scavenged engines, its prediction capability failed in such conditions. A similar trend could be observed with the experiments (squared dots in Figure 9.5) at the scavenge ratio around 0.3, when a “barrier” limited smaller scavenge ratios of being achieved. Further experiments could not be carried out below this scavenge ratio due to combustion instabilities at high levels of internal EGR. This threshold is sometimes referred as critical scavenge ratio and values around 0.2-0.3 are usually reported [56].

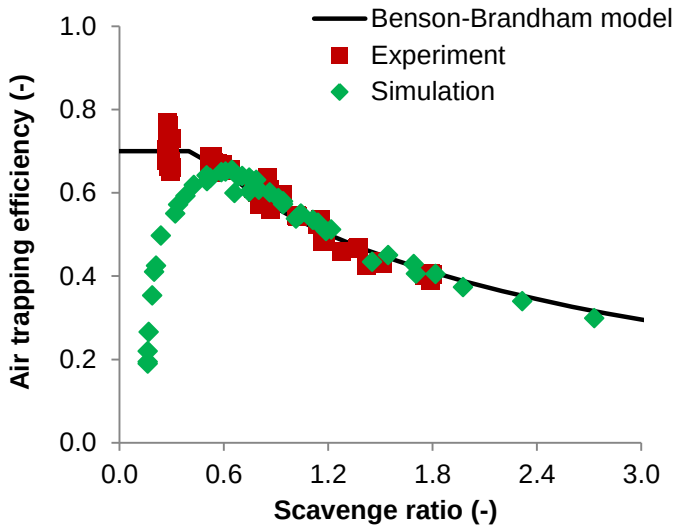

Figure 9.5 – Comparison between simulation and experimental results for the air trapping efficiency at different scavenge ratios.

After comparing the CFD flow model to the experiments, it was necessary to verify if the assumptions regarding a constant indicated efficiency of 0.325 and in-cylinder lambda of 1.09 were able to correlate to the firing tests. Figure 9.6 presents the IMEP obtained at several intake pressures for ethanol operation in chapter eight, together with the CFD results following the assumptions of indicated efficiency and in-cylinder lambda. The correlation for these cases with engine loads varying from 0.2 MPa to 1.0 MPa IMEP at 2000 rpm was considered acceptable. The largest difference was found at the intake pressure of 115 kPa mostly due to an overestimation of indicated efficiency in about 3%.

The slight over-prediction of the IMEP values were attributed to minor differences in exhaust pressure and in-cylinder lambda from the averaged values used, as well as blow-by losses which were not numerically considered.

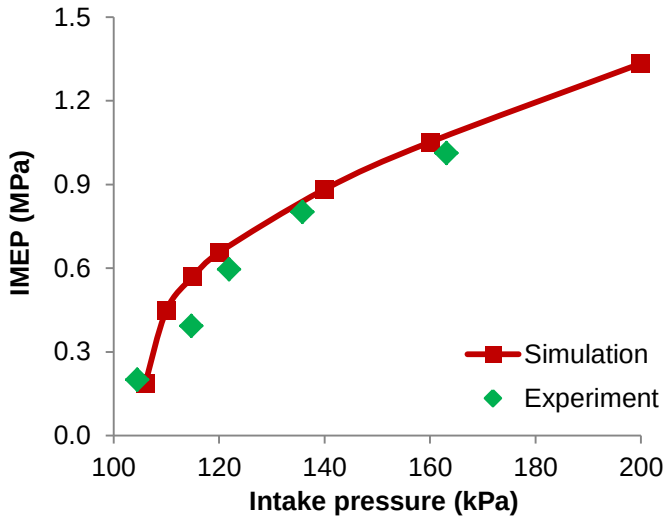

Figure 9.6 – Comparison between simulation and experiments at 2000 rpm and different intake pressures.

9.3.2 Analytical evaluation of a two-cylinder two-stroke engine concept

A two-cylinder 0.7 dm^3 two-stroke poppet valve engine was modelled and its performance evaluated by taking into consideration the engine friction and supercharger power consumption. The intake pressure and air flow rate results were matched with a Rotrex C15-20 mechanically driven radial flow compressor, which provided optimum values of efficiency alongside the engine's operational curve. The supercharger map and some of the engine operation points are presented in Figure 9.7, which were linked by a second order polynomial trend with a coefficient of determination close to the unit. Every efficiency island is cut by the compressor rotor speeds in rpm, which were limited on the left by surging, on the right by choking and on the top by the rotor's speed limit (180000 rpm).

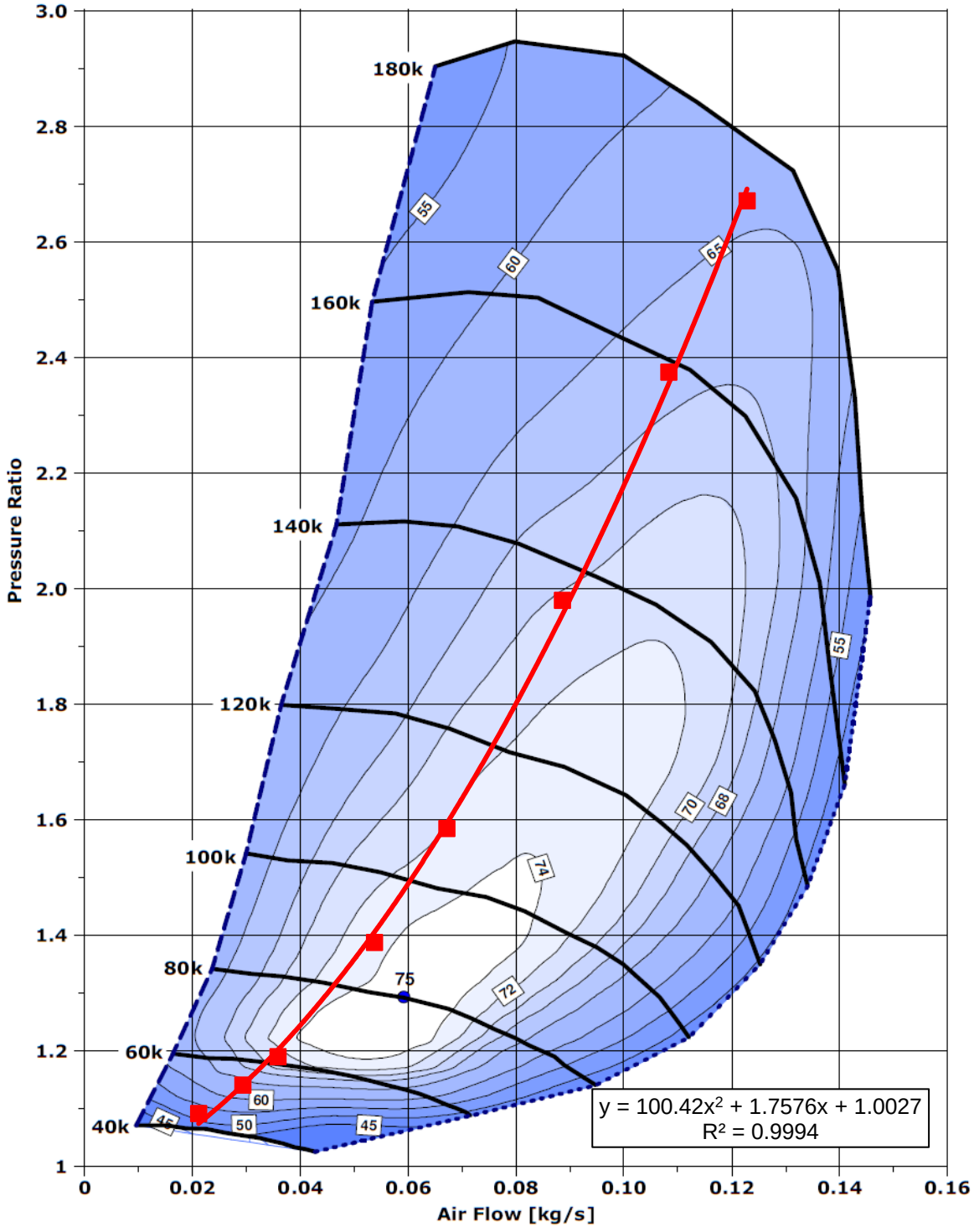

Figure 9.7 – Rotrex C15-20 supercharger efficiency map with estimated engine operation points.

Figure 9.8 presents the specific brake power as a function of the intake pressure from 1000 rpm to 5000 rpm. When both intake pressure and engine speed increased, the output power reached a maximum of 70 kW/dm^3 at 5000 rpm and 280 kPa of boost. At a constant intake pressure, the higher the engine speed the

smaller was the gain in power. For instance, from 1000 rpm to 2000 rpm the power nearly doubled at an intake pressure of 140 kPa. At the same intake condition and by varying the engine speed from 4000 rpm to 5000 rpm, the output power increased by merely 7%. It basically reflected the poorer charging and scavenging efficiencies found at higher engine speeds resulted from insufficient time available for the gas exchange process. At engine speeds above 3000 rpm higher specific power would be achieved by increasing the intake pressure, although the selected supercharger was limited to pressure ratios around 2.8. Moreover, the efficiency of superchargers usually drops at extreme high pressures, so the overall engine efficiency would be expected to fall as well.

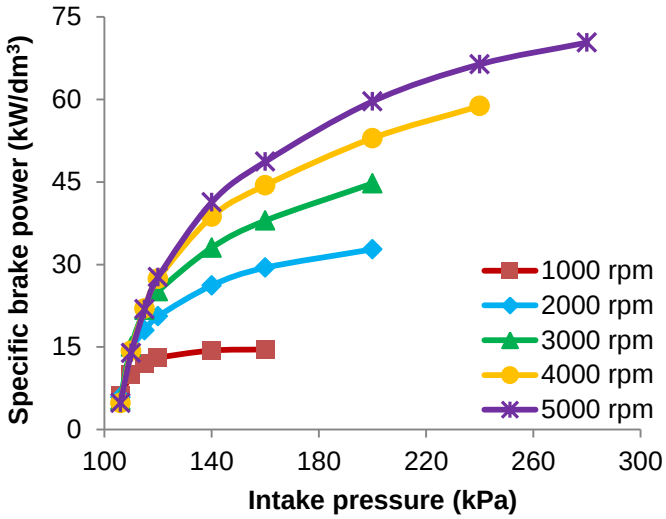

Figure 9.8 – Specific brake power at different engine speeds and intake pressures.

It is interesting to observe from Figure 9.8 the stabilization of output power at 1000 rpm after about 120 kPa of intake pressure. This reflected the lower rate of increase in charging and scavenging efficiencies presented in Figure 9.2 and Figure 9.3, respectively. After this intake pressure the engine output power was offset by the supercharger power consumption, so the brake power remained constant. Similarly, all other speeds are expected to have a point where any increment in boost pressure does not result in any higher brake power. Nevertheless, these higher pressure conditions were not considered as current compressors are usually unable to reach such circumstances efficiently.

As shown in Figure 9.9, both the absolute and relative values of the supercharger power consumption went up rapidly as the intake pressure (or load) increased at 2000 rpm. In comparison, the percentage of frictional losses decreased with the load and its absolute value remained almost constant. Similar trends were observed at 5000 rpm as seen in Figure 9.10, but with a higher fraction of friction losses. At each engine speed, the brake power was optimised at intermediate intake pressures because of the trade-off between friction and boosting parasitic losses. At 2000 rpm the best compromise in brake power was achieved with 120 kPa boost, whilst at full speed it occurred at 160 kPa.

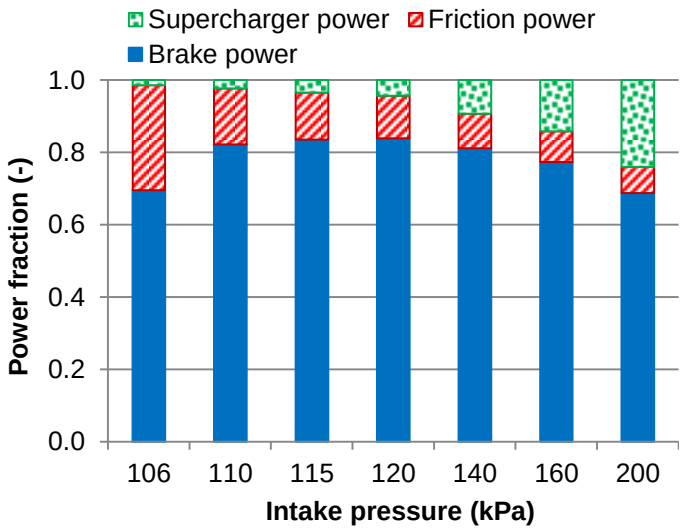

Figure 9.9 – Indicated power breakdown at 2000 rpm and different intake pressures.

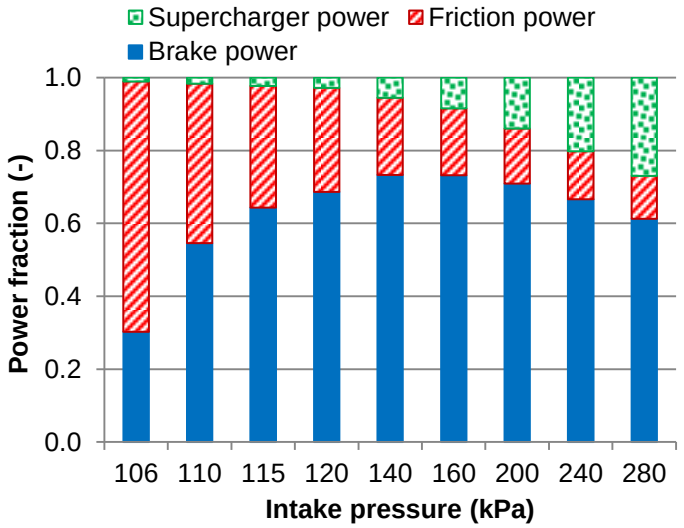

Figure 9.10 – Indicated power breakdown at 5000 rpm and different intake pressures.

As the engine speed increased from 2000 rpm to 5000 rpm the friction power increased by about four times at a constant intake pressure. Meanwhile, the supercharger power consumption fraction increased just a few percent due to a different operating point in a more/less efficiency island. Similarly to four-stroke engines, a large portion of the indicated power was consumed by friction at higher engine speeds and lower loads, although the situation was improved by increasing the load via higher boosting pressures.

Figure 9.11 shows that the maximum brake efficiency of 0.31 could be obtained at all engine speeds, but at a specific brake power less than 32kW/dm^3. In comparison to downsized four-stroke engines, similar efficiencies could be obtained at a specific brake power of 50 kW/dm^3 [71]. As the power requirement increased, the brake efficiency dropped at all speeds as a result of supercharging losses. At very low power demands, instead, friction losses prevailed and decreased the brake efficiency. Therefore, the supercharger power consumption played a more important role than engine friction throughout the regimes studied. The trade-off between output power and supercharging power consumption seen in Figure 9.8 had a direct effect on the brake efficiency at all engine speeds. In the worst case, at 1000 rpm, the brake efficiency monotonically decreased whilst no gains in output power were obtained after 13 kW/dm^3 and a boost pressures of 120 kPa.

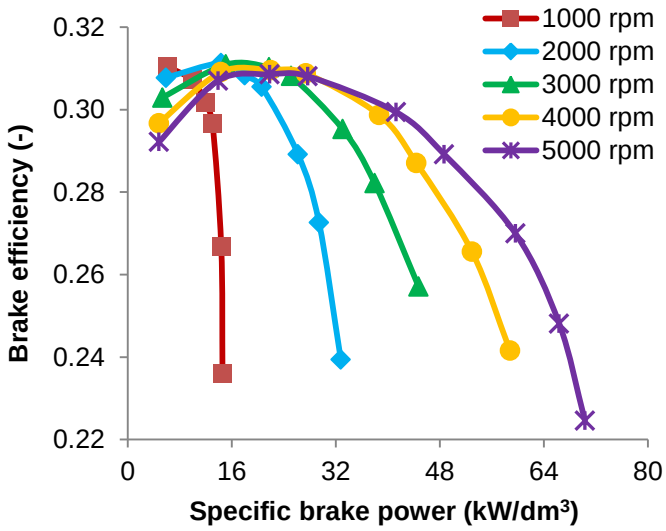

Figure 9.11 – Brake efficiency and specific brake power at different engine speeds.

In view of the compromise between specific brake power and brake efficiency, several arrangements were evaluated based on a single drive ratio between the crankshaft and the supercharger. To enable the two-cylinder 700 cm^3 two-stroke engine to achieve the maximum brake power at full speed, a supercharger drive ratio of 2.77 was chosen. The full load specific power and torque curves with this single drive ratio arrangement are presented in Figure 9.12. The maximum specific brake power of 70 kW/dm^3 and torque of 132 Nm/dm^3 were registered at 5000 rpm, although a significant 105 Nm/dm^3 was obtained at only 2000 rpm.

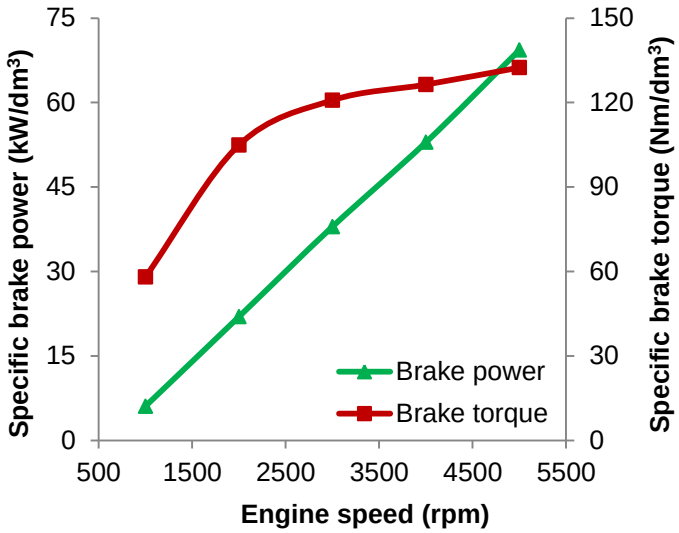

Figure 9.12 – Specific brake power and torque at full load and different engine speeds.

The brake torque output increased linearly with the engine speed until 2000 rpm, above which its rate of increase reduced due to poorer charging/scavenging. At this speed the scavenging efficiency levelled off and the charging efficiency started to decrease as shown in Figure 9.13. Hence, what actually ensured the brake torque to keep increasing after 2000 rpm was the improved air trapping efficiency. At 5000 rpm the charging efficiency dropped to 0.48 under an intake pressure of 270 kPa, whilst the scavenging efficiency remained unchanged at 0.8 since 2000 rpm. Conversely, the air trapping efficiency increased to its maximum value of 0.63 due to the shorter time available for air short-circuiting. The lowest torque was produced at 1000 rpm due to the combined minimum scavenging and charging efficiencies of 0.61 and 0.40, respectively. The internal EGR level remained below 0.4 at all full load conditions, which was the same threshold set in the development of a two-stroke poppet valve diesel engine [49].

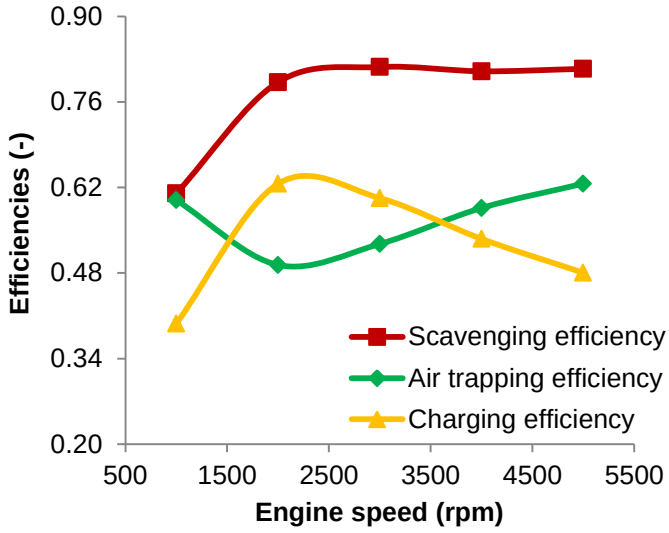

Figure 9.13 – Air trapping, charging and scavenging efficiencies at full load and different engine speeds.

The poor charging and scavenging efficiencies at lower engine speeds resulted from the constant drive ratio of 2.77 between the crankshaft and supercharger. The limiting design factor in this case was the compressor maximum rotor speed of 180000 rpm, so the drive ratio was chosen taking the maximum engine speed of 5000 rpm as the reference. The result was insufficient boost pressure at 1000 rpm due to the low compressor speed of 35000 rpm seen in Figure 9.14. It could be observed on the right axis of this plot that the intake pressure at the lowest engine speed was only 106 kPa, resulting in a modest engine load and in-cylinder peak pressure of 3.1 MPa. As the engine speed increased, the supercharger speed also increased and the intake pressure built-up. At 5000 rpm the maximum boost pressure of 270 kPa was achieved with a compressor speed of 175000 rpm. This resulted in the highest engine load and hence the highest in-cylinder peak pressure of 6.7 MPa.

Although the minimum boost pressure at 1000 rpm hindered the engine performance, the supercharger power consumption in this case was reduced and the brake efficiency maximised as seen on the right side of Figure 9.15. As the engine speed increased, the supercharger power consumption enlarged and the brake efficiency deteriorated. At 5000 rpm the efficiency dropped to 0.23, which represented a reduction of 26% compared to the maximum efficiency of 0.31 achieved at 1000 rpm. The friction power was found nearly constant throughout

the speeds tested at full load and accounted for 13% of the indicated power. Therefore, it was clear that at full load conditions the deteriorated brake efficiency achieved at higher engine speeds resulted from excessive engine power delivered to the supercharger. Until 3000 rpm the friction work was higher than the supercharging work, whilst above this speed the compressor power consumption prevailed. At 5000 rpm only about 60% of the indicated power was converted into brake power.

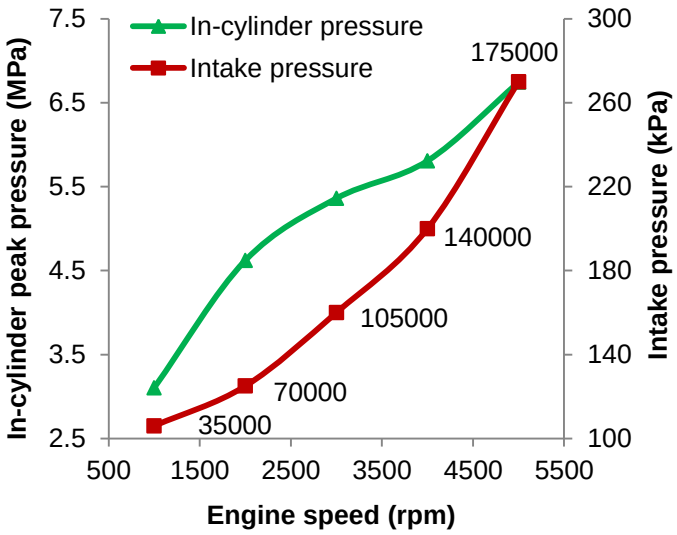

Figure 9.14 – In-cylinder peak pressure and intake pressure at full load and different engine speeds. The supercharger rotor speed (rpm) is presented next to the intake pressure curve.

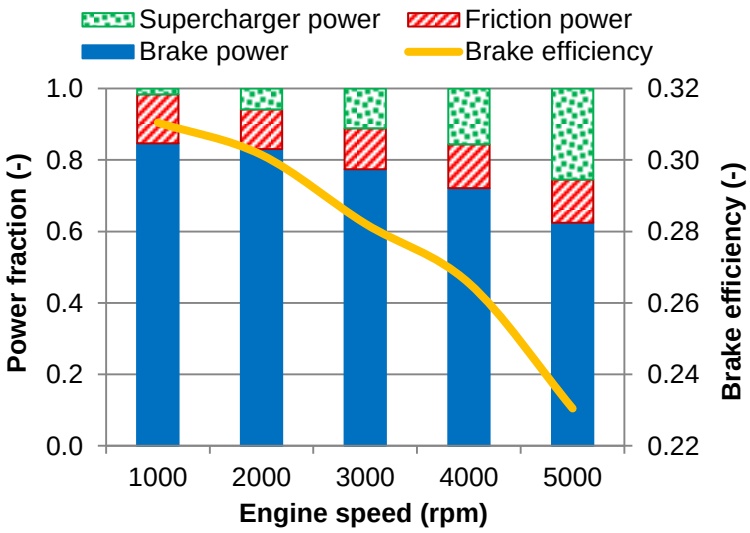

Figure 9.15 – Indicated power breakdown and brake efficiency at full load and different engine speeds.

Bearing in mind that the mechanically driven radial flow compressor chosen is amongst the most efficient superchargers currently available, it would be difficult to improve the brake efficiency by adopting other type of compressor. Instead, a possible way to improve brake efficiency at higher engine speeds would be increasing the intake/exhaust valve opening durations, so the same scavenging could be obtained at lower boost pressures. Nevertheless, the earlier EVO and later IVC would have a negative impact on the effective expansion and compression ratios, so a lower thermal efficiency would be expected a priori.

9.3.3 Dual drive ratio supercharging

The previous analysis with a constant supercharger drive ratio of 2.77 presented a low end torque especially at 1000 rpm. Higher boost pressures, given by greater compressor speeds, could not be achieved in such conditions due to the rotor's speed limitation of 180000 rpm at the engine speeds of 5000 rpm. A larger supercharger drive ratio would favour the engine torque at lower speeds, but it would reduce the maximum engine speed proportionally to avoid the compressor overspinning. A claimed method to overcome this issue is using a dual speed gearbox between the crankshaft and the compressor driven pulley [49]. In this case a greater compressor speed and hence a higher boost pressure could be achieved at lower engine speeds to improve torque. Meanwhile, halfway towards full engine speed the second drive ratio took over and avoided the supercharger rotor from reaching its limiting speed. The use of a variable speed transmission between crankshaft and supercharger was also evaluated by the same author, though its higher friction losses (15% against 2% of the dual drive system) resulted in a lower overall engine efficiency. Therefore, in this research a first gear ratio of 4.74 was chosen for engine speeds between 1000 rpm and 3000 rpm, whilst above this speed the lower drive ratio of 2.77 took over until 5000 rpm. The compressor rotor speed at each engine speed and intake pressure at full load is shown in Figure 9.16 alongside the in-cylinder pressures.

The dual drive system enabled the supercharger speed to increase by 70% at 1000 rpm, raising the intake pressure from 106 kPa to 120 kPa. At the engine speed of 3000 rpm the compressor rotor speed reached its maximum value of 180000 rpm, so the second gear was engaged. At 2000 rpm and 3000 rpm a

bypass valve, often referred as blow-off valve, was suggested to be used. This valve would recirculate part of the compressor outlet flow to its intake, so the boost pressure could be reduced and the torque curve smoothed. Without this valve there would be a peak torque at 3000 rpm of the same order of magnitude of that at 5000 rpm, with a consequent valley at 4000 rpm due to the lower supercharger speed. The in-cylinder pressure had a small variation of about 10% between 1000 rpm and 4000 rpm, with a maximum value of 6.74 MPa at 5000 rpm. The greater supercharger speed at lower engine speeds, with consequent higher boost pressure, improved the charging and scavenging efficiencies as presented in Figure 9.17.

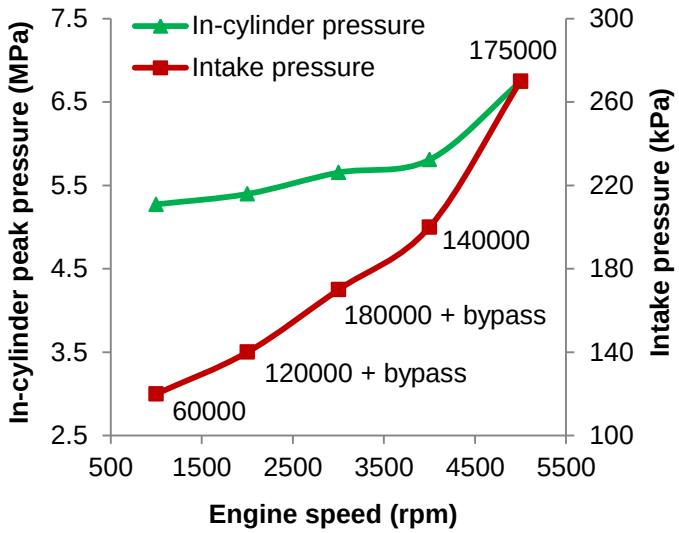

Figure 9.16 – In-cylinder peak pressure and intake pressure at full load and different engine speeds with a dual drive supercharger. The supercharger rotor speed (rpm) is presented next to the intake pressure curve.

Compared to the gas exchange results seen in Figure 9.13 with a single drive compressor, the use of a dual drive ratio enabled a more linear behaviour of the air trapping and charging efficiencies as shown in Figure 9.17. At 1000 rpm the charging and scavenging efficiencies increased by 98% and 45%, respectively, although the trapping efficiency dropped by 43%. The air trapping and charging efficiencies exhibited opposite trends with the engine speed and reached their extreme values of 0.63 and 0.48, respectively, at 5000 rpm. The scavenging efficiency performed consistently throughout the speeds tested, remaining around 0.81 from 3000 rpm onwards. The increase in internal EGR from 0.12 at 1000 rpm to 0.19 at 5000 rpm could help lowering NOx emissions particularly at

higher engines speeds, when the combustion rate increases and heat transfer is minimised. Such remarkable behaviour of the scavenging efficiency at full load resulted in a flat torque curve as seen in Figure 9.18. At 1000 rpm the specific torque more than doubled with the adoption of the dual drive compressor, whilst at 2000 rpm it increased by about 20%. At 5000 rpm the same maximum specific torque of 132 Nm/dm^3 and specific power of 70 kW/dm^3 were obtained.

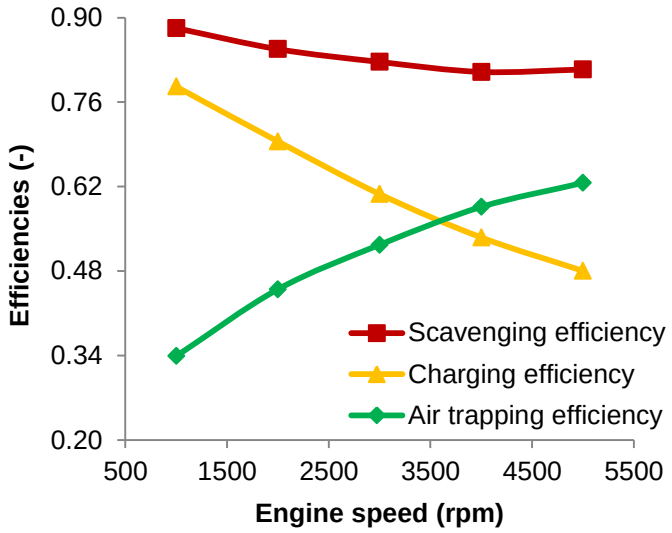

Figure 9.17 – Air trapping, charging and scavenging efficiencies at full load and different engine speeds with a dual drive supercharger.

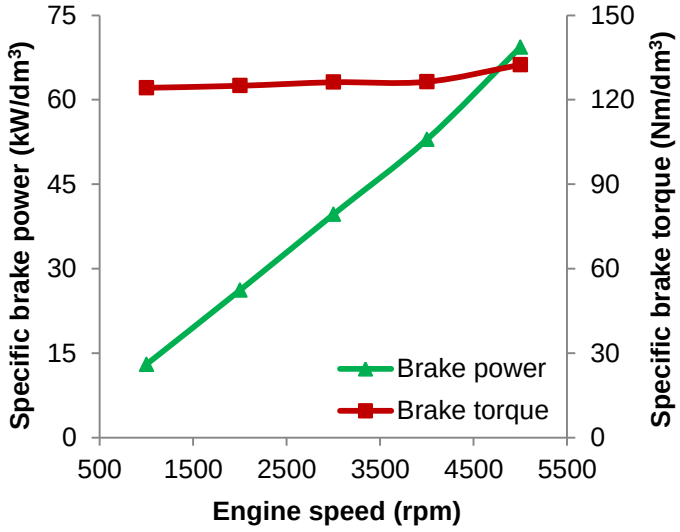

Figure 9.18 – Specific brake power and torque at full load and different engine speeds with a dual drive supercharger.

The full load flat torque curve from 1000 rpm to 5000 rpm represented a great advantage of the two-stroke poppet valve engine compared to gasoline four-stroke engines. These are usually not able to provide such great torque at lower

engine speeds due to knocking combustion or even super-knock. For instance, a torque of 124 Nm/dm^3 could be achieved at 1000 rpm with an IMEP of 0.86 MPa.

With the adoption of a dual drive ratio supercharger the brake efficiency at 1000 rpm dropped by 4% compared to the single drive design seen in Figure 9.19. A similar reduction was also found at 2000 rpm due to the larger supercharger power consumption, which in this case was of the same order of magnitude of the friction losses. At higher engine speeds the supercharger power consumption and friction power enlarged, although the former presented a steeper growth ratio. At 5000 rpm the compressor power requirement reduced the brake power by 22%, which was about twice as much as friction losses caused. This condition deteriorated the brake efficiency to only 0.23 and represented a reduction of 23% compared to the maximum value of about 0.30 found at 1000 rpm.

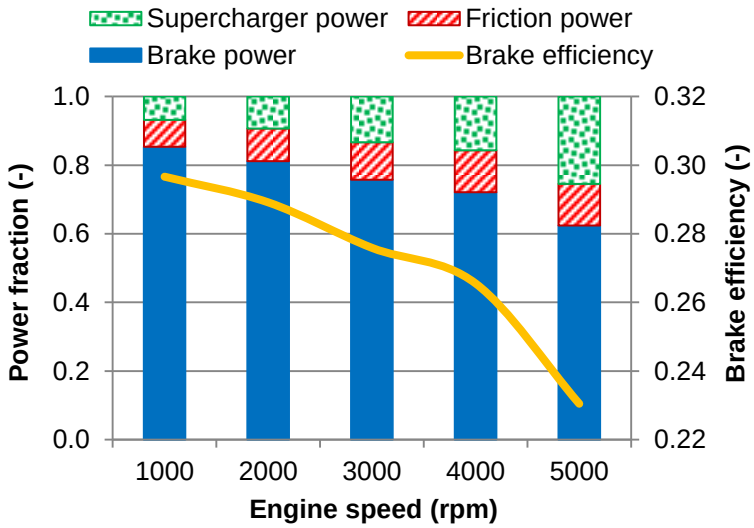

Figure 9.19 – Indicated power breakdown and brake efficiency at full load and different engine speeds with a dual drive supercharger.

Despite the solely investigation of the full load performance, lower engine loads could be achieved by recirculating (bypassing) the excess of intake air. This procedure works in a similar fashion to that used at 2000 rpm and 3000 rpm to avoid a peak torque with the dual drive system. The flow restriction imposed by the use of a bypass valve is reported to increase the fuel consumption by about 1% only [27]. This consideration is usually applied to supercharged four-stroke engines, where the compressor outflow is either bypassed to its inlet or the

supercharger is declutched from the crankshaft to avoid power losses at higher engine speeds.

9.3.4 Effects of low valve lift on the two-cylinder engine concept

As discussed in chapter six, the use of 3 mm of intake valve lift could help improving the air trapping efficiency by means of the masked region around the inlet valves. However, at higher engine loads the restriction imposed by such lower valve lift reduced the charging efficiency so the overall engine performance deteriorated. This section numerically evaluates the effects of using 3 mm of valve lift on the mid-low load range, where the charging efficiency is purposely minimised and the air trapping efficiency has margin for improvement.

The lower valve lift could improve the air trapping efficiency between scavenge ratios of 0.25 and 0.55 as presented in Figure 9.20. At a constant intake pressure the air trapping efficiency improved by 4% in average, although the charging efficiency dropped by 36% due to the increased flow restriction. The scavenging efficiency, though not presented in Figure 9.20, had an overall reduction of about 28% compared to full valve lift. The gains in air trapping efficiency with 3 mm of valve lift were maximised at lower engine speeds and higher loads, as the case with 115 kPa of intake pressure at 1000 rpm. In this condition the air trapping efficiency increased by 40%, even though the charging and scavenging efficiencies dropped by 25% and 13%, respectively.

To better illustrate the effects of different intake valve lifts, Figure 9.21 presents a cross section view of the combustion chamber at 180° CA ATDC, 1000 rpm and 110 kPa of boost pressure. The plot on the left represents the 3 mm of intake valve lift and on the right is the 8 mm case, with the different colours representing the residual gas fractions from zero to one. At full valve lift the reverse tumble flow was clearly stronger than that obtained with 3 mm of valve lift. In both conditions the in-cylinder core presented poor scavenging due to the recirculation of the fresh charge around this region, although the 8 mm case resulted on higher overall charge purity. The lower air trapping efficiency found at full intake valve lift was attributed to the air short-circuiting between intake and exhaust valves. Whilst the 3 mm of valve lift allowed only a thin jet of fresh

charge towards the back of the exhaust valve, the 8 mm lift permitted a greater air mass to escape to the exhaust as observed in Figure 9.21. In this condition the exhaust gas purity and the mean gas pressure increased, though its temperature dropped. The lower reverse tumble ratio at 3 mm of valve lift also reduced the TKE by about 30% at TDC. At the same intake pressure the lower valve lift dissipated part of the energy contained in the large scales of turbulence, so less energy was available to enhance the charge mixing and combustion.

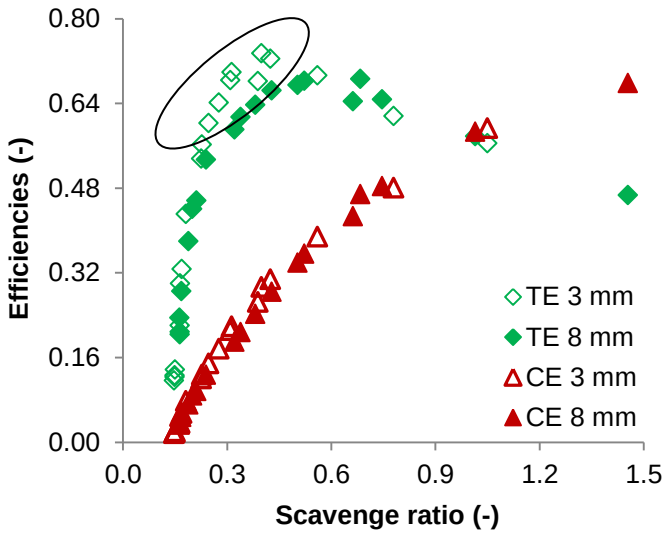

Figure 9.20 – Charging efficiency (CE) and air trapping efficiency (TE).

At similar intake pressures the charging and scavenging efficiencies dropped at lower intake valve lifts so the output power deteriorated. Therefore, to recover the engine performance the boost pressure had to be raised and consequently the supercharger power consumption increased. It could be observed that the charging and scavenging efficiencies dropped more than the improvement in the air trapping efficiency, so the overall gas exchange process deteriorated. If the reduction in valve lift could have improved more the air trapping efficiency by means of reduced air short-circuiting, then it would have compensated the higher boost pressure and the supercharger work would drop. In this situation the boost pressure would be higher but the air flow rate lower, so the compressor work would be minimised according to Equation (3.12). However, this was not the case and the brake efficiency deteriorated at all intake pressures and speeds tested with 3 mm of intake valve lift as seen in Figure 9.22. Since the simulations were run based on different intake pressures and the engine load was a result of the trapped air mass, it was not possible to compare low and high valve lift at

exactly the same output power. Thus, a mean difference of about 6% in the load was found in the comparison amongst low and high valve lifts.

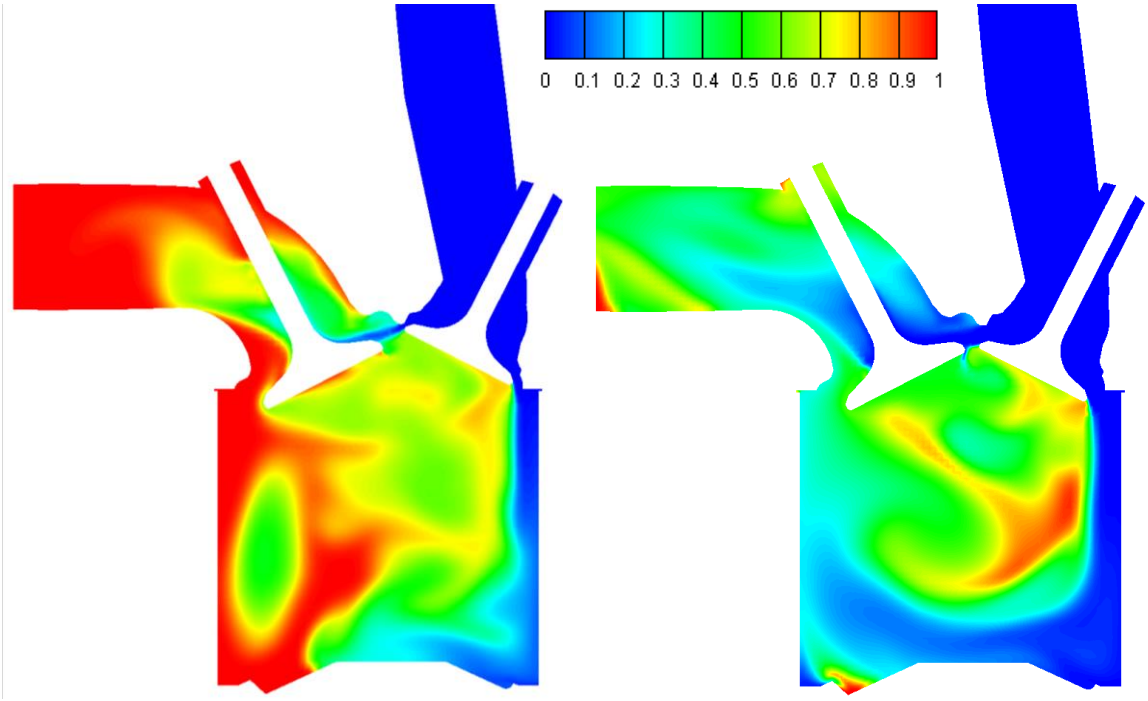

Figure 9.21 – Residual gas fraction at the valve section plane with 3 mm and 8 mm of intake valve lift, respectively. Engine conditions: 180° CA ATDC, 1000 rpm, 110 kPa of intake pressure.

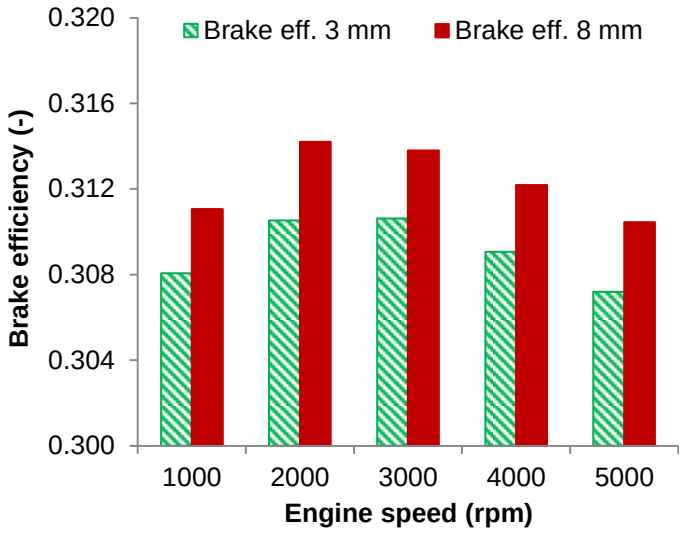

Figure 9.22 – Brake efficiency with 3 mm and 8 mm of intake valve lift at different engine speeds.

Comparing the brake efficiency between 3 mm and 8 mm of intake valve lift at similar loads, there was no significant change in fuel economy. As previously commented, there was a trade-off between greater air trapping efficiency and

poorer charging efficiency at low intake valve lifts. At 3 mm of lift the cylinder head mask was not uncovered and hence the air short-circuiting was minimised. However, the larger flow restriction compared to 8 mm of lift reduced the charging efficiency and compromised the engine performance. The result was a balance in brake efficiency with very similar values between 3 mm and 8 mm of valve lift, although the positive effect of full lift on the charging efficiency prevailed and improved the engine performance. Consequently, it could be inferred that the use of a cam profile switching (CPS) at lower loads would not necessarily result in better fuel economy in the two-stroke poppet valve engine. It differs from four-stroke engines where a CPS often improves the efficiency at low loads through reduced throttling losses and improved in-cylinder turbulence [27].

9.4 Summary

A transient cold flow CFD simulation was performed in the two-stroke poppet valve engine at speeds varying from 1000 rpm to 5000 rpm and intake pressures in the range from 105.1 kPa to 280 kPa. Besides the gas exchange examination, the numerical results were also used in the analytical study of a two-cylinder engine concept so that brake parameters could be obtained. The engine friction was considered alongside the power consumption from a radial flow mechanically driven supercharger, where single and dual drive ratios were evaluated at full load engine operation.

With every 1000 rpm increase in the engine speed at a constant boost pressure, the charging and scavenging efficiencies dropped by about 15% and 7%, respectively. Above 140 kPa of intake pressure there were slight gains in charging and scavenging efficiencies regardless the engine speed, as the supercharger power consumption increased more than the indicated power did. In this case the brake power gradually reduced and caused the brake efficiency to decrease.

The maximum specific brake power of 70 kW/dm^3 and specific brake torque of 132 Nm/dm^3 were registered at 5000 rpm. Greater engine performance would be possible to obtain at higher engine speeds, but at the expense of fuel economy. With a single drive ratio supercharger the maximum brake efficiency of 0.31 was

achieved at 1000 rpm. At 5000 rpm it deteriorated to 0.23 due to excessive compressor losses, which corresponded to more than twice the friction losses.

With the dual drive ratio supercharger the specific torque at 1000 rpm nearly doubled, whilst at 2000 rpm it improved by 20% despite of a slight deterioration in brake efficiency due to the higher compressor losses. The full speed performance remained similar to the single drive case. Compared to four-stroke engines, the two-cylinder 700 cm^3 two-stroke concept demonstrated outstanding low-end performance and a flat torque curve from 1000 rpm to 5000 rpm.

By reducing the intake valve lift from 8 mm to 3 mm, the air trapping efficiency could not be enhanced without deterioration of charging and scavenging efficiencies. Although the masked cylinder head considerably reduced the air short-circuiting at 3 mm of valve lift, the greater flow restriction raised the supercharger power consumption and deteriorated the engine performance. In this trade-off between minimised charge losses and higher intake restriction, the charging and scavenging efficiencies played a more important role and the engine brake efficiency decreased compared to full lift operation.

Chapter Ten
Conclusions and future work

10.1 Conclusions

Following the review of the relevant literature to this work, as well as the description of the experimental and numerical methodologies, the two-stroke poppet valve engine results were presented and discussed. Engine performance, emissions, charge preparation, combustion and gas exchange processes were analysed by means of experimental and numerical studies. The use of a fully variable electrohydraulic valve train enabled the optimisation of valve parameters in a wide range of engine operating conditions. The proposed fuel injection system was able to improve the overall engine performance and emissions, which were further enhanced by the replacement of gasoline by ethanol.

The effects of intake and exhaust valve timings, durations and lifts were experimentally evaluated in the two-stroke poppet valve engine. In all cases the output power was maximised with the greatest possible charging efficiency, although it was at the expense of higher intake pressures and lower air trapping efficiencies. At any given valve configuration the charging efficiency dropped as the engine speed increased. In a similar fashion to what occurs in four-stroke engines, this resulted from the shorter time available for gas exchange as well as higher flow frictional losses. Lower engine speeds benefited from shorter valve opening durations, whilst at higher speeds longer valve durations were required to improve the charging and scavenging processes. Excessively long valve opening durations minimised the effective compression/expansion ratios and air trapping efficiency, so the indicated power and efficiency decreased. Similarly, excessively short valve durations resulted in poor charging efficiency and hence power especially at higher engine speeds. The air trapping efficiency was greatly improved by lower intake and exhaust valve lifts, although the intake pressure had to be increased to compensate for the larger charge restriction. Similarly, the higher the exhaust backpressure the lower was the charging efficiency and consequently the output power.

The constant valve timings employed in the studies seen in chapters eight and nine represented a compromise in high load performance between 800 rpm and 2000 rpm obtained in chapter six. As the optimum valve timing change with the engine speed and load, the fuel efficiency results obtained in chapters eight and nine could have been improved by optimised valve parameters in case of a real world application. However, as shown in chapter five, the use of a simple cam phaser in the intake and exhaust valves may not result in expressive efficiency improvements. This is mainly because any gain in EER by retarding EVO/IVO resulted in deterioration of ECR with later EVC/IVC. Differently from a four-stroke engine where the intake and exhaust processes are independent, in the two-stroke engine both events are connected by a long valve overlap. Therefore, in the case of a real world vehicle application of a poppet valve engine, improved fuel economy is expected to be obtained with a more sophisticated VVA system. In other words, not only cam phasers are required but also variable valve opening durations as the BMW Valvetronic and the Fiat Multiair, to name a few.

The 3-D CFD analysis of cold flow and air-fuel mixture formation proved to be a useful tool for the comprehension of in-cylinder conditions. The charge preparation was found mainly dependent on the spray momentum and the time available for air-fuel mixing. Fuel impingement was mostly caused by over penetration of the fuel plume at reduced in-cylinder pressures, as the lower charge density was unable to aerodynamically break the fuel droplets. When replacing gasoline by ethanol, fuel impingement increased due to the larger fuel mass injected for the same energy input. The higher heat of vaporisation of ethanol hindered the mixing process of any impinged fuel, although it greatly reduced the in-cylinder temperature through evaporative cooling.

The higher the engine load the lesser was the residual gas trapped, so SI flame-propagated combustion remained as the main heat release process with gasoline. At lower engine speeds and loads the time available for heat transfer increased and the combustion process remained dominated by a propagating flame, though highly diluted by the residual gas trapped. On the other hand, at light loads and higher engine speeds the hot residual gas fraction induced the auto-ignition of the end-gas ahead of the flame front, which characterised a

hybrid combustion mode referred to as SACI. This situation evolved at higher engine speeds until no flame propagation was observed, so the combustion became purely governed by controlled auto-ignition (CAI). In the ethanol fuelled cases mainly flame propagation combustion was detected due to the lower combustion temperature given by ethanol's higher heat of vaporisation.

Over the two-stroke engine operation map ethanol presented about 10% improvement in indicated efficiency compared to gasoline. Furthermore, ethanol enabled MBT operation at all engine conditions tested whereas gasoline had the majority of running conditions under KLS. The combustion efficiency was maximised at mid-loads and engine speeds below 1600 rpm due to a competition amongst fuel impingement, residual gas temperature and time available for the charge preparation. At light loads and speeds the charge dilution hindered the oxidation process and deteriorated the combustion efficiency. As the load increased, the dilution effect promoted by the residual gas trapped reduced and the combustion completeness enhanced. However, the larger fuel mass injected at higher loads led to the formation of over rich regions and fuel impingement, which offset the gain in efficiency by higher charge purity. Similarly, at higher engine speeds the time available for mixture formation shortened and the poor charge homogeneity hindered the combustion process.

Engine-out emissions of CO, UHC and soot were largely influenced by the SOI timings, whilst NOx formation was found more sensitive to the engine speed and load. Different operating conditions required distinct SOI timings, although the engine speed had a more pronounced effect than the load in this case. As the SOI delayed towards TDC, the time available for mixture homogeneity shortened and the emissions of CO and soot increased due to poor oxidation of over rich regions. At extremely late injections, pool fires were expected to occur on the piston top and contribute to higher soot emissions through diffusion burning. When the SOI was advanced towards BDC more fuel was prone to short-circuit before IVC/EVC, so UHC emissions increased. Furthermore, early injections took place in a lower in-cylinder pressure, so longer spray penetrations increased fuel impingement on the liner and hence UHC production. The residual gas trapped also influenced emissions, especially at light loads and speeds when the

combustion temperature dropped and hindered the oxidation process. Ethanol operation globally increased CO and UHC emissions by about 8% and 19%, respectively. In the case of UHC it resulted from a larger fuel mass injected with poor mixture preparation and greater wall impingement. The rise in CO was attributed to lower combustion temperature resulted from enhanced charge cooling effect. Still, ethanol reduced NOx emissions by about 50% compared to gasoline operation, besides the production of no soot throughout the loads and speeds tested.

A 700 cm^3 two-cylinder two-stroke poppet valve engine was modelled to assess its brake performance with a Rotrex supercharger. The maximum specific brake power of 70 kW/dm^3 and specific brake torque of 132 Nm/dm^3 were obtained at 5000 rpm. Even greater performance would be possible to achieve at higher engine speeds and intake pressures, though at the expense of fuel economy. The sole use of the radial flow mechanically driven compressor demonstrated a severe reduction in engine efficiency at full load due to supercharging losses. At full load and high engine speeds the brake efficiency deteriorated due to the sum of friction and supercharging losses, although at lower speeds the supercharger had a predominant effect. With a dual drive ratio supercharger a flat full load torque was obtained from 1000 rpm to 5000 rpm.

10.2 Recommendations for future work

Despite the improvements obtained with the replacement of the standard fuel injection system, the short time available for mixture formation still demands a superior fuelling system especially at higher engine speeds and loads. This could be improved by adopting greater injection pressures (>25 MPa) and by moving the injector to a more central position. Centrally mounted injectors tend to produce less CO/smoke and more stable combustion with less over-rich regions and fuel impingement than side mounted injectors [178]. Nevertheless, this modification would result in (a) larger bore or (b) smaller valves to accommodate the fuel injector next to the spark plug. The option (a) would reduce the thermal efficiency by increasing the heat transfer area at TDC, whilst the second approach (b) would reduce the valve effective area and further compromise the gas exchange process. The adoption of a piezoelectric injector and the

corresponding driver would enable multiple fuel injections per cycle, so the combustion process could be improved by reducing the formation of over-rich regions. This type of injector would also allow the achievement of lower engine loads considering its improved fuel metering in a wide range of flow rates.

Regarding the scavenging inefficiencies, particularly at higher engine speeds and loads, it could be improved by raising the number of valves as demonstrated by [22] in a two-stroke poppet valve gasoline engine. By increasing the number of exhaust valves from two to three, the scavenging process was improved at the expense of larger bore and hence lower thermal efficiency. Moreover, the larger bore-to-stroke ratio increases the probability of knocking combustion as the end-gas residence time increases prior to the flame front arrival.

Improvements in air trapping efficiency are as important as those in scavenging performance, once the exhaust gas dilution compromises the application of aftertreatment and/or turbocharger due to the lower exhaust gas temperature. As demonstrated in chapter nine, the brake efficiency was deteriorated at full load and high engine speeds due to the supercharger power consumption, so a turbocharger could be used to recover part of the exhaust energy. Nevertheless, the adoption of a turbocharger would increase the exhaust backpressure so even greater intake pressures would be required to maintain the same scavenging levels. One-dimensional simulation is recommended in this case to evaluate the interaction amongst engine, supercharger and turbocharger [50].

List of references

[1] Intergovernmental Panel on Climate Change (IPCC). Climate Change – Summary for Policymakers. 2014.

[2] National Aeronautics and Space Administration – NASA. Global Climate Change n.d. http://climate.nasa.gov/ (accessed October 15, 2015).

[3] European commission. EU Transport in Figures - Statistical Pocketbook. 2014.

[4] Exxon Mobil Corporation. The Outlook for Energy: A View to 2040. 2015.

[5] International Council on Clean Transportation (ICCT). EU CO2 emission standards for passenger cars and light-commercial vehicles. 2014.

[6] Barlow T, Latham S, Mccrae I, Boulter P. A reference book of driving cycles for use in the measurement of road vehicle emissions. 2009.

[7] Delphi. Worldwide Emissions Standards - Passenger Cars and Light Duty Vehicles. 2015.

[8] Heywood JB. Internal combustion engine fundamentals. New York: McGraw-Hill; 1988.

[9] Zhao H, editor. Advanced Direct Injection Combustion Engine Technologies and Development. Cambridge: Woodhead Publishing; 2010.

[10] Smith J, Szekely Jr G, Solomon A, Parrish S. A Comparison of Spray-Guided Stratified-Charge Combustion Performance with Outwardly-Opening Piezo and Multi-Hole Solenoid Injectors. SAE Int J Engines 2011;4:2011–01 – 1217. doi:10.4271/2011-01-1217.

[11] King J, Feulner P. Spray-Guided Direct Injection For Boosted Gasoline Engines. MTZ Worldw 2013:10–5.

[12] de Francqueville L. Effects of Ethanol Addition in RON 95 Gasoline on GDI Stratified Combustion. SAE Tech. Pap., 2011. doi:10.4271/2011-24-0055.

[13] Zhao H, editor. HCCI and CAI engines for the automotive industry. Cambridge: Woodhead Publishing; 2007.

[14] Pacheco AF, Martins MES, Zhao H. New European Drive Cycle (NEDC) simulation of a passenger car with a HCCI engine: Emissions and fuel consumption results. Fuel 2013;111:733–9. doi:10.1016/j.fuel.2013.03.060.

[15] Sellnau M, Foster M, Hoyer K, Moore W, Sinnamon J, Husted H. Development of a Gasoline Direct Injection Compression Ignition (GDCI) Engine. SAE Int J Engines 2014;7:835–51. doi:10.4271/2014-01-1300.

[16] Lumsden G, OudeNijeweme D, Fraser N, Blaxill H. Development of a Turbocharged Direct Injection Downsizing Demonstrator Engine. SAE Int J Engines 2009;2:2009–01 – 1503. doi:10.4271/2009-01-1503.

[17] Eichhorn A, Lejsek D, Hettinger A, Kufferath A. Challenge Determining a Combustion System Concept for Downsized SI-engines - Comparison and Evaluation of Several Options for a Boosted 2-cylinder SI-engine. SAE Tech. Pap., 2013. doi:10.4271/2013-01-1730.

[18] Attard WP, Toulson E, Watson H, Hamori F. Abnormal Combustion

including Mega Knock in a 60% Downsized Highly Turbocharged PFI Engine. SAE Tech. Pap., 2010. doi:10.4271/2010-01-1456.

[19] Trattner A, Pertl P, Schmidt SP. Novel Range Extender Concepts for 2025 with Regard to Small Engine Technologies. SAE Int J Altern Powertrains 2011;1:556–83.

[20] Fraidl GK, Beste F, Kapus PE, Korman M, Sifferlinger B, Benda V. Challenges and Solutions for Range Extenders - From Concept Considerations to Practical Experiences. SAE Tech. Pap., 2011. doi:10.4271/2011-37-0019.

[21] Benajes J, Novella R, De Lima D, Tribotté P, Quechon N, Obernesser P, et al. Analysis of the combustion process, pollutant emissions and efficiency of an innovative 2-stroke HSDI engine designed for automotive applications. Appl Therm Eng 2013;58:181–93. doi:10.1016/j.applthermaleng.2013.03.050.

[22] Nomura K, Nakamura N. Development of a new two-stroke engine with poppet-valves: Toyota S-2 engine. In: Duret P, editor. A new Gener. two-stroke enignes Futur., Paris: Technip; 1993, p. 53–62.

[23] Heywood JB, Sher E. The two-stroke cycle engine: its development, operation and design. Warrendale: SAE International–Taylor and Franci; 1999.

[24] Sher E. Scavenging the two-stroke engine. Prog Energy Combust Sci 1990;16:95–124. doi:10.1016/0360-1285(90)90045-5.

[25] Clerk D. Motor worked by combustible gas or vapor. US patent 249307, 1881.

[26] Cock FWC, Day J. Gas-engine. British patent 544210, 1895.

[27] Stone R. Introduction to internal combution engines. 4th ed. Basingstoke: Palgrave Macmillan; 2012.

[28] Blair GP. Design and simulation of two-stroke engines. Warrendale: Society of Automotive Engineers; 1996.

[29] Kenny RG. Developments in two-stroke cycle engine exhaust emissions. Arch Proc Inst Mech Eng Part D J Automob Eng 1989-1996 (vols 203-210) 1992;206:93–106. doi:10.1243/PIME_PROC_1992_206_165_02.

[30] Shimizu R, Okimoto H, Tashima S, Fuse S. The Characteristics of Fuel Consumption and Exhaust Emissions of the Side Exhaust Port Rotary Engine. SAE Tech. Pap., 1995. doi:10.4271/950454.

[31] Kee RJ, Blair GP, Douglas R. Comparison of Performance Characteristics of Loop and Cross Scavenged Two-Stroke Engines. SAE Tech. Pap., 1990. doi:10.4271/901666.

[32] Naik S, Redon F, Regner G, Koszewnik J. Opposed-Piston 2-Stroke Multi-Cylinder Engine Dynamometer Demonstration. SAE Tech. Pap., 2015. doi:10.4271/2015-26-0038.

[33] Hooper PR, Al-Shemmeri T, Goodwin MJ. Advanced modern low-emission two-stroke cycle engines. Proc Inst Mech Eng Part D J Automob Eng 2011;225:1531–43. doi:10.1177/0954407011408649.

[34] Knoll R. AVL Two-Stroke Diesel Engine. SAE Tech. Pap., 1998. doi:10.4271/981038.

[35] Yang X, Okajima A, Takamoto Y, Obokata T. Numerical Study of Scavenging Flow in Poppet-Valved Two-Stroke Engines. SAE Tech. Pap., 1999. doi:10.4271/1999-01-1250.

[36] Turner JWG, Blundell DW, Pearson RJ, Patel R, Larkman DB, Burke P, et al. Project Omnivore: A Variable Compression Ratio ATAC 2-Stroke Engine for Ultra-Wide-Range HCCI Operation on a Variety of Fuels. SAE Int J Engines 2010;3:2010–01 – 1249. doi:10.4271/2010-01-1249.

[37] Blundell D, Turner J, Duret P, Lavy J, Oscarsson J, Emanuelsson G, et al. Design and Evaluation of the ELEVATE Two-stroke Automotive Engine. SAE Tech. Pap., 2003. doi:10.4271/2003-01-0403.

[38] Shawcross D, Pumphrey C, Arnall D. A Five-Million Kilometre, 100-Vehicle Fleet Trial, of an Air-Assist Direct Fuel Injected, Automotive 2-Stroke Engine. SAE Int. J. Fuels Lubr., 2000. doi:10.4271/2000-01-0898.

[39] Nakano M, Sato K, Ukawa H. A Two-Stroke Cycle Gasoline Engine with Poppet Valves on the Cylinder Head. SAE Tech. Pap., 1990. doi:10.4271/901664.

[40] Hundleby GE. Development of a Poppet-Valved Two-Stroke Engine - The Flagship Concept. SAE Tech. Pap., 1990. doi:10.4271/900802.

[41] Melchior J. 2T poppet valve patent 1976 British. British patent 1568302, 1976.

[42] Tribotte P, Ravet F, Dugue V, Obernesser P, Quechon N, Benajes J, et al. Two Strokes Diesel Engine - Promising Solution to Reduce CO2 Emissions. Procedia - Soc Behav Sci 2012;48:2295–314. doi:10.1016/j.sbspro.2012.06.1202.

[43] Ukawa H, Nakano M, Sato K. A Two-Stroke Cycle Engine with Poppet Valves in the Cylinder Head - Part III: An Application of Gaseous Fuel Direct Injection System. SAE Tech. Pap., 1993. doi:10.4271/930983.

[44] Sato K, Ukawa H, Nakano M. A Two-Stroke Cycle Gasoline Engine with Poppet Valves in the Cylinder Head - Part II. SAE Tech. Pap., 1992. doi:10.4271/920780.

[45] Li Z, He B, Zhao H. The Influence of Intake Port and Pent-Roof Structures on Reversed Tumble Generation of a Poppet-Valved Two-Stroke Gasoline Engine. SAE Tech. Pap., 2014. doi:10.4271/2014-01-1130.

[46] Osborne RJ, Stokes J, Lake TH, Carden PJ, Mullineux JD, Helle-Lorentzen R, et al. Development of a Two-Stroke/Four-Stroke Switching Gasoline Engine - The 2/4SIGHT Concept. SAE Tech. Pap., 2005. doi:10.4271/2005-01-1137.

[47] Cairns A, Zhao H, Todd A, Aleiferis P. A study of mechanical variable valve operation with gasoline-alcohol fuels in a spark ignition engine. Fuel 2013;106:802–13. doi:10.1016/j.fuel.2012.10.041.

[48] Taylor CF. The internal combustion engine in theory and practice - Vol. II. 2nd ed. Cambridge: MIT Press; 1985.

[49] Pohorelsky L, Brynych P, Macek J, Vallaude P-Y, Ricaud J-C, Obernesser P, et al. Air System Conception for a Downsized Two-Stroke Diesel Engine. SAE Tech. Pap., 2012. doi:10.4271/2012-01-0831.

[50] Brynych P, Macek J, Tribotte P, De Paola G, Ternel C. System Optimization for a 2-Stroke Diesel Engine with a Turbo Super Configuration Supporting Fuel Economy Improvement of Next Generation Engines. SAE Tech. Pap., 2014. doi:10.4271/2014-32-0011.

[51] Chadwell CJ, Walls M. Analysis of a SuperTurbocharged Downsized Engine Using 1-D CFD Simulation. SAE Tech. Pap., 2010. doi:10.4271/2010-01-1231.

[52] Turner JWG, Popplewell A, Marshall DJ, Johnson TR, Barker L, King J, et al. SuperGen on Ultraboost: Variable-Speed Centrifugal Supercharging as an Enabling Technology for Extreme Engine Downsizing. SAE Int J Engines 2015;8:2015–01 – 1282. doi:10.4271/2015-01-1282.

[53] Wellmann T, Govindswamy K, Orzechowski J, Srinivasan S. Influence of Automatic Engine Stop/Start Systems on Vehicle NVH and Launch Performance. SAE Int J Engines 2015;8:2015–01 – 2183. doi:10.4271/2015-01-2183.

[54] Stokes J, Hundleby GE, Lake TH, Christie MJ. Development Experience of a Poppet-Valved Two-Stroke Flagship Engine. SAE Tech. Pap., 1992. doi:10.4271/920778.

[55] Sher E, Hacohen Y, Refael S, Harari R. Minimizing Short-Circuiting Losses in 2-S Engines by Throttling the Exhaust Pipe. SAE Tech. Pap., 1990. doi:10.4271/901665.

[56] Hsieh P, Horng R, Huang H, Peng Y, Wang J. Effects of Exhaust Charge Control Valve on Combustion and Emissions of Two-Stroke Cycle Direct-Injection S.I. Engine. SAE Tech. Pap., 1992. doi:10.4271/922311.

[57] Ojapah MM. Experimental studies of performance and emissions in a 2/4-stroke engine with gasoline and ethanol. PhD thesis, Brunel University London, 2014.

[58] Duret P, Moreau J-F. Reduction of Pollutant Emissions of the IAPAC Two-Stroke Engine with Compressed Air Assisted Fuel Injection. SAE Tech. Pap., 1990. doi:10.4271/900801.

[59] Leighton S, Cebis M, Southern M, Ahern S, Horner L. The OCP Small Engine Fuel Injection System for Future Two-Stroke Marine Engines. SAE Tech. Pap., 1994. doi:10.4271/941687.

[60] Zhang Y, Ojapah M, Cairns A, Zhao H. 2-Stroke CAI Combustion Operation in a GDI Engine with Poppet Valves. SAE Tech. Pap., 2012. doi:10.4271/2012-01-1118.

[61] Asai M, Kurosaki T, Okada K. Analysis on Fuel Economy Improvement and Exhaust Emission Reduction in a Two-Stroke Engine by Using an Exhaust Valve. SAE Tech. Pap., 1995. doi:10.4271/951764.

[62] Laget O, Ternel C, Thiriot J, Charmasson S, Tribotte P, Vidal F. Preliminary design of a two-stroke uniflow diesel engine for passenger car. SAE Int J Engines 2013;6:596–613. doi:10.4271/2013-01-1719.

[63] Digital Library. SAE Int n.d. http://digitallibrary.sae.org/ (accessed November 22, 2015).

[64] Mattarelli E, Rinaldini CA. Two-Stroke Gasoline Engines for Small-Medium Passenger Cars. SAE Tech. Pap., 2015. doi:10.4271/2015-01-1284.

[65] Ma J, Zhao H, Freeland P, Hawley M, Xia J. Numerical Analysis of a Downsized 2-Stroke Uniflow Engine. SAE Int J Engines 2014;7:2014–01 – 9051. doi:10.4271/2014-01-9051.

[66] Lopez JJ, Novella R, Valero-Marco J, Coma G, Justet F. Evaluation of the Potential Benefits of an Automotive, Gasoline, 2-Stroke Engine. SAE Tech. Pap., 2015. doi:10.4271/2015-01-1261.

[67] Huo M, Huang Y, Hofbauer P. Piston Design Impact on the Scavenging and Combustion in an Opposed-Piston, Opposed-Cylinder (OPOC) Two-Stroke Engine. SAE Tech. Pap., 2015. doi:10.4271/2015-01-1269.

[68] Zhang Y, Zhao H, Ojapah M, Cairns A. CAI combustion of gasoline and its mixture with ethanol in a 2-stroke poppet valve DI gasoline engine. Fuel 2013;109:661–8. doi:10.1016/j.fuel.2013.03.002.

[69] Hancock D, Fraser N, Jeremy M, Sykes R, Blaxill H. A New 3 Cylinder 1.2l Advanced Downsizing Technology Demonstrator Engine. SAE Tech. Pap., 2008. doi:10.4271/2008-01-0611.

[70] Wetzel P. Downspeeding a Light Duty Diesel Passenger Car with a Combined Supercharger and Turbocharger Boosting System to Improve Vehicle Drive Cycle Fuel Economy. SAE Tech. Pap., 2013. doi:10.4271/2013-01-0932.

[71] Martin S, Beidl C, Mueller R. Responsiveness of a 30 Bar BMEP 3-Cylinder Engine: Opportunities and Limits of Turbocharged Downsizing. SAE Tech. Pap., 2014. doi:10.4271/2014-01-1646.

[72] Zaccardi J-M, Pagot A, Vangraefschepe F, Dognin C, Mokhtari S. Optimal Design for a Highly Downsized Gasoline Engine. SAE Tech. Pap., 2009. doi:10.4271/2009-01-1794.

[73] Turner JWG, Popplewell A, Patel R, Johnson TR, Darnton NJ, Richardson S, et al. Ultra Boost for Economy: Extending the Limits of Extreme Engine Downsizing. SAE Int J Engines 2014;7:2014–01 – 1185. doi:10.4271/2014-01-1185.

[74] Lewin T. HyBoost: the win-win option. Ricardo Q Rev 2012:12–7.

[75] Remmert S, Campbell S, Cracknell R, Schuetze A, Lewis A, Giles K, et al. Octane Appetite: The Relevance of a Lower Limit to the MON Specification in a Downsized, Highly Boosted DISI Engine. SAE Int J Fuels Lubr 2014;7:2014–01 – 2718. doi:10.4271/2014-01-2718.

[76] Baêta JGC, Pontoppidan M, Silva TRV. Exploring the limits of a down-sized ethanol direct injection spark ignited engine in different configurations in order to replace high-displacement gasoline engines. Energy Convers Manag 2015;105:858–71. doi:10.1016/j.enconman.2015.08.041.

[77] Cruff L, Kaiser M, Krause S, Harris R, Krueger U, Williams M. EBDI® -

Application of a Fully Flexible High BMEP Downsized Spark Ignited Engine. SAE Tech. Pap., 2010. doi:10.4271/2010-01-0587.

[78] Luisi S, Doria V, Stroppiana A, Millo F, Mirzaeian M. Experimental Investigation on Early and Late Intake Valve Closures for Knock Mitigation through Miller Cycle in a Downsized Turbocharged Engine. SAE Tech. Pap., 2015. doi:10.4271/2015-01-0760.

[79] Engines with small displacement. MTZ Worldw 2012;73.

[80] Shinagawa T, Kudo M, Matsubara W, Kawai T. The New Toyota 1.2-Liter ESTEC Turbocharged Direct Injection Gasoline Engine. SAE Tech. Pap., 2015. doi:10.4271/2015-01-1268.

[81] Dingle SF, Cairns A, Zhao H, Williams J, Williams O, Ali R. Lubricant Induced Pre-Ignition in an Optical SI Engine. SAE Tech. Pap., 2014. doi:10.4271/2014-01-1222.

[82] Kalghatgi GT, Bradley D. Pre-ignition and “super-knock” in turbo-charged spark-ignition engines. Int J Engine Res 2012;13:399–414. doi:10.1177/1468087411431890.

[83] Magar M, Spicher U, Palaveev S, Gohl M, Müller G, Lensch-Franzen C, et al. Experimental Studies on the Occurrence of Low-Speed Pre-Ignition in Turbocharged GDI Engines. SAE Int J Engines 2015;8:495–504. doi:10.4271/2015-01-0753.

[84] Lu Y, Pei P, Liu Y. An evaluation of a 2/4-stroke switchable secondary expansion internal combustion engine. Appl Therm Eng 2014;73:323–32. doi:10.1016/j.applthermaleng.2014.07.075.

[85] Wang X, Zhao H, Xie H, He B-Q. Numerical Study of the Effect of Piston Shapes and Fuel Injection Strategies on In-Cylinder Conditions in a PFI/GDI Gasoline Engine. SAE Int J Engines 2014;7:2014–01 – 2670. doi:10.4271/2014-01-2670.

[86] Sementa P, Maria Vaglieco B, Catapano F. Thermodynamic and optical characterizations of a high performance GDI engine operating in homogeneous and stratified charge mixture conditions fueled with gasoline and bio-ethanol. Fuel 2012;96:204–19. doi:10.1016/j.fuel.2011.12.068.

[87] Turkcan A, Ozsezen AN, Canakci M. Effects of second injection timing on combustion characteristics of a two stage direct injection gasoline-alcohol HCCI engine. Fuel 2013;111:30–9. doi:10.1016/j.fuel.2013.04.029.

[88] Li N, Xie H, Chen T, Li L, Zhao H. The effects of intake backflow on in-cylinder situation and auto ignition in a gasoline controlled auto ignition engine. Appl Energy 2013;101:756–64. doi:10.1016/j.apenergy.2012.07.050.

[89] Li L, Xie H, Chen T, Yu W, Zhao H. Experimental Study on Spark Assisted Compression Ignition (SACI) Combustion with Positive Valve Overlap in a HCCI Gasoline Engine. SAE Tech. Pap., 2012. doi:10.4271/2012-01-1126.

[90] Zhang Y, Zhao H. Investigation of combustion, performance and emission characteristics of 2-stroke and 4-stroke spark ignition and CAI/HCCI operations in a DI gasoline. Appl Energy 2014;130:244–55. doi:10.1016/j.apenergy.2014.05.036.

[91] Andwari AM, Aziz AA, Said MFM, Latiff ZA. Experimental investigation of the influence of internal and external EGR on the combustion characteristics of a controlled auto-ignition two-stroke cycle engine. Appl Energy 2014;134:1–10. doi:10.1016/j.apenergy.2014.08.006.

[92] Cairns A, Blaxill H. The Effects of Combined Internal and External Exhaust Gas Recirculation on Gasoline Controlled Auto-Ignition. SAE Tech. Pap., 2005. doi:10.4271/2005-01-0133.

[93] Chen T, Xie H, Li L, Zhang L, Wang X, Zhao H. Methods to achieve HCCI/CAI combustion at idle operation in a 4VVAS gasoline engine. Appl Energy 2014;116:41–51. doi:10.1016/j.apenergy.2013.09.044.

[94] Benajes J, Molina S, Novella R, De Lima D. Implementation of the Partially Premixed Combustion concept in a 2-stroke HSDI diesel engine fueled with gasoline. Appl Energy 2014;122:94–111. doi:10.1016/j.apenergy.2014.02.013.

[95] Wang Z, Wang J-X, Shuai S-J, Ma Q-J. Effects of Spark Ignition and Stratified Charge on Gasoline HCCI Combustion With Direct Injection. SAE Tech. Pap., 2005. doi:10.4271/2005-01-0137.

[96] Splitter D a., Reitz RD. Fuel reactivity effects on the efficiency and operational window of dual-fuel compression ignition engines. Fuel 2014;118:163–75. doi:10.1016/j.fuel.2013.10.045.

[97] Wissink M, Reitz RD. Direct Dual Fuel Stratification, a Path to Combine the Benefits of RCCI and PPC. SAE Int J Engines 2015;8:2015–01 – 0856. doi:10.4271/2015-01-0856.

[98] Olesky LM, Martz JB, Lavoie G a., Vavra J, Assanis DN, Babajimopoulos A. The effects of spark timing, unburned gas temperature, and negative valve overlap on the rates of stoichiometric spark assisted compression ignition combustion. Appl Energy 2013;105:407–17. doi:10.1016/j.apenergy.2013.01.038.

[99] Benajes J, Tormos B, Garcia A, Monsalve-Serrano J. Impact of Spark Assistance and Multiple Injections on Gasoline PPC Light Load. SAE Int J Engines 2014;7:2014–01 – 2669. doi:10.4271/2014-01-2669.

[100] Persson H, Sjöholm J, Kristensson E, Johansson B, Richter M, Aldén M. Study of Fuel Stratification on Spark Assisted Compression Ignition (SACI) Combustion with Ethanol Using High Speed Fuel PLIF. SAE Tech. Pap., 2008. doi:10.4271/2008-01-2401.

[101] Ortiz-Soto EA, Lavoie GA, Martz JB, Wooldridge MS, Assanis DN. Enhanced heat release analysis for advanced multi-mode combustion engine experiments. Appl Energy 2014;136:465–79. doi:10.1016/j.apenergy.2014.09.038.

[102] Sellnau M, Moore W, Sinnamon J, Hoyer K, Foster M, Husted H. GDCI Multi-Cylinder Engine for High Fuel Efficiency and Low Emissions. SAE Int J Engines 2015;8:775–90. doi:10.4271/2015-01-0834.

[103] Dec JE, Yang Y, Dernotte J, Ji C. Effects of Gasoline Reactivity and Ethanol Content on Boosted, Premixed and Partially Stratified Low-Temperature Gasoline Combustion (LTGC). SAE Int J Engines

2015;8:2015–01 – 0813. doi:10.4271/2015-01-0813.

[104] Benajes J, Novella R, De Lima D, Tribotte P. Investigation on Multiple Injection Strategies for Gasoline PPC Operation in a Newly Designed 2-Stroke HSDI Compression Ignition Engine. SAE Int J Engines 2015;8:2015–01 – 0830. doi:10.4271/2015-01-0830.

[105] International Energy Agency. Global EV Outlook 2015. 2015.

[106] Bishop JDK, Axon CJ, Tran M, Bonilla D, Banister D, McCulloch MD. Identifying the fuels and energy conversion technologies necessary to meet European passenger car emissions legislation to 2020. Fuel 2012;99:88–105. doi:10.1016/j.fuel.2012.04.045.

[107] Kim N, Moawad A, Shidore N, Rousseau A. Fuel Consumption and Cost Potential of Different Plug-In Hybrid Vehicle Architectures. SAE Int J Altern Powertrains 2015;4:2015–01 – 1160. doi:10.4271/2015-01-1160.

[108] Mattarelli E, Rinaldini CA, Cantore G, Agostinelli E. Comparison between 2 and 4-Stroke Engines for a 30 kW Range Extender. SAE Int J Altern Powertrains 2014;4:2014–32 – 0114. doi:10.4271/2014-32-0114.

[109] Mattarelli E, Rinaldini CA, Cantore G, Baldini P. 2-Stroke Externally Scavenged Engines for Range Extender Applications. SAE Tech. Pap., 2012. doi:10.4271/2012-01-1022.

[110] Kock F, Haag J, Friedrich HE. The Free Piston Linear Generator - Development of an Innovative, Compact, Highly Efficient Range-Extender Module. SAE Tech. Pap., 2013. doi:10.4271/2013-01-1727.

[111] Jia B, Zuo Z, Feng H, Tian G, Roskilly AP. Development Approach of a Spark-Ignited Free-Piston Engine Generator. SAE Tech. Pap., 2014. doi:10.4271/2014-01-2894.

[112] European commission. State of Art on Alternative Fuels Transport Systems in the European Union. 2015.

[113] Baeyens J, Kang Q, Appels L, Dewil R, Lv Y, Tan T. Challenges and opportunities in improving the production of bio-ethanol. Prog Energy Combust Sci 2015;47:60–88. doi:10.1016/j.pecs.2014.10.003.

[114] Renewable Fuel Association. Going global. 2015 Ethanol Industry outlook. 2015.

[115] U.S. Energy Information Administration. Biofuels: Ethanol and Biodiesel Explained 2015. http://www.eia.gov/Energyexplained/?page=biofuel_ethanol_home (accessed October 8, 2015).

[116] van den Wall Bake JD, Junginger M, Faaij A, Poot T, Walter A. Explaining the experience curve: Cost reductions of Brazilian ethanol from sugarcane. Biomass and Bioenergy 2009;33:644–58. doi:10.1016/j.biombioe.2008.10.006.

[117] Boretti A. Towards 40% efficiency with BMEP exceeding 30 bar in directly injected, turbocharged, spark ignition ethanol engines. Energy Convers Manag 2012;57:154–66. doi:10.1016/j.enconman.2011.12.011.

[118] Imprensa Nacional. Diário Oficial da União 2015:17.

[119] Cairns A, Stansfield P, Fraser N, Blaxill H, Gold M, Rogerson J, et al. A Study of Gasoline-Alcohol Blended Fuels in an Advanced Turbocharged DISI Engine. SAE Int J Fuels Lubr 2009;2:2009–01 – 0138. doi:10.4271/2009-01-0138.

[120] Kapus PE, Fuerhapter A, Fuchs H, Fraidl GK. Ethanol Direct Injection on Turbocharged SI Engines - Potential and Challenges. SAE Tech. Pap., 2007. doi:10.4271/2007-01-1408.

[121] Nakata K, Utsumi S, Ota A, Kawatake K, Kawai T, Tsunooka T. The Effect of Ethanol Fuel on a Spark Ignition Engine. SAE Tech. Pap., 2006. doi:10.4271/2006-01-3380.

[122] Jo YS, Lewis R, Bromberg L, Heywood JB. Performance Maps of Turbocharged SI Engines with Gasoline-Ethanol Blends: Torque, Efficiency, Compression Ratio, Knock Limits, and Octane. SAE Tech. Pap., 2014. doi:10.4271/2014-01-1206.

[123] Thewes M, Müther M, Brassat A, Pischinger S, Sehr A. Analysis of the Effect of Bio-Fuels on the Combustion in a Downsized DI SI Engine. SAE Int J Fuels Lubr 2012;5:274–88. doi:10.4271/2011-01-1991.

[124] Catapano F, Di Iorio S, Sementa P, Vaglieco BM. Characterization of Ethanol-Gasoline Blends Combustion processes and Particle Emissions in a GDI/PFI Small Engine. SAE Tech. Pap., 2014. doi:10.4271/2014-01-1382.

[125] Kim N, Cho S, Choi H, Song HH, Min K. The Efficiency and Emission Characteristics of Dual Fuel Combustion Using Gasoline Direct Injection and Ethanol Port Injection in an SI Engine. SAE Tech. Pap., 2014. doi:10.4271/2014-01-1208.

[126] Taniguchi S, Yoshida K, Tsukasaki Y. Feasibility Study of Ethanol Applications to A Direct Injection Gasoline Engine. SAE Tech. Pap., 2007. doi:10.4271/2007-01-2037.

[127] Stein RA, Anderson JE, Wallington TJ. An Overview of the Effects of Ethanol-Gasoline Blends on SI Engine Performance, Fuel Efficiency, and Emissions. SAE Int J Engines 2013;6:2013–01 – 1635. doi:10.4271/2013-01-1635.

[128] Leone TG, Olin ED, Anderson JE, Jung HH, Shelby MH, Stein RA. Effects of Fuel Octane Rating and Ethanol Content on Knock, Fuel Economy, and CO2 for a Turbocharged DI Engine. SAE Int J Fuels Lubr 2014;7:2014–01 – 1228. doi:10.4271/2014-01-1228.

[129] Yuen PK (P. K., Villaire W, Beckett J. Automotive Materials Engineering Challenges and Solutions for the Use of Ethanol and Methanol Blended Fuels. SAE Tech. Pap., 2010. doi:10.4271/2010-01-0729.

[130] Kar K, Cheng WK. Speciated Engine-Out Organic Gas Emissions from a PFI-SI Engine Operating on Ethanol/Gasoline Mixtures. SAE Int J Fuels Lubr 2009;2:91–101. doi:10.4271/2009-01-2673.

[131] Turner D, Xu H, Cracknell RF, Natarajan V, Chen X. Combustion performance of bio-ethanol at various blend ratios in a gasoline direct injection engine. Fuel 2011;90:1999–2006. doi:10.1016/j.fuel.2010.12.025.

[132] Daniel R, Wang C, Xu H, Tian G, Richardson D. Dual-Injection as a Knock Mitigation Strategy Using Pure Ethanol and Methanol. SAE Int J Fuels Lubr 2012;5:2012–01 – 1152. doi:10.4271/2012-01-1152.

[133] Zhang Y. Experimental investigation of CAI combustion in a two-stroke poppet valve DI engine. PhD thesis, Brunel University London, 2014.

[134] Zhao H, Ladommatos N. Engine combustion instrumentation and diagnostics, SAE International. SAE International; 2001.

[135] Sadakane S, Sugiyama M, Kishi H, Abe S, Harada J, Sonoda Y. Development of a New V-6 High Performance Stoichiometric Gasoline Direct Injection Engine. SAE Tech. Pap., 2005. doi:10.4271/2005-01-1152.

[136] British Standard BS EN 228:2012. Automotive fuels – Unleaded petrol – Requirements and test methods. BSI Standards Limited; 2012.

[137] Andreae MM, Cheng WK, Kenney T, Yang J. On HCCI Engine Knock. SAE Tech. Pap., 2007. doi:10.4271/2007-01-1858.

[138] Eng J a. Characterization of Pressure Waves in HCCI Combustion. SAE Tech. Pap., 2002. doi:10.4271/2002-01-2859.

[139] Xie H, Li L, Chen T, Yu W, Wang X, Zhao H. Study on spark assisted compression ignition (SACI) combustion with positive valve overlap at medium–high load. Appl Energy 2013;101:622–33. doi:10.1016/j.apenergy.2012.07.015.

[140] Rotrex. Rotrex C15 supercharger - Technical datasheet v5.0 n.d. http://www.rotrex.com/Home/Products/Fixed-Ratio-Superchargers (accessed March 10, 2015).

[141] Regulation No 49 - Uniform provisions concerning the measures to be taken against the emission of gaseous and particulate pollutants from compression-ignition and positive ignition engines for use in vehicles. Off J Eur Union 2013.

[142] de Melo TCC, de Brito MFM, Moreira MF, Machado GB, Fleischman R. Calculation of Uncertainty of Measurement for Diesel Engine ESC Test Emissions. SAE Tech. Pap., 2013. doi:10.4271/2013-36-0236.

[143] Wallner T. Correlation Between Speciated Hydrocarbon Emissions and Flame Ionization Detector Response for Gasoline/Alcohol Blends. J Eng Gas Turbines Power 2011;133:082801. doi:10.1115/1.4002893.

[144] Silvis WM. An Algorithm for Calculating the Air/Fuel Ratio from Exhaust Emissions. SAE Tech. Pap., 1997. doi:10.4271/970514.

[145] Olsen DB, Hutcherson GC, Willson BD, Mitchell CE. Development of the Tracer Gas Method for Large Bore Natural Gas Engines—Part II: Measurement of Scavenging Parameters. J Eng Gas Turbines Power 2002;124:686. doi:10.1115/1.1454117.

[146] Douglas R. AFR and Emissions Calculations for Two-Stroke Cycle Engines. SAE Tech. Pap., 1990. doi:10.4271/901599.

[147] Xu RY. A Convenient Technique for Determining Two-Stroke Emission Measurement Accuracy and A/F Ratio. SAE Tech. Pap., 1996. doi:10.4271/961804.

[148] Patankar S V. Numerical Heat Transfer and Fluid Flow. Taylor & Francis; 1980.

[149] Versteeg HK, Malalasekera W. An introduction to computational fluid dynamics: the finite volume method. 2nd ed. Harlow: Pearson Education Limited; 2007.

[150] Fontanesi S, Cicalese G, Severi E. Analysis of Turbulence Model Effect on the Characterization of the In-Cylinder Flow Field in a HSDI Diesel Engine. SAE Tech. Pap., 2013. doi:10.4271/2013-01-1107.

[151] Hanjalić K, Popovac M, Hadžiabdić M. A robust near-wall elliptic-relaxation eddy-viscosity turbulence model for CFD. Int J Heat Fluid Flow 2004;25:1047–51. doi:10.1016/j.ijheatfluidflow.2004.07.005.

[152] AVL LIST GmbH. AVL Fire CFD solver 2009.

[153] Patankar S., Spalding D. A calculation procedure for heat, mass and momentum transfer in three-dimensional parabolic flows. Int J Heat Mass Transf 1972;15:1787–806. doi:10.1016/0017-9310(72)90054-3.

[154] Rech C, Jr FVZ. Time Step Dependence in the Prediction of Flow Dynamics. Int J Mech Eng Autom 2014;1:41–6.

[155] Sjöberg M, Dec JE. An Investigation of the Relationship Between Measured Intake Temperature, BDC Temperature, and Combustion Phasing for Premixed and DI HCCI Engines. SAE Tech. Pap., 2004. doi:10.4271/2004-01-1900.

[156] Hu X, Lokhande BS. Simulation and Validation of IC Engine Swirl/Tumble Using Different Meshing Strategies. SAE Tech. Pap., 2006. doi:10.4271/2006-01-1195.

[157] AVL LIST GmbH. AVL Fire Spray Module 2013.

[158] Dukowicz JK. Quasi-steady droplet change in the presence of convection. n.d.

[159] O'Rourke PJ, Bracco F V. Modeling of Drop Interactions in Thick Sprays and a Comparison With Experiments. Proc Inst Mech Eng Part D J Automob Eng 1980;9:101–16.

[160] Bai C, Gosman a. D. Development of Methodology for Spray Impingement Simulation. SAE Tech. Pap., 1995. doi:10.4271/950283.

[161] AVL LIST GmbH. AVL Fire Wall Film Module 2013.

[162] Su TF, Patterson MA, Reitz RD, Farrell P V. Experimental and Numerical Studies of High Pressure Multiple Injection Sprays. SAE Tech. Pap., 1996. doi:10.4271/960861.

[163] Rotondi R, Bella G. Gasoline direct injection spray simulation. Int J Therm Sci 2006;45:168–79. doi:10.1016/j.ijthermalsci.2005.06.001.

[164] Cheng-jun HEBDU. Spray Characteristics of Various Alcohol - Gasoline Blends. J Ccombustion Sci Technol 2012;18.

[165] Li ZH, He BQ, Zhao H. Application of a hybrid breakup model for the spray simulation of a multi-hole injector used for a DISI gasoline engine. Appl Therm Eng 2014;65:282–92. doi:10.1016/j.applthermaleng.2013.12.063.

[166] Aleiferis PG, Van Romunde ZR. An analysis of spray development with iso-octane, n-pentane, gasoline, ethanol and n-butanol from a multi-hole injector under hot fuel conditions. Fuel 2013;105:143–68. doi:10.1016/j.fuel.2012.07.044.

[167] Wang Z, Qi Y, He X, Wang J, Shuai S, Law CK. Analysis of pre-ignition to super-knock: Hotspot-induced deflagration to detonation. Fuel 2015;144:222–7. doi:10.1016/j.fuel.2014.12.061.

[168] P. J. Brandham, Benson RS. A method for obtaining a quantitative assessment of the influence of charge efficiency on two stroke engine performance. IntJMechSci11303 1969;11:303–12.

[169] Benajes J, Novella R, De Lima D, Tribotte P. Analysis of combustion concepts in a newly designed two-stroke high-speed direct injection compression ignition engine. Int J Engine Res 2014;16:52–67. doi:10.1177/1468087414562867.

[170] Costa M, Allocca L, Montanaro A, Sorge U, Iorio B. Multiple Injection in a Mixed Mode GDI Boosted Engine. SAE Tech. Pap., 2010. doi:10.4271/2010-01-1496.

[171] Li Y, Zhao H, Stansfield P, Freeland P. Synergy between Boost and Valve Timings in a Highly Boosted Direct Injection Gasoline Engine Operating with Miller Cycle. SAE Tech. Pap., 2015. doi:10.4271/2015-01-1262.

[172] Augoye A, Aleiferis P. Characterization of Flame Development with Hydrous and Anhydrous Ethanol Fuels in a Spark-Ignition Engine with Direct Injection and Port Injection Systems. SAE Tech. Pap., 2014. doi:10.4271/2014-01-2623.

[173] de O. Carvalho L, de Melo TCC, de Azevedo Cruz Neto RM. Investigation on the Fuel and Engine Parameters that Affect the Half Mass Fraction Burned (CA50) Optimum Crank Angle. SAE Tech. Pap., 2012. doi:10.4271/2012-36-0498.

[174] Caton J a. Combustion phasing for maximum efficiency for conventional and high efficiency engines. Energy Convers Manag 2014;77:564–76. doi:10.1016/j.enconman.2013.09.060.

[175] Chen SK, Flynn PF. Development of a Single Cylinder Compression Ignition Research Engine. SAE Tech. Pap., 1965. doi:10.4271/650733.

[176] Ricardo plc. Ricardo WAVE 8.4 user manual 2011.

[177] Rotrex superchargers A/S n.d. http://www.rotrex.com (accessed September 18, 2015).

[178] Kawamoto M, Honda T, Katashiba H, Sumida M, Fukutomi N, Kawajiri K. A Study of Center and Side Injection in Spray Guided DISI Concept. SAE Tech. Pap., 2005. doi:10.4271/2005-01-0106.

Appendix

Publications related to this research

Dalla Nora M, Zhao H. High load performance and combustion analysis of a four-valve direct injection gasoline engine running in the two-stroke cycle. Applied Energy 2015;159:117–31. doi:10.1016/j.apenergy.2015.08.122.

Dalla Nora M, Zhang Y, Lanzanova T, Pedrozo V B, Zhao H. Extreme engine downsizing by doubling the firing frequency in a boosted direct injection gasoline engine. Internal Combustion Engines Conference, Institution of Mechanical Engineers (IMechE), 2-3 December 2015, London.

Dalla Nora M, Lanzanova T, Zhang Y, Zhao H. Engine downsizing through two-stroke operation in a four-valve GDI engine. SAE Tech. Pap., 2016. doi:10.4271/2016-01-0674.

Zhang Y, Dalla Nora M, Zhao H. Investigation of Valve Timings on Lean Boost CAI Operation in a Two-stroke Poppet Valve DI Engine. SAE Tech. Pap., 2015. doi:10.4271/2015-01-1794.

Zhang Y, Dalla Nora M, Zhao H. Comparison of Performance, Efficiency and Emissions between Gasoline and E85 in a Two-Stroke Poppet Valve Engine with Lean Boost CAI Operation. SAE Tech. Pap., 2015. doi:10.4271/2015-01-0827.